École doctorale n° 432 : Sciences des Métiers de l'ingénieur

Doctorat

T H È S E

pour obtenir le grade de docteur délivré par

l'École Nationale Supérieure d'Arts et Métiers

Spécialité " Génie Mécanique – Procédés de Fabrication "

présentée et soutenue publiquement par

Wenyu CHENG

le 11 Décembre 2019

Modélisation de l'usinage de l'alliage de titane Ti-6Al-4V utilisant un modèle constitutif prenant en compte l'état de contrainte dans la zone de déformation

Modelling of machining of Ti-6Al-4V titanium Alloy using a constitutive model accounting for the state of stress in the deformation zone

Directeur de thèse : **José OUTEIRO**
Co-Directeur de thèse : **Jean-Philippe COSTES**

Jury
M. Philippe Lorong, Professeur des Universités, PIMM, Arts et Métiers — Président
M. Volker Schulze, Professor, wbk, Karlsruher Institut für Technologie — Rapporteur
M. Pedro Rosa, Professor, IDMEC, Universidade de Lisboa — Rapporteur
M. Abdelhadi Moufki, Professeur des Universités, LEM3, Université de Lorraine — Examinateur
M. José Outeiro, Maître de Conférences - HDR, LaBoMaP, Arts et Métiers — Examinateur
M. Jean-Philippe Costes, Maître de Conférences - HDR, LaBoMaP, Arts et Métiers — Examinateur
M. Rachid M'Saoubi, PhD, Seco Tools AB — Invité
M. Habib Karaouni, PhD, Safran Tech — Invité

T
H
È
S
E

Arts et Métiers - Campus de Cluny
Laboratoire Bourguignon des Matériaux et Procédés

Arts et Metier Institute of Technology

Modelling of machining of Ti-6Al-4V titanium Alloy using a constitutive model accounting for the state of stress in the deformation zone

Wenyu CHENG

2019[©]

Acknowledgements

Lucas Putigny, Stéphane Derom, and Engineers Gilles Detroyat, Jean-Claude Butaud and Denis Lagadrillère.

I am thankful to my colleagues and best friends in LaBoMaP for their interest in my work and for all the great memories, Pierre Lequien, Johan Merzouki, Tristan Régnier, Rémi Curti, Iheb Cherif, Rabiae Arif, Yutao Zhang, Edouard Ducroux, Bastien Toubhans, Come Legrand, Ivan Hamm, Francisco Silva, Seifeddine MEJRI and, Xiang Xu and Guangchao Nie.

I would like to thanks to my friends Yutao Zhang, Yao Xiao, Ronghua Ma, Jun Gao for the alleviation of the research pressure and sharing of practical life advice.

Finally, and most importantly, special thanks are given to my whole family for their unconditional support in these three years. Thanks to my brother Wenguang Cheng who always listens to me and takes care of me. Thanks to my true love Li Li for her understanding when I am overstressed, for her encouragement when I am depressed, and for her company when I am lonely. The last of last, thanks are given to my parents.

Table of contents

Nomenclature

a	(mm)	Minimum radius of the neck cross section of round bars
$A,\ m,\ n,\ B,\ C,\ E,$ $c_\eta, c_\theta^t, c_\theta^c, c_\theta^s,\ a$	(-)	Material coefficients used in the proposed plasticity model
A_c	(mm^2)	Shearing area
a_C, b_C, c_C, d_C	(-)	Material constants in model proposed by Calamaz et al.
a_e	(mm)	Axial depth of cut
$A_{jc}, B_{jc}, C_{jc}, m_{jc}, n_{jc}$	(-)	Coefficients of the J-C plasticity model
a_p	(mm)	(Radial) depth of cut
$A_U, B_U, C_U, H_U, E_U, n_U, m_U,$ $D_U, D_{1U}, D_{2U}, D_{3U}$	(-)	Material coefficients in model proposed by Umbrello et al.
$B_{ZA}, \beta_0, \beta_1, B_0, \alpha_0, \alpha_1$	(-)	Material coefficients in Z-A model
b_{ZH}, m_{ZH}	(-)	Material coefficients in Z-H equation
C_{0ZH}, C_{1ZH}	(-)	Material coefficients in $H\text{-}P$ equation
C_{1R}, C_{2R}	(-)	Material coefficients in Rice and Tracey model
c_p	(J/kg/^{o}C)	Specific heat of material
C_{US}, n_D, m_D	(-)	Coefficients of friction model
d_0	(μm)	Initial grain size in Z-H equation
$D_1\text{-}D_{7,}\ \lambda,\ G_f$	(-)	Material coefficients in proposed damage model
$D_{1jc} - D_{5jc}$	(-)	Damage coefficients of the J-C damage model
D_{CL}	(-)	Damage parameter of Cockroft and Latham model
D_{de}	(-)	Scalar internal variable in damage evolution model
D_w	(mm)	Diameter of the workpiece
E	(MPa)	Young's modulus
f	(mm/rev)	Feed
F_c	(N)	Cutting force
F_n	(N)	Normal force
F_s	(N)	Shear force
F_T	(N)	Thrust force
G_f	(KJ/m^2)	Fracture energy
h	(mm)	Uncut chip thickness
H_0	(-)	Null hypothesis
h_{cv}	(W/kg/^{o}C)	Convection heat transfer coefficient of the process
I_1	(-)	First stress invariant
J_3	(-)	Third deviatoric stress invariant
K_c	(KJ/m^2)	Fracture toughness
l	(mm)	Characteristic length of the finite element
n_T	(rev/min)	Rotational speed
Pe	(-)	Péclet number
P_n	(-)	Normal plane
P_r	(-)	Reference plane
P_s	(-)	Cutting edge plane
P_{sp}	(bar)	Shot-peening pressure
R	(mm)	Local radius of the neck of round bars

r_ε	(mm)	Nose radius
r_n	(μm)	Edge radius
S_s	(MPa)	Shear strength of the work material
T_{melt}	(°C)	Melting temperature of the workpiece material
T_{room}	(°C)	Reference ambient temperature
$\bar{u}$	(mm)	Equivalent plastic displacement
T_{sp}	(s)	Shot-peening time
V_c	(mm/min)	Cutting speed
V_f	(mm/min)	Feed rate
$w_1, w_2, A_{wi}, \alpha_{wi}, \gamma_{wi}, \beta_{wi}$	(-)	Material constants in Wilkins damage model
α	(°)	Clearance angle
$\dot{\gamma}_S$	(/s)	Shear strain rate
γ_S	(-)	Shear strain
γ	(°)	Rake angle
$\dot{\varepsilon}_0$	(/s)	Reference strain rate
$\bar{\varepsilon}_f^p$	(-)	Plastic strain at fracture
$\bar{\varepsilon}_i^p$	(-)	Plastic strain at damage initiation
η_0	(-)	Reference stress triaxiality
η	(-)	Stress triaxiality
$\bar{\theta}$	(-)	Lode angle parameter
θ	(°)	Lode angle
κ_r	(°)	Cutting edge angle
κ'_r	(°)	Minor cutting edge angle
λ_s	(°)	Inclination angle
λ	(W/m/°C)	Thermal conductivity
$\bar{\mu}_f$	(mm)	Equivalent plastic displacement at complete fracture
μ	(-)	Coefficient of friction
ζ	(-)	Chip compression ratio
$\bar{\sigma}$	(MPa)	True equivalent stress
$\tilde{\sigma}$	(MPa)	Hypothetical undamaged equivalent stress
$\sigma_1, \sigma_2, \sigma_3$	(MPa)	Principal stress
σ_a	(MPa)	Athermal stress
σ_d	(MPa)	Dislocation drag stress
σ_n	(MPa)	Normal stresses perpendicular to tool rake face
σ_{th}	(MPa)	Thermal stress
τ	(MPa)	Frictional stress
τ_p	MPa)	Shear flow stress
ν	(-)	Poisson's ratio
φ	(°)	Shear angle

Abbreviation

ALE	Arbitrary lagrangian-eulerian
ANOVA	Analysis of Variance
ASA	Adaptive simulated annealing
B-W model	Bai-Wierzbicki model
BUE	Built-up edge
BUL	Built-up layer
CCR	Chip compression ratio
CMM	Coordinate-measuring machine
CMS	Curve mapping segment
DE	Discrete element
Depth MRS	Depth below surface as MRS is achieved
DIC	Digital image correlation technique
DN	Double notched
DoE	Design of Experiments
Dof	Degrees of freedom
FDZ	First deformation zone
FE	Finite element
FWHM	Full Width at Half Maximum
H-P	Hall–Petch
HSM	High speed machining
J-C model	Johnson-Cook model
Layer RS	Thickness of the layer affected by the residual stress
LFOP	Leapfrog Optimizer for Constrained Minimization
MRR	Material removal rate
MRS	Maximum residual stress in compression direction
MSE	Mean squared error
MTS	Mechanical threshold stress
NFP	Notched flat plate
NRB	Notched round bar
OC	Orthogonal cutting
OFHC	Oxygen Free High Conductivity copper
SDZ	Second deformation zone
SHPB	Split hopkinson pressure bar
SPH	Smoothed particle hydrodynamics
SRB	Smooth round bar
SRS	Residual stress near the surface
SSB	Variability between group means
SSE	Variability within groups means
SST	Sum of SSB and SSE
TDZ	Third deformation zone
TTL	Transistor-transistor logic
XRD	X-ray powder diffraction
Z-A model	Zerilli and Armstrong model
Z-H	Zener–Hollomon
ZOI	Zone of interest

Introduction

Titanium alloys are widely used in the aero plane industry due to their super mechanical properties, such as high strength/weight ratio, acceptable mechanical strength at high temperatures, high resistance to creep and corrosion. Besides these excellent performances, the cost is another determining factor to select the design material in aero plane industry. The castability, formability, machinability and weldability have a great impact on the cost. The demands of aero industry are to ensure the performance of components while simultaneously minimize the overall costs. Therefore, titanium alloys, as difficult-to-machine alloys, mount a great challenge to the researchers.

Finishing turning is one of the machining operations frequently used in the modern industry to produce the high value-added parts, such as the components of aeroengine and airframe. During the machining process, the quality and performance of workpiece directly depend on the surface integrity. However, owing to its poor machinability, the surface of Ti-6Al-4V alloy is easily damaged in the machining procedure. Additionally, high tensile stresses are usually distributed on the machined surface, and these stresses decrease at a high rate in depth direction, reaching a maximum compressive residual stress in the sub-surface layer. The tensile residual stresses on the surface of the material would cause crack initiation and fatigue failure of machined products. Besides the residual stress, the surface integrity includes surface hardness, roughness, grain size and phase transformation. They are affected by the cutting tools and cutting parameters. Cutting speed values can affect the amount of microchip debris on the surface, and material plucking, tearing, dragging, and smearing can be affected by depth of cut among other parameters [1]. The super-finishing cutting edge of the inserts substantially enhances the tool life during the high speed machining of Ti-6Al-4V titanium alloy [2]. In this case, the copious investigations are performed to predict the surface integrity and optimize the machining process.

In machinability studies, statistical design of experiments is a practical method to investigate the relation between cutting parameters and test results. However, the large number of tests means a high cost and considerable efforts, while the small test size could not accurately estimate the effects of all the investigated cutting parameters. Moreover, not all the desired information could be easily obtained from the experiments. For instance, the observation of plastic deformation of the workpiece in first deformation zone needs a well-designed experimental setup. As a result, there has been increasing focus on the numerical methods to enhance the product quality and machining efficiency. Compared with the high cost of physical

experiments for the optimization, finite element modelling and simulation of machining of such difficult-to-cut materials offer an attractive and cost-effective choice. The predictive ability of such simulations depends on several factors, including the constitutive model, boundary condition, friction model and chip formation technique. Concerning the constitutive model, it should take into account not only the determination of the material plasticity under similar conditions as those observed in machining, but also under which conditions the fracture would occur and how to model it properly. In this case, the objective of this PhD thesis is to develop a constitutive model for accurate prediction of the surface integrity induced by machining Ti-6Al-4V alloy.

This thesis report is composed of five chapters, which are organized as follows.

Chapter 1 presents a literature review about metal cutting process, surface integrity and modelling and simulation. First, metal cutting fundamentals are presented, including the definition, theory and a short description of the turning operation. Then, recent research works on surface integrity generated by machining of Ti-6Al-4V alloy are described, in particular, the effect of cutting parameters on the residual stress distribution in the machined surface and subsurface. Finally, the existing numerical models of machining Ti-6Al-4V alloy are reviewed, with special attention to the constitutive models and corresponding tests used to characterize the mechanical behavior of metallic materials.

Chapter 2 describes the formulation of the proposed constitutive model based on existing models from literature. Different parameters influencing the mechanical behavior of the work material in metal cutting are analysed, including the strain hardening, strain rate, state of stress, microstructure and temperature. Then, the most relevant parameters affecting the mechanical behavior of Ti-6Al-4V in machining are included in the constitutive model to obtain simple and effective equations. This constitutive model includes both plasticity and damage parts (damage initiation and damage evolution).

Chapter 3 describes the complete procedure to determine the coefficients of the proposed constitutive model. To generate the states of stress and the strain rates representative of machining operations, mechanical tests are performed using a specially designed experimental setup. This includes a specimen geometry designed to generate different states of stress, as well as a digital image correlation technique (DIC) to obtain the strains during the mechanical tests. For the determination of the coefficients of the constitutive model, the yield stress and fracture

locus obtained from these tests are used in an optimization-based procedure. This procedure is implemented in LS-Dyna/LS-Opt software, connected with ABAQUS for the numerical simulations. The proposed constitutive model is imported in ABAQUS software through both VUMAT and UMAT subroutines. To verify the accuracy of the proposed constitutive model to represent the mechanical behavior of the Ti-6Al-4V alloy under different states of stress, force-displacement curves obtained using this model and the Johnson-Cook (*J-C*) model are compared with the curves obtained experimentally.

In Chapter 4, an orthogonal cutting (OC) model of Ti-6Al-4V alloy including the proposed constitutive model is developed and applied to predict the forces, chip geometry, chip compression ratio (CCR), residual stresses distributions in the machined surface and subsurface, and thickness of plastically deformed layer. To determine the accuracy of the OC model to predict the above-presented results, orthogonal cutting tests and residual stress analysis by X-ray diffraction are performed, followed by a comparison between simulated and experimental results.

In Chapter 5, turning model of Ti-6Al-4V alloy including the proposed constitutive model is developed and applied to predict the forces, chip geometry, residual stresses distributions in the machined surface and subsurface and thickness of plastically deformed layer. To determine the accuracy of the turning model to predict the above-presented results, turning tests and residual stress analysis by X-ray diffraction are performed, followed by a comparison between simulated and experimental results.

Chapter 1:
Literature review

1.1 Metal cutting fundamentals

1.1.1 Metal cutting definition

Metal cutting is one of the oldest processes for shaping components in the manufacturing industry. There are three principal operations: turning, drilling and milling. Astakhov [3] introduced the system concept into metal cutting. According to this concept, the process of metal cutting is defined as a forming process, which the external energy is applied to the cutting system causing the purposeful fracture of the layer being removed. Based on this definition, the following features illustrate the reasons why metal cutting is different from the other closely related manufacturing processes and operations [4]:

1) Bending moment: the bending moment forms the combined stress in the deformation zone which significantly reduces the resistance of the work material being cut.

2) Purposeful fracture of the layer being removed under combined stress. The fracture occurs in each successive cycle of chip formation. Atkin [5] also presented that the fracture is a significant component of total cutting work.

3) Stress singularity at the cutting edge: the maximum combined stress does not occur at the cutting edge, whereas a crack forms in front of the cutting edge. In this case, the tool wear occurs at a certain distance from the cutting edge that allows it to maintain the accuracy of metal cutting over the entire time of tool life.

4) Cyclical nature: metal cutting is inherently a cyclical process. A single chip fragment forms in each chip formation cycle. As a result, considered at the appropriate magnification, the chip structure consists of chip fragments and connectors. Based on simulation results in literature, the maximum stress, the size of the region of high stresses in the workpiece ahead of the cutting tool and the temperature in first deformation zone vary cyclically during the cutting process, which validate the cyclical nature of metal cutting [6].

1.1.2 Metal cutting theory

Researchers provide different models to analyze processes of metal cutting. However, several assumptions of these models are not realistic and influence the accuracy of predicted results. There are two typical analytical models: single-shear plane model and shear-zone model.

1.1.2.1 Single shear plane model

The single-shear plane model was originally introduced in 1870 by Time [7]. It is the most usual model used in the textbooks due to its simplicity. It is developed by using the orthogonal cutting (OC), as shown in Fig. 1. Constant t_1 represents the thickness of uncut chip which is removed by shearing during the tool advancement. The shear zone is quite thin compared with its length, i.e. shear plane AB. The angle between the shear plane and the machined surface is called shear angle, represented by φ. Other two important angles which determine the characteristics of the metal cutting process are the rake angle (γ) and the clearance angle (α). Rake angle is an angle between newly machined surface and the rake face where chip and tool keep in contact, while the clearance angle is an angle between newly machined surface and the tool flank face.
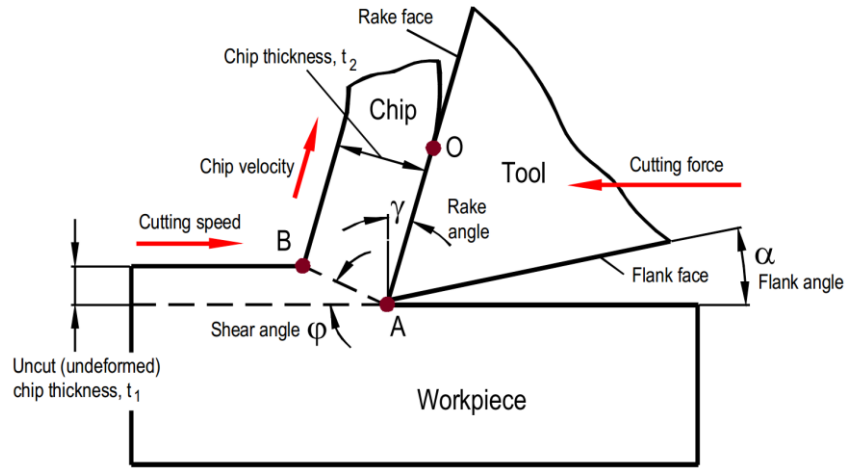
Fig. 1: Single-shear plane model [8].

As the tool moves, the layers being cut becomes chip and slides along the rake face of the tool. Due to the sever plastic deformation, the chip curls away from that face beyond a particular point O. The constant t_2 is the thickness of the chip. Thus, chip compression ratio (*CCR*) ζ is defined as the ratio between the chip thickness and the uncut chip thickness as shown in Eq.1:

$$\zeta = \frac{t_2}{t_1} = \frac{V_c}{V_1} \quad (\zeta > 1)$$

Eq. 1

where V_c is the cutting speed, V_1 is the chip speed. Then the shear angle is calculated in Eq. 2.

6

$$\varphi = \arctan\left(\frac{\cos\gamma}{\zeta - \sin\gamma}\right)$$

<div align="right">*Eq. 2*</div>

In the analysis of metal cutting process, three deformation zones in the cutting process are used to characterize the mechanical, tribological and surface engineering aspects, as shown in Fig. 2.

1) Zone I - First deformation zone (FDZ): intense plastic deformation take place in this zone as the edge of the tool moves. High heat is generated by the severe plastic deformation in this zone.

2) Zone II - Secondary deformation zone (SDZ): The deformation is due to the friction between the chip and the rake face of the tool.

3) Zone III - Third deformation zone (TDZ): When the flank surface of tool rubs the machined surface, an intense deformation in this zone is produced. This can influence the surface integrity of the workpiece, such as the residual stresses and the surface roughness.
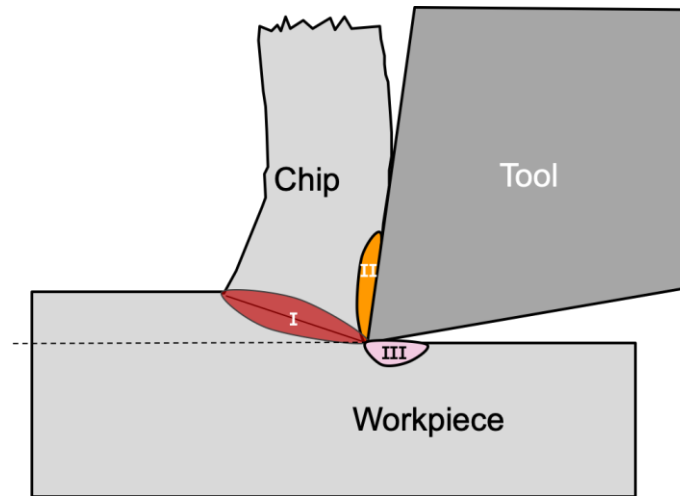
Fig. 2: Deformation zones in metal cutting.

To analyse the cutting process, Merchant [9] adds a force diagram to the model. It is illustrated in Fig. 3. The total force is represented by a pair of forces, R (that the workpiece applies to the chip) and R' (that the tool applies to the chip) which holds the chip in equilibrium. R' is resolved into F the tangent to the tool rake face and N the normal to the rake face, and the tangent of the angle between R' and N is the friction coefficient μ. In contrast, R can be resolved in two ways: the first is into F_n (normal force) describing the compression on the shear plane and F_s (shear

force) causing the workpiece's deformation. The second is into F_c (cutting force) and F_T (thrust force). Based on this force diagram, the cutting force can be deduced by Eq. 3.

$$F_c = \frac{S_s \cdot A_c \cdot \cos(\mu - \gamma)}{\sin\varphi \cdot \cos(\varphi + \mu - \gamma)}$$

Eq. 3

Where S_s is the shear strength of the work material and A_c is the shearing area.
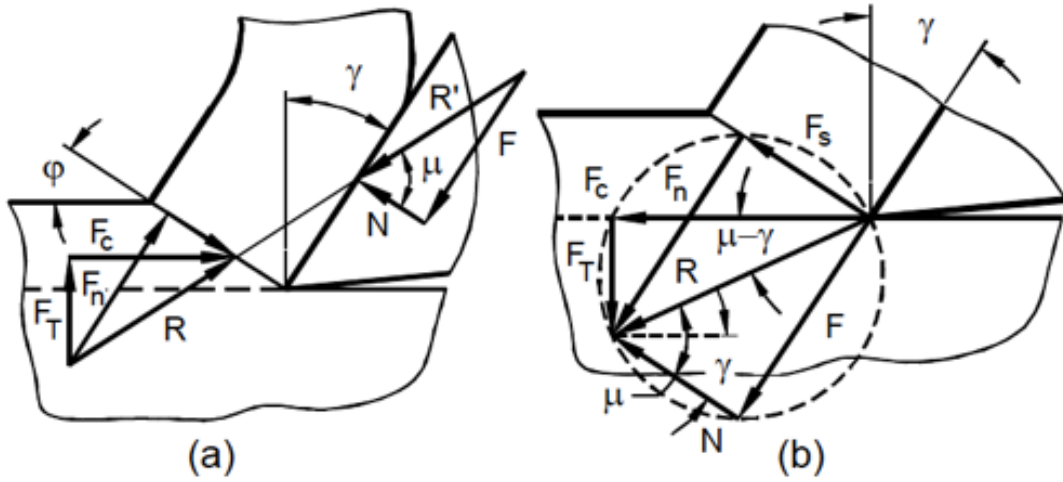
Fig. 3: (a) original and (b) modified force diagrams [9].

Another model can be cited: the card model, as shown in Fig. 4, proposed by Piispanen. It is introduced to explain the formation of chips in the metal cutting process. Merchant used it to illustrate shear strain and velocity diagram [9].
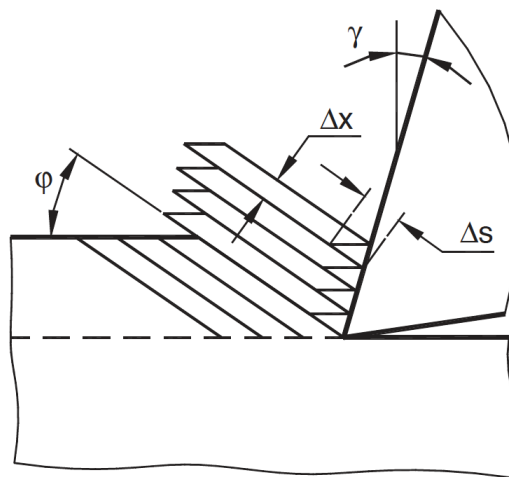
Fig. 4: Card model to represent chip formation [10].

The thickness of a card-like element is assumed to be tiny, Δx, which keeps the continuity of the workpiece. Each element keeps a constant distance Δs with its neighbour along the normal

direction of thickness. The shear strain γ_S and shear strain rate $\dot{\gamma}_S$ can be expressed by the following equations:

$$\gamma_S = \frac{\Delta s}{\Delta x} = \frac{\cos\gamma}{\cos(\varphi-\gamma)\sin\varphi} = \frac{\zeta^2 - 2\zeta\sin\gamma + 1}{\zeta\cos\gamma} \qquad \text{Eq. 4}$$

$$\dot{\gamma}_S = \frac{\Delta s}{\Delta x \cdot \Delta t} = \frac{\cos\gamma}{\cos(\varphi-\gamma)}\frac{V_c}{\Delta y} \qquad \text{Eq. 5}$$

However, the values of the shear strain calculated using Eq. 4 for several cutting conditions are much higher than the fracture strain. Furthermore, when $\zeta=1$, the chip thickness is equal to the uncut chip thickness. According to Astakhov and Shvets [11], this reveals a contradiction. Since CCR is a measure of plastic deformation, this indicates that no plastic deformation occurs, but the shear strain given by Eq. 4 remains significant [11].

The calculation of the shear strain rate highly depends on the assumed thickness of the shear plane according to Eq. 5. Therefore, the calculated shear strain rate is extremely high, ranging from 10^4/s to 10^6/s or even more. This high value means that the plastic deformation observed in metal cutting should be governed by twinning instead of the slip-line theory. However, the observed micrographs of the chip deformation zone shows that the typical plastic deformation in metal cutting is caused by slip [3]. Additionally, Ernst and Merchant model induces several drawbacks, including the incorrect velocity and force diagrams and the assumption of constant friction coefficient [132]. For instance, the bending moment because of the parallel shift of the resultant cutting force is not considered in the force diagram.

1.1.2.2 Shear zone model

Considering all these inadequacies in the single shear model, the shear zone model was introduced to analyze the metal cutting process. It includes two types: one is the Zorev's pie-shaped shear zone model [13] and the Oxley's parallel-sided shear zone model [14].

The pie-shaped shear zone mode is shown in Fig. 5a. The line OL means the first plastic deformation occurring as shear, line OM along means the last shear deformations occurring, and line LM is the deformed section of the workpiece free surface. The line OP, called specific shear plane by Zorev, passes through the cutting edge, the line of intersection of the outer surface of the layer being removed, and the chip. The definition of shear plane angle φ_{sp} is

similar to the shear angle defined in the single shear model. The strain rate and the strain can be calculated based on the observed plastic flow patterns in the experiments.

The parallel-sided shear zone model is shown in Fig. 5b. The plastic deformation is assumed to begin at the line CD (inlet boundary) inclined to the free surface at an angle corresponding to the shear angle and to end at the line EF (outlet boundary). Both two lines are assumed to be parallel to the shear plane AB. The thickness of this first shear zone is h and separated by the shear plane, line AB. Astakhov et al. [15] use this model to analyze the velocity diagram in the orthogonal metal cutting. The shear zone is divided into two unequal regions, one part is wide region where the velocity change takes places at a low rate, and the other is the narrow region where this change takes place at a high rate. The experimental results of microhardness tests and metallographically study validate this theory.

(a)   (b)
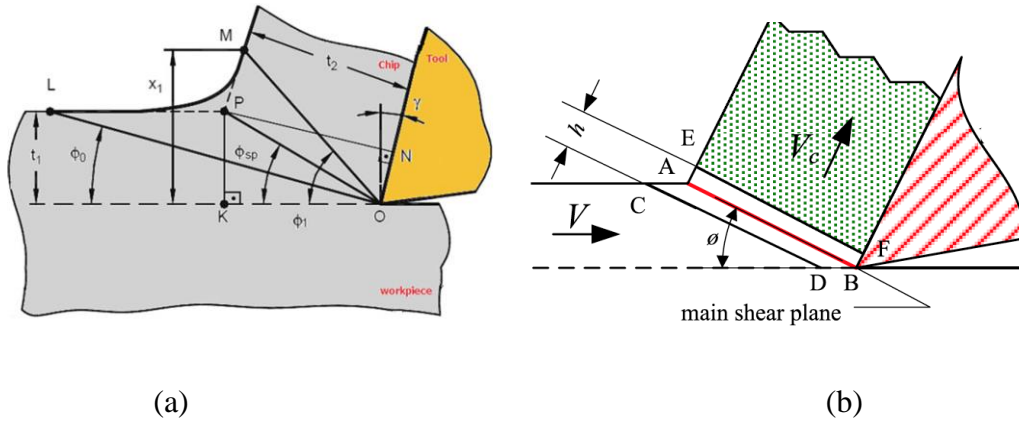
Fig. 5 Shear zone model: (a) pie-shaped shear zone model [13]; (b) parallel-sided shear zone model [14].

1.1.3. Longitudinal turning operation

Turning is one of the most well-known and commonly used operation, and the industrial demands on chip control, process efficiency and surface integrity are high. During the turning process, the cylindrical workpiece performs the rotary motion while the tool carries out the translational motion. Fig. 6 illustrates a typical turning configuration. The motion of the tool is called feed, and is represented by f. When the feed is parallel to the axial direction, the operation is known as the longitudinal turning. The feed direction of face turning is parallel to the radial direction. Profiling turning occurs when the feed direction adjusts according to the profile of the machined workpiece due to coordinated feed motions along the coordinate axes. The tool cutting edge angle and depth of cut are represented by κ_r and a_p respectively. The cutting speed,

V_c, is the rate at which the workpiece surface is passed by the cutting edge. It is calculated by Eq. 6:

$$V_c = \frac{\pi D_w n_T}{1000} \quad (m/min)$$

Eq. 6

where D_w is diameter of the workpiece in millimetres (mm), and n_T is the rotation speed in rev/min (or r.p.m.).

In the practical metal cutting process, the rotation speed is calculated based on the given cutting speed and workpiece, then this speed is applied into the spindle of the machine. In contrast, the feed motion is provided to the tool or the workpiece. The feed rate, V_f, is calculated in Eq. 7.

$$v_f = f \cdot n_T = f \cdot \frac{1000 V_c}{\pi D_w} \quad (mm/min)$$

Eq. 7

where f is feed in the unit of mm/rev. It is the distance at which the tool advanced into the workpiece per one revolution.
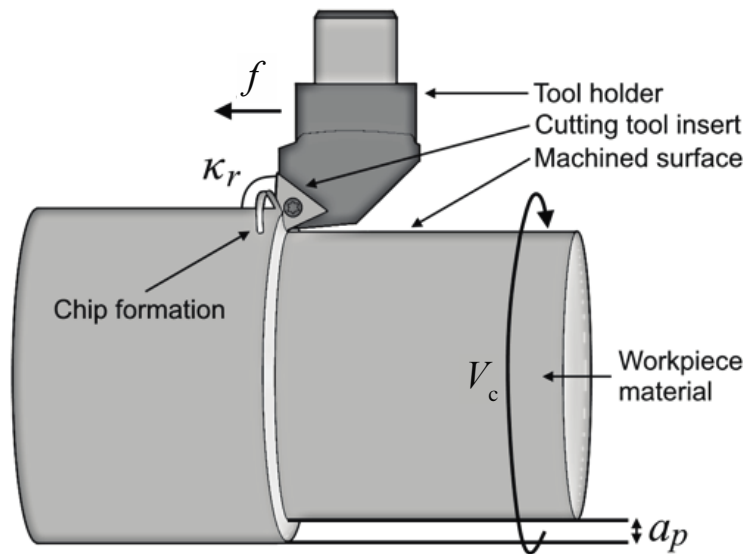
Fig. 6 Schematic illustration of the turning operation.

To evaluate how fast the metal cutting operation can remove the material from the workpiece, the material removal rate, MRR, is introduced. It is calculated in Eq. 8. The MRR is increased when the cutting speed, feed or depth of cut are raised under certain demands on tool life, surface finishing, efficiency of metal cutting, etc.

$$MRR = V_c \cdot f \cdot a_p \qquad\qquad \text{Eq. 8}$$

1.2 Surface integrity in metal cutting titanium alloys

1.2.1 General properties and applications of Ti-6Al-4V alloy

The use of titanium and its alloys has increased recently owing to its outstanding properties and improvements of their machinability. It has been applied into many fields: aerospace, automobile production, dentistry or other biomechanical applications. This alloy has a useful application property, including high strength/weight ratio, good fatigue strength with intermediate fracture toughness. Apart from those mentioned performances, the main drivers for titanium's use in aerospace applications are excellent corrosion resistance, maintenance of strength and hardness at high temperature and relatively low density. Compared with the stainless steel, it has much better corrosion resistance when applied in the sea or moist atmosphere. Specifically, it could resist pitting corrosion, acid corrosion and stress corrosion well. At temperatures between 300°C and 500°C, its strength is about ten times higher than the aluminium alloy. The main area of application for aerospace titanium alloys is in the gas turbine engine. Approximately one third of the structural weight of modern turbine engines is made up of titanium [16]. The fan blades and disks of jet engine are normally manufactured from Ti-6Al-4V alloy. It is shown in Fig. 7.
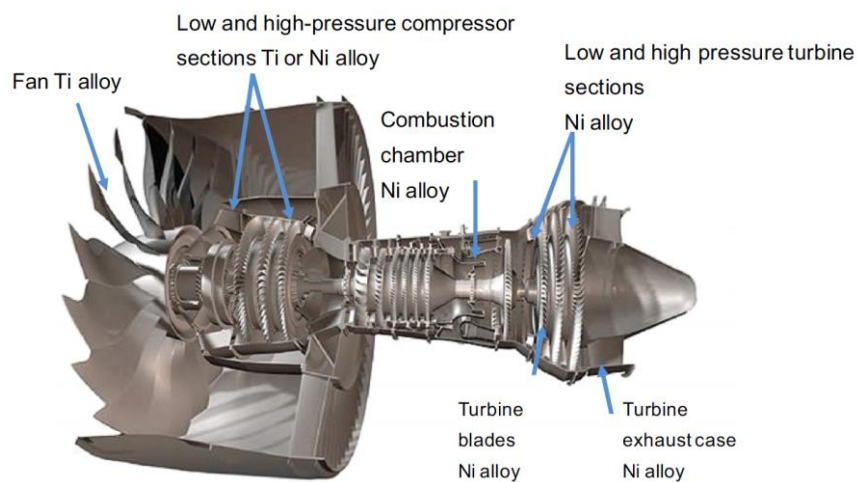
Fig. 7: Cross section of a jet engine [23].

Other important applications of Ti-6Al-4V appear in the medical field. It is widely used in the implant of bones owing to its properties [17]. As a biomaterial, it fulfils well the following requirements: corrosion resistance; biocompatibility; bio-adhesion; favourable mechanical

properties; process ability (casting, deformation, powder metallurgy, machinability, welding, brazing) and cost [18].

1.2.2 Machinability of Ti-6Al-4V alloy

Machinability is the term used to describe how easily a material can be cut to the desired shape (surface finish and tolerance) with respect to the tooling and metal cutting processes involved [19]. There are several standards to evaluate the machinability, including cutting tool life, metal removal rate and surface integrity of the machined workpiece. However, the superior physical properties of titanium alloys, induce poor machinability [20]. The properties responsible for those drawbacks are:

1) Strain rate sensitivity and readily work hardening.
2) Poor thermal conductivity leading to high cutting temperature, that leads to increased wear of the cutting tools.
3) High chemical affinity of cutting tools leading to diffusion wear.
4) Low modulus of elasticity of titanium leads to significant spring back after deformation under load. This causes titanium parts to move away from the cutting tool during metal cutting.
5) Vibration of machine tool systems due to high cutting forces.

Several papers aimed to find the optimal combinations of cutting tools and cutting parameters to improve workpieces machinability. This object can be resolved into two contents: enhance the life of the cutting tool and ensure good surface integrity after metal cutting. There are several kinds of materials of cutting tools for cutting these difficult-to-machine alloys. These tools need to satisfy the following requirements: good wear resistance; high strength and toughness; good thermal shock properties and adequate chemical stability at elevated temperature [21].

1.2.3 Surface integrity of titanium alloy

In the sector of energy, aerospace and biomedical field, the need for excellent performance of the material, especially alloys, never ceases. This performance includes usually good chemical stabilities and high mechanical properties. However, it is difficult to machine such materials, and sometimes metal cutting process even damages the performance of the workpiece. Additionally, the surfaces produced by the cutting process play an important role in the functional performance and life of the workpieces. Numerous researchers focus on developing

new production methods and high manufacturing technologies to improve the surface integrity. In our case, surface integrity is defined as the inherent or enhanced condition of a surface produced by the metal cutting process. It can be categorized into three aspects:

1) The topological state, including the surface roughness and defects;
2) The metallurgical state, including the microstructure, the phase transformation, and the grain size and shape;
3) The mechanical state, including the residual stresses and the hardness;

Titanium alloys are generally used for a component, which require the greatest reliability, and therefore the surface integrity must be maintained. However, during metal cutting and grinding operations, the surface of titanium alloys is easily damaged because of their poor machinability. Several studies on surface integrity parameters have been carried out, and the following section will introduce the recent advances of surface integrity in Ti-6Al-4V alloy metal cutting.

1.2.3.1 Topological state

The topological state of the machined surface is the direct criterion to evaluate the surface integrity, including the carbide cracking, feed marks, surface tearing and cavities, micro-cracks, etc. The cutting parameters can affect these defects to a certain level.

Fig. 8 shows the feed marks in the surface after turning Ti-6Al-4V with PCD inserts under coolant flow [22] and the surface after milling Ti-6242S [1]. As can be seen in Fig. 8a, the surfaces generated consist of well-defined uniform feed marks running perpendicular to the tool feed direction. Deformation of feed marks occurs as a result of plastic flow of material during the cutting process. In Fig. 8b, the lay pattern is produced by the feed marks due to tool rotation and the tool movement in feed direction. Although feed marks are effective in metal cutting, their severity can be altered by varying and optimizing the feed rate [1].

Other than the feed marks, there are several other surface defects including carbide cracking, tearing surface and built-up layer, as can be seen in Fig. 9. The carbide cracking means carbide particles moving from the machined surface or the tool to get stuck on the workpiece surface. This phenomenon is often observed in the titanium and Inconel alloys, which makes the fatigue life of the workpieces decrease substantially [23]. Fig. 9a shows the micro-pit inside the machined surface attributed to brittle fractures of hard carbide inclusion within the immediate surface [22]. The carbide particles from the strengthening components are considered to be

unable to deform, which makes them to be removed completely at once, leaving cavities behind. Fig. 9b depicts a machined surface of Ti-6242s in which tearing surface is observed [1]. The part of cutting tool (small part that peel off from its origin to form tool wear) and built-up edge (BUE), which is deposited on the machined surface, present a potential to produce tearing of the machined surface. Since a small part of the cutting tool (made of carbide) and/or the part of BUE (deformped chip) are harder than the workpiece material, they slide between the tool and the machined surface, and they scratch and tear away the machined surface. Built-up layer (BUL), proposed by Ginting and Nouari [1] is caused by molten chip deposited on the machined surface. Fig. 9c shows the fine chip particles adhering to the machined surface. It is believed that BUL is caused by the high cutting heat produced by dry metal cutting.

(a)   (b)
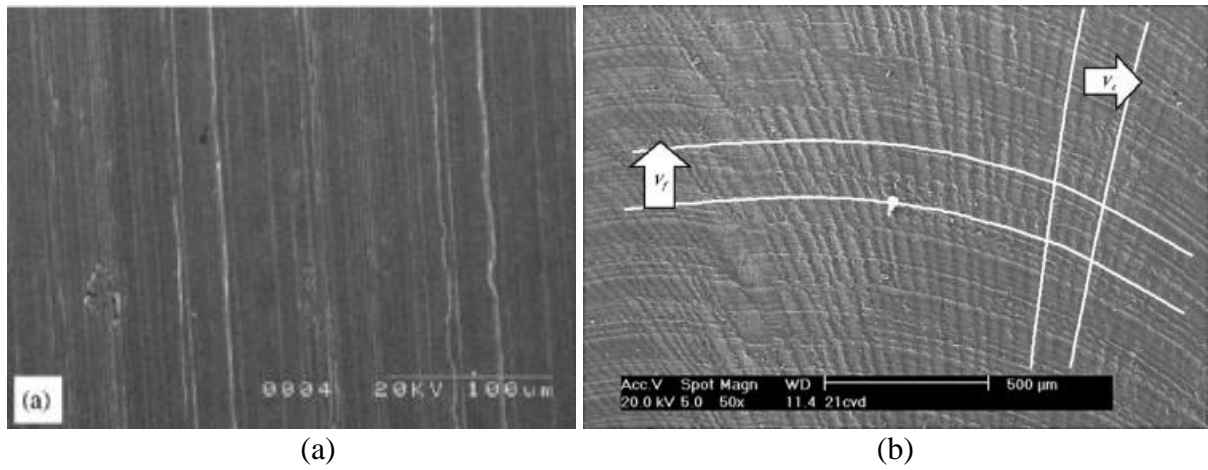
Fig. 8: (a) Surface generated when turning Ti-6Al-4V (V_c = 175 m/min, f = 0.15 mm, a_p = 0.5 mm) [22]; (b) Lay pattern when milling Ti-6242S (V_c = 125 m/min, f_z = 0.2 mm/tooth, a_p = 2.5 mm) [1].

(a)   (b)   (c)
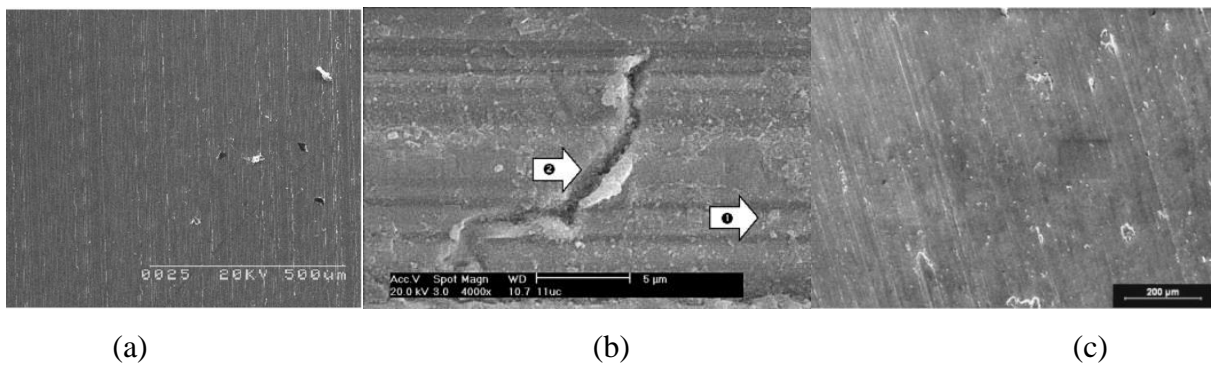
Fig. 9 Surface defects in machining titanium alloy: (a) Surface generated when turning Ti-6Al-4V (V_c = 200 m/min, f = 0.15 mm, a_p = 0.5 mm) [22]; (b) Tearing surface produced by milling Ti-6242s (V_c = 100 m/min, f_z = 0.15 mm/tooth, a_e = 2 mm, a_p = 8.8 mm) [1]; (c) Surface produced by milling Ti-6Al-4V (V_c = 78 m/min, f = 0.133 mm, a_p = 2.35 mm) [25].

Although surface defects were usual for most of the metal cutting operations, their extents were different for the different metal cutting environments [24]. As shown in Fig. 10, smearing and

15

chip re-deposition were observed on all samples machined at 30 m/min cutting speed under dry, flood and cryogenic conditions. However, the severity of these phenomena was more pronounced in the case of conventional metal cutting environments of dry and flood.
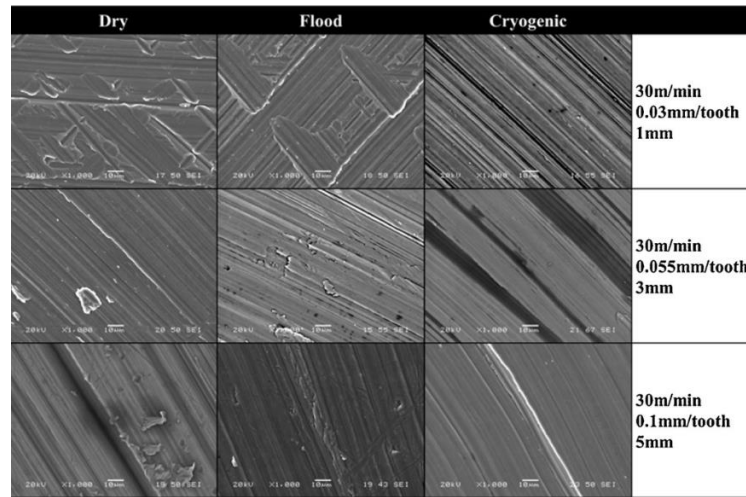
Fig. 10: Surface of machined samples in end milling Ti-6Al-4V [24].

1.2.3.2 Metallurgical state

The metallurgical state of the surface including microstructure, phase transformation, grain size and shape is affected by the cutting parameters in the metal cutting test.

The cross-section views of the microstructure in the subsurface under different cutting parameters are shown in Fig. 11. Fig. 11a shows the microstructures of the machined surface when metal cutting was performed with 883-MR4 tools under dry cutting conditions [26]. It was found that while metal cutting under dry conditions, a thin layer of disturbed or plastically deformed layer (also called white layer) was formed immediately underneath the machined surface. In Fig. 11b, a thin layer of a disturbed or plastically deformed layer was also formed immediately beneath the machined surface by the milling of hemispherical tool [27]. Fig. 11c gives images of the subsurface deformation produced when drilling Ti-6Al-4V using MQLSE (Minimum quantity lubrication synthetic ester oil) [28]. Hughes et al. [29], when turning Ti-6Al-4V with lubrication, showed deformed grain boundaries in the direction of cutting (as illustrated in Fig. 11d). Particularly, only very shallow depths of deformation (about 6 μm) were found across all the operating parameters employed in their trials.

In contrary, while high-speed side milling of Ti-6Al-4V, Wang [30] did not observe the formation of a white layer. As can be seen in Fig. 12, there is no obvious plastic deformation layer or white layer in the subsurface under different combinations of cutting parameters.

16

Furthermore, as observed by Ezugwu et al. [22], there was no evidence of sub-surface defects such as cracks, laps, visible tears or plastic deformation in finish turning Ti-6Al-4V alloy with PCD tools using both conventional and high-pressure coolant supplies. In his experiments, the cutting speed increases from 175 m/min to 250 m/min, the depth of cut and feed are 0.5 mm, 0.15 mm, respectively, which are typical for finish metal cutting conditions. Moussaoui [25] also does not observe obvious defects and plastic deformation under the machined surface in both rough and finish milling of Ti-6Al-4V with coated carbides. The maximum cutting speed is 78 m/min in his milling tests. In his review, the cutting conditions were much less severe to cause plastic deformation and lengthening of the grains. In this case, it is believed that the occurrence of plastic deformation layer or white layer in metal cutting Ti-6Al-4V alloy requires specific cutting conditions.

(a)   (b)

(c)   (d)
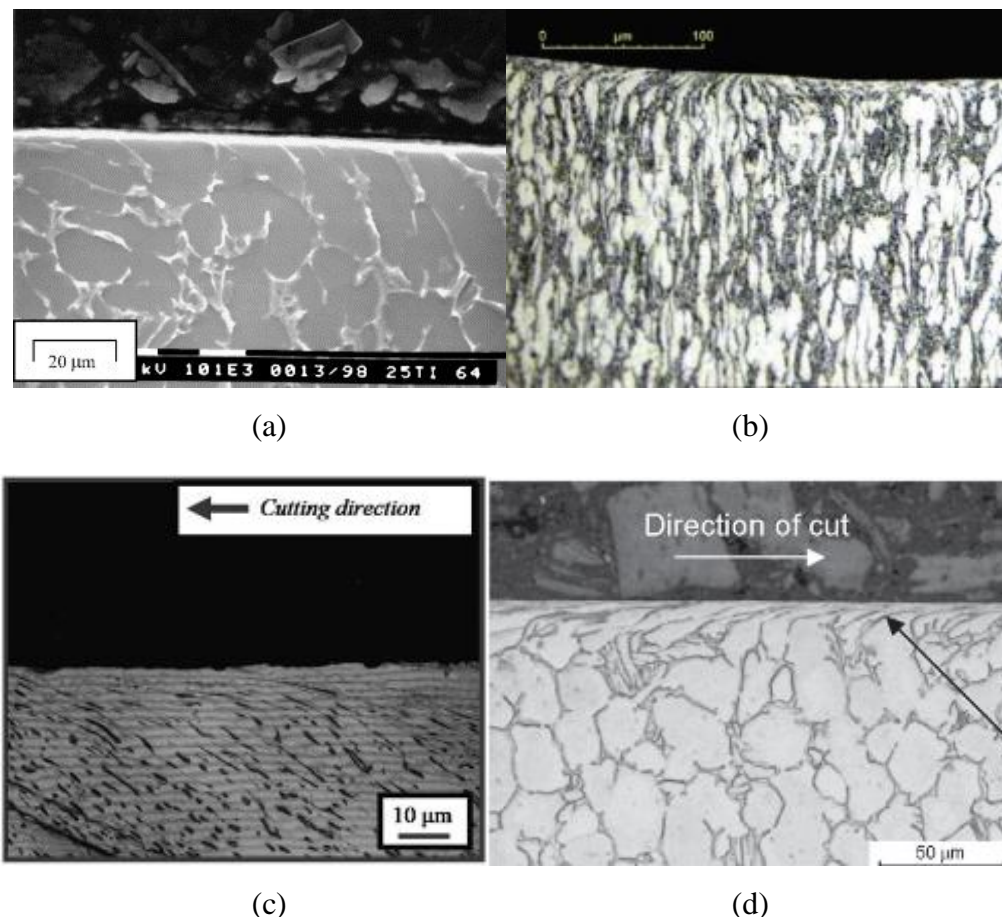
Fig. 11: Microstructural deformation of Ti-6Al-4V (a) Microstructure of machined surface after 10s of cutting (V_c = 100 m/min, f = 0.25 mm) [26]; (b) Microstructure alteration of the top machined concave surface by ball-end mill with a diameter of 16 mm [27]; (c) Subsurface deformation after drilling Ti-6Al-4V (V_c = 100 m/min, f = 0.1 mm) [28]; (d) Typical microstructural deformation of Ti-6Al-4V with cutting fluid supply (5 bar and 30 L/min) [29].
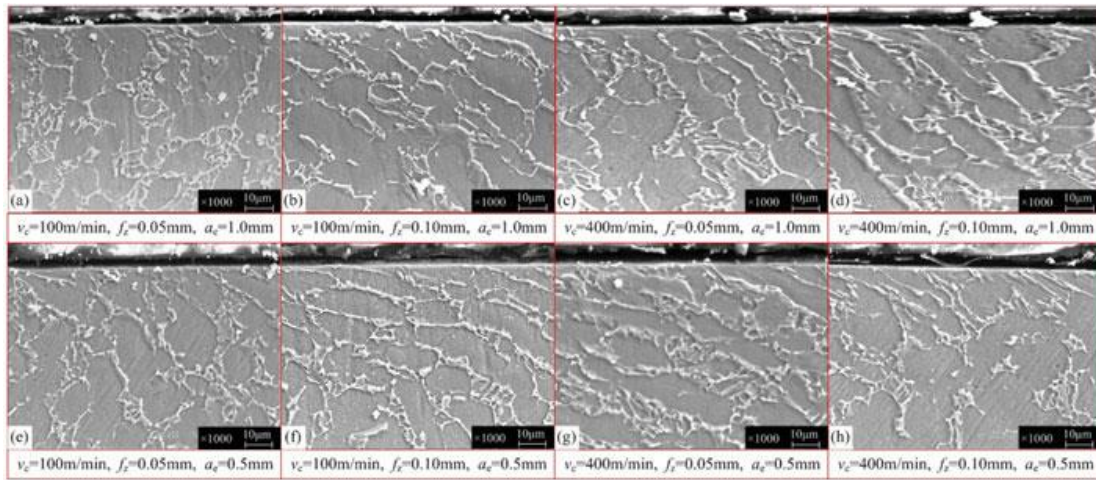
Fig. 12: SEM images of subsurface micro-structure changes of Ti-6Al-4V under different cutting parameters [30].

Besides phase deformation, microstructural changes such as the absence of β phase close to the hole surface have been shown in drilling Ti-6Al-4V [31]. Similar results were also reported by Li et al. [32]. The phase transformation from β phase to α phase was induced by high temperatures resulted from the severe plastic deformations. Then, Rotella [33] showed that dry metal cutting could achieve a higher β volume fraction for Ti-6Al-4V, which is beneficial for increased material strength at room temperature.

1.2.3.3 Mechanical state

The key feature of surface integrity is the distribution of residual stresses which influences significantly the workpiece's performance. After metal cutting of titanium alloy, high tensile stresses are usually distributed on the machined surface, and these stresses decrease at a high rate in depth direction, reaching a maximum compressive residual stress in the sub-surface layer. However, the tensile residual stresses on the surface of the material would cause crack initiation and fatigue failure of end products, so they need to be removed or prevented.

The effect of cutting speed on residual stresses at the surface in cutting and feed directions is shown in Fig. 13a [34]. The underlying mechanism for the residual stress variation is due to the combined effects of mechanical and thermal deformations. Fig. 13b shows that compressive residual normal stress generally decreases with the feed. The variation of the residual stress at the feed of 0.08 mm/tooth does not affect the curve trends. The shear residual stress becomes more compressive when the feed increases.

(a)   (b)
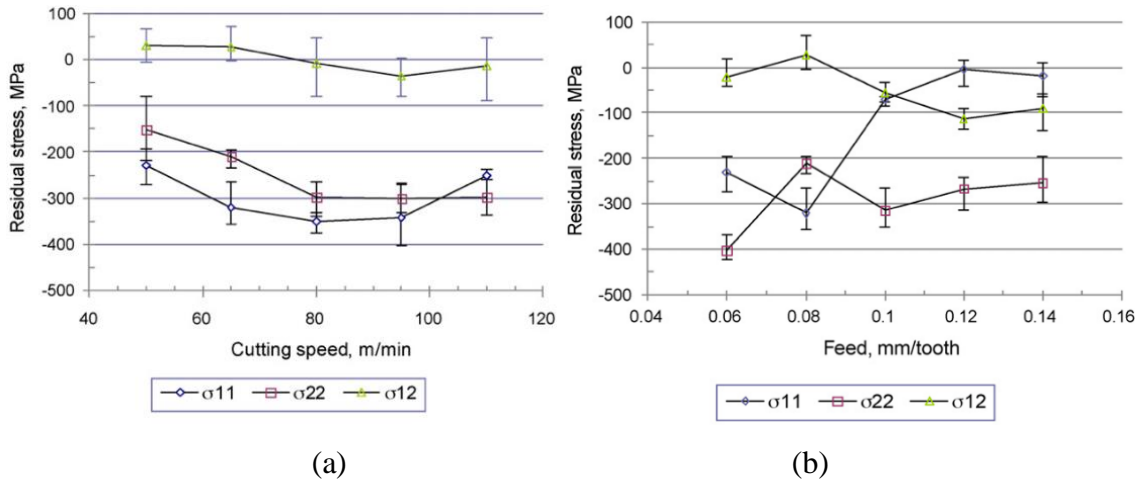
Fig. 13: The influence of (a)cutting speed and (b) feed on surface residual stress [34].

Fig. 14 illustrates not only the experimental stress distribution after turning Ti-6Al-4V, but also the related simulation results. As can be seen, the dispersion between simulated results is significant when different models are used.
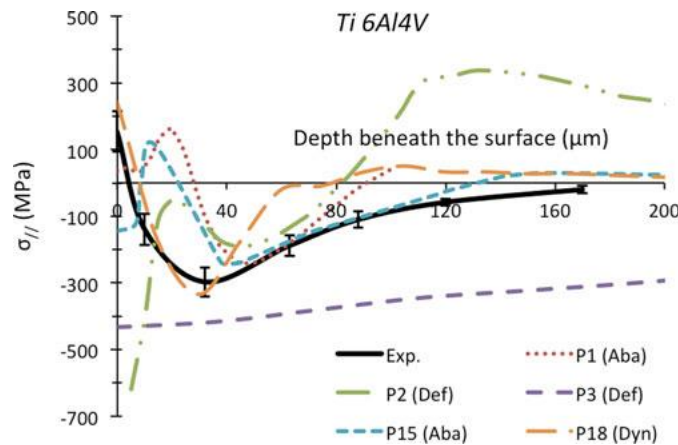
Fig. 14: Simulated (color lines) and measured (black line) in-depth residual stress $\sigma_\parallel$ profiles, for Ti-6Al-4V alloy [35].

To comprehensively cover the surface integrity characteristics, also hardness needs to be measured and correlated with the microstructure of the material beneath the surface. The distribution of the microhardness along the depth below the machined surface is a significant indicator to show the surface integrity.

Fig. 15 shows the plots of microhardness depth profiles in metal cutting of Ti-6Al-4V. In Fig. 15a, some researchers [26], [30], [34] measured microhardness values on the machined surface and in the subsurface under various cutting parameters. The first microhardness measurement was made on the top surface, and the other micro-hardness measurements were taken below the machined surface. It can be seen that the microhardness on the machined surface is much higher

than the average hardness of the bulk material, which indicates that the surface experienced significant work hardening induced by the surface deformation during the milling process. However, the material beneath the top layer is softer than the interior workpiece. Che-Haron and Hugehg consider that the reason is the 'overageing' of the titanium as a result of the very high cutting temperatures developed [26], [29]. Nevertheless, Warren and Guo [36] believe that the measured low microhardness value in the subsurface is caused by edge effect induced by the indenter size. Sun et.al. [30], [34] thought that the thermal softening induced by high temperature in the metal cutting process is the main cause.

(a)   (b)

(c)   (d)
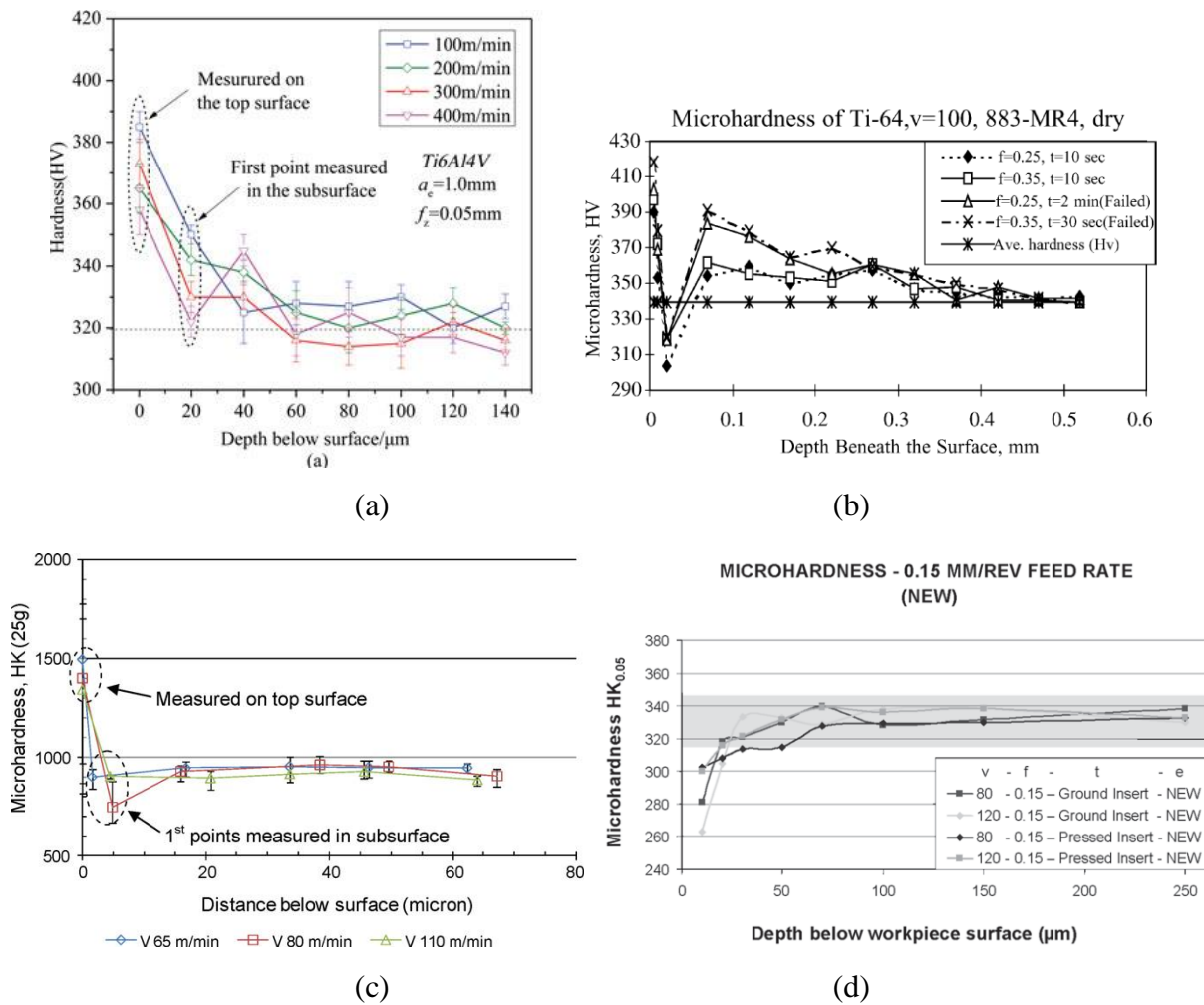
Fig. 15: Microhardness depth profiles in metal cutting of Ti-6Al-4V: (a) Microhardness distribution and variation on the machined surface and in the subsurface (f_z = 0.05 mm/tooth, a_p = 1.0 mm) [30]; (b) Microhardness value beneath the machined surface when metal cutting with 883 insert [34]; (c) Microhardness distribution and variation in the subsurface (f_z = 0.08 mm/tooth, a_p = 4 mm, a_e = 1.5 mm) [26]; (d) Knoop microhardness depth profiles in turning Ti-6Al-4V [29].

Definitely, surface integrity is one of the most significant aspects to evaluate the performance of the workpiece after metal cutting. Cutting tools, cutting parameters and properties of the

work material play major roles in the surface integrity, so they should be accurately chosen. To make those choices avoiding the high time consuming and cost of the experimental work, material modelling and process simulation could provide answers.

1.3 Metal cutting modelling and simulation

Titanium alloys belong to difficult-to-machine alloys which require higher cutting energy compared with other low-strength alloys. It is a big challenge to machine the workpiece without decreasing its mechanical property. Therefore, numerous investigators make great efforts to satisfy the surface integrity in the metal cutting. Modelling and simulation of metal cutting operations have become very popular today with many universities, research institutions and companies developing and/or using various models for predicting the metal cutting performance (especially surface integrity). However, truly predictive models for metal cutting operations are still lacking, particularly for surface integrity predictions. Their quality depends on how accurate the material constitutive models are to describe the mechanical behavior of the work material in metal cutting [35]. This includes: (1) examining the capability and limitations of the existing models; (2) modification and enhancement of the models, and their implementation in commercial FE codes; (3) obtaining model parameters under conditions pertinent to metal cutting process; (4) validation and verification of the model. Definitely, one of the objectives in this PhD project is to develop a constitutive model for accurate prediction of the surface integrity induced by machining Ti-6Al-4V alloy. This model aims to be part of a numerical simulation of the machining process. Generally, such task needs to be led following a clear strategy: to make a numerical simulation of the process, here metal cutting, we need to follow those steps:

1) Select the numerical method (FE, SPH, DE…) and formulation (Lagrangian, Eulerian, ALE…)
2) Create the model geometry (2D or 3D)
3) Define the boundary conditions and interactions between the different parts, make assumptions and justify them (for reasons of simplification or non-significance…)
4) Define the accurate materials constitutive models, make assumptions according to the application and justify them
5) Choosing the accurate elements type, size, meshing, … (depending on the solving method) taking into consideration the result accuracy and the calculation time
6) Optimizing calculations according to the returned results.

In our case, the accuracy of the predictions will be very sensitive to the following aspects: the considered boundary conditions, the interactions modelling, the formulation and the material constitutive model.

1.3.1 Boundary conditions

The accuracy of boundary conditions is vital to a successful metal cutting numerical model. As an example, Fig. 16 shows the generic boundary conditions in FE modelling of dry orthogonal cutting. It is important to decide the temperature distribution and movements of the cutting tool and the workpiece in the calculation. The movement can be defined in the simulation, while the temperature distribution needs to be investigated carefully.
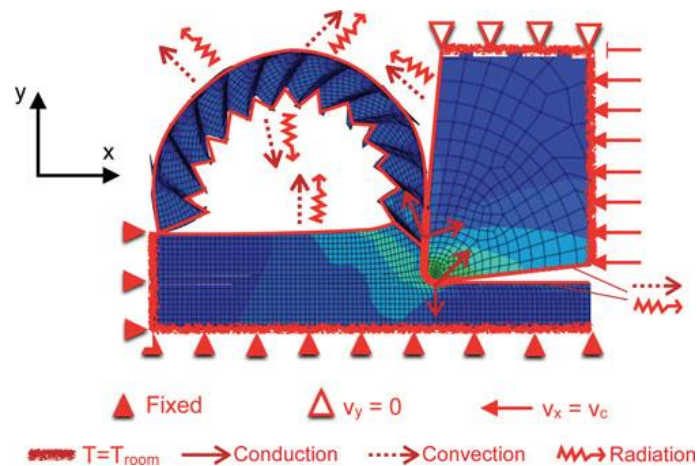
Fig. 16: Representation of initial boundary conditions [35].

The heat generated in the metal cutting comes mainly from the strong plastic deformation of the work material and the friction between the tool and the chip. And most of the heat generated in the first deformation zone goes into the chip while a small part of heat is conducted toward the tool and the workpiece. The heat generated by friction in the region between the tool flank face and the machined surface makes is closely tied to the surface temperature of the workpiece. Additionally, the friction between the chip and the rake face also produces a non-negligible amount of heat. Therefore, the proper numerical or analytical methods need to calculate the peak and average temperatures in the shear zone and the tool rake face, investigate the heat partition phenomena and obtain the temperature fields within the cutting tool, chip and the workpiece. A steady state two-dimensional analytical model was proposed by Trigger and Chao to predict the average temperature rise of the chip in metal cutting [37]. There are four main assumptions in their model:

1）Existence of two heat sources which distribute the energy uniformly: one is in the shear plane, and the other is on the tool chip interface.

2）90% of the heat flows into the chip and 10% flows into the work material.

3）Blok's partition principle is used to compute the distribution of thermal energy at the shear plane [38]

4）Work surface and the machined surface are considered as adiabatic boundaries.

Apart from this model, many other models can be found in literature. Young and Chou proposed an analytical model to predict the tool-chip interface temperature distribution during orthogonal metal cutting [39]. Then, a three-dimensional model was proposed for the prediction of temperature fields in continuous and interrupted metal cutting processes [40]. In particular, the finite element method is used to investigate the temperature distribution. The success of this method depends highly on the chosen constitutive model. Thermo-viscoplastic model, rigid plastic model and thermomechanical model were proposed by several researchers to analyze the flow of the cutting heat and temperature distribution in both the workpiece and the tool [41]-[43].

1.3.2 Contact model

The high normal pressure on the interface between the chip and the tool rake face plays an important role in the contact regions and the friction parameters. Many researchers tried to estimate the friction behavior in this interface. Generally, a relationship between normal and shear stress over the tool rake face is used to characterize the friction behavior. By measuring the normal and the shear stresses directly in the metal cutting tests, the obtained data can be used to identify or validate the contact model. Two common approaches to measure the normal and frictional stress distributions on the tool rake face are repeatedly reported in literature: split-tool and photo elastic methods [44].

The contact between the tool and the chip is firstly modelled by some Coulomb-type models, where the frictional stresses (τ), parallel with tool rake face, were assumed to be proportional to the normal stresses, perpendicular to tool rake face (σ_n), with a coefficient of friction (μ), as shown in Eq. 9.

$$\tau = \mu \cdot \sigma_n \qquad\qquad Eq.\ 9$$

23

This model could get a good simulated result in the region between the tool flank face and the workpiece, while the region between the tool rake face and the chip in high speed machining does not match the reality well. To improve the accuracy of simulation, several friction models were proposed. Based on the analysis of the stress distribution on the tool-chip interface, Zorev presented a stick-slip friction model [45]. The stress distribution is shown in Fig. 17. The normal stress is at its maximum at the tool tip and then decreases gradually to 0 along the tool-chip interface. Sticking friction occurs in the region where the frictional shearing stress τ is equal to the average shear flow stress τ_p. In contrast, the sliding friction occurs over the remaining tool-chip contact area where the frictional shearing stress is calculated by the friction coefficient μ. This relation is displayed in Eq. 10 which is applied into the modelling of orthogonal cutting by many researchers:

$$\tau = \begin{cases} \tau_p & (\text{if } \mu\sigma_n \geq \tau_p) \quad 0 < x < l_p \\ \mu\sigma_n & (\text{if } \mu\sigma_n < \tau_p) \quad l_p < x < l_c \end{cases} \qquad \tau_p = \frac{\bar{\sigma}}{\sqrt{3}} \qquad\qquad Eq.\ 10$$

where µ is the Coulomb's friction coefficient, l_c is the total contact length between the chip and the tool rake face, and l_p is the contact length on the sticking region of the tool rake face.
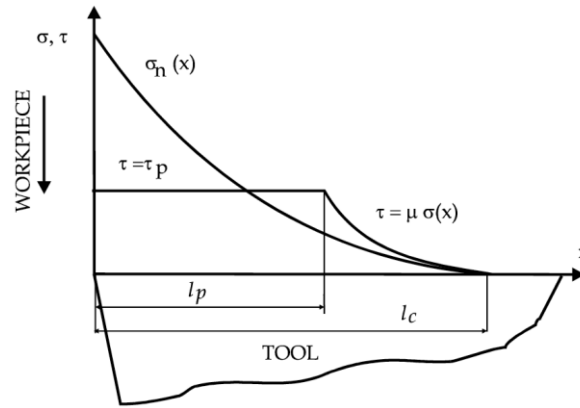
Fig. 17: Stresses distribution on the tool rake face [35].

Usui and Shirakashi [46] derived an empirical stress characteristic equation as a friction model at the tool-interface as given with Eq. 11. When the normal stress is very large, its value approaches the value of average shear flow stress τ_p (sticking region). Otherwise, the classical Coulomb's law is applied (sliding zone). This model uses a non-linear friction model to relate normal stress and frictional one:

$$\tau = \tau_p \left[1 - e^{-(C_{US}\sigma_n / \tau_p)} \right] \qquad\qquad Eq.\ 11$$

where C_{US} is a characteristic coefficient of friction obtained from the experiments.

Dirikolu et al. [47] modified this model by multiplying τ_p by a friction factor m_D and introducing an exponent. It is shown in Eq. 12:

$$\tau = m_D \tau_p \left[1 - e^{-(C_{US}\sigma_n/\tau_p)} \right]^{\frac{1}{n_D}} \qquad\qquad Eq.\ 12$$

where n_D is an exponent that in practice is found to vary from 1 to 3 [48].

Özel [44] compared the experimental results with the simulated data with above friction models, from Eq. 9 to Eq. 12. It shows that the predicting chip geometry, forces, stresses on the tool and the temperatures at the tool-chip interface are heavily influenced by the used friction models. More accurate predictions are achieved when using friction models based on the measured normal and frictional stresses on the tool rake face and when implemented as variable friction models at the tool-chip contact in the FE simulations.

1.3.3 The model formulation

In order to predict the chip formation accurately by simulation, different techniques are proposed. Generally, there are two typical types to simulate the metal cutting: finite element method (FEM) and meshless methods. In FEM modelling of metal cutting, three kinds of formulations can be used: Lagrangian, Eulerian and Arbitrary Lagrangian-Eulerian (ALE). In a Lagrangian analysis, the computational grid deforms with the material whereas in a Eulerian analysis, it is fixed in space. The ALE approach is a general formulation attempting to combine the advantages of the Lagrangian and the Eulerian, while minimizing as far as possible their respective drawbacks.

The Lagrangian formulation is widely used into the analysis of the solid structure. It can accurately describe the motion interface and follow the movement tracks of nodes. When modelling the metal cutting, it calculates from the start to the steady state [49]. Meanwhile, the chip geometry, history of stress, strain and temperature distributions could be recorded and compared with the experimental data. However, the model requires large computational times to reach the steady state. The large distortion of some elements in the simulation (which is the case of metal cutting) may impair the reliability of the simulated results and computational stability. The element deletion and node splitting techniques are widely used to simulate the chip formation, as can be seen in Fig. 18.

Element deletion technique is a geometry-based approach in which a sacrificial element zone is defined in the layer between the workpiece and the uncut chip. A damage model needs to be defined for the sacrificial elements. As the tool advances into the workpiece, the element is deleted based on the given damage model. Fig. 18b presents the node separation technique, which is also a geometry based approach. A predefined parting line is used to separate the chip from the workpiece. At each point on the parting line, two nodes are tied together in the beginning. When the tool approached the tied pair of nodes, the nodes are separated based on the predefined criterion, such as the tool node distance, critical effective stress, and critical effective plastic strain. Instead of choosing the criterion, the proper determination of the critical value is more interesting.

(a)
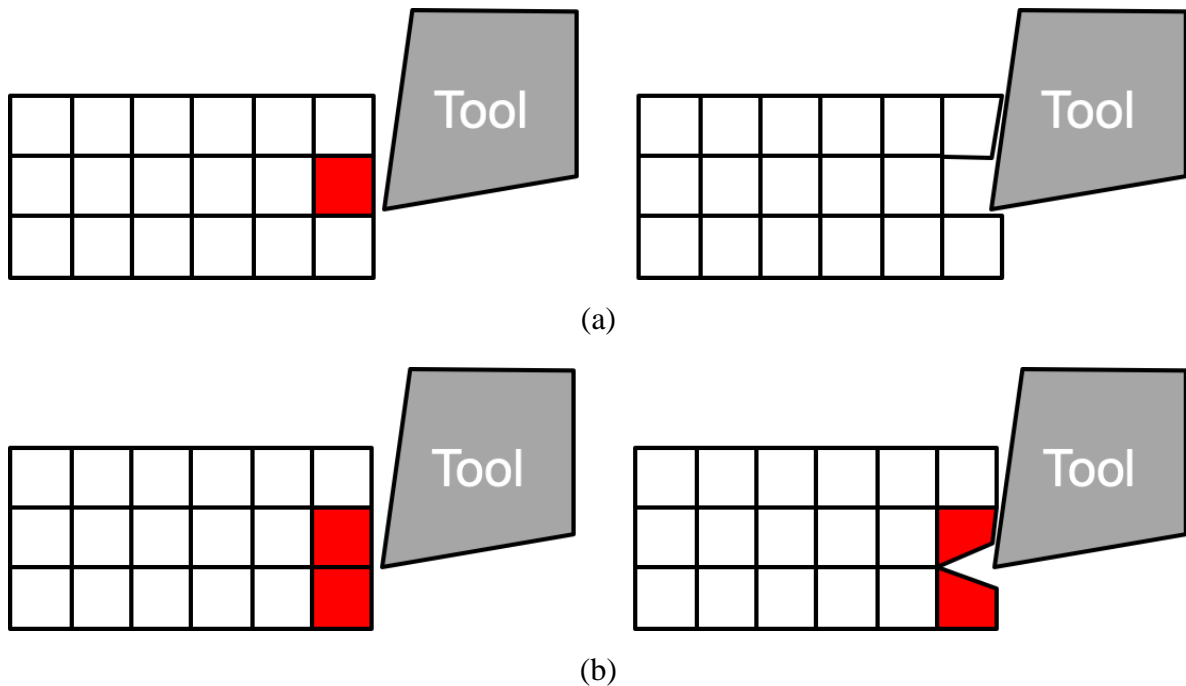
(b)
Fig. 18: Simulation techniques for chip formation: (a) element deletion, (b) node splitting.

Remeshing technique is a practical method to prevent mesh distortion, as can be seen in Fig. 19. This technique is included in many commercial FE software, such as ABAQUS, Ls_Dyna, Deform and Advantage. Many researchers [50], [51] used it to simulate the chip formation. When the tool penetrates the elements of the chip, the elements will deform and trigger the remeshing step. Then, the new mesh is generated and replaces the former mesh, which could match the tool edge with less deformation. However, the remeshing will dense the meshes used in the simulation, and increased the computational cost. The frequency of the remeshing procedure will also influence the interpolation process and the computational time.

Unlike the Lagrangian formulation, the material flows through the fixed mesh in the Eulerian approach, so the problem of element distortion is avoided. It is not proper to simulate the transition from the initial to the steady state of the cutting process, as the chip geometry and the shear angle are predefined before the simulation. This approach could reduce the computational time due to the predefined meshing. However, the boundaries of the chip must be known in advance. Furthermore, it is necessary to do experiments to obtain the chip geometry and shear angle before the simulation.
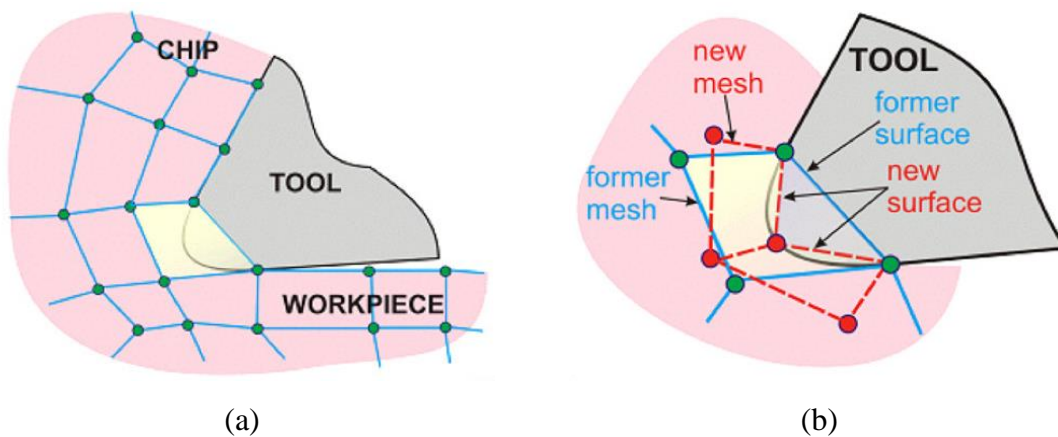
<div align="center">(a)   (b)</div>
Fig. 19: Remeshing procedure in chip formation: (a) penetration of tool edge, (b) remeshing [51].

ALE formulation which combines the Lagrangian and the Eulerian methods, has been proposed to model machining operations. Associated with the ALE formulation, the chip formation is usually modelled to simulate the material flow around the cutting edge. With a careful numerical treatment of the advection terms, the ALE method can alleviate the element distortion problem of the Lagrangian approach. However, it has two major drawbacks in the simulation of metal cutting. In fact, a remeshing procedure is necessary in the ALE formulation and consequently the state variables of the meshes are remapped. Moreover, no physical separation occurs while generating the chip, which is inadequate to simulate the chip formation process, in particular in brittle materials where this separation is caused by a fracture process [35].

Recently, the meshless technique, namely the Smooth Particle Hydrodynamics (SPH) Lagrangian method is also applied to model the chip formation. Instead of a mesh, the model is defined by several points (particles) with a field around them. SPH method applied to metal cutting modelling involves two main advantages:

1) High strains are modelled easily. Compared with the mesh, the particles move relatively to each other in a disordered way without topological restriction. This can

be considered as particles rearranging without topological restriction, thus no remeshing is needed.

2) The chip formation is easy to produce. The relative motion of the particles creates the opening. The new free surfaces are given by the particles position.

Limido et al. [52] applied the SPH method to simulate high speed metal cutting. The matches of chip geometry and cutting forces between experimental and simulated results proves the applicability of SPH method. Then Xi. et al. [53] developed a coupled SPH-FE models to investigate the machining of Ti-6Al-4V alloy in Ls-Dyna. Both 2D and 3D models were developed to investigate chip formation and cutting forces, respectively. However, the biggest challenge of the SPH method is the large computation cost.

1.3.4 Constitutive models

1.3.4.1 Constitutive models for metal cutting simulation

Metal cutting is peculiar, that the imposed deformations (strains, strain rates, temperatures, and state of stress) give a complex thermomechanical loading history. The quality of the predictions depends mainly on how accurate the constitutive models are to describe the thermomechanical behavior of the work material in metal cutting [54]. Thus, it is important to select an appropriate model reproducing the strain-stress relationship of the workpiece in metal cutting. The complexity of these relationships ranges from isotropic elastic models suitable for macroscale structural modelling, to formulations of crystal plasticity designed to capture the dislocation effect and the grain scale inelastic behavior [12]. However, there are several disadvantages in the present models used in the metal cutting. The reasons are included in the following points:

1) Some models designed for impact or other applications are used in the metal cutting. These models could not represent the properties of the workpiece accurately. For example, Johnson-Cook model which is the mainly used and available in most of the commercial FE codes is designed for impact [55]. Effects of the state of stress on the first deformation zone (FDZ) are not included in this model;

2) Based on the understanding of metal cutting, some models use only the plasticity model to describe the chip formation and ignore the damage criterion.

3) The model coefficients are very sensitive to any changes in the metallurgical conditions of the work material.

4) The process of coefficients determination is rarely accurate. Depending on the applied determination method, different constitutive model sets of coefficients can be generated for the same material.

Therefore, a key point in metal cutting modelling is to use an accurate constitutive and well determined coefficient, able to describe the work material behavior under the loading conditions specific to this process. It can be phenomenological or physical based.

a) <u>Phenomenological models</u>

The Johnson-Cook (*J-C*) model is extensively used in commercial finite element analysis (FEA) software [55]. Considering strain hardening effect, strain rate effect and temperature-dependence, the *J-C* plasticity model is presented by Eq. 13. The *J-C* damage model considers several effects on damage: stress triaxiality, strain rate and temperature as expressed in Eq. 14:

$$\tilde{\sigma} = \left(A_{jc} + B_{jc} \varepsilon_p^{n_{jc}} \right) \left[1 + C_{jc} \ln\left(\frac{\dot{\varepsilon}}{\dot{\varepsilon}_0} \right) \right] \left[1 - \left(\frac{T - T_{room}}{T_{melt} - T_{room}} \right)^{m_{jc}} \right]$$

Eq. 13

$$\bar{\varepsilon}_p^i = \left(D_{1jc} + D_{2jc} e^{D_{3jc}\eta} \right) \left[1 + D_{4jc} \ln\left(\frac{\dot{\bar{\varepsilon}}^p}{\dot{\varepsilon}_0} \right) \right] \left[1 + D_{5jc} \frac{T - T_{room}}{T_{melt} - T_{room}} \right]$$

Eq. 14

where A_{jc}, B_{jc}, C_{jc}, m_{jc} and n_{jc} are the coefficients of the plasticity model, and $\dot{\varepsilon}_0$ is the reference strain rate. T_{room} is the reference ambient temperature; T_{melt} is the melting temperature of the workpiece material, and T is the current process temperature; D_{1jc}–D_{5jc} are damage coefficients, and η is the stress triaxiality.

Using the *J-C* plasticity and damage models, Pan et al. [56] and Zhang et al. [57] performed the simulations of orthogonal cutting of A2024-T351 aluminium alloy and Ti-6Al-4V alloy, respectively. Besides the *J-C* damage model, Yang et al. [58] coupled the *J-C* plasticity model with the Cockroft and Latham model [59] to simulate orthogonal cutting of hydrogenated Ti-6Al-4V alloy. The Cockroft and Latham model is expressed in Eq. 15:

$$D_{CL} = \int_0^{\bar{\varepsilon}_f} \sigma_1 d\bar{\varepsilon}$$

Eq. 15

where $\bar{\varepsilon}_f$ is the effective strain at fracture; σ_1 is the maximum principal stress and D_{CL} is the damage parameter. When the integral of the largest tensile principal stress component over the plastic strain path reaches the critical value, fracture occurs.

In order to investigate the influence of the coefficients values of the *J-C* plasticity model on the deformation behavior of Ti-6Al-4V alloy and AISI 316L steel in the metal cutting process, the Cockroft and Latham model is exploited as the damage model to simulate the chip separation [60], [61]. Though the *J-C* model had a robust nature of aptly modelling the deformation behavior of workpiece in metal cutting, the variance of the coefficients values could predict different cutting forces and chip geometries. It is necessary to develop constitutive models based on machining tests besides exploring methods to determine its coefficients.

The Cockroft and Latham model did not consider the effect of stress triaxiality on the fracture strain, which affects its accuracy. In contrast, Bao-Wierzbicki [62] used a piecewise function to describe the fracture strain $\bar{\varepsilon}_p^i$ over an entire range of stress triaxiality. Wang and Liu [63] added the effects of strain rate and temperature as in the *J-C* damage model into the Bao-Wierzbicki piecewise function, as shown in Eq. 16. Then this model is coupled with the *J-C* plasticity model to simulate the high speed machining (HSM) of Ti-6Al-4V alloy. It has proved that the stress triaxiality plays a vital role in serrated chip formation during HSM of Ti-6Al-4V alloy.

$$\bar{\varepsilon}_f = \bar{\varepsilon}_f^0 \left[1 + D_{4jc}\, ln\left(\frac{\bar{\dot{\varepsilon}}^p}{\dot{\epsilon}_0}\right)\right]\left[1 + D_{5jc}\frac{T - T_{room}}{T_{melt} - T_{room}}\right] \qquad Eq.\ 16$$

where $\bar{\varepsilon}_f^0$ is a piecewise function obtained by fitting the experimental data.

The effect of deviatoric stress ratio *A* was included in the ductile fracture by Wilkins et al. [64]. Two factors enhance strain damage: hydrostatic tension and asymmetric strain. The expression for the damage parameter D_{wi} is shown in Eq. 17.

$$D_{wi} = \int_0^{\bar{\varepsilon}_f} w_1 w_2 d_{\bar{\varepsilon}} = \int_0^{\bar{\varepsilon}_f} \left(\frac{1}{1 - \alpha_{wi}\sigma_m}\right)^{\gamma_{wi}} (2 - A_{wi})^{\beta_{wi}} d\bar{\varepsilon} \qquad Eq.\ 17$$

where w_1 is the hydrostatic pressure weighting; w_2 is the asymmetric strain weighting. α_{wi}, γ_{wi}, and β_{wi} are material coefficients. $A_{wi} = \max\left(\frac{s_2}{s_3}, \frac{s_2}{s_1}\right)$, is the maximum ratio of deviatoric principal stresses (s_1, s_2, s_3). Fracture occurs when the damage parameter D_{wi} reaches a critical value.

Coupled with *J-C* plasticity model, Wilkins model had been applied in simulation of metal cutting aluminium alloy A2024-T351 [65]. Then, different damage models in the simulation of metal cutting were evaluated. Compared with the *J-C* damage model and the modified Bao-

Wierzbicki model, the Wilkins model cannot predict continuous chip formation, cutting force or surface roughness accurately. Also, it was concluded that damage model with damage evolution predicted better chip morphology than the ones without damage evolution.

In ductile metals, final fracture is preceded by extreme plastic deformation and damage evolution. Damage cannot be represented accurately by considering damage initiation only. Hence, damage evolution should also be considered. Hillerborg et al. [66] proposed a fracture energy formulation that is often used to describe damage evolution. Fracture energy, G_f theoretically is a function of fracture toughness K_c, Young's modulus E and Poisson's ratio v (Eq. 18). It is noteworthy that value of fracture toughness depends on the fracture modes according to fracture mechanics. It is assumed that in the case of the orthogonal cutting process, the two fracture modes (mode I and II) can coexist (Fig. 20) [67]. Mode I is a tensile mode (opening mode normal to the plane of the fracture), whereas mode II is a shearing one (sliding mode acting parallel to the plane of the fracture). Consequently, two different values of fracture energy could be used as input data in the simulation: $(G_f)_I$ for the chip and $(G_f)_{II}$ for the defined path of crack:

$$(G_f)_{I,II} = \left(\frac{1-\vartheta^2}{E}\right)(K_c^2)_{I,II} \qquad \qquad Eq.\ 18$$

where the subscripts I and II in Eq. 18 arise because of the different ways of loading. They refer to loading via modes I and II, respectively.

The progress of damage evolution is controlled by a scalar internal variable D_{de}. The damage behavior is represented by the behavior of undamaged material, and the true stress $\bar{\sigma}$ can be replaced by the equivalent stress $\tilde{\sigma}$ (Eq. 19).

$$\bar{\sigma} = (1 - D_{de})\tilde{\sigma} \qquad \qquad Eq.\ 19$$

where D_{de} is a positive definite parameter with a range of $0 \leq D_{de} \leq 1$.

An exponential damage evolution rule is widely used in the FE code to calculate this parameter D_{de}. It is given in Eq. 20:

$$D_{de} = 1 - exp\left(-\int_0^{\bar{u}} \frac{\bar{u}}{G_f} d\bar{u}\right) \qquad \qquad Eq.\ 20$$

where $\bar{u}$ is the equivalent plastic displacement.
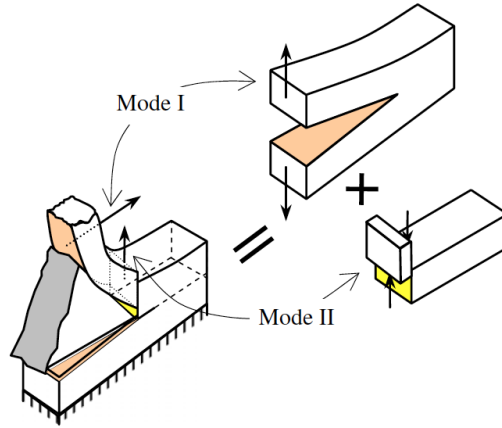
Fig. 20: Schematic orthogonal cutting model of chip formation under mixed fracture modes [67].

The *J-C* model coupled with the exponential damage evolution model is applied into the simulation of orthogonal cutting aluminium alloy A2024-T351 (Mabrouki et al., 2008). Two different values of fracture energy were used as input data in ABAQUS/explicit: $(G_f)_I$ for the chip and $(G_f)_{II}$ for the defined path of crack. Chen et al. [68] also used *J-C* model with the exponential damage evolution model to simulate the machining of Ti-6Al-4V alloy under high cutting speeds. The value of fracture energy in their research was obtained by comparing the experimental results (cutting forces, chip geometries) and the simulated data iteratively.

The *J-C* model was modified to better reproduce the mechanical behavior of the workpiece in metal cutting. In one case, Calamaz et al. [69] proposed a newly developed model (TANH model) based on the *J-C* plasticity model to describe the mechanical behavior of Ti-6Al-4V alloy. The equations are expressed in Eq. 21 and Eq. 22:

$$\sigma = \left(A_C + B_C \varepsilon^{n_C} \left(\frac{1}{\exp\left(\varepsilon^{a_C}\right)} \right) \right) \left(1 + C_C \ln \frac{\dot{\varepsilon}}{\dot{\varepsilon}_0} \right) \left(1 - \left(\frac{T - T_r}{T_m - T_r} \right)^{m_C} \right) \left(D_C + (1 - D_C) \tanh \left(\frac{1}{\left(\varepsilon + S_C\right)^{c_C}} \right) \right) \qquad Eq.\ 21$$

$$D_C = 1 - \left(\frac{T}{T_m} \right)^{d_C} \qquad S_C = \left(\frac{T}{T_m} \right)^{b_C} \qquad\qquad Eq.\ 22$$

where a_C, b_C, c_C and d_C are material constants.

b) Models including microstructure

More than the effects of strain hardening, strain rate and temperature, this new plasticity model considers the effect of the hypothesis of dynamic recovery and recrystallisation mechanism. At low strains, the flow stress increases in a similar way as the *J-C* model. Beyond a certain strain,

the flow stress decreases until a strain about 1.5 after which a nearly constant stress is obtained. Then an automatic remesh technique with this modified *J-C* model was implemented into the simulation of orthogonal cutting Ti-6Al-4V alloy. Compared with the *J-C* model, this modified model achieved a better prediction of the segmented chips under low cutting speeds and feeds.

Based on the modified *J-C* model proposed by Calamaz et al., Rotella and Umbrello [70] added the material grain-size effect. The equation is given in Eq. 23:

$$\sigma = \left(\left(a_{RU} + \frac{k_{RU}}{\sqrt{d}} \right) + B_{RU}\varepsilon^{n_{RU}} \right) \left(1 + C_{RU} \ln \frac{\dot{\varepsilon}}{\dot{\varepsilon}_0} \right) \left(1 - \left(\frac{T-T_r}{T_m-T_r} \right)^{m_{RU}} \right) \left[M_{RU} + (1-M_{RU})\tanh\left(\frac{1}{\left(\varepsilon+P_{RU}\right)^{c_{RU}}} \right)^{s_{RU}} \right] \qquad Eq.\ 23$$

where d is the predicted grain size, coefficient a_{RU} and k_{RU} are used in the grain size term; coefficients B_{RU}, C_{RU}, n_{RU} and m_{RU} are similar to the ones in *J-C* plasticity model (Eq. 13); coefficients M_{RU}, p_{RU}, c_{RU} and S_{RU} are used in the strain softening term.

Moreover, Zener–Hollomon (*Z-H*) equation was used to predict the recrystallized grain size, while the hardness variation was predicted by using the Hall–Petch (*H-P*) equation. The equations are shown below,

$$d = d_0 \cdot b_{ZH} \cdot Z^{m_{ZH}} \qquad\qquad Z = \dot{\varepsilon}e^{\frac{Q}{RT}} \qquad\qquad Eq.\ 24$$

$$HV = C_{0ZH} + C_{1ZH} \cdot d^{-0.5} \qquad\qquad Eq.\ 25$$

where d_0 is the initial grain size, b_{ZH} and m_{ZH} are two material coefficients, $\dot{\varepsilon}$ is the strain-rate, R is the universal gas constant; C_{0ZH} and C_{1ZH} are two coefficients relating the hardness and the grain size.

A critical strain ε_{cr} is imported to decide if the recrystallization occurs or not. At a certain time, if the calculated strain is higher than the critical value, the recrystallization takes place, and a new grain size and a new hardness are calculated using the *Z-H* equation (Eq. 24) and *H-P* equation (Eq. 25), respectively. In contrast, the recrystallization would not happen due to the low value of strain, so the grain size and the hardness keep unchanged. This model and the corresponding procedure are applied in the simulation of orthogonal cutting Ti-6Al-4V alloy under dry and cryogenic cooling conditions. The evolution of grain size and hardness in the machined surface were then well predicted. Later, *the Z-H* and *H-P* equations are modified based on the research of Rotella [70]. In fact, the variation of grain size and hardness in both

the chip and the machined surface was predicted in the simulation of high speed orthogonal machining of Ti-6Al-4Valloy [71].

Umbrello et al. [72] added the effect of hardness into the term of strain hardening of *J-C* plasticity model, and the hardness-based plasticity and fracture models were proposed for numerical simulation of machining AISI H13 steel. The equations are expressed in Eq. 26 and Eq. 27:

$$\sigma = \left(A_U + F_U + G_U \varepsilon + B_U \varepsilon^{n_U} \right) \left(1 + C_U \ln \frac{\dot{\varepsilon}}{\dot{\varepsilon}_0} \right) \left[H_U - E_U \left(\frac{T - T_r}{T_m - T_r} \right)^{m_U} \right] \qquad Eq. 26$$

$$D_U = \int_0^{\bar{\varepsilon}_f} \sigma_1 d\bar{\varepsilon}_{pl} = D_{1U} HRC^2 + D_{2U} HRC + D_{3U} \qquad Eq. 27$$

where F_U and G_U are the third-order polynomial functions of the hardness; A_U, B_U, C_U, H_U, E_U, n_U and m_U are the material coefficients; D_U is the damage parameter, and D_{1U}, D_{2U} and D_{3U} are material coefficients.

In addition, Buchkremer et al. [73] modified the constitutive models proposed by Bai and Wierzbicki [74] by including the temperature and strain-rate effects (Eq. 28). Though the effect of stress triaxiality is neglected, the effect of Lode angle is kept in the plasticity model.

$$\begin{aligned} \tilde{\sigma}_{yld} &= \sigma\left(\bar{\varepsilon}^p, \dot{\bar{\varepsilon}}^p \right) \cdot f(T) \cdot f\left(\bar{\theta} \right) \\ &= \left[\sigma\left(\varepsilon^p \right) \left(b_1 \ln \dot{\bar{\varepsilon}}^p + b_2 \right) + b_3 \dot{\bar{\varepsilon}}^p \right] \left[c_1 \exp(c_2 T) + c_3 \right] \left[c_\theta^s + \left(c_\theta^{ax} - c_\theta^s \right) \left(\gamma - \frac{\gamma^{m+1}}{m+1} \right) \right] \end{aligned} \qquad Eq. 28$$

where the coefficients b_1, b_2 and b_3 are used in strain hardening and strain rate term; the coefficients c_1, c_2 and c_3 are used in temperature term; the coefficients c_θ^{ax}, c_θ^s are used in Lode angle term. A damage model including a symmetric damage initiation law and a damage evolution law was also proposed. The equations are given in Eq. 29 and Eq. 30:

$$\bar{\varepsilon}_i^p = \left(D_{B1} e^{-D_{B2}\eta} + D_{B5} e^{-D_{B6}\eta} \right) \bar{\theta}^2 + D_{B3} e^{-D_{B4}\eta} \qquad Eq. 29$$

$$\bar{\sigma} = (1 - D_B) \cdot \tilde{\sigma} \qquad D_B = \begin{cases} \int_{\bar{\varepsilon}^i}^{\bar{\varepsilon}} \frac{\bar{\sigma}}{E_f} d\varepsilon & \bar{\varepsilon}^i < \bar{\varepsilon}^p < \bar{\varepsilon}^f \\ D_{cri} & \bar{\varepsilon}^p \geq \bar{\varepsilon}^f \end{cases} \qquad Eq. 30$$

where D_{B1}-D_{B5}, D_{cri}, and E_f are the material coefficients. $\bar{\varepsilon}^i$ is the plastic strain at damage initiation; $\bar{\varepsilon}^f$ is the plastic strain at final fracture. Using this model, the cutting forces, temperatures and chip geometries were well predicted in the simulation of turning AISI 1045 steel. It revealed that the constitutive model including the effect of state of stress has a strong potential in the simulation of the machining process.

c) <u>Physical based models</u>

Another type of constitutive models to capture the mechanical behavior at large strain, high strain rate and temperature is the physical-based model which is derived from the physical theory. Zerilli and Armstrong [75] proposed a constitutive relation (Z-A) based on a thermal activation analysis. Due to the crystalline structures of materials, different constitutive relations were proposed for the FCC, BCC and HCP materials. The Ti-6Al-4V alloy belongs to the HCP structure, and the related Z-A form is given in Eq. 31:

$$\sigma = \sigma_a + B_{ZA}e^{-(\beta_0 - \beta_1 \ln\dot{\varepsilon})T} + B_0\sqrt{\varepsilon}e^{-(\alpha_0 - \alpha_1 \ln\dot{\varepsilon})T} \qquad Eq.\ 31$$

where σ_a is the athermal component of flow stress due to solute atoms and grain boundaries, and B_{ZA}, β_0, β_1, B_0, α_0, α_1 are material coefficients.

To better represent the dynamic recovery process at large strains, the strain hardening term was modified and a similar strain softening term in Calamaz modified *J-C* model [69] was incorporated, as shown in Eq. 32-Eq. 35 [76]:

$$\sigma = \left[\sigma_a + B_{ZA}e^{-(\beta_0 - \beta_1 \ln\dot{\varepsilon})T} + B_0\sqrt{\varepsilon_r\left(1 - e^{-\varepsilon/\varepsilon_r}\right)}e^{-(\alpha_0 - \alpha_1 \ln\dot{\varepsilon})T} \right]\left[H_{ZA} + \left(1 - H_{ZA}\right)\left(\tanh\left(\frac{a_{ZA}}{\varepsilon}\right)\right)^{k_{ZA}} \right] \quad Eq.\ 32$$

$$H_{ZA} = \begin{cases} 1 & \dot{\varepsilon} < \dot{\varepsilon}_0 \\ \left[1/\log10\left(\dot{\varepsilon}\right)\right]^{h_0} & \dot{\varepsilon} \geq \dot{\varepsilon}_0 \end{cases} \qquad Eq.\ 33$$

$$a_{ZA} = a_1 \times \left[\log10\left(\dot{\varepsilon}\right) - a_2\right]^2 + a_3 \qquad Eq.\ 34$$

$$k_{ZA} = \left[\log10\left(\dot{\varepsilon}\right)\right]^{k_0} \qquad Eq.\ 35$$

where ε_r is the characteristic strain for dynamic recovery. Strain softening parameters H_{ZA}, a_{ZA}, K_{ZA} are dependent on the strain rates.

This model was implemented in the commercial finite element software AdvantEdge to simulate the orthogonal cutting of Ti-6Al-4V alloy. However, the coefficients of Z-A model are obtained from the reference directly, while the coefficients related with strain softening parameters H_{ZA}, a_{ZA}, K_{ZA} are determined by an iterative procedure with the data of cutting tests. It compromises the reliability of the simulated results to some extent.

Moreover, a Mechanical Threshold Stress (*MTS*) derived from the interactions of movable dislocations with microstructural barriers is used to predict the recrystallization, dislocation drag resistance of material at high strain rates [77]. Melkote et al. [78] extended *MTS* model by incorporating an additional deformation mechanism. The flow strength is a sum of an athermal stress, σ_a, a thermal stress, σ_{th}, and a dislocation drag stress, σ_d, as follows:

$$\sigma = \sigma_a + \sigma_{th} + \sigma_d \qquad \qquad Eq.\ 36$$

The thermal stress, σ_{th} represents the strength of interactions of movable dislocations with short-range barriers. The form is given in Eq. 37.

$$\sigma_{th} = \left[1 - \left(\frac{kT}{g_0 \mu_{MTS} b_{MTS}^3} \ln\left(\frac{\dot{\varepsilon}_0}{\varepsilon}\right)\right)^{1/q}\right]^{1/p} \sigma_0 \qquad \qquad Eq.\ 37$$

where k is the Boltzmann's constant, T is the absolute temperature, g_0 is the normalized activation energy at 0 K, μ_{MTS} is the temperature dependent shear modulus, b_{MTS} is the magnitude of the Burgers vector, $\dot{\varepsilon}_0$ is a reference strain rate, σ_0 is the stress required to overcome short range obstacles at 0 K, p and q are coefficients defining the shape of energy barriers associated with short range obstacles.

The athermal stress, σ_a, is the sum of stresses σ_G and σ_ρ, which required to overcome the resistance to dislocation motion offered by grain boundaries and dislocation forests, respectively, as shown in Eq. 38.

$$\sigma_a = \sigma_G + \sigma_\rho = \frac{\alpha_G^0 \tanh\left(\frac{d}{D_{gz}^{-0.5}}\right)^{v_{MTS}} \mu_{MTS}\sqrt{b_{MTS}}}{\sqrt{D_{gz}}} + \alpha_\rho \mu_{MTS} b_{MTS} \sqrt{\rho} \qquad Eq.\ 38$$

where α_G^0, α_ρ, d and v_{MTS} are the material coefficients; D_{gz} is the average grain size and ρ is the dislocation density. The dislocation drag stress, σ_d is given as follows:

$$\sigma_d = \alpha_d \dot{\varepsilon} \qquad \qquad \textit{Eq. 39}$$

where α_d is the dislocation drag coefficient. Then this extended MTS model is applied into the simulation of orthogonal cutting pure titanium alloy [78]. It could not only give a reasonably accurate prediction of the cutting forces and chip morphology, but also simulate the distribution of grain size and dislocation density. However, the difficulty of determining the numerous coefficients in the model limits the application of the extended MTS model.

1.3.4.2 Constitutive models for Ti-6Al-4V alloys

Some advances can be found concerning the particular case of modelling the mechanical behavior of Ti-6Al-4V alloys during machining. In fact, Allahverdizadeh et.al. [79] modified the Mohr-Coulomb model to reproduce the ductile fracture of Ti-6Al-4V alloy, as presented in Eq. 40.

$$\bar{\varepsilon}_f = \left\{ \frac{A_{MC}}{C_2} \left[C_3 + \frac{\sqrt{3}}{2-\sqrt{3}} (1 - C_3) \left(sec\left(\frac{\bar{\theta}\pi}{6}\right) - 1 \right) \right] \left[\sqrt{\frac{1+C_1^2}{3}} cos\left(\frac{\bar{\theta}\pi}{6}\right) + \right.$$

$$\left. C_1 \left(\eta + \frac{1}{3} sin\left(\frac{\bar{\theta}\pi}{6}\right) \right) \right] \right\}^{-1/N_{MC}} \qquad \textit{Eq. 40}$$

where coefficients A_{MC} and N_{MC} are derived from the plasticity law; coefficients C_1, C_2 and C_3 refer directly to fracture.

The effects of both stress triaxiality and Lode angle were included in this model, and the failure displacements of mechanical tests are well predicted. It revealed that the fracture behavior of Ti-6Al-4V alloy depends on the stress triaxiality and Lode angle. However, Bai and Wierzbicki [97] pointed out that this model does not consider the middle principle stress. It predicts plane stress fracture well, but does not provide a good prediction of the fracture of round bars in tension, which is the axial symmetry condition.

In addition, Kotkunde et al. [80] compared different constitutive models of Ti-6Al-4V alloy, which consider the effect of microstructure. It was concluded that compared with the other models including modified *J-C* model, modified Arrhenius model, Rusinek-Klepaczko model, the modified *Z-A* model was the best candidate based on the combined consideration of statistical measures, number of material constants, physical basis and computational complexity.

1.4 Summary of the chapter

In the energy and aerospace sectors the need for highly efficient materials never ceases. However, such materials and usually difficult-to-cut ones, generate accelerated tool wear and compromise the machined surface integrity, which plays an important role in the functional performance and life of the components, particularly while altering the topological state, metallurgical and mechanical states.

Cutting conditions (including tool geometry) and work material properties play roles in modifying the surface integrity. The most effective and economical approach to get the optimized machining parameters is to perform numerical simulations. The predictability of such simulations depends on several factors, including the constitutive model, boundary conditions, friction model and numerical chip formation technique.

Based on the definition of the metal cutting, the proper modelling of the work material should consider the determination of the evolution of the material flow stress under similar conditions as those observed in metal cutting, as well as the determination of the conditions of fracture occurrence. As a result, the proposed constitutive model should include both plasticity and damage part, which will be discussed in the following chapter. For the boundary conditions in the simulation, the coupled temperature - displacement analysis is included in the present work. The accuracy of the predicted results, including cutting forces, chip geometry, temperature distribution also depends highly on the used friction model. The widely used Zorev model, based on the stress distribution on the interface between the chip and the tool rake face, is a good option to be applied into the model. At last, different chip formation techniques are proposed to simulate the real process of metal cutting. The Lagrangian finite element method will be used with the damage model to simulate the chip formation, and the computation cost is relatively lower than the remeshing and SPH method. Nevertheless, the problem of element distortion needs to be carefully treated.

Finally, the constitutive model of Ti-6Al-4V alloy should be wisely chosen, including both the plasticity and damage. In the machining test, the states of stress in FDZ varies with the cutting conditions, and it affects the mechanical behavior of the Ti-6Al-4V alloy. Most of the constitutive models available in literature are not able to represent this influence on both plasticity and damage accurately. The next chapter will treat this issue by proposing a new constitutive model for the Ti-6Al-4V titanium considering the state of stress.

Chapter 2:

Constitutive model of Ti-6Al-4V alloy

2.1 Introduction

The constitutive models describe the relationship between stress and strain. Fig. 21 represents schematically a typical stress-strain curve of a mechanical test for a common metallic material, presenting the elastic and plastic material response until fracture. The solid line is the real curve. The dashed line is a hypothetical undamaged stress–strain curve commonly used to represent the work material behavior in metal cutting modelling without fracture consideration. As shown, at point B, the experimental yield surface starts to depart from the virtual undamaged yield surface. Point B marks the damage initiation. From this point on, both the elastic modulus and the plastic flow resistance degrade with increasing strain. The macroscopic measured response from point B to point E corresponds to microscopic damage evolution till final fracture. The difference between solid line representing experimental data and dashed line representing hypothetic undamaged curve is evaluated by damage parameter D. When D equals 1, the complete fracture occurs at point E corresponding to fracture strain $\bar{\varepsilon}_f^p$. To describe this mechanical behavior starting from elastic-plastic deformation to complete fracture, two parts should be included in the constitutive model: plasticity and damage.
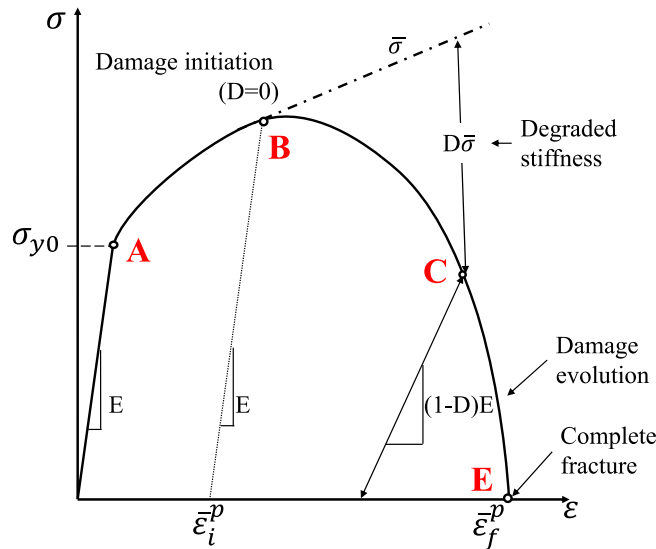

Fig. 21: Schematic representation of a typical stress-strain curve [81].

2.2 Plasticity model

As discussed in chapter 1, numerical simulation of machining is an effective method to predict those outcomes without performing time consuming and expensive machining tests and postprocess experimental analysis, which in some cases uses destructive methods. The

constitutive model, which describes the mechanical behavior of the work material, is crucial for the simulations. Among the constitutive models in the literature, those that are commonly used in machining simulations are discussed in the following sections.

2.2.1 Models including the strain rate and strain hardening effects

The mechanical strength of Ti-6Al-4V alloy, as a ductile material, is highly influenced by the plastic deformation and deformation rate. In the metal cutting, the workpiece undergoes large strain and high strain rate. As a result, it is necessary to include the effects of strain hardening and strain rate into the constitutive model which describes the mechanical behavior of the workpiece in metal cutting. The *J-C* model is embedded in many commercial FEA software [55], which considers the effects of strain hardening, strain rate and temperature-dependence. This model can be used in numerous situations, including high velocity impact, metal forming, metal forging and machining. With the result of quasi-static compression test, coefficients of A_{jc}, B_{jc} and n_{jc} in Eq. 13 can be determined; With the SHPB tests, effects of strain rate and temperature can be certified. However, different methods of coefficients identification from the experiments data leads to a large variation for the same material. Table 1 shows *J-C* model coefficients of Ti-6Al-4V identified by different researchers.

Table 1: *J-C* model coefficients of Ti-6Al-4V alloy.

References	A_{jc} (MPa)	B_{jc} (MPa)	C_{jc}	m_{jc}	n_{jc}
[105]	896	656	0.0128	0.8	0.5
[106]	782.7	498.4	0.028	1.0	0.28
[107]	862	331	0.012	0.8	0.34

As can be seen, the coefficients of this model are sensitive to the identification process and to the initial mechanical and metallurgical state of the work material, which means the coefficients need to be adjusted for different applications. On the other hand, this model neglects some effects, such as flow softening and the state of stress. To overcome these deficiencies, the *J-C* model was modified by many researchers.

Santos et al. [83] also proposed a modified *J-C* model that includes what they called flow softening, which fits the stress-strain curves of aluminium 1050 alloy obtained from tests at high strain rates better, when compared to the traditional *J-C* model. This model includes the softening effect only based on strain softening. The modified model is shown in Eq. 41.

$$\bar{\sigma} = \left[A_{Sa} + e^{m_{Sa}\varepsilon_p}\varepsilon_p^{n_{Sa}}\right]\left[B_{Sa} + C_{Sa}ln\left(E_{Sa} + \frac{\dot{\varepsilon}}{\dot{\varepsilon}_0}\right)\right] \qquad Eq.\ 41$$

where the coefficients A_{Sa}, B_{Sa}, C_{Sa}, E_{Sa}, m_{Sa} and n_{Sa} are to be determined from the experimental data.

Fig. 22 shows the stress-strain curve of aluminium 1050 at uniaxial compression tests under different strain rates. Simulated results of *J-C* model and modified *J-C* model by Santos et al. [83] are compared with the experimental data. Evidently, modified *J-C* model matches the experimental data better than the *J-C* model, especially when the strain rates are very high. For those reasons, the terms in this model for effects of strain and strain rate will be included in the proposed constitutive model.
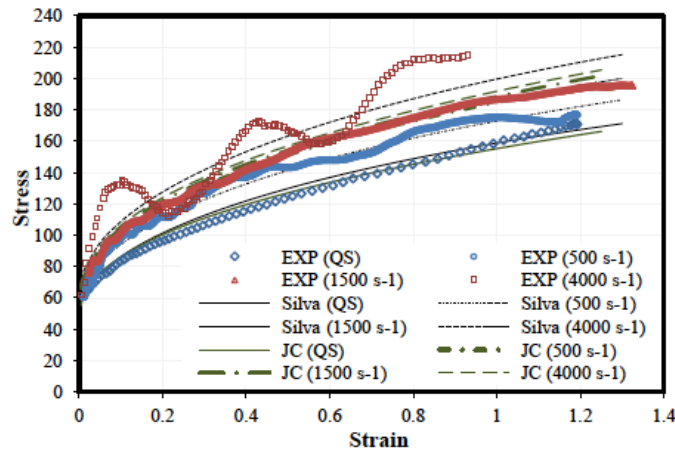
Fig. 22: Stress-strain data obtained from high strain-rate tests of aluminium 1050 [83].

2.2.2 Models including the state of stress effect

According to the classical von-Mises theory of metal plasticity, effect of hydrostatic pressure on plastic flow is assumed to be negligible, and the third stress invariant of the stress deviator does not influence the flow stress. However, this assumption is not enough to give a great accuracy of ductile fracture. For that reason, more refined flow stress model has to be introduced. The stress triaxiality state parameter and the Lode angel parameter are introduced to describe the material state of stress, as shown in Fig. 23. An arbitrary stress tensor $[\sigma_{ij}]$ can be represented by three principal stresses: σ_1, σ_2, σ_3. The stress triaxiality η is defined as the ratio of the mean stress σ_m to the equivalent von Mises stress $\bar{\sigma}$.

$$\eta = \frac{\sigma_m}{\bar{\sigma}} = \frac{\sigma_1 + \sigma_2 + \sigma_3}{3\bar{\sigma}} = \frac{I_1}{3\bar{\sigma}} \qquad Eq.\ 42$$

The Lode angle parameter $\bar{\theta}$ proposed by Bai and Wierzbick [74] is used to describe the effect of the Lode angle in their investigation. Fig. 23 illustrates the definition of the Lode angle on the deviatoric plane (or π plane). It is the angle between the stress tensor which goes through the deviatoric plane and the directions of the principal stresses. The Lode angle θ is defined as follows:

$$\theta = \arccos\left(\frac{27}{2}\frac{J_3}{\bar{\sigma}^3}\right)$$

Eq. 43

where J_3 is the third deviatoric stress invariant. The following equation shows the Lode angle parameter:

$$\bar{\theta} = 1 - \frac{6}{\pi}\theta$$

Eq. 44

where $\bar{\theta}$ is the Lode angle parameter. The range of $\bar{\theta}$ is [-1, 1], as the range of Lode angle θ is [0, π/3]. These equations show that the stress triaxiality depends on the first stress invariant I_1, while the Lode angle is a function of the third deviatoric stress invariant J_3 and the von Mises equivalent stress, $\bar{\sigma}$.

(a)   (b)
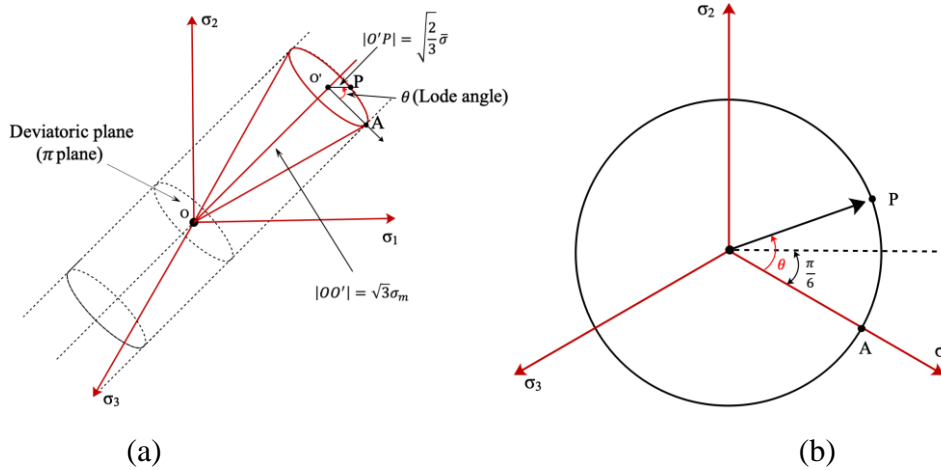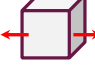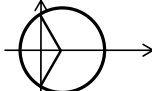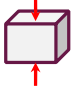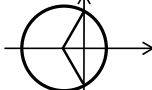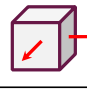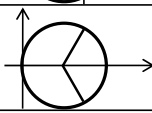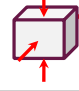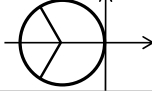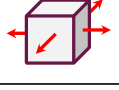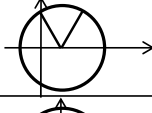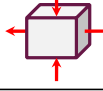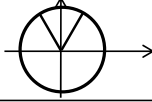
Fig. 23: (a) The space of principal stresses; (b) Lode angle definition on the π plane [74].

Xu and Liu [84] summarize the Lode angle from regular tests, and it is presented in Table 2. Different tests can get different values of Lode angle. Thus, it gives the feasibility to analyze the effect of Lode angle on the property of the material.

Table 2: Stress states of different tests [84].

Stress state	Stress value			Force scheme	Stress circle	$\cos(\theta)$
	σ_1	σ_2	σ_3			
Axial symmetry tension	σ	0	0			1
Axial symmetry compression	0	0	$-\sigma$			0.5
Bi-axial symmetry tension	σ	σ	0			0.5
Bi-axial symmetry compression	0	$-\sigma$	$-\sigma$			1
Bi-axial symmetry tension	2σ	0	0			$\dfrac{\sqrt{3}}{2}$
Torsion	σ	0	0			$\dfrac{\sqrt{3}}{2}$

However, most of the constitutive models do not account for the influence of the state of stress on the work material behavior. Several research works have demonstrated the significant effect of the state of stress not only on damage characterization but also on plasticity. A wide range of stress state distributed in the deformation zone takes place in the cutting process depending upon various cutting parameters. Abushawashi et al. [4] showed that the state of stress could control the strength of the produced chip. Specifically, the state of stress in the first deformation zone (FDZ) controls the material plastic strain limit. Bai and Wierzbicki [74] proposed the plasticity model with stress triaxiality and Lode angle dependence, and determined its coefficients by mechanical tests. It is given in Eq. 45:

$$\tilde{\sigma} = A_{\mathrm{BW}}\left(\varepsilon_0 + \bar{\varepsilon}_p\right)^{n_{\mathrm{BW}}}\left[1 - c_\eta\left(\eta - \eta_0\right)\right]\left[c_\theta^s + \left(c_\theta^{\mathrm{ax}} - c_\theta^s\right)\left(\gamma - \frac{\gamma^{a+1}}{a+1}\right)\right] \qquad Eq.\ 45$$

where A_{BW} and n_{BW} are the coefficients of material strain hardening function; η_0 is the reference value of stress triaxiality from the reference test; c_η is a material constant needing to be calibrated, which represents the hydrostatic pressure effect on material plasticity. The parameter γ represents the difference between von Mises and Tresca equivalent stresses in the deviatoric stress plane.

After using this plasticity model, the force-displacement curves are compared between experimental and simulated results in the tensile tests of flat grooved plates, as shown in Fig. 24. Without any corrections, a big difference exists between experimental and simulation results. The correction with the Lode angle improves the accuracy more than correction with the hydrostatic pressure. Therefore, these effects cannot be neglected for the plasticity model of Aluminium 2024-T351.
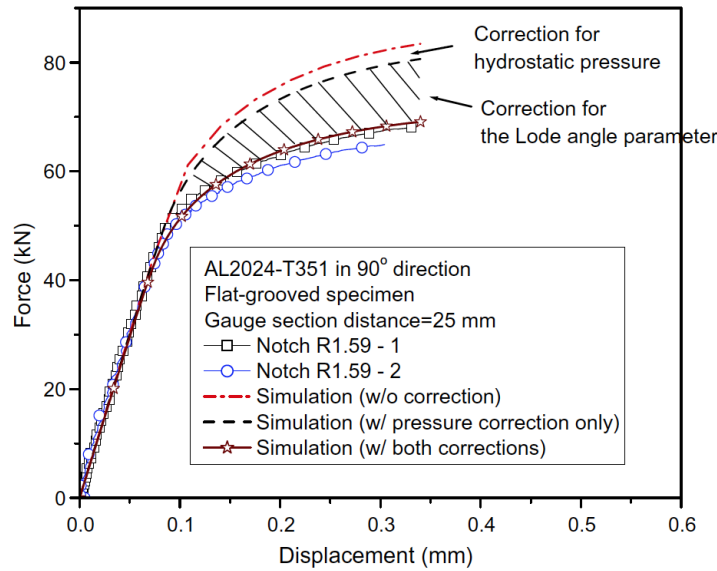
Fig. 24: A comparison of force–displacement curves between experimental results and simulation results: flat grooved specimens [74].

Then Algarni et.al. [85] modified the parameter c_θ^s in *B-W* (Bai-Wierzbicki) plasticity model to improve its accuracy. In the modified *B-W* model, c_θ^s is assumed to be the function of the equivalent plastic strain and the Lode angle parameter. The yield behavior was assumed to be symmetric between tension and compression due to the lack of experimental data. It is noted that the yield surface becomes a little concave at large plastic strain. Further research needs to be done to certify this abnormality. Also, an extended modified *B-W* model was proposed by Buchkremer et.al. [73]. The multiplicative terms representing the effects of the strain rate and the temperature were added, but the effect of stress triaxiality is neglected in the model. Then, this model is applied to the longitudinal turning simulation of the steel AISI 1045. The experimentally and numerically obtained cutting forces, chip geometries and cutting temperatures are in close agreement. It can be concluded that the integration of the effects of strain rate and temperature by multiplicative factors with the effect of the state of stress can enhance the predictability of model in metal cutting simulation.

Though, the modified *B-W* model can give a good description of the evolution of the yield surface. However, the unreal concave representation at large plastic strains damages its validity. The extended modified *B-W* model neglects the effect of stress triaxiality which is important in the case of Ti-6Al-4V alloy. For this reason, the terms representing the effects of stress triaxiality and Lode angle parameter in the *B-W* model will be adopted and included in the proposed model.

2.2.3 Models including the microstructural effects

The plasticity models described above are designed as phenomenological since the material behavior is described by empirically fitted functions, which contain several macroscopic variables, such as temperature, plastic strain and plastic strain rate. Other types of plasticity model are those mentioned by Melkote et al. [12] as physical-based models, since they integrate microstructural aspects (i.e., grain-size, dislocation density, etc.) in the material mechanical behavior.

The Zerilli–Armstrong (*Z–A*) constitutive model equations are motivated by the well-known theory of thermal activation of dislocations [75]. They model the plasticity as a summation of athermal and thermal stress terms that are functions of the strain, strain rate, and temperature. Differences in the flow stress behaviors of FCC, BCC, and HCP metals are captured by the equations, which accounts for the coupling of strain hardening, strain rate hardening, and thermal softening, as appropriate for the crystal structure of the metal under consideration. Eq. 46 is used for the FCC metals while Eq. 47 is used for BCC metals:

$$\sigma = \sigma_{th} + \sigma_G = B_0\sqrt{\varepsilon}e^{-\alpha_0 T + \alpha_1 T\,ln(\dot{\varepsilon}^*)} + \sigma_G \qquad\qquad Eq.\ 46$$

$$\sigma = \sigma_{th} + \sigma_G = B_{ZA}e^{-\alpha_0 T + \alpha_1 T\,ln(\dot{\varepsilon}^*)} + K_{ZA}\varepsilon^{n_{ZA}} + \sigma_G \qquad\qquad Eq.\ 47$$

where B_{ZA}, B_0, α_0, α_1 are the coefficients to be determined, σ_G is the contribution due to solutes and initial dislocation density; For BCC metals, $K_{ZA}\varepsilon^{n_{ZA}}$ is added to describe the strain dependence.

Jaspers and Dautzenberg [86] used the *Z–A* equations to describe the plasticity of AISI 1045 steel (BCC) and AA6082-T6 (FCC). They found that the model for AISI 1045 steel described the plasticity well, while the FCC equation for AA6082-T6 did not fit the plasticity data very well. Liu et al. [76] modified the HCP *Z–A* model to account for increased softening, which

was attributed to dynamic recovery and recrystallization at large strains and temperatures, to simulate chip segmentation in orthogonal cutting of Ti-6Al-4V. This dislocation-mechanics-based constitutive relation is suitable to describe the effect of microstructure. However, work-hardening rate ($d\sigma/d\varepsilon$) is independent from the temperature and strain rate, this could damage its accuracy for the large deformation application [87]. For most alloys, work-hardening behaviors are actually dependent on the temperature and strain rate. Therefore, the *Z–A* model is not a good candidate for modeling the work-hardening behaviors of materials with strong temperature and strain-rate dependences. Some modifications need to be performed when applying it into the simulation of metal cutting.

Rotella and Umbrello [70] considered the material grain-size effect in the plasticity model proposed by Calamaz et al. [69], and then applied it in orthogonal cutting simulation of Ti-6Al-4V alloy under cryogenic cooling conditions. An updating strategy was implemented in the FE code to simulate the material's microstructure changes including the grain size and the hardness variation. In the user routine, Zener-Hollomon equation has been used to predict the dynamic recrystallization and the grain size modification, while the hardness variation was included in the Hall-Petch equation. A very good agreement was found in the prediction of the surface hardness on the machined workpiece for cutting tests. This accuracy of the results can be attributed to the fact that the prediction of the surface hardness was carried out by using the Hall-Petch equation in combination with the modification of the flow stress due to the new grain size. However, all the values of coefficients in the model were determined through an iterative calibration process by using data of metal cutting tests. This may limit the application of the determined constitutive model into other operations, like impact and forming. The coefficients of friction model are also determined in this iterative process, which could influence the determined values of the constitutive model.

Another case is the Mechanical Threshold Stress (*MTS*) model [77], involving both the thermal and athermal stresses related to the dislocation density and grain size. Melkote et al. [78] extended the *MTS* model to simulate chip formation of pure titanium. The effects of dynamic recovery, dislocation drag, and dynamic recrystallization were considered in their model. Although these models intrinsically describe the microstructure evolution and the mechanical behavior of the work material, their complexity regarding the large number of coefficients to be determined through several types of experimental tests limits their application. Additionally, Denguir et al. [88] proposed a constitutive model (plasticity and damage) incorporating, not

only the strain-hardening, strain-rate and temperature effects, but also the microstructural and state of stress effects to describe the mechanical behavior of Oxygen Free High Conductivity (*OFHC*) copper in metal cutting. They showed better surface integrity prediction when the proposed constitutive model was compared with the *J-C* model.

The key features of these models are the capability to simulate microstructure and mechanical properties of the machined surface. Moreover, they can accurately describe the material response to loading outside the model calibration range. However, these models are limitedly used in metal cutting modelling and simulation because of the complexity and relatively numerous coefficients. In our case, for simplification reasons, the effect of microstructure will be neglected in the proposed model.

2.2.4 Models including the temperature effects

A so-called strain-softening term which depends on the temperature was integrated into the *J-C* model by Calamaz et al. [69], to better predict the segmented chip with small uncut chip thickness and low cutting speed in orthogonal cutting simulation of Ti-6Al-4V alloy. However, both cutting and feed forces are underestimated under different cutting conditions. Then Sima and Ozel [82] did a minor modification of the Calamaz et al. [69] model to further control the thermal softening effect. It enables the prediction of a segmented chip under low cutting speeds and feeds in the simulation of orthogonal cutting of Ti-6Al-4V alloy. Though the flow softening term increases the degree of chip serration chip, it produces more curved chips. Additionally, some model coefficients were determined by fitting between the measured and the predicted results from orthogonal cutting tests, without performing any material characterization tests.

According to Astakhov [3], metal cutting can be considered as a cold-working process when the work material in the FDZ is deformed, because most of the heat generated by plastic deformation in this zone is transported by the chip. To support this statement, the following thermal analysis is used. For a moving body, the energy conservation equation is deduced by Bejan [89], which describes the temperature distribution. The form is in Eq. 48:

$$\underbrace{k_{tc}A_{ch}\frac{d^2T}{dx^2}}_{\text{Axial conduction}} - \underbrace{(\dot{m}c_p)\frac{dT}{dx}}_{\text{Advection}} - \underbrace{h_{cv}p_B(\theta_{ch}-\theta_{en})}_{\text{Convection loss}} + \underbrace{\dot{q}A_{ch}}_{\text{Heat generation}} = 0 \qquad Eq.\ 48$$

where A_{ch} is cross–sectional area, $\dot{m}$ is the mass flow rate, p_B is the perimeter, k_{tc} is the thermo–conductivity of the work material (or material of the chip), c_p is the specific heat of this material, and h_{cv} is the convection heat transfer coefficient of the process, θ_{ch} and θ_{ev} are the temperatures of the chip and the environment, respectively.

The convection loss can be neglected because the chip's high velocity. Therefore, the role of advection in metal cutting needs to be analyzed. Usually, the whole amount of heat due to the plastic deformation is generated along this plane. The heat transfer is balanced in this plane due to two mechanisms of heat conduction: thermo–conductivity that attempts to bring a portion of the generated heat into the layer being removed and advection that attempts to bring a portion of this heat into the chip due to its motion, as can be seen in Fig. 25. The ratio of the portions of the heat generated on the shear plane due to thermo–conductivity and that one due to advection is determined by the Péclet number (Eq. 49) [89]:

$$Pe = \frac{\text{Heat of advection}}{\text{Heat of conduction}} = \frac{V_p L_p}{w_p} \qquad\qquad Eq.\ 49$$

where V_p is the velocity scale, L_p is the length scale, and w_p is the thermal diffusivity.
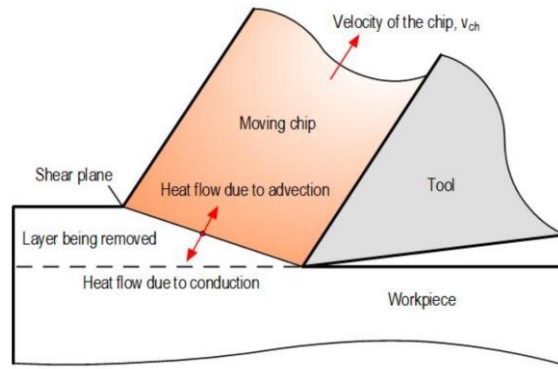
Fig. 25: Simplified model of chip formation in metal cutting [4].

When the Péclet number is applied to metal cutting, V_p represents the chip velocity relative to the tool rake face (m/s), L_p represents the uncut chip thickness (mm) and w_p represents the thermal diffusivity (m^2/s). For example, in orthogonal cutting of Ti-6Al-4V using the typical cutting conditions (cutting speed $V_P = 0.917$ m/s (55 m/min) and $L_p = 0.15$ mm), the chip compression ratio ζ is equal to 1.5. Considering the thermal diffusivity w_p of Ti-6Al-4V as equal to 7.15×10^{-6} m^2/s, the Peclet number is equal to 12. Therefore, 92% of the heat produced by plastic deformation in the FDZ flows into the chip, while only 8% of this heat flows into the

workpiece. Moreover, the heat generated by friction at the tool–chip interface does not flow to the FDZ, for the same reason (heat advection).

2.3 Damage model

As discussed in chapter 1, machining must be treated as the purposeful fracture of the layer being removed, as metal cutting is the physical separation of the layer being removed (in the form of chips) from the rest of the workpiece [3]. Therefore, the proper modelling of the work material in metal cutting should consider not only the material flow stress (plasticity), but also the conditions to fracture occurs. Therefore, the constitutive model should also include a damage part.

2.3.1 Damage initiation

The damage models include two groups: one is physics based, the other is phenomenological. For the physic based ones, the equations are deduced by analyzing the behavior of micro voids. In contrary, phenomenological models try to use proper equations to describe different effects with numerous experimental data, rather than considering the physical theory.

According to the physics based model, Rice and Tracey [90] described the ductile fracture process as the growth and coalescence of microscopic voids under the superposition of hydrostatic stresses. Then, a fracture locus was introduced based on the ratio between the hydrostatic and the equivalent stresses, often referred to as stress triaxiality. It can be seen in Eq. 50.

$$\bar{\varepsilon}_p^i = C_{1R} e^{C_{2R}\eta} \qquad\qquad Eq.\ 50$$

where C_{1R} and C_{2R} are two coefficients of the exponential function to be determined.

This model has been widely adopted by other researchers. For example, Johnson and Cook [55] proposed a damage model accounting for several effects on damage initiation: stress triaxiality, strain rate and temperature, as shown in Eq. 14 of Chapter 1. Compared with Rice-Tracey model, the term in *J-C* damage model representing the effect of stress triaxiality could better capture the fracture loci of the steel AISI 1045 [91]. Furthermore, the *J-C* damage model has found numerous applications, containing metal cutting problems, because of its simplicity of formulation, the ease of calibration and the wide availability of material coefficients for many ductile metals.

Bao and Wierzbicki [62] designed a series of tests (upsetting test, tensile test, shear test and compression test) to determine the fracture strain in the entire range of stress triaxiality for 2024-T351 aluminium alloy. A piecewise function considering the effect of stress triaxiality is used to describe the fracture strain $\bar{\varepsilon}_p^i$, including three branches. Similarly, Giglio et al. [92] used Bao-Wierzbicki law to describe the fracture behavior of Ti-6Al-4V alloy, as can be seen in Fig. 26. There is a cut-off region in which the damage does not occur, i.e., $\eta <$-1/3. It is evident from Fig. 26 that the relation between fracture strain and stress triaxiality cannot be described by a monotonic function. Besides the stress triaxiality, some other parameters may influence the fracture ductility.
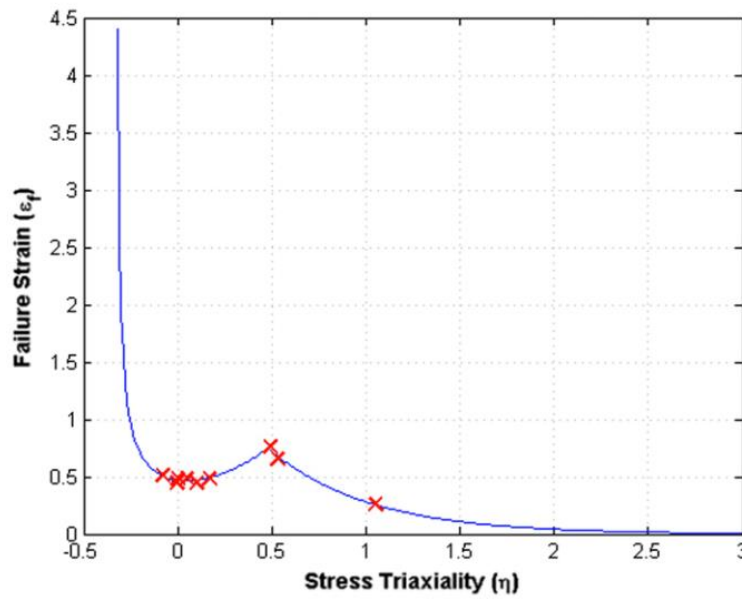
Fig. 26: Fracture locus of the Ti-6Al-4V alloy according to the Bao–Wierzbicki model [62].

Wilkins et al. [64] was first to introduce the effect of deviatoric stress ratio *A*, which is related to Lode angle parameter $\bar{\theta}$ on ductile fracture. The fracture is assumed to be the result of the history of strain damage to the material, and the model was applied in ballistics processes such as penetration and perforation where fracture occurs. However, it has rarely, if ever, been used in metal cutting processes. When calibrated properly, the Wilkins damage model is able to be implemented for metal cutting problems with appropriate damage evolution rules, a more comprehensive and realistic fracture criterion can be formed to better capture the physical responses in the cutting chip formation process. It predicts reasonably well the trend of experimental points in the range $0 \leq \eta \leq 1/3$, but underestimates the material ductility for $1/3 \leq \eta \leq 2/3$ [93].

Then, Bai and Wierzbicki [74] added the Lode angle effect into the fracture locus apart from the stress triaxiality effect. They proposed a constitutive model considering the state of stress, described by both stress triaxiality and Lode angle. Regarding the effect of $\bar{\theta}$ on fracture locus, a parabolic function is proposed [74]. In order to cover a wide range of stress state, a new type of butterfly shape specimen is designed, as shown in Fig. 27a. It has several advantages including the same fracture initiation location (the center of the specimen) under all loading combinations, and ability to generate a wide range of stress state using only one type of specimen. By using the test data of this specimen, fracture surface is depicted in Fig. 27b. Compared with a symmetric 3D fracture surface based on Wilkins model, an asymmetric 3D fracture locus is obtained.

Additionally, Erice and Gálvez [94] introduced the Lode angle dependency in the *J-C* damage model. To interpret the Lode angle effect, the term used in Xue-Wierzbicki [95] is adopted in the model. To certify the significant influences of Lode angle and damage evolution on the fracture prediction for precipitation hardened Inconel 718 alloy, both the tensile tests of smooth axisymmetric and plane strain specimens are implemented. Only both of the Lode angle and damage evolution are included, the complex fracture behavior can be well predicted.

It should be noted that the extension to the classical metal plasticity and ductile fracture locus may not be necessary for all metallic materials. For example, the 1045 steel shows no obvious effect of hydrostatic pressure and Lode angle dependence on metal plasticity, and the DH36 steel shows no apparent dependence on the Lode angle parameter on the fracture locus [96]. Hence, every material needs a careful executed calibration procedure with regards to both plasticity and fracture.

(a)   (b)
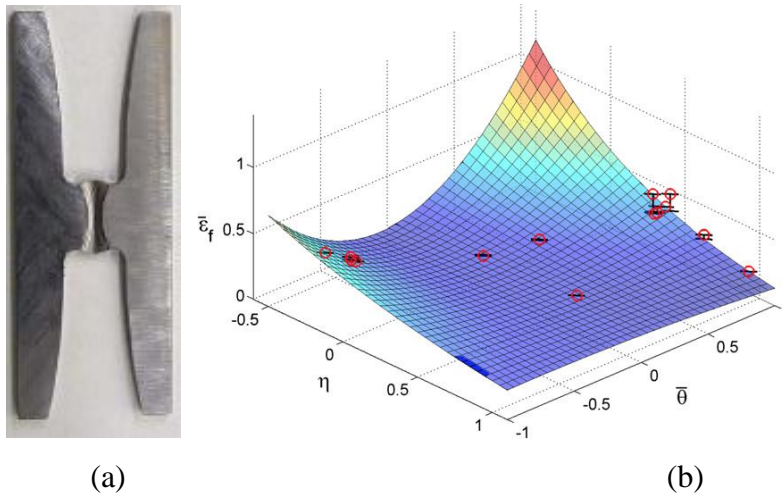
Fig. 27: (a) Butterfly specimen; (b) 3D fracture surface of 2024-T351 aluminium alloy [74].

Algarni et.al. [98] modified the extended *M-C* fracture criterion, *MMC* model, and coupled with the damage evolution criterion. The *MMC* model predicted well the damage behavior of Inconel 718 alloy, as an excellent correlation between FE simulations and experimental results are achieved. After, Allahverdizadeh et.al. [79] used *MMC* model to reproduce the ductile fracture of Ti-6Al-4V alloy and achieved good agreement between simulated and experimental force-displacements. Fig. 28 shows the 3D fracture surface of Ti-6Al-4V alloy. Not only stress triaxiality, but also Lode angle could influence the fracture strain of Ti-6Al-4V alloy. That's why both of the effects should be included in the proposed damage model.
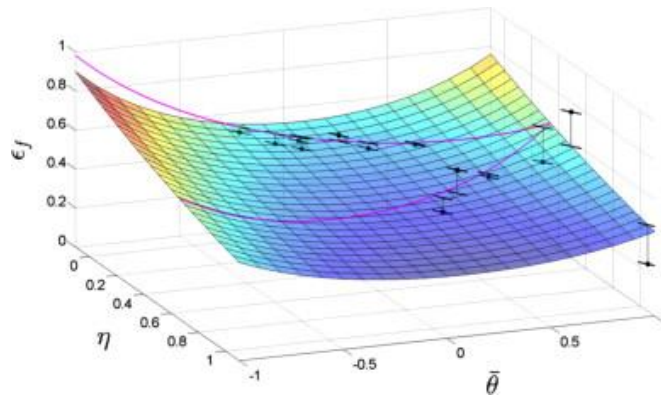
Fig. 28: 3D fracture surface of Ti-6Al-4V alloy [79].

2.3.2 Damage evolution

Liu et.al. [65] investigated *J-C* plasticity model integrating different damage models for simulation of metal cutting 2024-T3 aluminium alloy. It was concluded that damage model with damage evolution predicted better chip morphology than the ones without damage evolution. *J-C* model with mode I damage evolution is good enough for predicting accurate cutting forces compared to *J-C* model with mixed mode damage evolution. Buchkremer et al. [73] extended both the plasticity and the damage models proposed by Bai and Wierzbicki [74] by including the temperature and strain-rate effects. A damage evolution law is also combined in the model. They predicted the forces, temperatures, chip formation and flow with high accuracy in simulation of turning AISI 1045 steel.

Abushawashi et al. [99] considered only the effect of stress triaxiality in both of the plasticity and damage model, since the constitutive model is applied into the simulation of orthogonal cutting, which has the constant Lode angle parameter. The exponentially damage evolution law is slightly modified. They predicted well the chip geometry and cutting force in the simulation. They found that the material plastic strain limit in the first deformation zone is controlled by

the value of stress triaxiality in orthogonal cutting of AISI 1045 steel. Wang and Liu [63] investigated the stress triaxiality effect on the generation of segmented chips during machining of Ti-6Al-4V alloy. It was found that its value in the first deformation zone ranges from -0.6 to 0.6.

2.4 Proposed constitutive model for Ti-6Al-4V titanium alloy

After reviewing different constitutive models available in the literature for several work materials, including for the Ti-6Al-4V titanium alloy, a model used for machining Ti-6Al-4V titanium alloy need to be formulated. A simple and effective constitutive model should include the most relevant factors affecting the mechanical behaviour of the Ti-6Al-4V titanium alloy in the FDZ in machining. These effects are the following:

a) <u>Strain hardening and strain-rate effect.</u> For most of the metals or alloys, the strain hardening plays an important role in the mechanical behavior. It is obvious that the strain-rate influences the mechanical behavior of the workpiece, such as plasticity and fracture strain. A high strain rate is assumed to be experienced by the workpiece. Thus, effect of the strain-rate needs to be added to the proposed constitute model.

b) <u>State of stress effect.</u> The state of stress influences both the plasticity and fracture of the work material as demonstrated by Bai and Wierzbicki. It is described by two parameters: the stress triaxiality η and the Lode angle parameter $\bar{\theta}$. According to the references [94], [97], [98], consideration of the effects of these two parameters reduces the differences between the predicted and the measured results. Particularly, the Lode angle has a higher influence on the material plasticity than the stress triaxiality, whereas the inverse is the case concerning the fracture strain. Thus, the state of stress should also be included in the constitutive model through the Lode angle and stress triaxiality parameters.

As far as the temperature effect is concerned, as demonstrated in section 2.2.4, almost the heat generated in the FDZ in metal cutting goes into the chip due to mass transportation, i.e. advection, and only a small amount of this heat flows into the uncut workpiece by conduction. For this reason, the temperature of the work material in the FDZ just ahead of the tool hardly exceeds 200°C for several work materials [133-135]. Researchers of the National Institute of Standards and Technology (NIST) in the USA have developed a special setup for high resolution and high speed temperature measurement by infrared thermography. They have shown that for the case of Ti-6Al-4V titanium alloy, this temperature does not exceed 384°C

[136]. This temperature is not high enough to significantly influence the mechanical behavior of Ti-6Al-4V titanium alloy in the FDZ. In addition, the mechanical tests at high strain rates already include the thermal softening in the mechanical response of the Ti-6Al-4V titanium alloy due to the conversion of plastic deformation into heat. Since the proposed model is related to the mechanical behavior of the Ti-6Al-4V titanium alloy in the FDZ, the term of this model related to the temperature is not considered in the proposed constitutive model.

Two parts are included in the proposed constitutive model: plasticity and damage. The proposed plasticity model is shown in Eq. 51, incorporating the strain hardening, strain rate and state of stress effects. The first two terms are based on the Johnson - Cook [55] and Santos et al. [83] models, respectively. Furthermore, the last two terms of Eq. 51 are related to the state of stress effect, which is characterized by the stress triaxiality and the Lode angle parameter obtained from the Bai and Wierzbicki [74] model.

$$\bar{\sigma} = \underbrace{\left[A + m\bar{\varepsilon}_p^n\right]}_{\substack{\text{Strain hardening} \\ \text{effect}}} \times \underbrace{\left[B + C\ln\left(E + \frac{\dot{\bar{\varepsilon}}_p}{\dot{\bar{\varepsilon}}_0}\right)\right]}_{\substack{\text{Strain rate (visco)} \\ \text{effect}}} \times \underbrace{\left[1 - c_\eta\left(\eta - \eta_0\right)\right]}_{\substack{\text{Stress triaxiality} \\ \text{effect}}} \times$$

$$\underbrace{\left[c_\theta^s + \left(c_\theta^{ax} - c_\theta^s\right)\left(\gamma - \frac{\gamma^{a+1}}{a+1}\right)\right]}_{\text{Lode angle effect}}$$

Eq. 51

$$\gamma = \frac{\sqrt{3}}{2-\sqrt{3}}\left[\sec\left(-\frac{\bar{\theta}\pi}{6}\right) - 1\right]$$

Eq. 52

$$c_\theta^{ax} = \begin{cases} c_\theta^t & \text{if} \quad \bar{\theta} > 0 \\ c_\theta^c & \text{if} \quad \bar{\theta} \leq 0 \end{cases}$$

Eq. 53

In the previous equations: i) the coefficients A, m and n are used in the strain hardening term; ii) the coefficients B, C and E are used in the strain rate term; iii) the coefficient c_η is used in the stress triaxiality term; iv) the coefficients c_θ^t, c_θ^c, c_θ^s and a are used in the Lode angle term; v) η_0 is the reference stress triaxiality and $\dot{\varepsilon}_0$ is the reference strain rate; vi) γ describes the difference between Tresca and von-Mises equivalent stresses on the deviatoric stress plane, as represented in Eq. 52; and vii) the coefficients c_θ^t, c_θ^c, c_θ^s are interdependent and at least one of them equals 1. Considering the compression test of cylindrical specimens at quasi-static conditions as a reference, η_0 equals -1/3, $\dot{\varepsilon}_0$ equals 0.05 s^{-1} and c_θ^c equals 1.

The damage model includes damage initiation and damage evolution, as shown from Eq. 54 to Eq. 56, based on Bai and Wierzbicki [74] and Abushawashi [91] models. Eq. 54 represents the damage initiation, while Eq. 55 and Eq. 56 represent the damage evolution. Fracture surface depends on both the stress triaxiality and Lode angle parameter. The work material strength decreases as the strain increases after damage initiation, and the fracture energy is estimated by the material stiffness degradation.

$$\bar{\varepsilon}_i^p = \left\{ \left[\frac{1}{2} \left(D_1 e^{-D_2\eta} + D_5 e^{-D_6\eta} \right) - D_3 e^{-D_4\eta} \right] \bar{\theta}^2 + \frac{1}{2} \left(D_1 e^{-D_2\eta} - D_5 e^{-D_6\eta} \right) \bar{\theta} + D_3 e^{-D_4\eta} \right\} \times$$
$$\left[1 + D_7 \ln \left(\frac{\dot{\varepsilon}}{\dot{\varepsilon}_0} \right) \right]$$

$$\textit{Eq. 54}$$

$$\bar{\sigma} = (1-D)\tilde{\sigma}, \quad D = \frac{1-\exp\left(\lambda\varepsilon^*\right)}{1-\exp(\lambda)}, \quad \varepsilon^* = \frac{\bar{\varepsilon}^p - \bar{\varepsilon}_i^p}{\bar{\varepsilon}_f^p - \bar{\varepsilon}_i^p} \qquad \textit{Eq. 55}$$

$$G_f = \int_{\bar{\varepsilon}_i^p}^{\bar{\varepsilon}_f^p} l\bar{\sigma} d\bar{\varepsilon}^p = \int_0^{\bar{u}_f} \bar{\sigma} d\bar{u} \qquad \textit{Eq. 56}$$

In these equations, D_1-D_7, λ ,and G_f are the material coefficients, λ controls the material degradation rate and G_f is the material fracture energy density; $\bar{\varepsilon}_i^p$ is the plastic strain at damage initiation; $\bar{\varepsilon}_f^p$ is the plastic strain when all the stiffness and the fracture energy of the material have been lost and dissipated, respectively; $\tilde{\sigma}$ is the hypothetical undamaged stress evaluated by Eq. 51); l is the characteristic length of the finite element; $\bar{u} = 0$ relates to the equivalent plastic displacement before damage initiates; and $\bar{u}_f$ is the equivalent plastic displacement at complete fracture.

As shown in Eq. 56, a characteristic length is introduced to describe the fracture energy. Therefore, the energy dissipated in the damage evolution is defined as per unit area, rather than per unit volume. In this case, a stress-displacement response instead of the stress-strain response is used to describe the material softening after damage initiation.

2.5 Summary of the chapter

In this chapter, constitutive models used in metal cutting simulation in general and for Ti-6Al-4V in particular, is analysed. Then, a constitutive model describing the plasticity and fracture of the Ti-6Al-4V alloy for metal cutting simulation is proposed. The distinguished feature of

this model is the accounting for the state of stress effect in the work material deformation and fracture, in addition to the traditional strain hardening and strain-rate effects. Thermal softening term is not included in the proposed model for two reasons. First, the mechanical tests at high strain rates already include the temperature effect due to the conversion of plastic deformation into heat. Second, the temperature of the workpiece in the FDZ hardly exceeds 200°C due to mass transportation (i.e. heat advection) by the moving chip. In the following chapter, the coefficients of this model will be determined using an innovative experimental and modelling approach.

Chapter 3:
Determination of the coefficients of the
constitutive model

3.1 Application to determine the coefficients of the constitutive model

The predictability of manufacturing process simulation is highly dependent on the accuracy of the constitutive model to describe the mechanical behavior of the work material. To generate the states of stress and strain rates representative of this process, mechanical tests were performed using a specific experimental setup. This included a specimen geometry designed to generate different states of stress, as well as a digital image correlation technique (*DIC*) to obtain the strains during the mechanical tests. For the determination of the coefficients of the constitutive model, the yield stress and fracture locus obtained from these tests were used in an optimization-based procedure. To verify the accuracy of the proposed constitutive model to represent the mechanical behavior of the Ti-6Al-4V alloy under different states of stress, force-displacement curves obtained using this model and the Johnson-Cook (*J-C*) model are compared with the curves obtained experimentally. Fig. 29 shows the procedure used to determine the coefficients of the proposed constitutive model presented in Chapter 2.
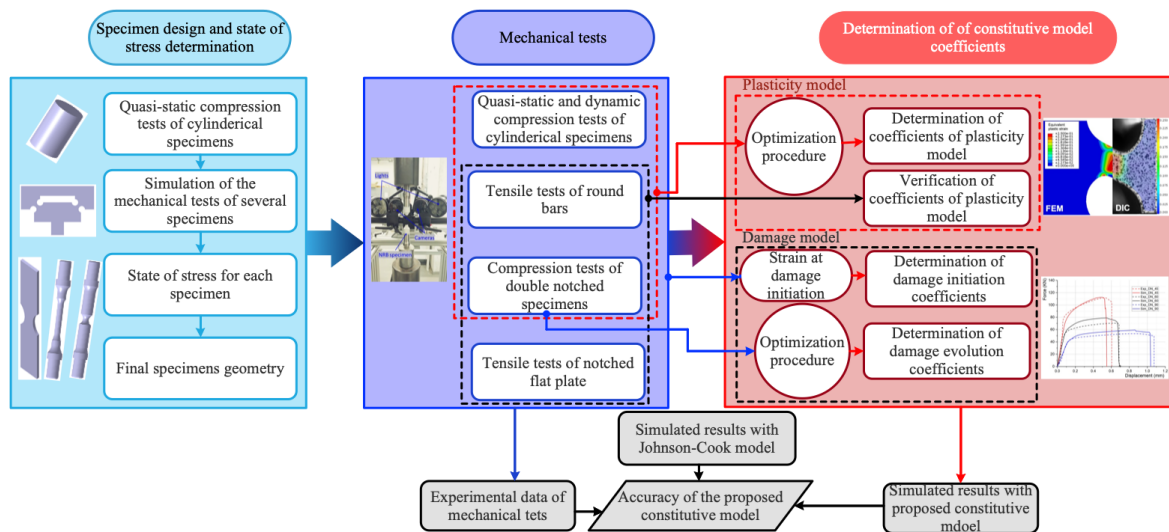
Fig. 29: Flowchart of coefficients determination of constitutive model

3.2 Properties of Ti-6Al-4V alloy used in this study

Table 3 shows the chemical composition (weight percentage) of the Ti-6Al-4V titanium alloy used in this study, obtained by rolling and annealing. Almost 90% of this alloy is titanium, followed by 6% of aluminium, 4% of vanadium, 0.3% (max) of iron and 0.2% (max) of oxygen.

Table 3: Nominal chemical composition of Ti-6Al-4V (as received).

Element	Al	V	Fe max.	O max.	N max.	H max.	C max.	Ti
Composition (wt. %)	5.50-6.75	3.50–4.50	0.30	0.20	0.05	0.01	0.08	Base

Fig. 30 shows its microstructure of this alloy, which is composed by two-phase structure (α + β). The good balance between α and β phases makes it achieve high strength level without losing ductility [16]. The α phase (white color) shows equiaxed microstructure, while the β phase (black color) presents lamellar microstructure.
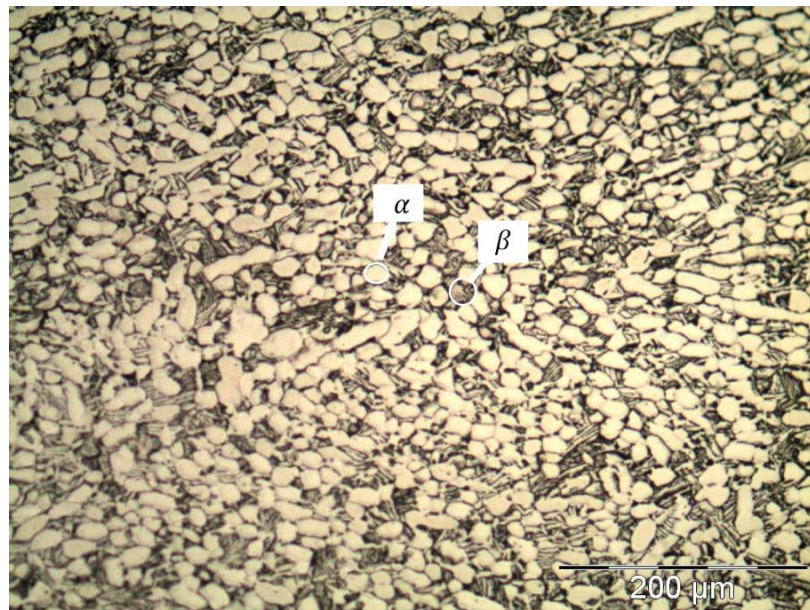
Fig. 30: Microstructure of an as-received Ti-6Al-4V alloy.

The physical properties of Ti-6Al-4V alloy are shown in Table 4. The high tensile strength and relatively low density lead to a large specific strength, which makes this alloy widely used in aerospace industry. In addition, the lower thermal conductivity of this alloy when compared to the steels could cause high localized temperatures at the tool-chip interface during the machining process, thus accelerating the tool wear.

Table 4: Physical properties of Ti-6Al-4V alloy (as received).

Tensile strength (MPa)	0.2% proof stress (MPa)	Elongation	Density (g/cm^3)	Melting point (^{o}C)	Measured hardness (HV$_{100}$)	Thermal conductivity at 20 ^{o}C (W/m/K)
900 – 1600	830	8%	4.42	1650	363	6.6

A raw block of 70 mm x 90 mm x 1020 mm was used in this study for both mechanical and machining tests. The homogeneity and isotopy of this block were investigated by analysing the

microstructure and mechanical properties in the three directions. Fig. 31 illustrates the hardness measurements of raw block. Five different surfaces from A to E are selected to measure the Brinell (macro)hardness. The Brinell hardness was measured using a 2.5 mm tungsten carbide ball and a loading of 187.5 kgf. The obtained hardness values in the 5 surfaces are very similar (HBW_A= 304±7, HBW_B= 305±3, HBW_C= 304±6, HBW_D= 310±7 and HBW_E= 290±6).

On the other hand, two samples were extracted from the raw block: one from the centre (sample #1) and the other from the border (sample #2) (see Fig. 31a). Then, these two samples are mounted in the resin and polished (Fig. 31b). Finally, the microhardness and grain size are investigated using OM-Olympus Vanox-T AH-2. The Vickers microhardness was measured using a loading of 300 gf with 10s loading time. As shown in Fig. 31b, the measured microhardness in the middle of the surface of sample #1 is 335±19 HV, while in sample #2 is 326±15 HV. Meanwhile, the grain sizes of two samples are measured based on standard ASTM E112-12 [100]. The grain size at the cross section of sample #1 in Fig. 31b is 17.3±1.4 µm, and of sample #2 is 14.2±1.7 µm. Therefore, the average microhardness, hardness and grain size of this block are 330±18 HV, 303±8 HBW and 15.5±1.8 µm, respectively.

Meanwhile, the mechanical properties of the Ti-6Al-4V alloy were measured by the material supplier in different directions (longitudinal, transversal and short transversal) and shown in

Table 5. Based on the results shown in this figure, the Ti-6Al-4V alloy used to manufacture the specimens for both mechanical and machining tests can be considered nearly homogeneous and isotropic.

(a)   (b)
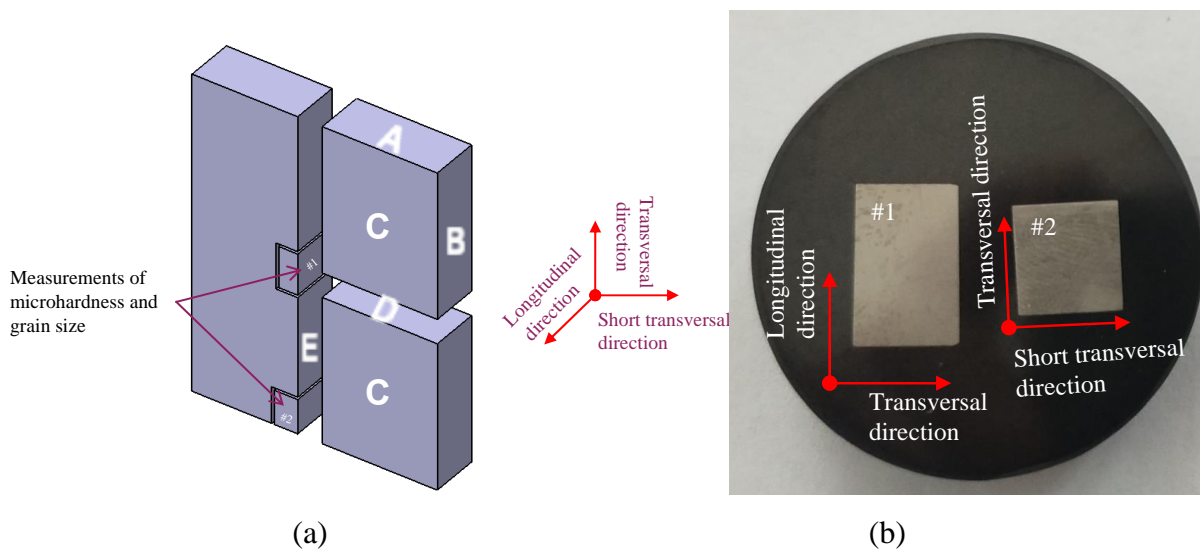
Fig. 31: (a) Hardness measurements of raw block, (b) Measurement of microhardness and grain size.

Table 5: Mechanical property of Ti-6Al-4V alloy raw block measured in three directions ([a] elongation measured using a gage length of 4×D, where D is the initial diameter of the sample used in the tensile tests. [b] elongation measured using a gage length of $5.65 \times A_0^{1/2}$, where A_0 is the initial are of the samples cross-sectional).

Direction	Yield strength (0.2%) (MPa)	Ultimate tensile strength (MPa)	Elongation 4×D [a] (%)	Elongation $5.65 \times A_0^{1/2}$ [b] (%)	Elongation 5×D (%)	Reduction area (%)
Longitudinal	871 ± 6	945 ± 16	18.5 ± 2.1	17.3 ± 0.4	17.3 ± 0.4	30.5 ± 28
Transversal	871 ± 2	935 ± 2	19 .0± 1.4	16.0 ± 1.4	16.0 ± 1.4	33.3 ± 5.3
Short transversal	834 ± 0	951 ± 2	-	11.8 ± 0.4	-	21.3 ± 1.8

3.3 Mechanical tests

3.3.1 Specimen's geometry and state of stress

As far as the specimen geometry is concerned, when combined with the loading conditions, it should be able to reproduce several states of stress and strain rates usually found in metal cutting. There are two solutions to generate different states of stress in the specimens during the mechanical tests. One is to use advanced machines allowing complex multi-axial loadings to be performed with simple designed specimens [101]. The other solution is to use (complex) specially designed specimens to get the desired state of stress by applying simple loadings (tensile, compressive, torsion). The latter solution is relatively simple because the loading conditions are easier to control, and the gauge areas are fixed.

The aim of specimen design is to achieve the capability to generate a broad range of states of stress. Fig. 32 shows the possible states of stress generated by combining several specimen geometries and loading types (tension/compression) used in this work. The cylindrical specimen, double notch (DN), notched round bar (NRB), smooth round bar (SRB) and notched flat plate (NFP) specimens permitted several states of stress levels to be generated by varying their geometries. The values of state of stress were determined by the simulation of mechanical tests using all the specimens.

Fig. 33 shows the axisymmetric specimen (cylindrical, SRB and NRB) geometries. The cylindrical specimen (Fig. 33*a*) was used in the compression tests at different strain rates, with a constant state of stress (stress triaxiality equals -1/3 and Lode angle parameter equals -1 for quasi-static conditions) [74]. Before designing other specimen geometries, quasi-static

compression tests of cylindrical specimens were performed to obtain the flow stress. Then, this flow stress was applied in the simulations of the mechanical tests of other specimen geometries to determine their states of stress.
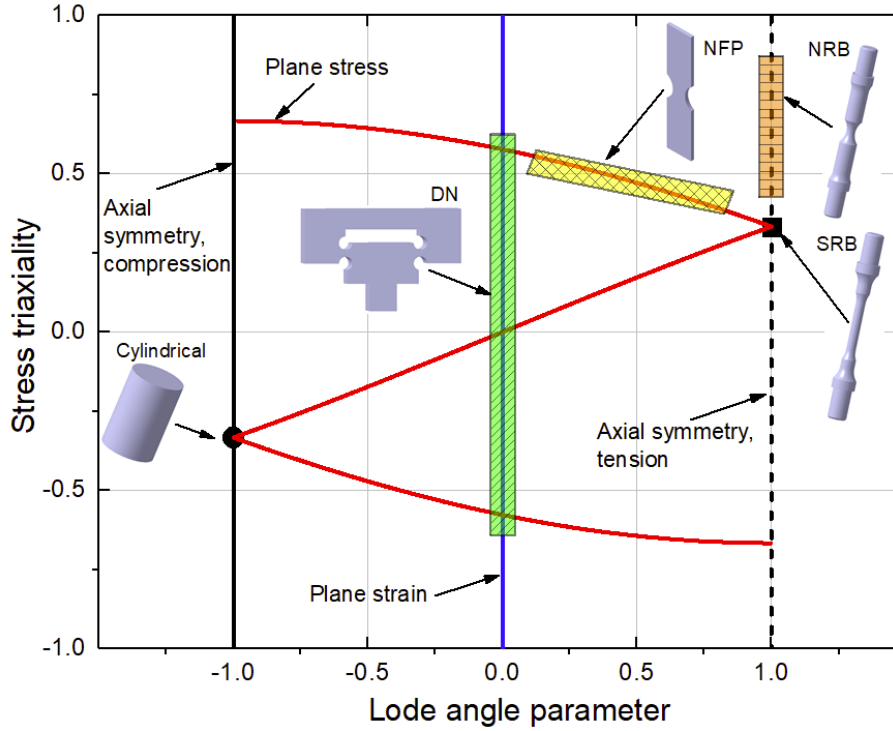
Fig. 32: States of stress and corresponding specimen geometries (cylindrical specimen; DN – double notched; NRB – notched round bar; SRB – smooth round bar; NFP – notched flat plate).

In contrast, the SRB (Fig. 33*b*) was used in the tensile tests under quasi-static conditions to obtain a stress triaxiality of 1/3 and a Lode angle parameter of 1[74]. The NRB (Fig. 33*b*) was introduced to generate values of stress triaxiality between 0.33 and 0.90, keeping the Lode angle parameter constant and equal to 1 [74]. The stress triaxiality values of these specimens in the center of the neck region can be estimated by Eq. 2 [74].

$$\eta_{\text{center}} = \frac{1}{3} + \ln\left(1 + \frac{a}{2R}\right)$$

Eq. 57

a represents the minimum radius of the neck cross section and *R* represents the local radius of the neck, as shown in Fig. 33*b*. To vary the stress triaxiality from 0.33 to 0.90, three values of *R* were used (6, 12 and 30), keeping the diameter of the neck cross-section constant at 6 mm.

(a)   (b)
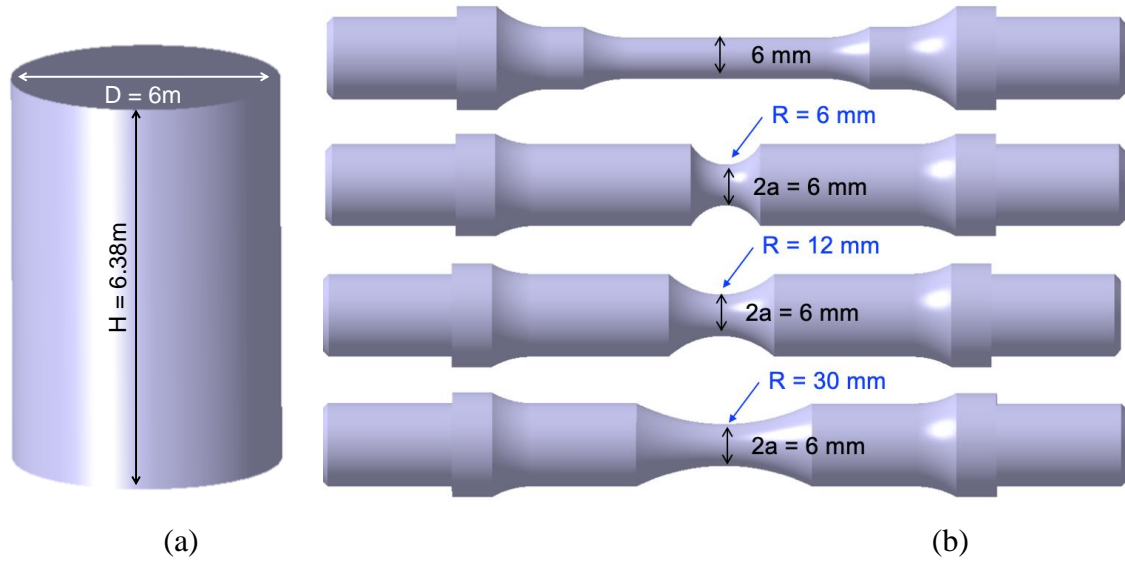
Fig. 33: Nominal geometry of the axisymmetric specimens: (a) cylindrical specimen used in compression tests at several strain-rates; (b) smooth and notched round bars used in quasi-static tensile tests.

The value of stress triaxiality was evaluated by simulations of the mechanical tests using ABAQUS FEA software. Fig. 34 shows an example of simulating a tensile test of notched round bar with R equal to 12 mm. Fig. 34a illustrates the model and the corresponding boundary conditions. To describe the material plasticity in all the mechanical tests simulations presented in this chapter, the stress-strain curves (before damage initiation) acquired from the quasi-static compression test of cylindrical specimens were used. These curves were included in ABAQUS software as a table representing the stress in function of the strain. The two extremities of the bar were fixed to a rigid body representing the machine clamping system. The bottom extremity of the bar was fixed, while the upper one moved at a constant loading speed of 1 mm/s. The 4-node axisymmetric elements (*CAX4R*) were applied in ABAQUS/Explicit, and the minimum element size was 0.2 mm x 0.3 mm. Fig. 34b and Fig. 34c show the distributions of the equivalent plastic strain and the stress triaxiality, respectively, when the value of maximum equivalent plastic strain in the bar reaches 0.4. This strain limit was chosen since, according to Allahverdizadeh [79], the strain at damage initiation for Ti-6Al-4V alloy under different states of stress is in the range between 0.3 and 0.5. Fig. 34d shows the evolution of the equivalent plastic strain and the stress triaxiality from the center to the border of the specimen (in the direction of x axis).

Since their values are largest in the center, this location is considered as the damage initiation point. Then, the stress triaxiality was plotted as a function of the equivalent plastic strain in this location (Fig. 34e). Analyzing this figure, the value of stress triaxiality varies between 0.72 and

0.89 when the strain at damage initiation is between 0.3 and 0.5 [79]. The stress triaxiality for the other specimen geometries was evaluated using similar methodology.

Fig. 34: Simulation of the tensile tests of NRB_R12: (a) FE model with boundary conditions; (b) distribution of the equivalent plastic strain; (c) distribution of the stress triaxiality; (d) distribution of the equivalent plastic strain and stress triaxiality in the direction of x axis; (e) Relation between the stress triaxiality and the equivalent plastic strain in the center of the bar.

The notched flat plate (*NFP*) geometry (Fig. 35) was used to obtain the state of stress values under plane stress conditions. In this case, by varying the neck radius (R), different values of stress triaxiality and Lode angle parameter are generated. There were three types of notched flat plate: *NFP_R10* (R = 10 mm), *NFP_R20* (R = 20 mm) and *NFP_R40* (R = 40 mm). The thickness of all these specimens was 2.35 mm to ensure plane stress conditions.

The same methodology as applied for the notched round bars was also applied to evaluate the values of two state of stress parameters for the notched flat plate. An example of notched flat plate with *R* equal to 10 mm is presented in Fig. 36. Half of the specimen geometry and the

corresponding boundary conditions used in the model are shown in Fig. 36*a*. 3D elements (*C3D8R*) were used, with a minimum element size of 0.3 mm x 0.6 mm x 0.78 mm. Fig. 36*b* and Fig. 36*c* show the distributions of the equivalent plastic strain and the stress triaxiality, respectively. These distributions were obtained when the value of maximum equivalent plastic strain in the plate was equal to 0.4. Fig. 36*d* shows the evolution of the stress triaxiality and the equivalent plastic strain from the center to the border (in the direction of *x* axis). It is found that the largest value of stress triaxiality is located at the center of this specimen. Thererfore, the stress triaxiality was plotted as a function of the equivalent plastic strain in this location, where the largest stress triaxiality is obtained. The range of stress triaxiality varies between 0.59 and 0.74 when the strain at damage initiation is between 0.3 and 0.5 [79]. As far as the Lode angle parameter is concerned, the corresponding values are between -0.08 and -1 (yellow region in Fig. 32).
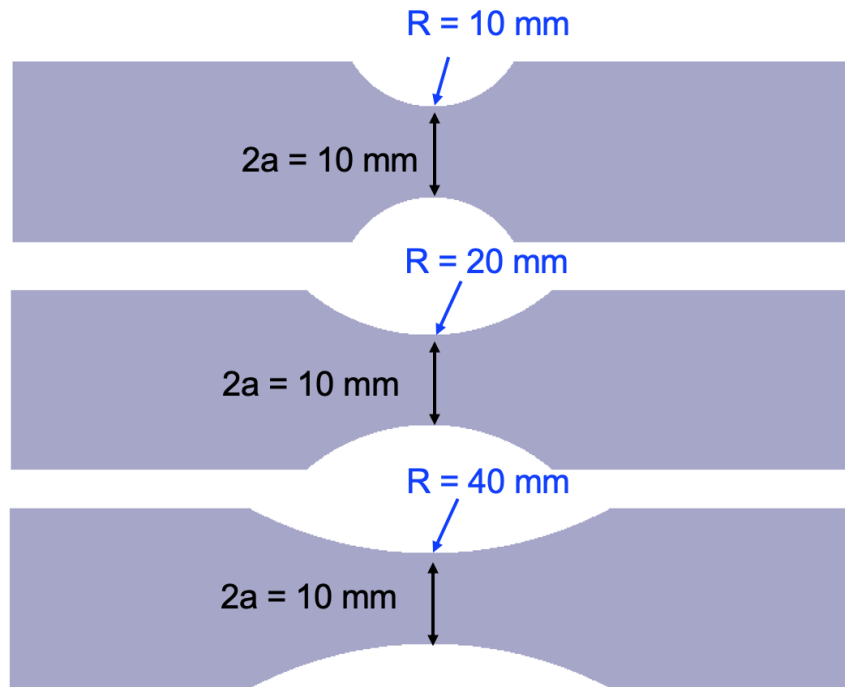
Fig. 35: Nominal geometry of the notched flat plates applied in quasi-static tensile tests. *a* is the half width of the necking cross section and *R* is the local radius of a neck in the notched flat plate.

Finally, to generate different stress triaxiality values keeping the Lode angle parameter equal to zero (plane strain conditions), the double notched specimen introduced by Abushawashi et al. [91] was used in the compression tests. This specimen has the advantage of generating both negative and positive stress triaxiality values, whereas the flat grooved specimen used by Bai and Wierzbicki [74] in tensile tests can only generate positive stress triaxiality values.

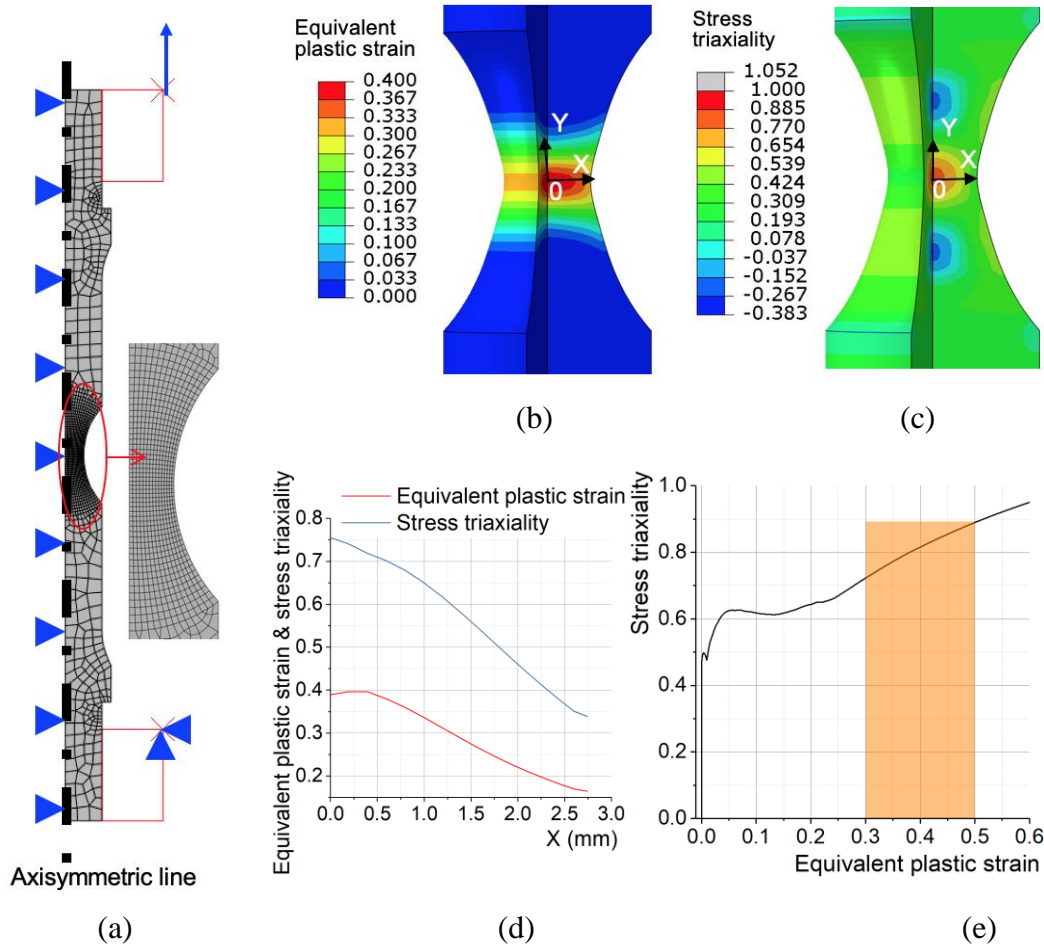Fig. 36: Simulation of tensile tests of NFP_10: (a) *FE* model with boundary conditions; (b) distribution of the equivalent plastic strain; (c) distribution of the stress triaxiality; (d) distribution of the equivalent plastic strain and stress triaxiality in the direction of x axis; (e) Relation between the stress triaxiality and the equivalent plastic strain in the center of the plate.

Different stress triaxiality values generated by the double notched specimen (*DN*) in compression tests are generated by varying the pressure angle. This angle is between the line passing through the centers of the two arcs and the (horizontal) line normal to the loading force, as shown in Fig. 37. Three double notched specimens with different pressure angles are presented in this figure. However, five pressure angles were selected for this study: 30°, 45°, 60°, 90° and 120° (references *DN_30*, *DN_45*, *DN_60*, *DN_90* and *DN_120*, respectively). A pressure angle less than 90° generates negative stress triaxiality, while positive stress triaxiality is generated by a pressure angle greater than 90°. These pressure angles generate stress

triaxialities values between –0.7 and +0.6. Additionally, the thickness of all these specimens was 25 mm to ensure plane strain conditions, so that the Lode angle parameter was zero.

<center>(a)   (b)   (c)</center>
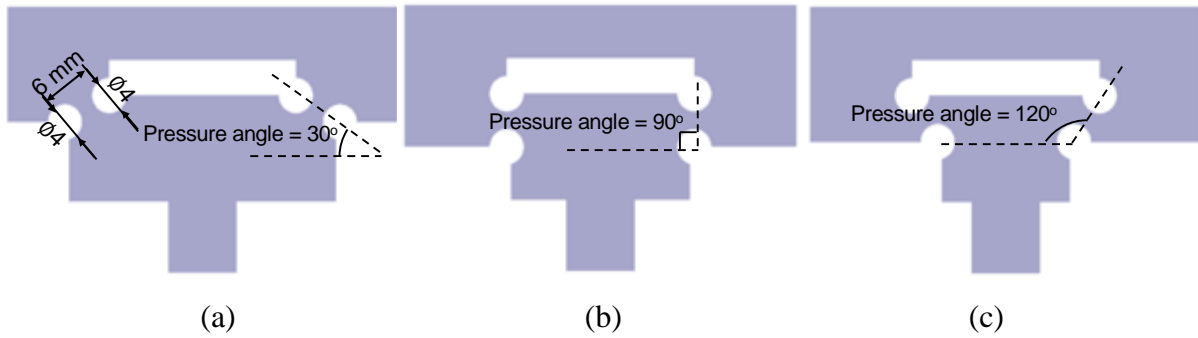
Fig. 37: Nominal geometry of the double notched specimen used in quasi-static compression tests: (a) pressure angle less than 90º; (b) pressure angle 90º; (c) pressure angle greater than 90º.

In order to determine the pressure angles that generate a broad range of stress triaxiality in the region between two arcs, simulations of the compression tests using specimens with different pressure angles were performed. For instance, Fig. 38 presents the simulation of the compression test of the DN_60. Fig. 38*a* shows the model of half of a specimen geometry and the corresponding boundary conditions. A 4-node axisymmetric element (*CAP4R*) was used, and the minimum element size was 0.07 mm x 0.1 mm.

Fig. 38*b* and Fig. 38*c* show the distributions of the equivalent plastic strain and the stress triaxiality, respectively, when the value of maximum equivalent plastic strain in the specimen reaches 0.4. To find the exact location of maximum stress triaxiality, a line connecting the maximum equivalent plastic strain values between both arcs was drawn. Then, the distribution of stress triaxiality and the equivalent plastic strain were plotted along this line (Fig. 38*d)*. As can be seen, the largest value of stress triaxiality is located in the middle of the two arcs. Therefore, the stress triaxiality was plotted as a function of the equivalent plastic strain in this location, and represented in Fig. 38*e*. This figure reveals that the value of stress triaxiality for this specimen is between -0.31 and -0.29.

The procedure described above permitted determination of the range of states of stress generated by each specimen geometry. This information is important to select suitable specimen geometries to cover the broad range of state of stress represented in Fig. 32. The exact state of stress value for each specimen will be calculated in the following section after the coefficients of the proposed plasticity model have been determined.

(a)   (d)   (e)
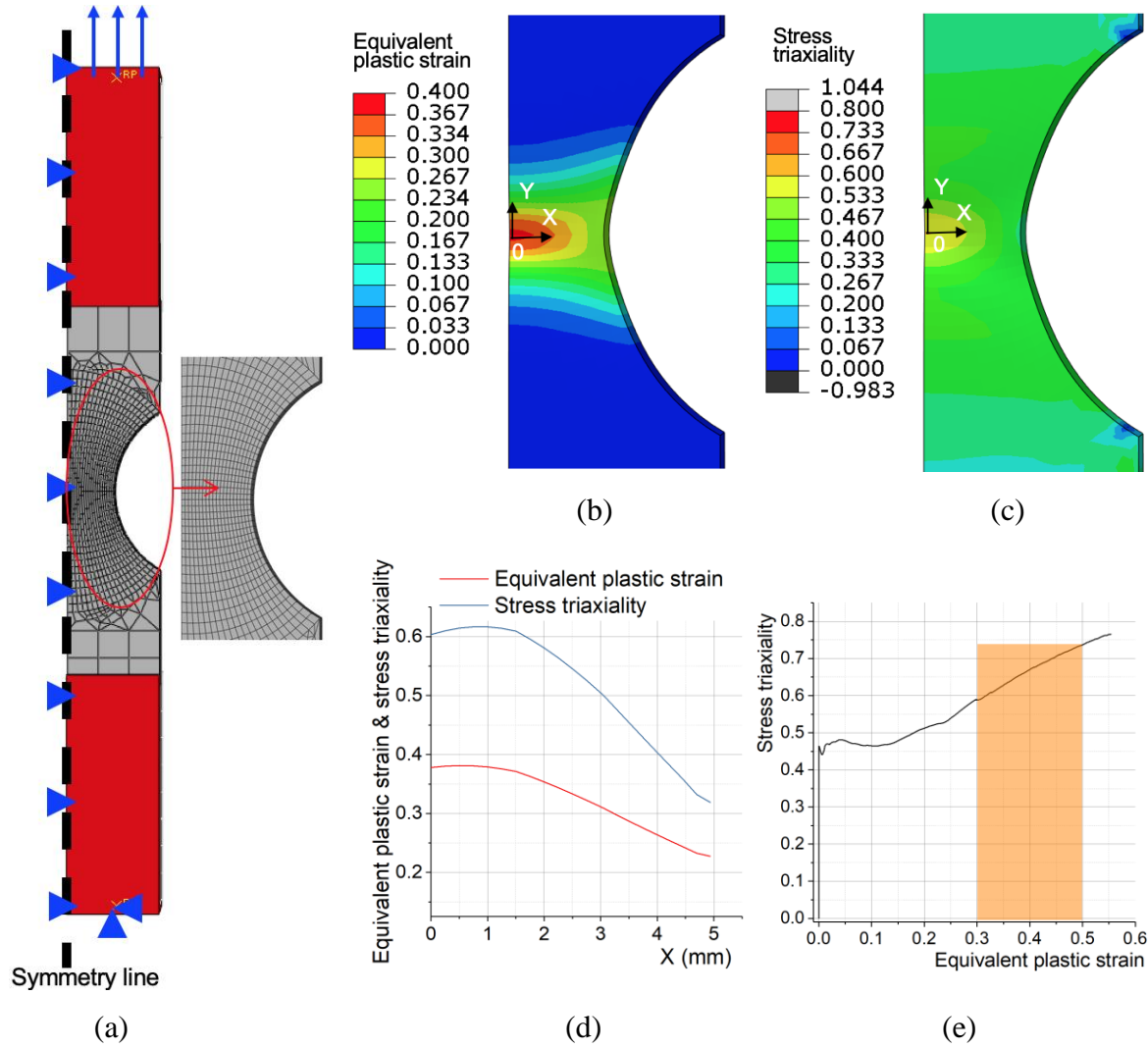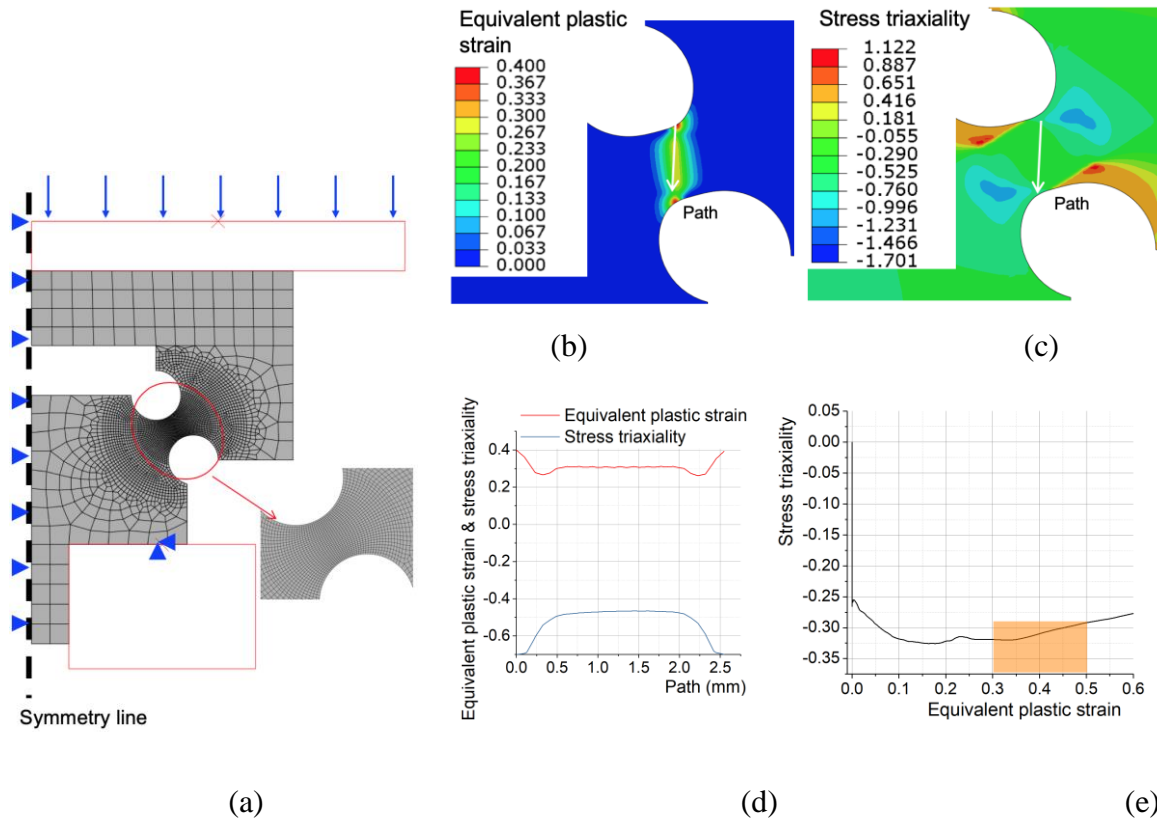
Fig. 38: Simulation of compression tests of DN_60: a) *FE* model with boundary conditions; (b) distribution of the equivalent plastic strain; (c) distribution of the stress triaxiality; (d) distribution of the equivalent plastic strain and stress triaxiality along the line connecting the maximum equivalent plastic strain values between both arcs; (e) relation between stress triaxiality and equivalent plastic strain in the center of the path.

3.3.2 Specimen manufacturing and control

All the specimens were extracted from the same Ti-6Al-4V block, obtained by hot rolling and annealing. The extraction of specimens from raw block was performed considering the samples loading direction aligned with the block longitudinal direction. This is the case of almost all the samples used in this thesis, except for the double notched specimen where no preferential direction exists due to different orientations of the pressure angles (Fig. 39).

Since even small variations in the specimen geometry may have a non-negligible influence on the results of the mechanical tests, the geometry of all the specimens was inspected before conducting the mechanical tests, and specimens outside tolerance were re-fabricated or rejected. The DN specimens were inspected using a CMM (Coordinate-measuring machine) (Fig. 40). The results of this inspection are presented in Appendix A. The geometry of round bars and

NFP were investigated using a vertical profile projector (Fig. 41). The resolution and measurement uncertainty of this machine are 1 µm and 5 µm, respectively.
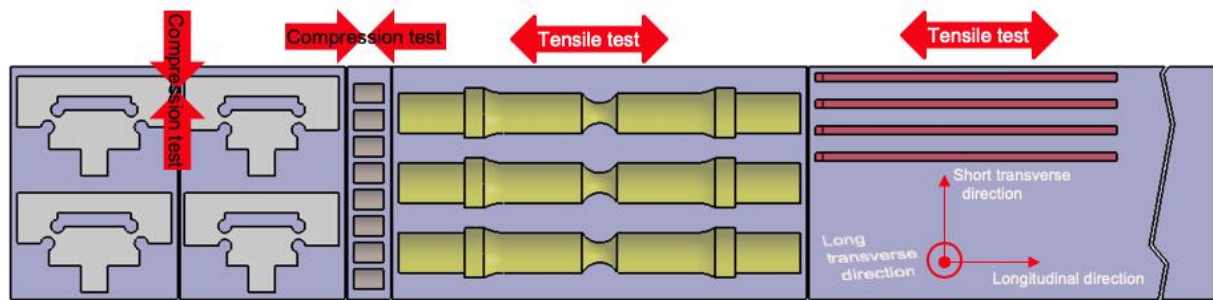
DN	Cylin.	SRB & NRB	NFP
[91]	[102]	[103]	[103]

Fig. 39: Extraction of specimens from raw block.
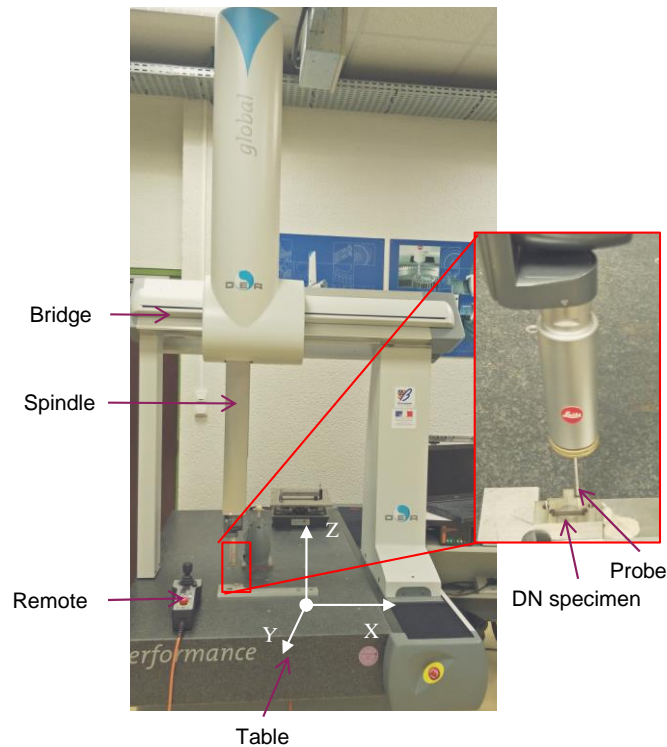
Fig. 40: Geometry inspection of DN specimens using CMM.

Fig. 42 shows the comparison between the technical specifications (technical drawings) and the results of the geometry inspection for the NRB_R6. Three key geometrical features were inspected, including the diameter of bar (D), the diameter of the neck cross section at half length of the bar (A), and the radius of the neck (R). Four NRB_R6 specimens had been fabricated, and all inspected geometrical parameters are within the specified tolerances. The measured

values are presented in the following table. Similar results were also obtained for the other types of round bars (SRB, NRB_R12 and NRB_R30), as shown in appendix A.
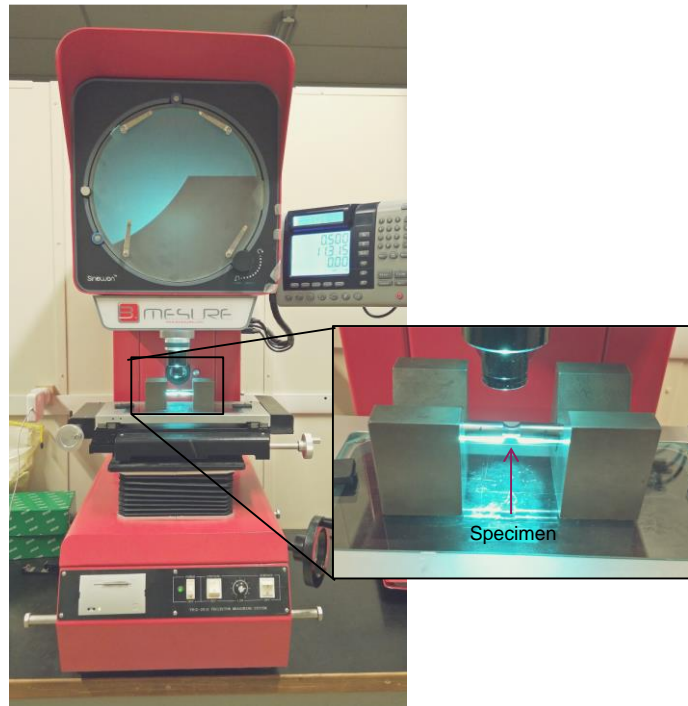
Fig. 41: Geometry inspection of the round bars and NFP using vertical profile projector.
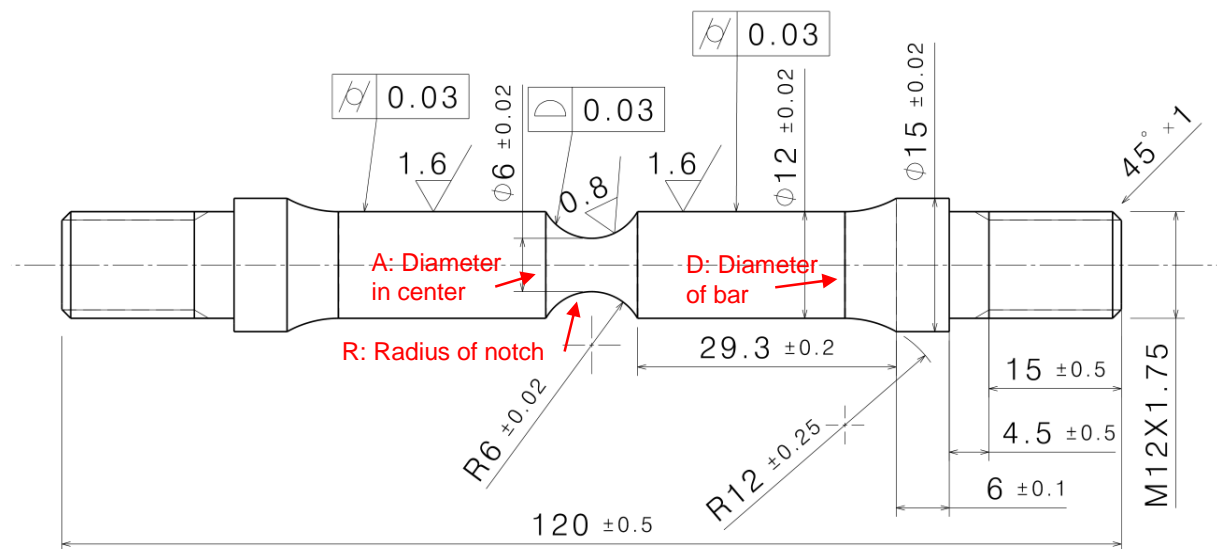
No.	A (mm)	R (mm)	D (mm)
#1	6.012 ± 0.004	6.002 ± 0.007	11.983 ± 0.005
#2	6.004 ± 0.000	6.010 ± 0.010	11.990 ± 0.009
#3	6.014 ± 0.006	5.994 ± 0.008	12.000 ± 0.007
#4	6.013 ± 0.001	5.997 ± 0.006	11.991 ± 0.003

Fig. 42: Results of the geometry inspection of NRB_ R6.

Fig. 43 presents the geometry inspection of NFP_R20. Four NFP_R20 specimens had been fabricated and inspected using the vertical profile projector. Different geometrical features were compared, including the plate width, width of the neck cross section at half length of the plate (*A*), the neck radius (*R*), and the plate thickness. The measure values of thickness are very similar but slightly out of the specified tolerance. This is due to the polish procedure to eliminate the surface influenced by the manufacture process (EDM). Similar results were also obtained for the other types of NFP (NFP_R10 and NFP_R40), as shown in appendix A. In this case, the average thickness of the samples (2.35 mm) is used in the simulations of the tensile tests of notched flat plates.
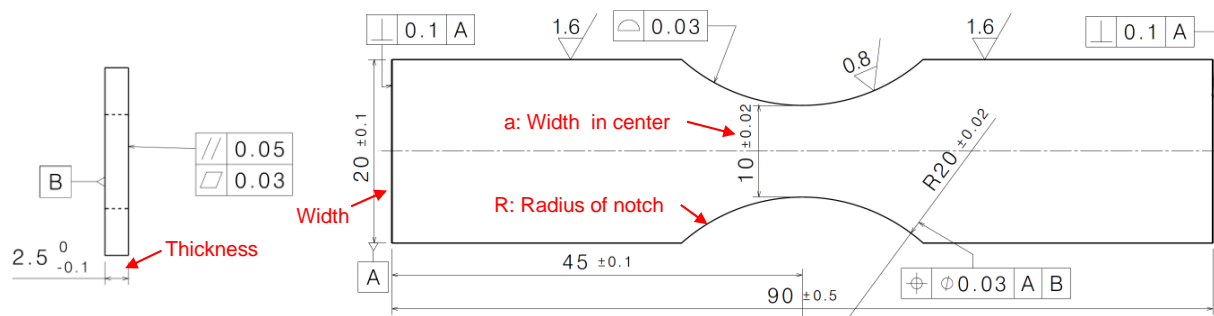
No.	A (mm)	R (mm)	Thickness (mm)	Width (mm)
#1	10.490	20.005 ± 0.066	2.334 ± 0.015	19.823 ± 0.046
#2	10.246	20.030 ± 0.091	2.322 ± 0.016	19.766 ± 0.051
#3	9.946	20.005 ± 0.066	2.318 ± 0.007	19.789 ± 0.038
#4	9.863	20.005 ± 0.066	2.340 ± 0.009	19.795 ± 0.039

Fig. 43: Results of the geometry inspection of NFP_R20.

3.4 Experimental setup

Table 6 shows four configurations of mechanical tests used in this study. Each test was conducted twice to check the repeatability of the experimental results. Quasi-static (compression and tensile) tests of all specimen geometries were performed on a servohydraulic machine, while the compression tests of cylindrical specimens at different strain rates were performed using a Split Hopkinson Pressure Bar (*SHPB*) apparatus.

To obtain the displacement or strain distribution on the specimen surface, a Digital Image Correlation (*DIC*) technique was applied in the quasi-static mechanical tests [104]. Compared to strain gauges and extensometers, this is not affected by necking, which often complicates the determination of the strain at damage initiation. A commercial *3D DIC* system from *GOM*

composed of two *CCD* cameras and software was applied to the round bars due to the curved surface (Fig. 44*b*). Additionally, an extensometer was used in the tensile tests of round bars to measure the local displacement between two gauge points (Fig. 44*a*). Thus, the displacement was acquired by both *3D DIC* and extensometer. These mechanical tests were conducted at the Institute for Applied Materials (IAM-WK) of the Karlsruhe Institute of Technology (KIT), Germany.

Table 6: Configurations of the mechanical tests.

Config.	Test type	Specimen	Strain rate	Setup
1	Compression	Cylindrical	0.05 s^{-1} (quasi-static), 429 s^{-1}, 950 s^{-1}, 5115 s^{-1}	Servo-hydraulic machine & *SHPB* apparatus
2	Compression	Double notched	Quasi-static	Servo-hydraulic machine & *2D DIC* system
3	Tensile	Round bars	Quasi-static	Servo-hydraulic machine & *3D DIC* system
4	Tensile	Notched flat plate	Quasi-static	Servo-hydraulic machine & *2D DIC* system

(a)   (b)
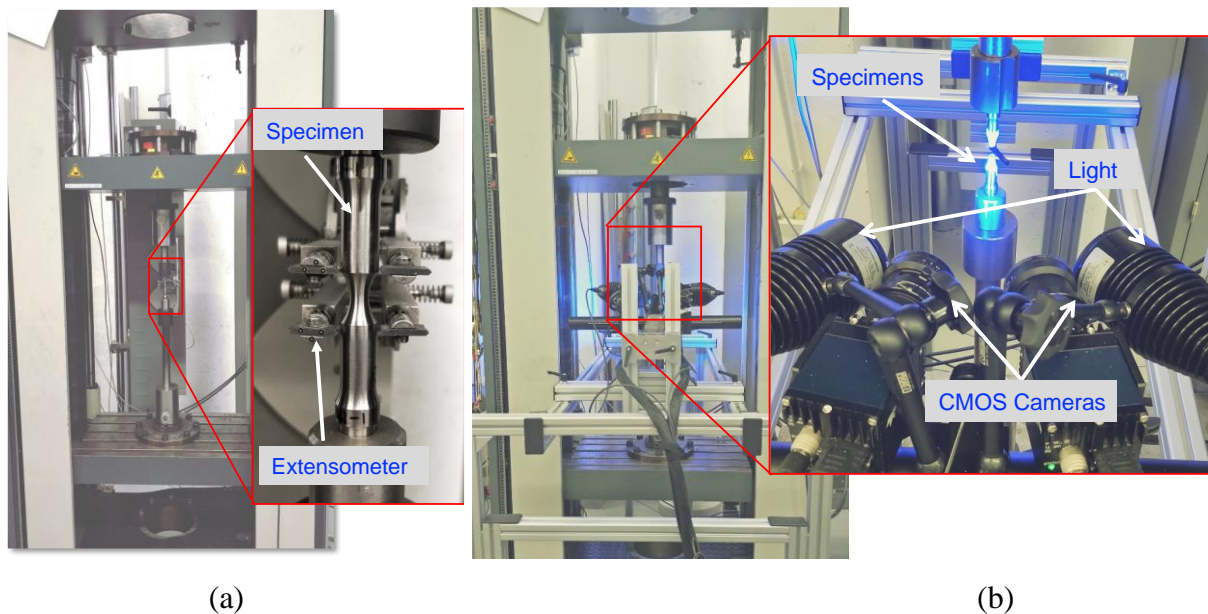
Fig. 44: Tensile test of a round bar on a servo-hydraulic machine equipped with: (a) extensometer; (b) *3D DIC* system.

A *2D DIC* system composed of *CMOS* camera and GOM software was applied for the planar specimens, such as double notched specimen and notched flat plates, as shown in Fig. 45. A table was assembled and placed through the servo-hydraulic machine. The camera was attached

to the table by a sliding block. After specimen was positioned, the objective centerline of cameral should keep consistent with the centerline of zone of interest of specimen. Owing to this table, it is easy to translate the cameral along three axes and locate its position. These mechanical tests were conducted at LaBoMaP laboratory of Arst et Metiers, Campus of Cluny.
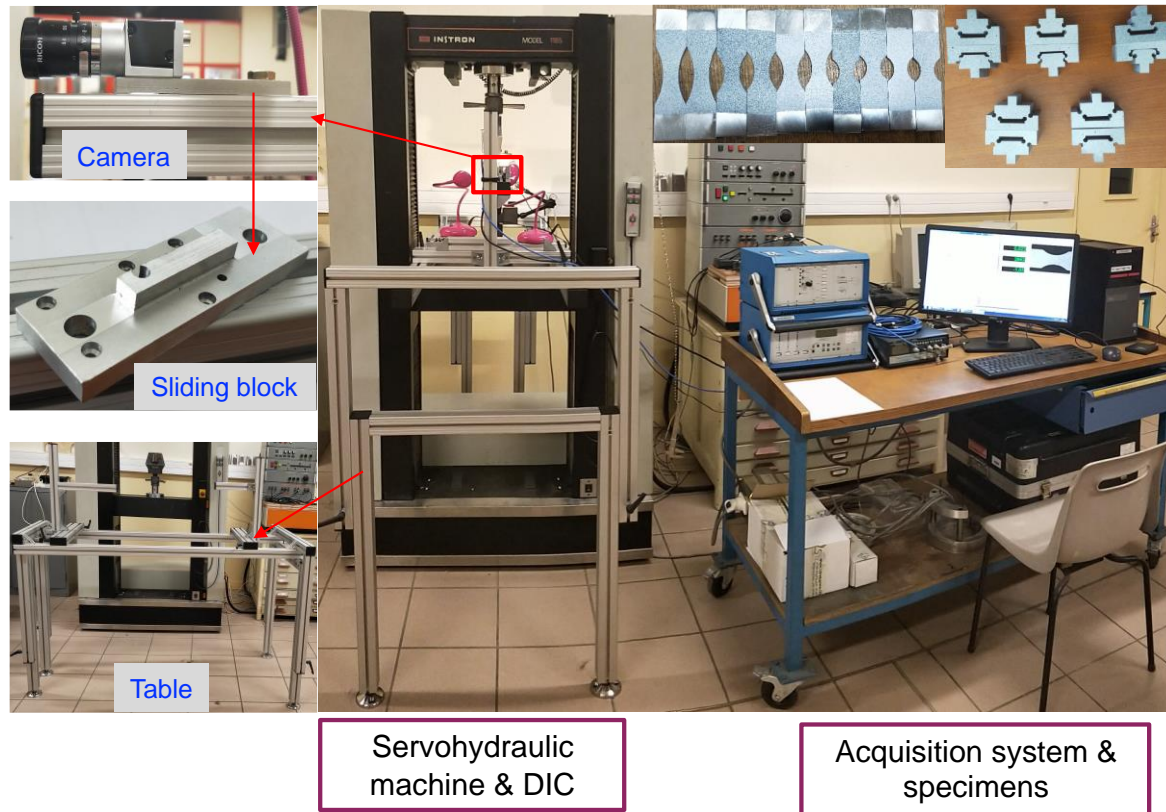
Fig. 45: Designed *2D DIC* system.

3.5 Determination of the constitutive model coefficients

The determination of the constitutive model coefficients is an important task in the model setup. The goal is the determination of the coefficients values for a give material based on experimental data, mainly coming from mechanical tests. Melkote et al. [12] present different methods, including direct and inverse methods, which can be used to determine the constitutive model coefficients. The inverse methods based on optimization algorithms are appropriate for determining the coefficients of complex constitutive models involving many variables. The inverse method consists of simulating the experimental test by modifying the constitutive model parameters iteratively to minimize the difference between the predicted and measured data. As mentioned by Melkote et al. [12], several optimization algorithms can be used for this purpose, organized in three main groups: gradient-based, derivative-free search and evolutionary algorithms. Depending on the applied determination method, different constitutive model

coefficients can be generated. So, this may contributes to the dispersion of coefficients values found in the literature for the same material, as it is the case of the JC model of Ti-6Al-4V titanium alloy [105]-[107].

In this chapter, an optimization-based procedure is proposed to determine the constitutive model coefficients of Ti-6Al-4V titanium alloy. To determine the model coefficients, different specimens and tests configurations are designed and the corresponding mechanical tests are performed. Then, based on the experimental data from these mechanical tests, the coefficients are determined using the optimization-based method implemented in LS-DYNA/LS-Opt software.

3.5.1 Young's modulus determination

The Young's modulus needs to be known before determining the plasticity model coefficients. According to the Ti-6Al-4V alloy supplier, the Young's modulus is between 107 and 122 GPa, and the Poisson's ratio is 0.31. Then, quasi-static tensile tests of smooth round bars were performed to determine its exact value. Fig. 46a presents the force-displacement curves obtained from the tensile tests of SRB. The accuracy of DIC system is validated by the comparison between force-displacement curves using 3D DIC and extensometer. Fig. 46b shows the stress - strain curves which were obtained from the quasi-static tensile test of smooth round bar. The red dashed line matches linear stress–strain behavior well in a small strain region. Therefore, the Young's modulus (E) is 114 GP based on the calculation of the slope of this line.

(a)   (b)
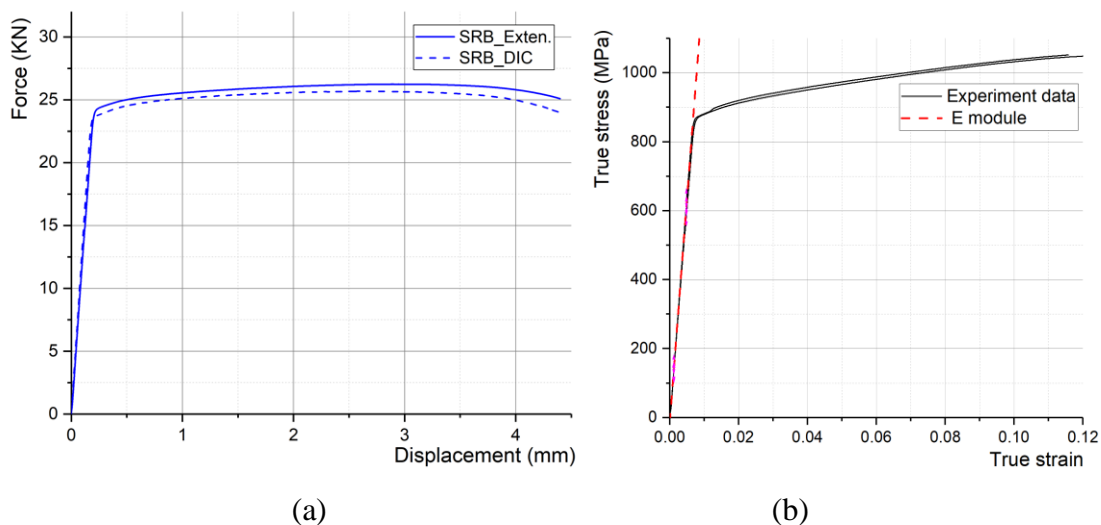
Fig. 46: Tensile tests of SRB: (a) Force – displacement curves of tensile tests of SRB using both 3D DIC and extensometer; Stress-strain curves of SRB.

3.5.2 Procedure for determination of the plasticity model coefficients

Fig. 47 shows the procedure to determine the plasticity model coefficients. The procedure started with the first configuration shown in Table 7, used to determine the coefficients, A, B, C, m, n and E, related to the strain hardening and strain rate effects. The quasi-static compression test of a cylindrical specimen was defined as the reference test. Therefore, the reference coefficients used in the plasticity model were defined as: $\eta_0 = -1/3$, $\dot{\varepsilon}_0 = 0.05$ s^{-1} and $c_\theta^c = 1$. Finally, the second and third configurations shown in Table 7 were used to determine the coefficients of the state of stress effect. The second configuration was used to determine the coefficient c_η and c_θ^s, while c_θ^t and a were determined using the third configuration. In each step, some initial model coefficients are determined using a direct method, based on the nonlinear least square method. Then, these coefficients are used as initial values in an optimization-based procedure to determine their optimal ones.

As shown in Fig. 47, this procedure consists into simulate the experimental test by modifying the constitutive model parameters iteratively to minimize the difference between the predicted and experimental measured force-displacement curves. At each iteration a new set of coefficients are calculated by an optimization-based procedure. This procedure is implemented in LS-Opt software, an optimization software module from LS-Dyna. This software can be connected to FEA software to run the numerical simulations, such as ABAQUS/explicit, used in this work.

Fig. 48 shows the flowchart of the implementation of the optimization-based procedure in Ls-Opt software. The procedure is composed by the following seven steps: 1) coefficients initialization (initial values); 2) selection of the best coefficients values from a given range, using a Design of Experiments (DoE) method; 3) run mechanical tests simulations in ABAQUS/Explicit; 4) build metamodel; 5) comparison between calculated and measured force-displacement curves, applying Curve Mapping Segment (CMS) or Mean Squared Error (MSE) methods; 6) execute metamodel optimization using hybrid adaptive simulated annealing (ASA) and Leapfrog Optimizer for Constrained Minimization (LFOP) algorithms; and 7) verification of the termination criterion.

Compression tests of cylindrical specimens at several strain rates

Quasi-static compression tests of double notched specimens

Quasi-static tensile tests of notched round bars

Force – displacement (F_{exp})

Force – displacement (F_{exp})

Force – displacement (F_{exp})

Initial *A, B, C, m, n, E*

Initial C_η, C_θ^s

Initial C_θ^t, *a*

Eq. A

Eq. B

Eq. C

Optimization procedure

Optimization procedure

Optimization procedure

Determined A, B, C, m, n, E

Determined C_η, C_θ^s

Determined C_θ^t, a

Eq. A	Eq. B	Eq. C
$\overline{\sigma} = f(\varepsilon) \cdot f(\dot{\varepsilon})$	$\overline{\sigma} = f(\varepsilon) \cdot f(\dot{\varepsilon}) \cdot f(\eta) \cdot c_\theta^s$	$\overline{\sigma} = f(\varepsilon) \cdot f(\dot{\varepsilon}) \cdot f(\eta) \cdot f(\overline{\theta})$

Input

Output

Formulation of plasticity model

Experimental force – displacement (F_{exp})

Optimized coefficients

Simulation of mechanical tests

Predicted force – displacement (F_{sim})

$F_{sim} - F_{exp}$ < error

Yes

No

Coefficients update

Optimization procedure

Fig. 47: Flowchart of the procedure to determine the plasticity model coefficients.
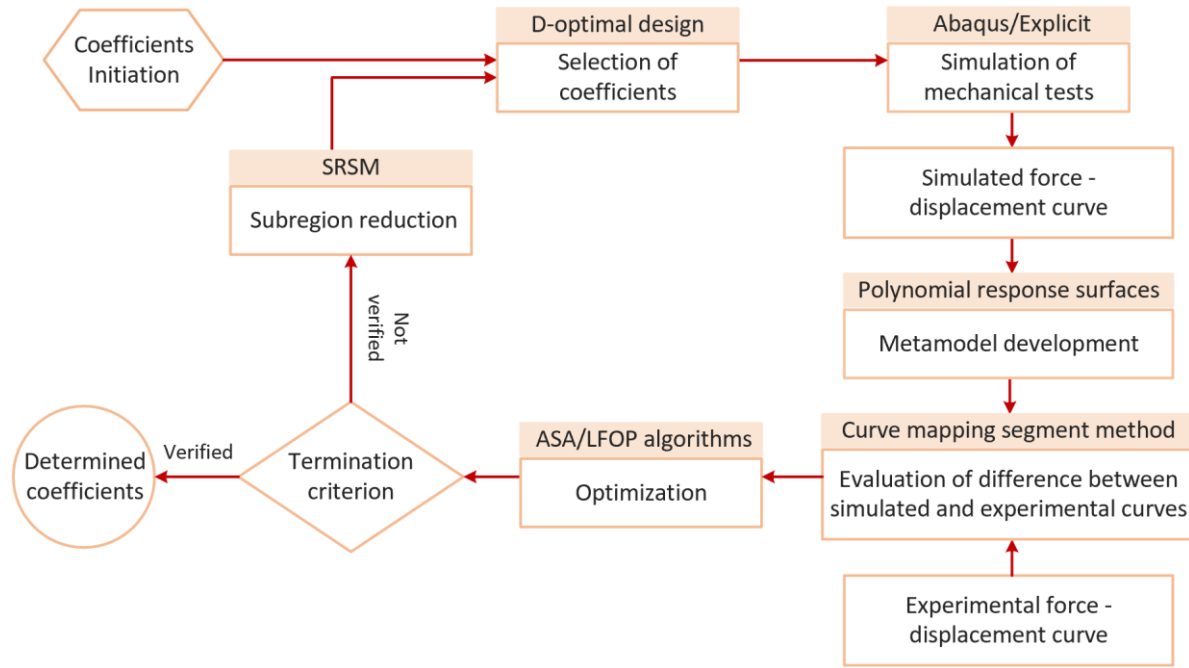
Fig. 48: Flowchart of the optimization-based procedure for the model coefficients determination.

First, a sort of initial model coefficients values were determined using a direct method, based on nonlinear least squares. These initial coefficients values were used to initialize the optimization-based procedure. Then, a DoE method (D-optimal design) is applied to select the best (optimal) set of coefficients values to build a response surface. For small number of coefficients, the full factorial design is used, otherwise a space filling method is applied [108]. Therefore, a good balance between accuracy and computational time can achieved. Next, these coefficients were used in the proposed constitutive model, which were imported into ABAQUS/Explicit through a *VUMAT* subroutine to simulate the mechanical tests. A metamodel was created based on the simulated and experimental force-displacement curves. The difference between these two curves was evaluated by a curve mapping segment method [109], which calculates the smallest area between the measured and calculated force-displacement curves (Fig. 49a). In this method, a segment with the same length as the measured curve is moving from the starting point to the end point of the calculated curve, until the smallest polygon between this segment and measured curve is found [109]. Additionally, the MSE method calculates the sum of the squares of the distances in the y-coordinate between the target points and the interpolated points on the calculated curve (Fig. 49b). Compared with the MSE method, the CMS method incorporates both the ordinate and the abscissa into the difference computation, so the hysteretic curve and vertical sections of curve can be identified [109].

(a)   (b)
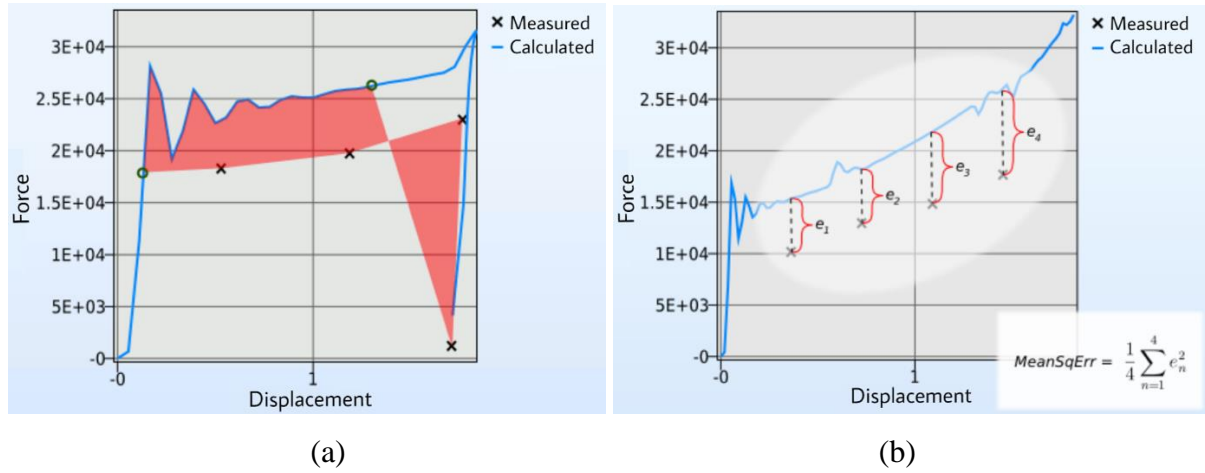
Fig. 49: Difference between calculated and measured force-displacement curves evaluated by (a) MSE method; (b) CMS method [109].

In the next step, the difference was minimized by a hybrid algorithm, which used an *ASA* algorithm to find an approximate global solution, followed by *LFOP* algorithm to sharpen this solution [108]. Finally, a termination criterion including the force-displacement error and maximum number of iterations was checked. If it was not satisfied, a new response surface was built in the next iteration by the sequential response surface method (*SRSM*). The typical feature of this method is that the size of the subregion (range of determined coefficients) is adjusted at each iteration, which gives higher accuracy when optimizing using metamodels. The optimization-based process stopped when the termination criterion was satisfied, and the final coefficient values were obtained.

3.5.3 Determination of the coefficients of the plasticity model

To determine the coefficients corresponding to the strain hardening and strain rate effects, compression tests of cylindrical specimens were performed at different strain rates of 0.05 s^{-1}, 429 s^{-1}, 950 s^{-1} and 5115 s^{-1}. The force - displacement curves were obtained for each test, then the corresponding true stress-true strain curves were determined. Only the stress-strain curve before damage initiation was applied in the determination procedure. A compression test was also simulated by ABAQUS/Explicit. Fig. 50 shows the model of half of the cylindrical specimen geometry and the corresponding boundary conditions. A mesh composed of 0.3 mm 4-node axisymmetric elements (*CAX4R*) was used. The friction coefficient between upper and bottom dies and specimen was 0.12, obtained using the ring compression test method. The loading speed (*V*) for different strain rates was determined by Eq. 58 and applied to the upper die, while the bottom die was static.

$$V = \dot{\varepsilon} * h \qquad\qquad Eq.\ 58$$

In this equation, $\dot{\varepsilon}$ is the strain rate and h is the specimen height.
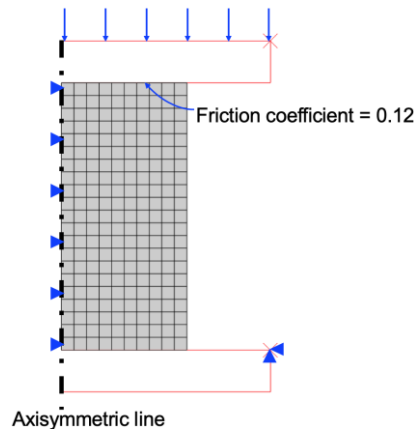
Fig. 50: FE model of the compression test of the cylindrical specimen.

Since the quasi-static compression test of a cylindrical specimen is the reference test, Eq. 51 is reduced to the first two terms (*Equation (A)* in Fig. 47), i.e., the strain hardening and strain rate effects. Applying the optimization procedure represented in Fig. 47 the values of the coefficients were modified iteratively to minimize the difference between the experimental and the simulated force-displacement curves for all the strain rates. Fig. 51 shows the implementation of the optimization-based procedure in Ls-Opt software. An example of coefficients determination using the compression tests of cylindrical specimens is presented. The above mentioned seven steps are well performed in Ls-Opt software.
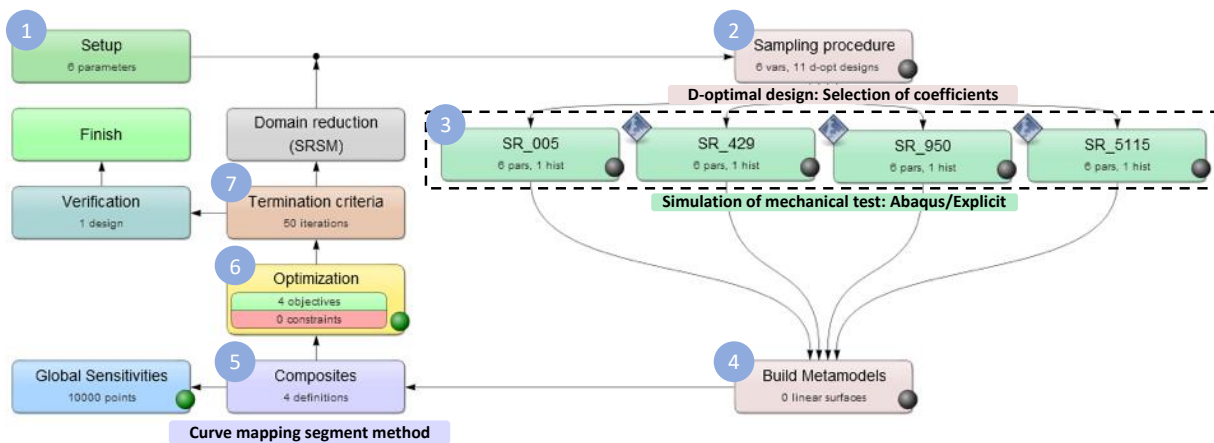
Fig. 51: Optimization-based procedure of the model coefficients determination using the compression tests of cylindrical specimens in Ls-Opt software.

Fig. 52 shows both simulated and experimental force-displacement curves after applying the optimization procedure.

Fig. 52: Simulated and experimental force–displacement curves of the compression tests over cylindrical specimens after applying the optimization procedure.

Fig. 53 shows both experimental true stress - true strain curves for several strain-rates, and the modelled true stress in function of the true strain and strain-rate. The latter surface plot represents only the first two terms of Eq. 51 using the determined coefficients. It is seen that the stress surface matches quite well with the experimental data represented by the red dots. The coefficient values determined are summarized in Table 7.
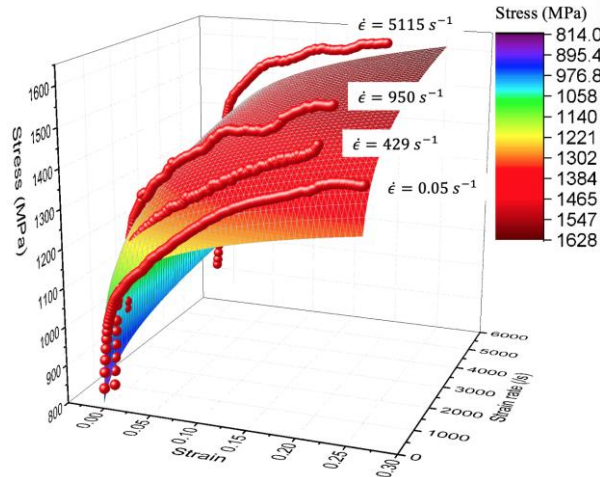
Fig. 53: Experimental true stress – true strain curves and the stress surface calculated considering the first two terms of *Equation* (4) and using the determined coefficients.

As shown Fig. 47 the next step consisted of determining the coefficients c_η and c_θ^s, related to the state of stress effect, using the DN specimens. Five pressure angles of 30°, 45°, 60°, 90° and 120° were submitted to compression tests under the same quasi-static loading conditions, and the corresponding force-displacement curves were obtained. Applying the same optimization procedure described above and represented in Fig. 48, c_η and c_θ^s coefficients were determined,

and are shown in Table 7. Fig. 54a shows both simulated and experimental force-displacement curves after applying the optimization procedure.

Table 7: Determined coefficients of the plasticity model.

	Strain hardening			Strain rate			Reference	
Coefficient	A (MPa)	m	n	B	C	E	$\dot{\varepsilon}_0$ (s^{-1})	η_0
Value	812.1	625.7	0.176	0.400	0.073	3949	0.05	-1/3

	Stress triaxiality	Lode angle			
Coefficient	c_η	c_θ^s	c_θ^t	c_θ^c	a
Value	0.212	0.795	1.061	1	4

Finally, to determine the remaining coefficients related to the state of stress effect, c_θ^t and a, different NRB were used in the quasi-static tensile tests. The same minimum diameter of 6 mm was used with three different local neck radii R of 6 mm, 12 mm and 30 mm. Applying the same optimization procedure as described above and represented in Fig. 47, c_θ^t and a coefficients were determined, and are shown in Table 7. Fig. 54b shows both the simulated and experimental force-displacement curves after applying the optimization procedure.

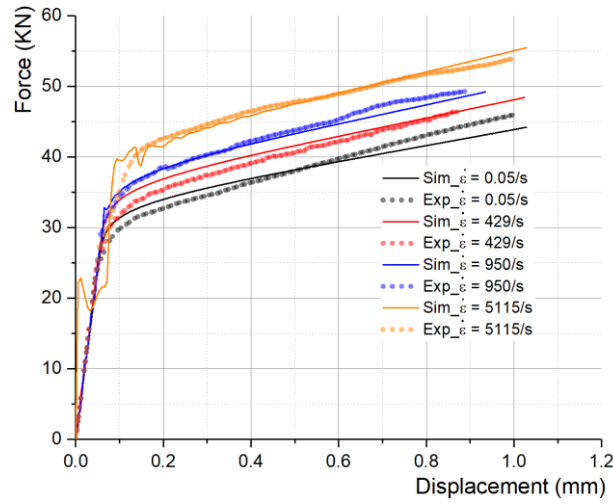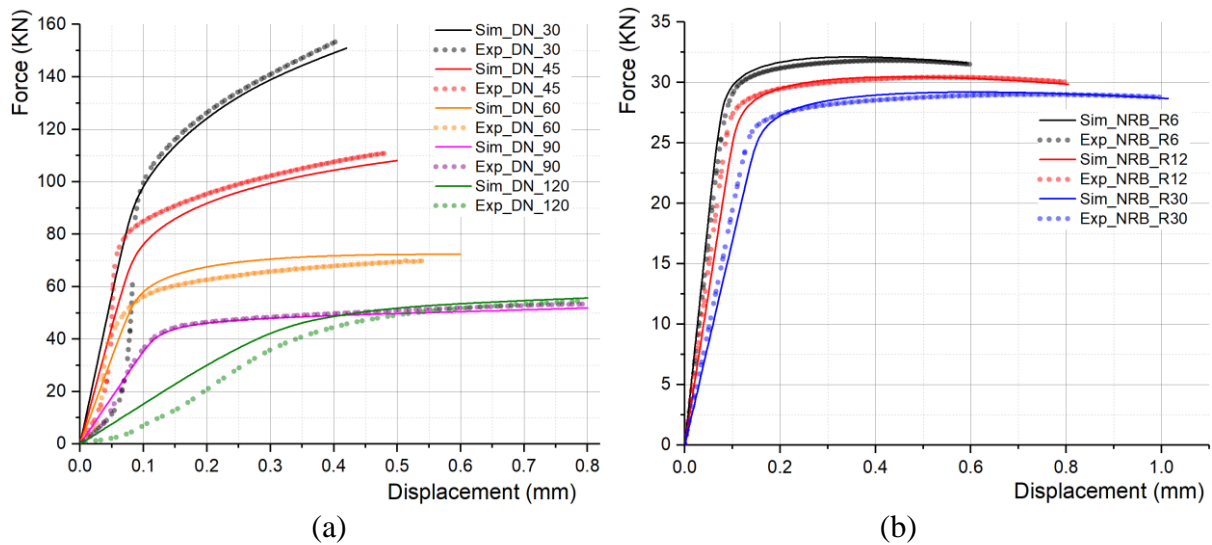Fig. 54: Simulated and experimental force-displacement curves of: (a) compression tests on double notched specimens; (b) tensile tests on notched round bars.

3.6 Verification of plasticity model

After the determination of the plasticity model coefficients, simulations of the tensile tests of NFP (fourth configuration in Table 6) were conducted to verify the accuracy of the plasticity model. It is worth pointing out that these specimens were not used in the coefficient

determination process. The model of the tensile test is almost the same as that in section 3.1, except for the plasticity model, which is replaced by the model given by Eq. 51 with the corresponding coefficients shown in Table 7. Fig. 55a compares the simulated force-displacement curves with those measured for the NFP_R10 specimen.

(a)

(b)

(c)
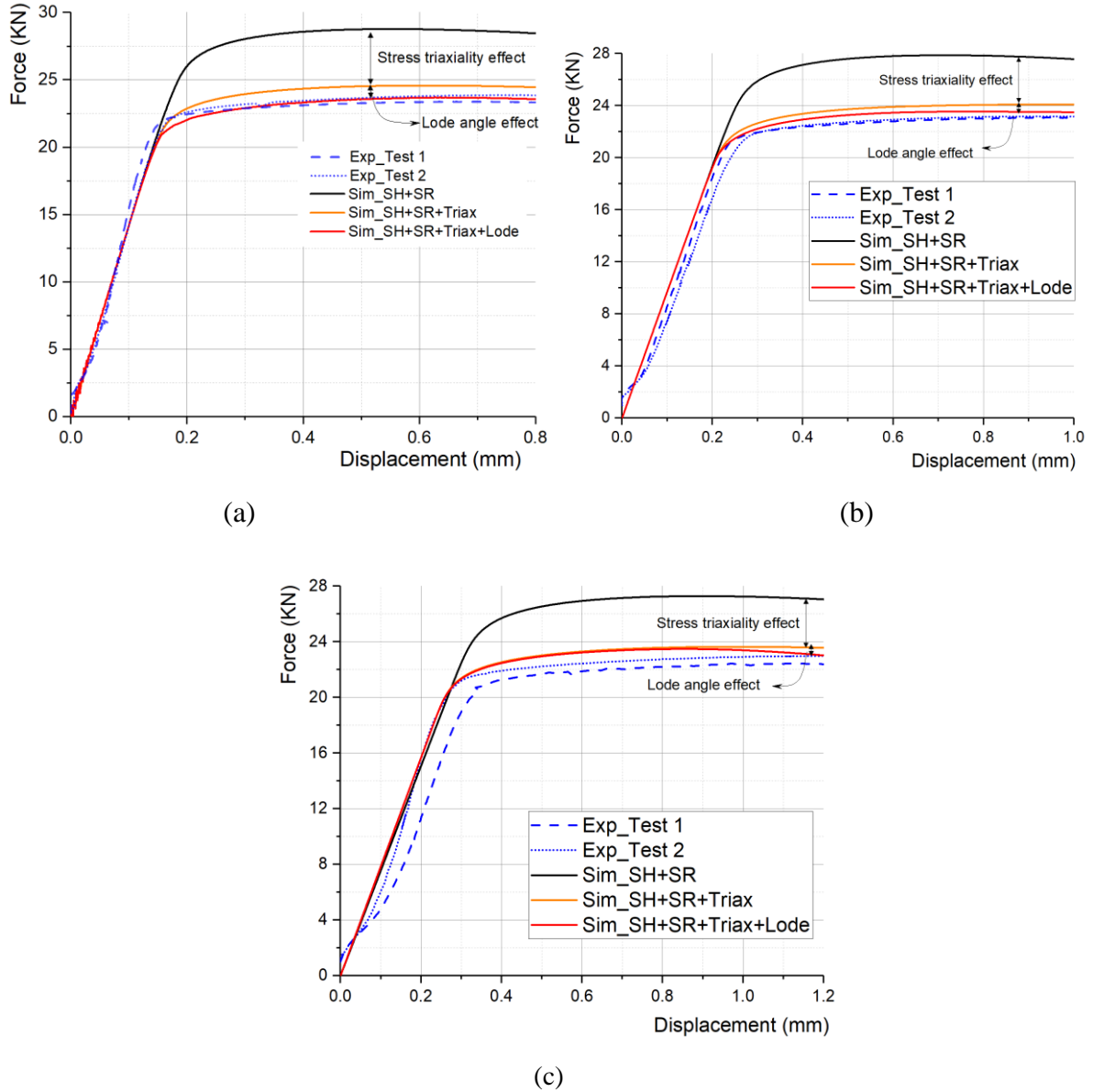
Fig. 55: A comparison between simulated and experimental force–displacement curves for (a) NFP_R10; (b) NFP_R20; (c) NFP_R40.

To estimate the contribution of each effect on the flow stress, three simulations were performed corresponding to three plasticity models: 1) *Equation (4)* with the strain hardening (*SH*) and strain rate (*SR*) effects only; b) Eq. 51 with the *SH*, *SR* and stress triaxiality (*Triax*) effects; c) Eq. 51 with all the effects, including the Lode angle effect (*Lode*). A large difference is observed (23%) between the simulated and experimental force-displacement curves when the plasticity

model includes the strain and strain rate effects only. This difference is reduced to 4.1% when the stress triaxiality effect is also included in the plasticity model. Finally, the simulated force-displacement curve matches quite well with the experimental ones after also considering the Lode angle effect. The same influences of the strain hardening, strain rate, triaxiality and Lode angle on the force-displacement curves are observed for the other two notched flat specimens (NFP_R20 and NFP_R40). Therefore, it can be concluded that the state of stress effect, characterized by the stress triaxiality and the Lode angle, has a significant effect on the plasticity of Ti-6Al-4V titanium alloy.

The accuracy of the constitutive model to reproduce the mechanical behavior of the Ti-6Al-4V alloy was also verified by comparing the simulated and measured plastic strain distributions at the same time as the deformation process (before damage initiation), for both DN and NRB specimens. Fig. 56 shows experimentally determined (by *DIC*) and simulated (FEM) strain distributions of these two types of specimen (DN with a pressure angle of 90º and NRB with a notch radius of 6 mm).

(a)   (b)
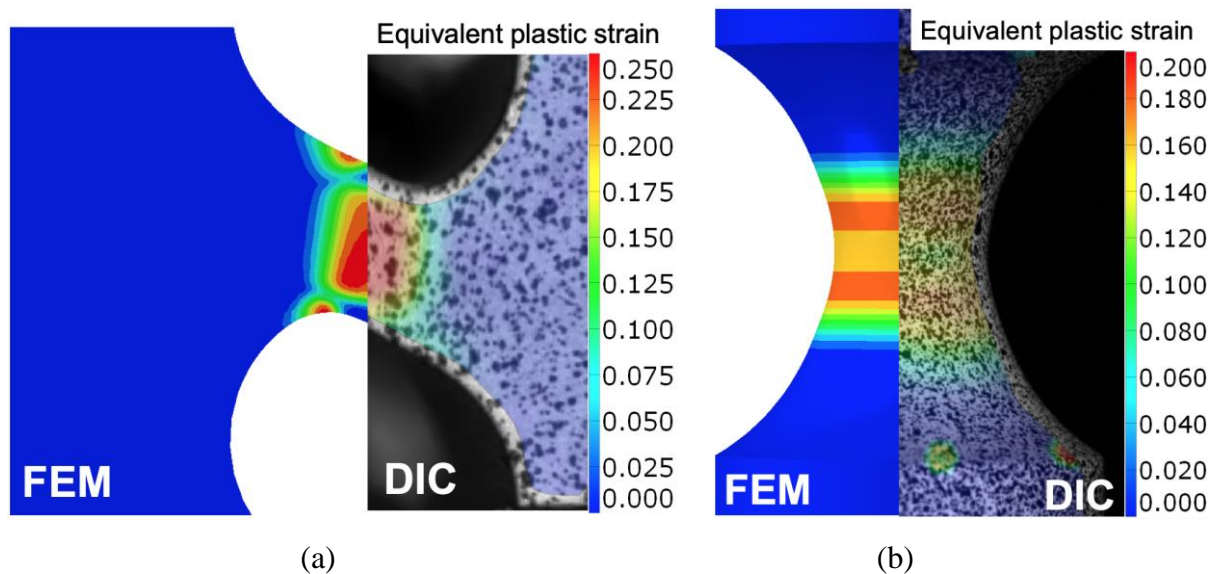
Fig. 56: Equivalent plastic strain distribution in the DN (a) and NRB (b) before damage initiation, obtained by numerical simulation (left side) and determined by DIC (right side).

3.7 Determination of the coefficients of the damage model

Fig. 57 gives the specimens used in the tests after fracture. The fracture occurred in the center of round bars and NFP. For DN specimens, the fracture occurred in both sides of the specimen gauges simultaneously.

(a)   (b)

(c)
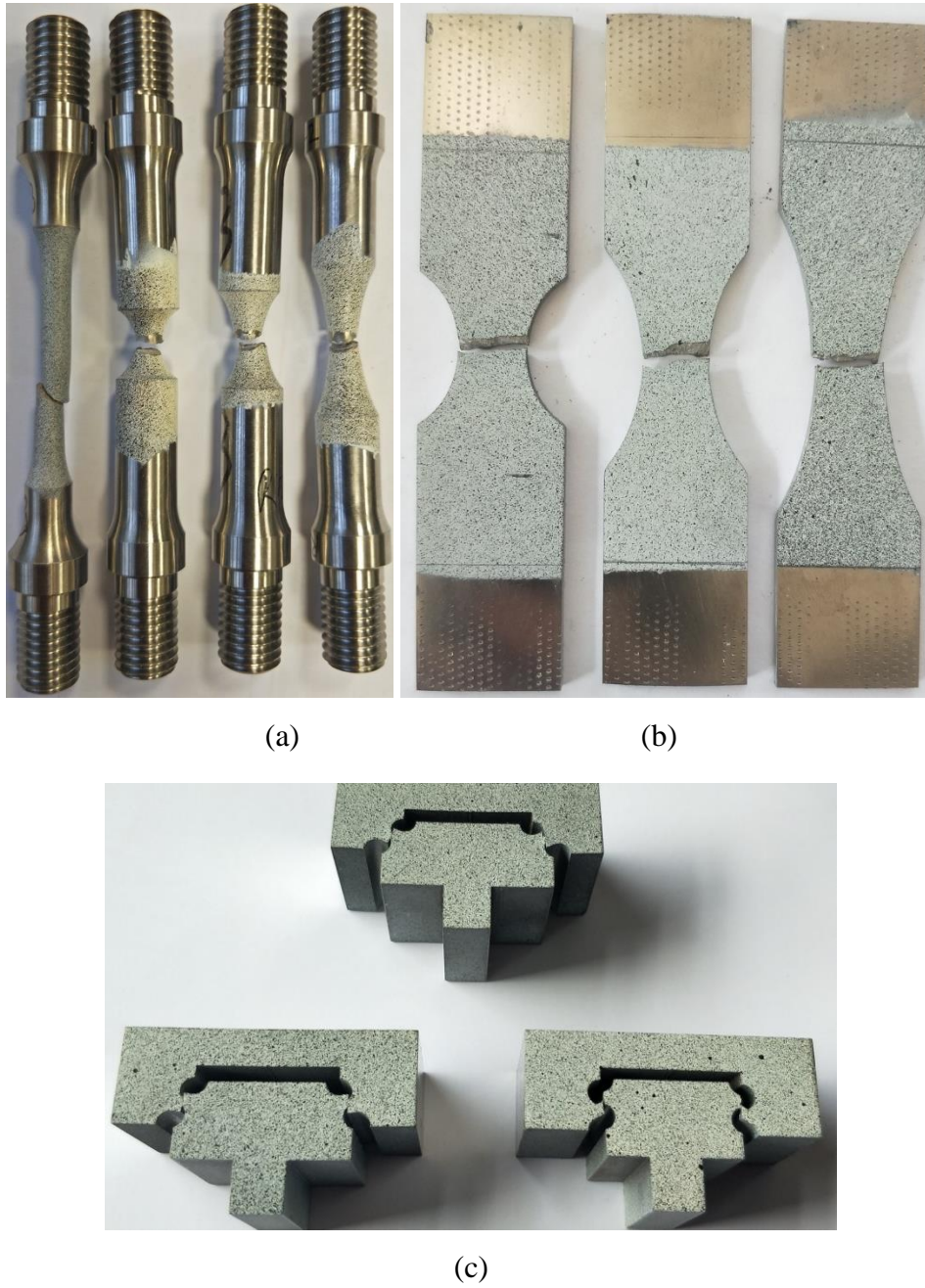
Fig. 57: Specimens after mechanical tests: (a) round bars; (b) NFP; (c) DN.

Fig. 58 shows the procedure for the determination of the coefficients of Eq. 54, corresponding to damage initiation. First, experimental mechanical tests using all the specimen geometries were conducted and the corresponding force-displacement curves obtained. Numerical simulations of these mechanical tests were also performed to obtain the corresponding simulated force-displacement curves. Second, simulated and experimental curves for each test were compared, and the displacement at damage initiation d_i obtained. Third, the images taken by the *DIC* system cameras corresponding to the displacement at damage initiation were selected for *DIC* analysis, in order to calculate the equivalent plastic strain at damage initiation, $\bar{\varepsilon}_i^p$. Knowing $\bar{\varepsilon}_i^p$, the stress triaxiality η and Lode angle parameter $\bar{\theta}$ can be obtained from the

numerical simulations when the damage is initiated [99]. Using both equivalent plastic strain at damage initiation and state of stress, the coefficients of Eq. 54, were determined.
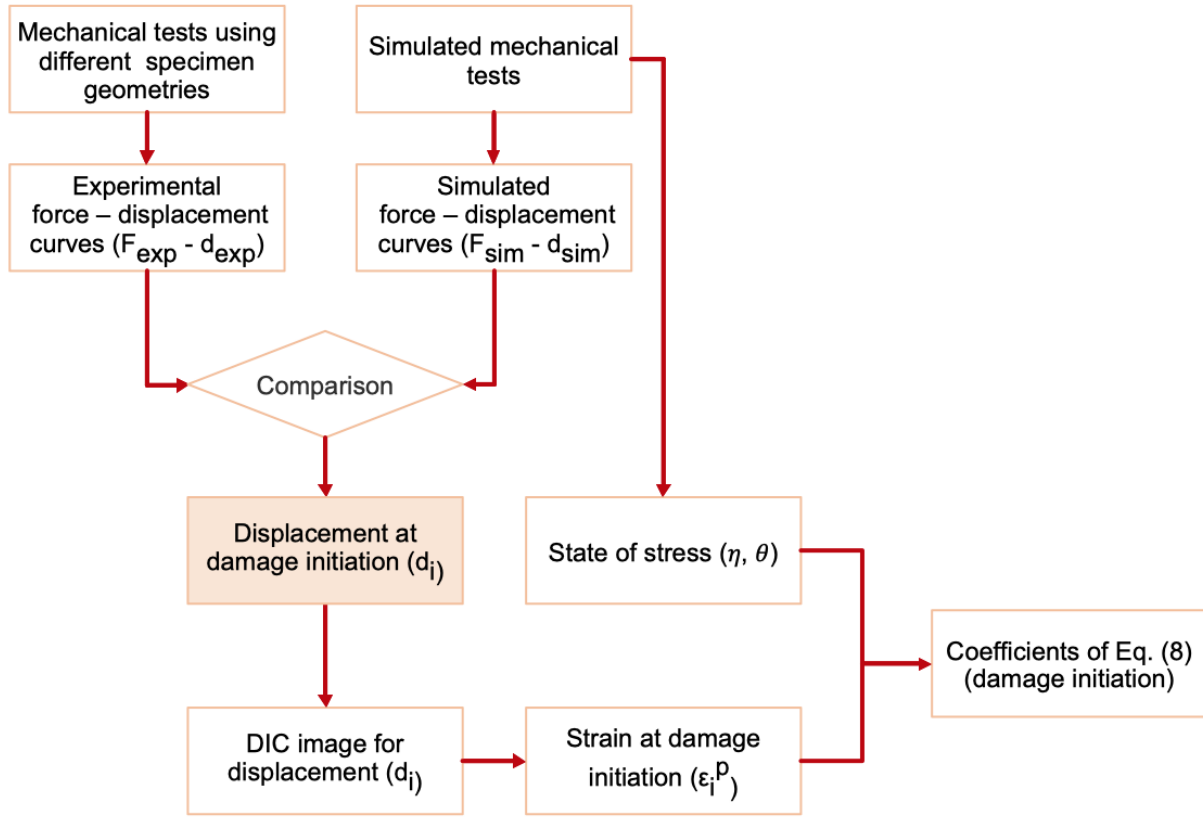
Fig. 58: Flowchart of the procedure for the determination of the damage initiation coefficients.

To illustrate this procedure, the example of DN_90 is used in the compression tests (Fig. 59*a*) and numerical simulations (Fig. 59*b*). The displacement at damage initiation was determined by comparing the simulated and experimental force-displacement curves, as shown in Fig. 59*c*. This figure shows that the two curves have identical evolution until a displacement of 0.75 mm, then they follow different directions. Taking this value as the displacement at damage initiation, the corresponding strain at damage initiation $\bar{\varepsilon}_i^p$ can be obtained by analyzing the distribution of equivalent plastic strain in the specimens, determined experimentally using the *DIC* technique, as illustrated in Fig. 54*a*. The value of $\bar{\varepsilon}_i^p$ is the average of the two maximum values shown in this figure, and is equal to 0.275.

To determine the stress triaxiality at damage initiation, the distribution of equivalent plastic strain obtained from the simulation was used, as shown in Fig. 59*b*. In this figure, a path corresponding to a straight line crossing the regions of maximum equivalent plastic strain was drawn. Plotting both simulated equivalent plastic strain and stress triaxiality along this path

(Fig. 59*d*), the stress triaxiality at damage initiation can be determined. It is located in the middle of the path and is equal to -0.08, since the damage initiates where the stress triaxiality is more positive/less negative. Additionally, the calculated stress triaxiality is not equal to zero because this specimen cannot reproduce simple shear. As mentioned above, the Lode angle parameter is equal to 0 for this specimen due to the plane strain conditions. However, the exact value of the Lode angle parameter is not known for the notched flat specimen. Therefore, after knowing the location of damage initiation, which corresponds to the maximum value of stress triaxiality, the value of the Lode angle parameter was determined at the same location.

(a)   (b)

(c)   (d)
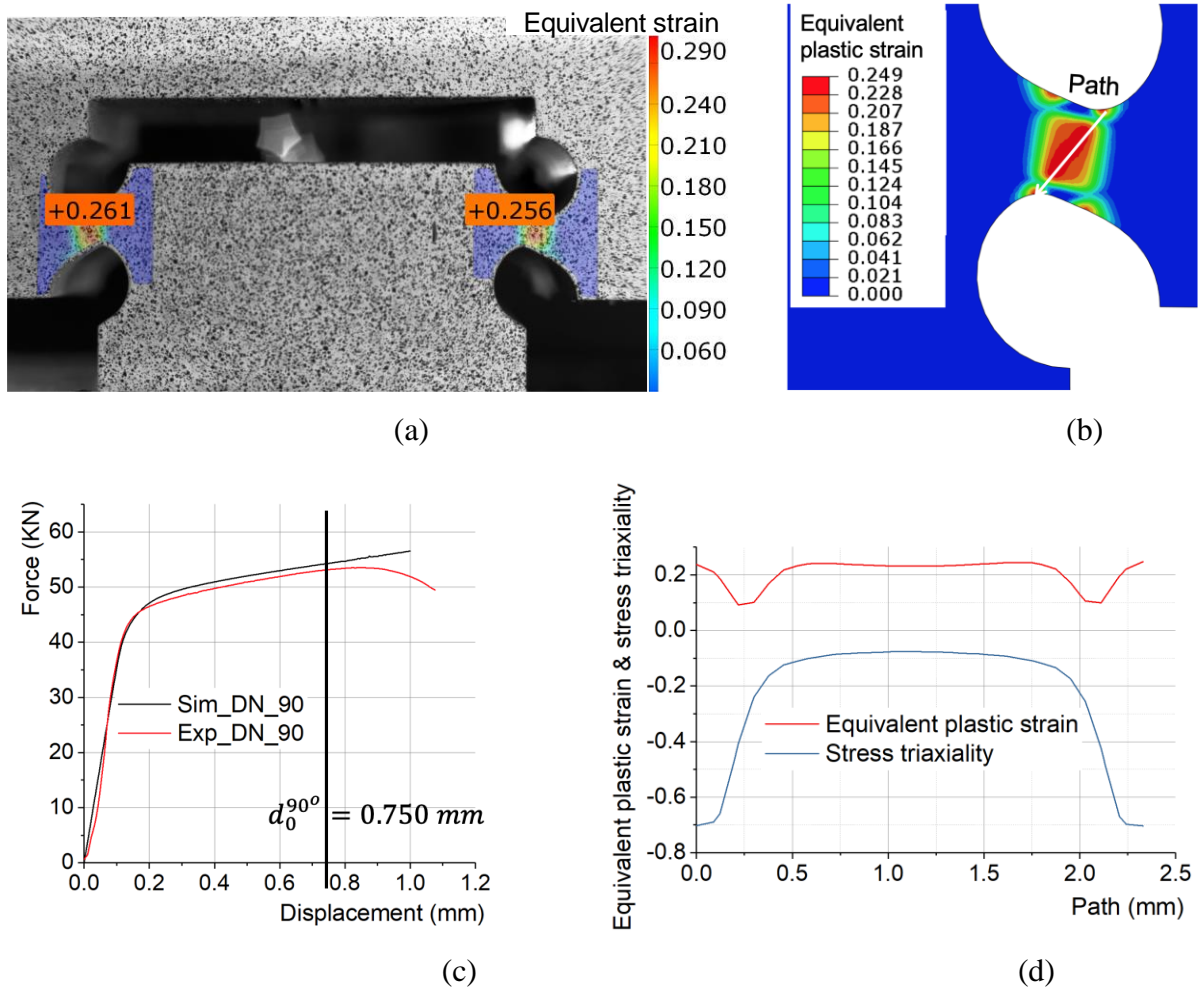
Fig. 59: Simulated and experimental results for *DN_90*: (a) experimental strain distribution at damage initiation obtained by DIC; (b) simulated strain distribution at damage initiation; (c) simulated and experimental force-displacement curves; (d) distribution of equivalent plastic strain and stress triaxiality along the selected path in (a).

The same procedure was applied to the other specimens to get the state of stress (η and θ) and the equivalent plastic strain ($\bar{\varepsilon}_i^p$) at damage initiation. All the values are summarized in Table 8, and the *3D* fracture locus was built in the space of ($\bar{\varepsilon}_i^p$, η, $\bar{\theta}$), as shown in Fig. 60.
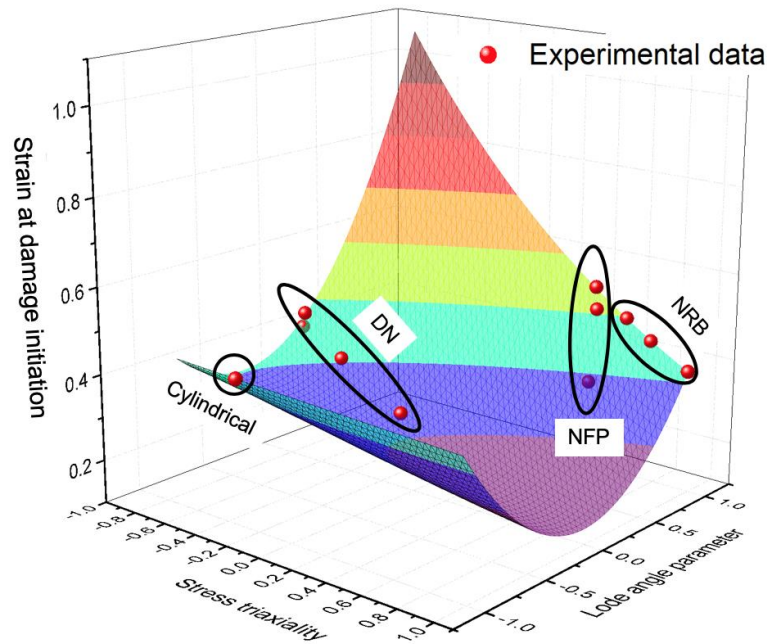
Fig. 60: Fracture surface of the Ti-6Al-4V alloy.

Table 8: A summary of the strains at damage initiation for all the specimens.

Type of specimen	Strain at damage initiation, $\bar{\varepsilon}_i^p$	Stress triaxiality, η	Lode angle parameter, $\bar{\theta}$
Cylindrical	0.435	-0.333	-1
DN_30	0.423	-0.709	0
DN_45	0.457	-0.696	0
DN_60	0.37	-0.458	0
DN_90	0.277	-0.08	0
NRB_R6	0.384	0.976	1
NRB_R12	0.435	0.763	1
NRB_R30	0.476	0.623	1
NFP_R10	0.306	0.427	0.971
NFP_R20	0.545	0.487	0.922
NFP_R40	0.489	0.479	0.947

A wide range of state of stress is covered by the designed specimens, where the stress triaxiality varies from -0.709 to 0.976 and the Lode angle parameter varies from -1 to 1. According to Bai and Wierzbicki [74], boundary limits can be used to construct the fracture surface. Thus, three limiting cases are proposed: $\bar{\theta} = -1$, corresponding to the compression tests of cylindrical specimens; $\bar{\theta} = 0$, corresponding to the compression tests of double notched specimens; $\bar{\theta} = 1$, corresponding to the tensile tests of notched round bars. For each boundary limit, an exponential function was applied to characterize the relation between the strain at damage initiation and stress triaxiality based on the theory of Rice [90]. It is extremely difficult to determine the coefficients by fitting all the experimental points into the formulation of the

damage initiation presented in Eq. 54. Thus, three boundary limits were determined independently. First, D_3, D_4 and D_5, D_6 were determined by fitting the experimental points into boundary limits $\bar{\theta} = 0$ and $\bar{\theta} = 1$, respectively. Secondly, the remaining experimental points were used to determine the coefficients D_1, D_2 related to the boundary line $\bar{\theta} = -1$. Finally, the compression tests of the cylindrical specimens at different strain rates were used to determine D_7 coefficient associated with the strain rate effect. All the determined damage model coefficients are shown in Table 9.

Table 9: Determined coefficients of the damage model.

Damage coefficients	D_1	D_2	D_3	D_4	D_5	D_6	D_7
	0.694	0.608	0.263	0.734	0.430	0.040	-0.028

In the case of the damage evolution, both the exponent parameter λ, and the fracture energy density G_f, were determined by applying the optimization procedure mentioned above. Only the simulated and experimental force-displacement curves of the compression tests of double notched specimens were used. Fig. 61 illustrates the comparison between simulated and experimental force displacement curves after optimization, corresponding to G_f and λ equal to 18.5 KJ/m^2 and 9.4, respectively. After this optimization, the difference of fracture displacement between the simulation and the experimental test is 9% in the compression test of DN_45, and smaller for the other two specimens. Moreover, the experimentally determined (by DIC) and simulated plastic strain distributions in the specimens after damage initiation were also compared for specimens DN_90 and NRB_R10.
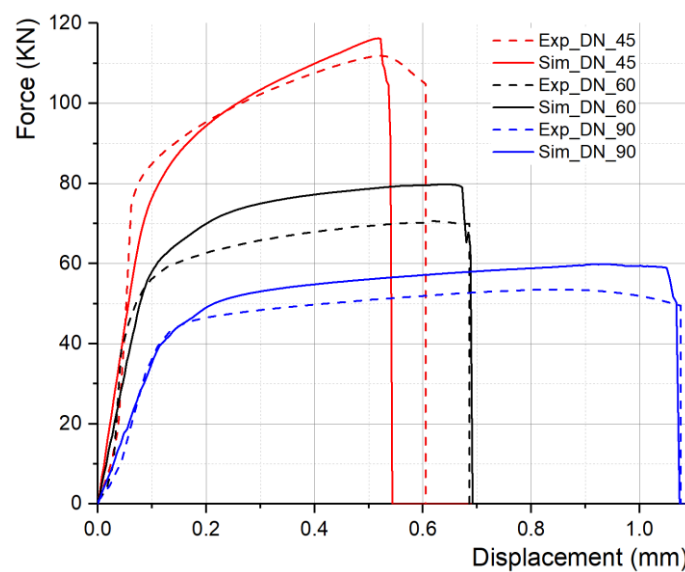
Fig. 61: FE force–displacement response for double notched specimens compared to the experiments with damage evolution model.

As can be seen in Fig. 62, the simulated and experimental distributions after damage initialtion are nearly identical. Therefore, the damage evolution process is predicted well by the proposed damage model.

(a)   (b)
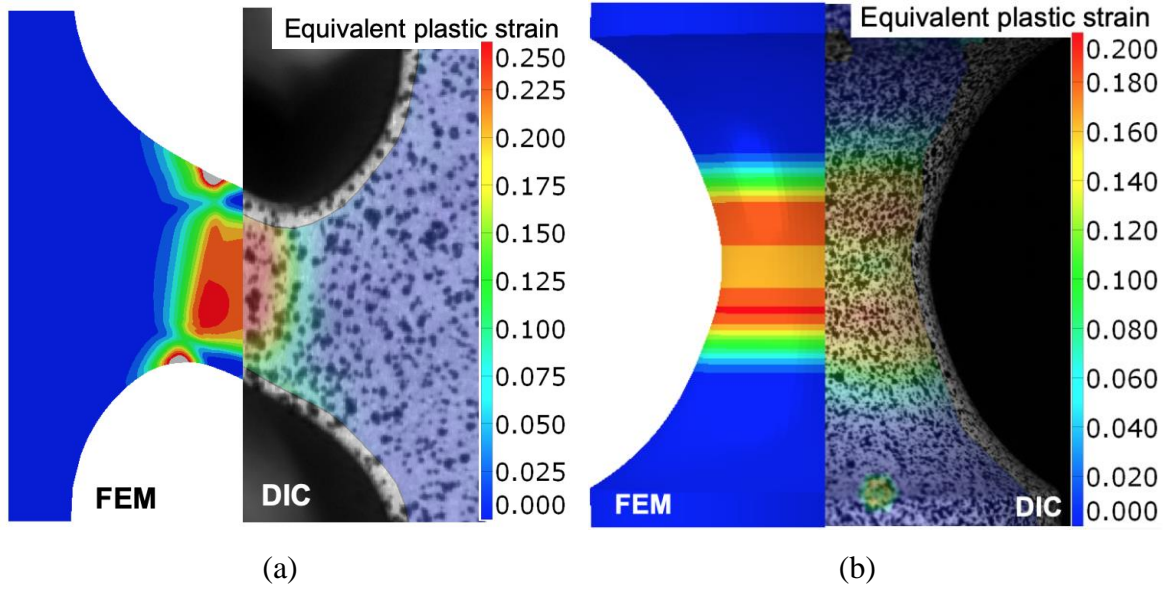
Fig. 62: Equivalent plastic strain distribution in the DN (a) and NRB (b) after damage initiation, obtained by numerical simulation (left side) and determined by DIC (right side).

3.8 Comparison of the proposed model and the Johnson-Cook model

To evaluate the precision of the proposed model to represent the mechanical behavior of the Ti-6Al-4V alloy in metal cutting, true stress-true strain curves obtained by this model were compared with the curves generated by the *J-C* constitutive model, which is extensively applied in the finite element analysis of the metal cutting process. *J-C* plasticity and damage models are given by Eq. 59-Eq. 62, without the thermal softening term.

$$\tilde{\sigma} = \left(A_{jc} + B_{jc} \varepsilon_p^{n_{jc}} \right) \left[1 + C_{jc} \ln\left(\frac{\dot{\varepsilon}}{\dot{\varepsilon}_0} \right) \right]$$

Eq. 59

$$\bar{\varepsilon}_i = \left(D_{1jc} + D_{2jc} e^{D_{3jc}\eta} \right) \left[1 + D_{4jc} \ln\left(\frac{\dot{\varepsilon}}{\dot{\varepsilon}_0} \right) \right]$$

Eq. 60

$$D_{de} = 1 - \exp\left(-\int_0^{\bar{u}} \frac{\bar{\sigma}_y}{G_f} d\bar{u} \right); \ G_f = \int_{\bar{\varepsilon}_i^p}^{\bar{\varepsilon}_f^p} l\bar{\sigma}_y d\bar{\varepsilon} = \int_0^{\bar{u}_f} \bar{\sigma}_y d\bar{u}$$

Eq. 61

$$\bar{\sigma} = \left(1 - D_{de} \right) \tilde{\sigma}$$

Eq. 62

A_{jc}, B_{jc}, C_{jc} and n_{jc} are the coefficients of the plasticity model, and $\dot{\varepsilon}_0$ is the reference strain rate which equals 0.05 s^{-1}. D_{1jc} – D_{4jc} are the damage coefficients and G_f is the fracture energy density. $\bar{\varepsilon}_i$ is the plastic strain at damage initiation and $\bar{\varepsilon}_f$ is the plastic strain when all the stiffness and fracture energy of the material have been lost and dissipated, respectively. $\tilde{\sigma}$ is the hypothetical undamaged stress evaluated by Eq. 59, l is characteristic length of the finite element in the simulation. $\bar{\mu} = 0$ is the equivalent plastic displacement before damage initiation while $\bar{\mu}_f$ is the equivalent plastic displacement at complete fracture.

The coefficients of the *J-C* model were also determined using the mechanical tests data. Compression tests of cylindrical specimens at different strain rates were used to determine the coefficients of the plasticity model (A_{jc}, B_{jc}, C_{jc} and n_{jc}), and the damage model coefficient related to the strain rate effect (D_{4jc}). Compression tests of double notched specimens were used to determine the damage model coefficients associated with the stress triaxiality effect (D_{1jc} – D_{3jc}). The value of G_f, was already determined in above section. Table 10 shows the determined coefficients of the *J-C* constitutive model for the Ti-6Al-4V alloy.

Table 10: Determined coefficients of the *J-C* model.

	Plasticity				Damage					
Coef.	A_{jc}	B_{jc}	n_{jc}	C_{jc}	D_{1jc}	D_{2jc}	D_{3jc}	D_{4jc}	G_f (KJ/m^2)	$\dot{\varepsilon}_0$ (s^{-1})
Value	812	844	0.261	0.015	0.245	0.081	-1.276	-0.028	18.5	0.05

Then, the numerical simulations of the mechanical tests were conducted with the *J-C* model, and the results obtained were compared with those obtained by the proposed constitutive model, as well as the experimental data. Fig. 63 shows these results for four different specimen geometries that generate different states of stress: cylindrical specimen (*C*), double notched specimen having a pressure angle of 90° (*DN_90*), notched flat plate specimen with *R* equal to 10 mm (*NFP_R10*) and notched round bar with *R* equal to 12 mm (*NRB_R12*).

Both the proposed and *J-C* constitutive models used in the simulations of the compression tests of the cylindrical specimen at a strain rate of 950 s^{-1} generate force-displacement curves that match the experimental ones quite well. However, when the *J-C* model is applied in the numerical simulations of the compression test of double notched specimen, tensile test of notched flat plate and notched round bars specimen, the predicted force-displacement curves are considerably overestimated. In particular, higher forces and displacements at fracture were obtained using the *J-C* model, when compared to the proposed constitutive model and the experimental results. Therefore, the *J-C* model is not able to represent the mechanical behavior

of Ti-6Al-4V alloy under different states of stress, while the proposed model shows good accuracy.
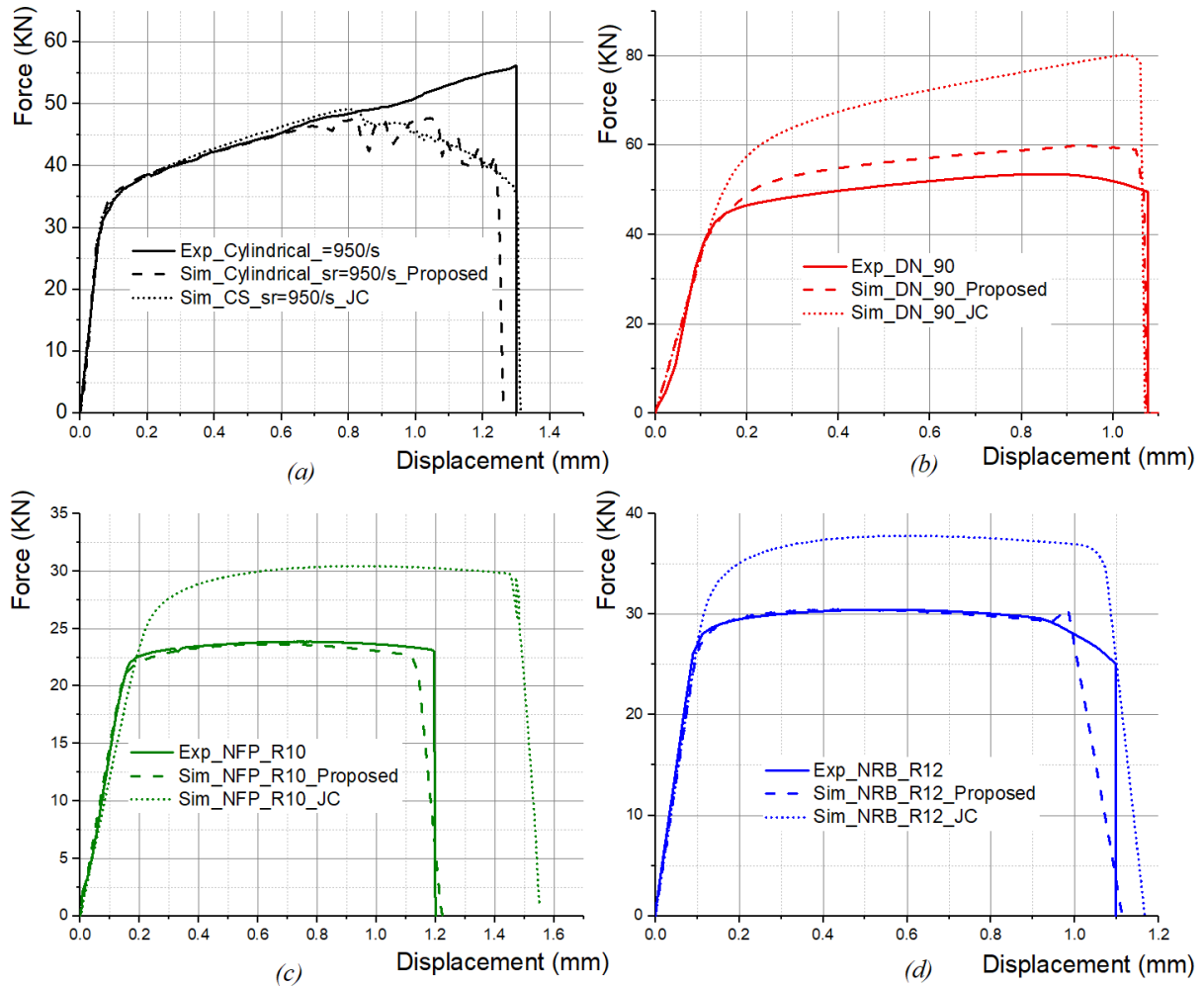
Fig. 63: A comparison of force-displacement curves from experimental data and simulated results with the proposed constitutive model and the *J-C* model: (a) compression test of cylindrical specimens at a strain rate of 950 s^{-1}; (b) quasi-static compression test of *DN_90*; (c) quasi-static tensile test of *NFP_R10*; (d) quasi-static tensile test of *NRB_R12*.

3.9 Summary of the chapter

A constitutive model describing the mechanical behavior of Ti-6Al-4V titanium alloy that includes both the plasticity and damage is proposed. It accounts for the effects of strain hardening, strain-rate and the state of stress in both the plasticity and damage regions. This model can be used to describe the work material behavior in manufacturing process simulations involving crack propagation and neglecting the thermal effects on the mechanical behavior. This is the case for work material in the first deformation zone in metal cutting, where its

separation from the workpiece is caused by crack propagation. Moreover, most of the heat produced due to plastic deformation in this zone flows into the chip, and only a small amount flows into the workpiece.

Numerical simulations of the tensile and compression tests with several specimen geometries permitted the state of stress (stress triaxiality and the Lode angle parameter) representative of the metal cutting process to be obtained. Then, experimental mechanical tests were conducted and the force–displacement curves obtained were used in a hybrid numerical/experimental optimization-based procedure to determine the constitutive model coefficients.

Additional force-displacement curves from mechanical tests of specimen geometries not used in the determination of coefficients procedure were obtained. The comparison between these experimental curves and the simulated ones (using the proposed constitutive model with the determined coefficients) confirmed the accuracy of the proposed constitutive model to describe the mechanical behavior of Ti-6Al-4V alloy under different states of stress. The accuracy was also confirmed by a benchmark test considering the proposed constitutive model and the *J-C* model. These simulations show the importance of the stress triaxiality and the Lode angle in the improvement of constitutive model accuracy.

Chapter 4:

Assessment of machining performance and surface integrity in orthogonal cutting of Ti-6Al-4V using the developed constitutive model

4.1 Orthogonal cutting model

To simulate the cutting of Ti-6Al-4V alloy, a constitutive model and its coefficients have been proposed and determined in Chapter 2 and Chapter 3, respectively. The model describes the mechanical behavior from the elastic-plastic deformation to complete fracture. This chapter presents the application of this model to metal cutting simulations. Meanwhile, the orthogonal cutting tests will be implemented under different cutting conditions. At last, the results of cutting tests will be compared with the simulated data, including the cutting forces, chip geometry, in-depth residual stress profiles and thickness of plastically deformed layer.

4.1.1 Model description

To test the adequateness of the proposed constitutive model to predict metal cutting performance, 2D orthogonal cutting model of Ti-6Al-4V titanium alloy is developed, as can be seen in Fig. 64. The quadrilateral continuum elements CPE4RT are used in the coupled temperature-displacement simulations using ABAQUS/Explicit FEA software. Refined elements are used in the parts of chip and intermediate layer to better simulate the cutting process, where the mesh size is 17 µm x 10 µm. Meanwhile, the mesh along the depth of workpiece surface are also refined to calculate the distribution of residual stress, where the mesh size was defined as 17 µm x 7.5 µm.

Fig. 64: 2D orthogonal cutting model.
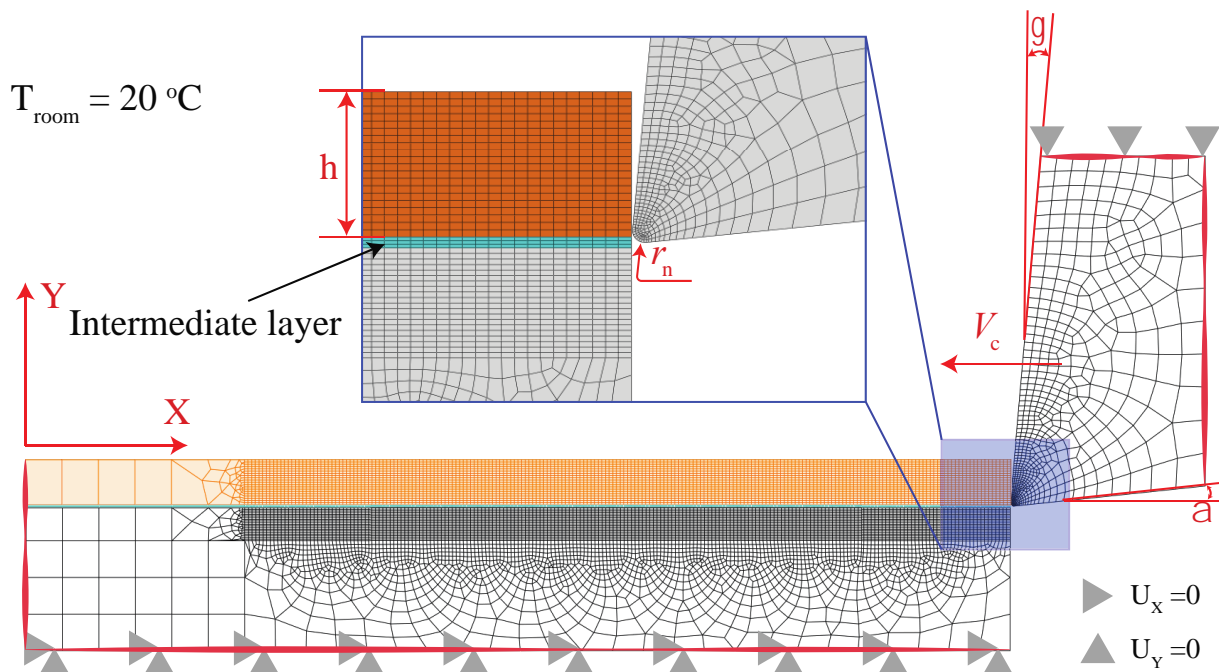
During the cutting simulations, the workpiece is fixed while the tool advanced at a constant cutting speed V_c. The intermediate layer is applied to simulate the physical separation of the layer being removed (in the form of chips) from the rest of workpiece, using the element deletion technique. An initial temperature of 20 °C is imposed to both the tool and the workpiece. The red lines on the boundary of workpiece and tool are the boundary condition of temperature, which indicates that the temperatures of these boundaries are fixed at room temperature, 20 °C.

The proposed constitutive model is implemented through a *VUMAT* subroutine. The geometry of tool can be modified according to the tools used in the experiments, including the rake angle (γ), clearance angle (α), and cutting-edge radius of (r_n). Similarly, different cutting conditions can be implemented in the simulation, including the cutting speed (V_c), the uncut chip thickness (h) and the width of cut. Thermal properties of Ti-6Al-4V alloy are provided by the company TIMET, while information of the tool material is taken from the reference [35]. The thermal and physical properties of the workpiece and the tool are summarized in Table 11.

Table 11: Thermal and physical properties of the workpiece and the tool.

Physical properties	Workpiece	Tool
Density, ρ (kg/m^3)	4420	13967
Elastic modulus, E (GPa)	114	627.5
Poisson's ration, ν	0.31	0.25
Specific heat, C_p (J/kg/°C)	670	100
Thermal conductivity, λ (W/m/°C)	6.6	9.7
Expansion coef., α_v (μm/m/°C)	9	5.174

The contact conditions over the tool-chip and the tool-workpiece, interfaces are modelled using the Zorev's model (Eq. 10). To determine the relation between the friction coefficient and the sliding speed at these interfaces, the inverse method is used. First, the data of friction tests from literature [110] are used as the lower limit (red points in Fig. 65), while the data from orthogonal cutting tests based on designed cutting conditions are used as the upper limit (balck points in Fig. 65). Then, OC simulations using several friction curves within this range are performed. The curve that gave the best forces and chip geometry predictions (when compared to the experimental results) is used in all the machining simulations (blue curve in Fig. 65).
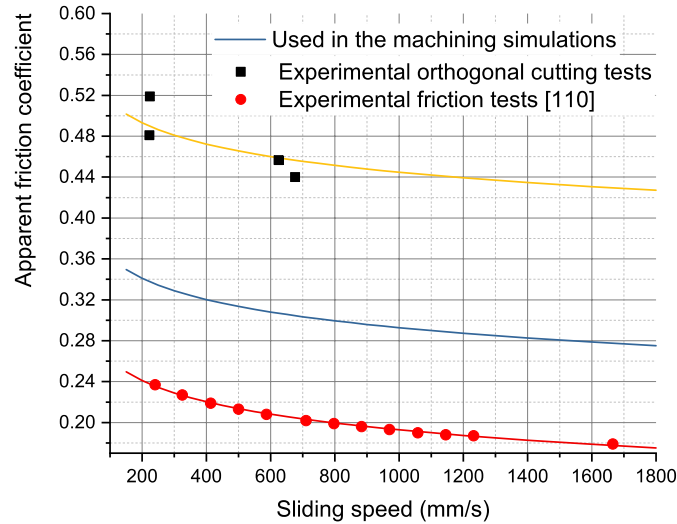
Fig. 65: Relation between friction coefficient and sliding speed.

4.1.2 Residual stress simulation

The model predicting the residual stress was constructed and the procedure was shown in Fig. 66. It includes two steps: the first step is to perform the simulation of the orthogonal cutting test, especially the interaction between the workpiece and the moving tool. As mentioned above, this step was implemented in ABAQUS/Explicit with VUMAT subroutine. The simulated chip geometry and cutting forces are used to be compared with the experimental data, while the distributions of temperature, stress and strain in the machined workpiece are transferred to the next step.
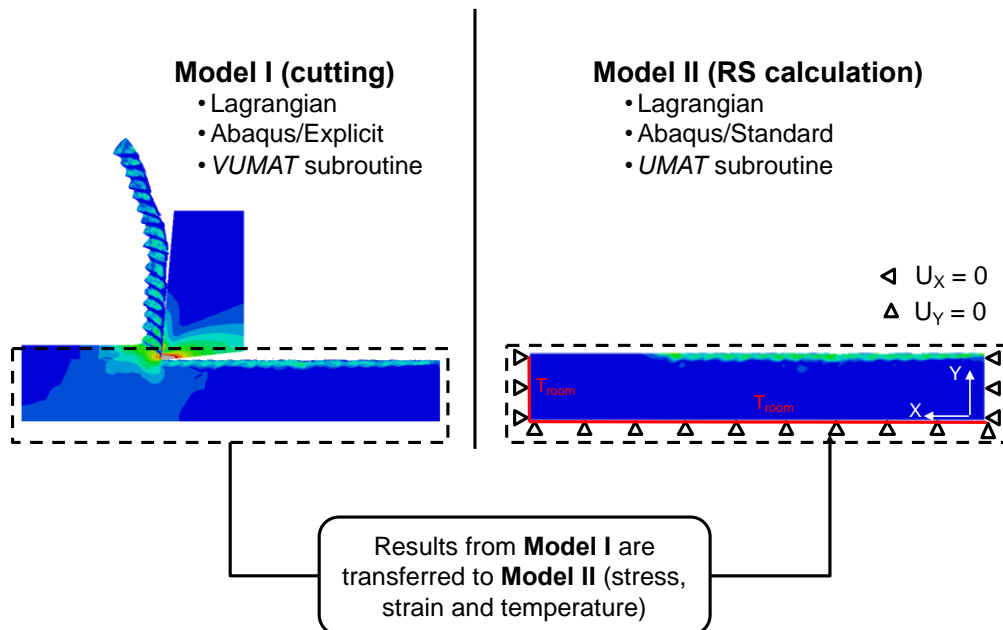
Fig. 66: Procedure of the residual stress analysis.

In the second step, simulation of the residual stress was performed, i.e., unloading and cooling of the workpiece until reaching the mechanical equilibrium and room temperature in the workpiece. It is implemented in ABAQUS/Standard with *UMAT* subroutine. Particularly, the constitutive model used in these two models are exactly the same. The initial state of Model II is obtained from the last step of Model I. To reduce the calculation cost, only the machined workpiece was maintained in the Model II, and the mesh pattern was also kept. The boundary condition was presented in Fig. 66. The red lines represent the boundary condition of temperature, while the triangles represent the boundary condition of displacement.

4.2 Experimental setup and cutting conditions

4.2.1 Tool geometry/material and cutting regime parameters

In orthogonal cutting tests, the uncoated cemented carbide (WC-Co) inserts (references TNMA160408 and TPUN160308) and tool holders (references DTFNR2020K16 and CTFPR2020-16) used in the tests are provided by Seco Tools, as shown in Fig. 67. The shank of tool holders have been modified using a Gambin CNC 4-axis milling machine to get an inclination angle $\lambda_s = 2^o$ to reduce the effect of lateral burrs in the orthogonal cutting tests, that a DIC system was integrated into the experimental setup, and the lateral burrs would damage the objective of the camera and reduce the quality of the recorded images. The insert TNMA160408 was installed into the toolholder DTFNR2020K16, while the insert TPUN160308 was installed into the toolholder CTFPR2020-16.

The geometry of the insert was checked carefully by Alicona 3D microscope machine before the tests. Fig. 68 shows the results of all the measured data. Each kind of insert has two different designed values of edge radii, that is 10 μm and 30 μm. Thus, TPUN_r10 and TPUN_r30 represents insert TPUN160308 with edge radius 10 and 30 μm respectively, while TNMA_r10 and TNMA_r30 represents insert TNMA160408 with edge radius 10 and 30 μm respectively. However, the measured value of edge radius for both TPUN_r10 and TNMA_r10 is about 16 μm with small deviations. To ensure the accuracy of cutting parameters, the value of edge radius 16 μm is used for TPUN_r10 and TNMA_r10 in the following tests and simulations. The measured values of edge radius for TPUN_r30 and TNMA_r30 are similar to the designed values 30 μm. Compared with the designed values of rake angle and clearance angle, the measured values of all the inserts match and the deviation is relatively small. Thus, the rake

angle of TPUN_r10 and TPUN_r30 is 5°, while the one of TNMA_r10 and TNMA_r30 is -6°. The clearance angle of all the inserts is 6°.

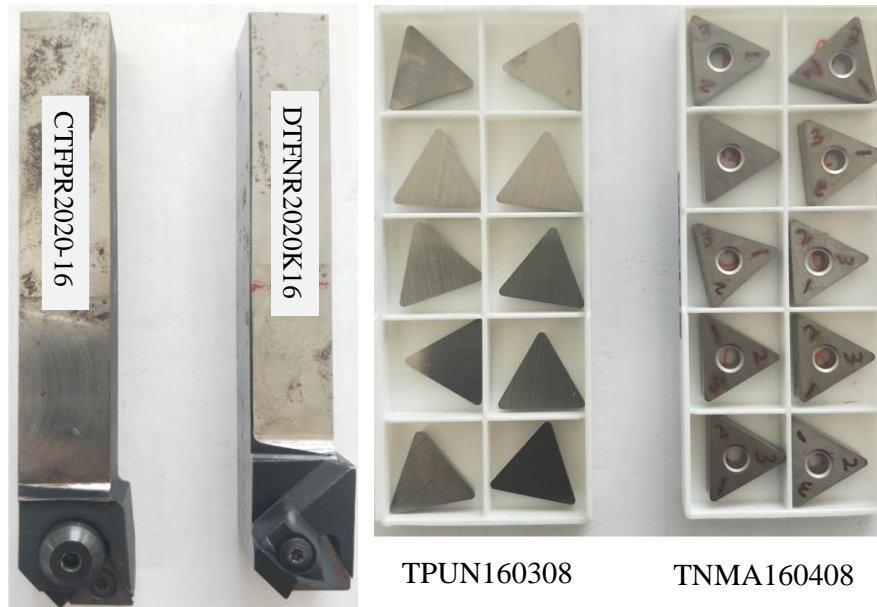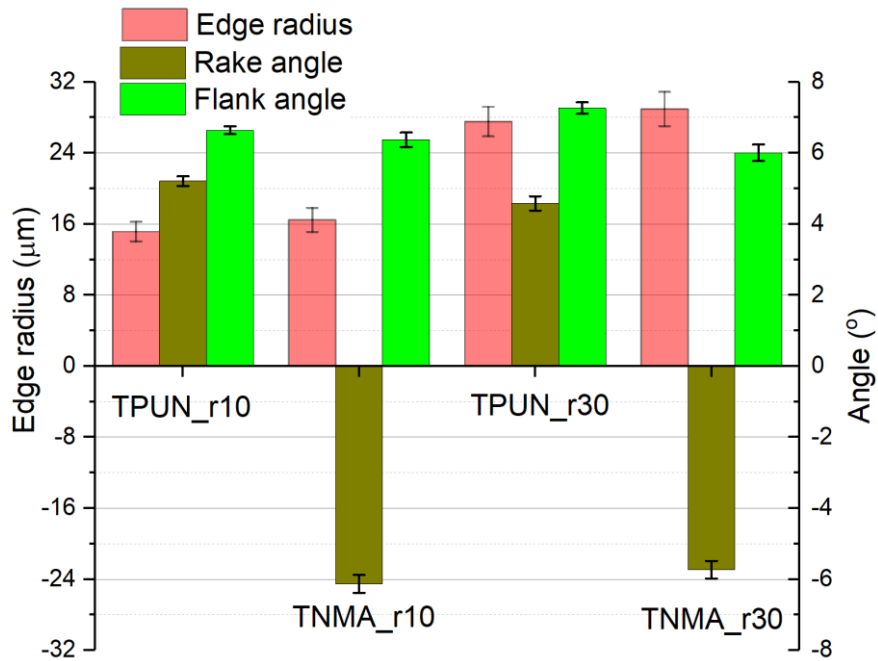Fig. 67: Tool holders and inserts used in the orthogonal cutting of Ti-6Al-4V alloy.

Fig. 68: Measured values of insert geometries.

Besides the insert geometries, there are other cutting parameters to be determined. Each parameter influences the cutting process. Four cutting parameters, including the cutting speed V_c, the uncut chip thickness h, the rake angle γ and the edge radius r_n were investigated in this

study. The values of the cutting parameters are summarized in Table 12. There are two different levels for the cutting parameters to be investigates. All the tests are performed in dry conditions.

Table 12: Cutting parameters of orthogonal cutting.

Cutting parameters	Low level	High level
Cutting speed, V_c (m/min)	20	60
Uncut chip thickness, h (mm)	0.15	0.2
Tool cutting edge radius, r_n (µm)	16 ± 1.1	30 ± 1.9
Tool rake angle, γ (°)	5 ± 0.13	-6 ± 0.25
Tool clearance angle, α (°)	6 ± 0.23	
Width of cut (mm)	4	
Cooling condition	Dry cutting	

4.2.2 Design of experiments (DoE)

4.2.2.1 DoE principles

Researchers, financial analysts and industrial field hunt for patterns in a tremendous amount of data by using increasingly powerful statistical tools and methods. These methods are based on several concepts like knowledge discovery, data mining and information visualization. Moreover, they employed specific techniques including decision trees, principal component analysis and several other methods. One of the most powerful statistical methods is the design of experiments (DoE). It is known as the experimental design. DoE is a statistical methodology that allows the experimentalists to establish statistical correlation between a set of input factors and output responses. In the machining process, the input factors include cutting speed, feed, depth of cut, etc. (parameters related to the machine and the process configuration), while the output response can be the cutting forces, tool life, surface integrity, etc. (entities related to the product). Depending on the number of factors and experimental objective, different DoE methods can be applied.

The factorial experiments, in which the lines are combined with levels of several factors, is a very useful method issued from the DoE. It's very common to be used in the technological field with a small number of levels, i.e., 2 levels per each factor. The design of k treatment factors with only 2 levels is called the 2^k factorial design. These designs are created to explore a large number of factors, with each factor having the minimal number of levels, just two. Since all the factors in this study have 2 levels, the following text will focus on the 2^k factorial designs.

The simplest way is to apply the full factorial design, which performs all the 2^k tests with all the possible combinations between the factors and their levels. This type of design allows the

calculation of the average estimation of each effect and interactions. However, when the number of factors exceeds more than 5 factors, the number of tests would raise dramatically, which consumes lots of time and recourse. In the machining operation, it means a great number of cutting tools, a significant amount of workpieces and various cutting programs. Thus, this method induces big dilemma between keeping an accurate estimation and results or optimization in time and resources.

Another method is to use screening DoE, which can investigate a large number of factors using a relatively small number of tests [111]. However, the accuracy of this screening DoE is reduced. Not all the factor effects can be estimated, because factors are aliased with one another. If factors A and B are aliased, the effect of interaction between A and B is actually estimated, instead of only effect for A. To describe the degree to which the estimated main effects are aliased (or confounded) with estimated 2-lev·el interactions, 3-level interactions, etc., the resolution term is imported. Four resolution levels and their meanings are given in Table 13 [112]:

Table 13: Resolution levels in experimental design [112].

Resolution level	Explanation
II	Main effects are linearly combined with each other ($\beta_i+\beta_j$)
III	Main effects are linearly combined with two-way interactions ($\beta_i+\beta_{jk}$)
IV	Main effects are linearly combined with three-way interactions ($\beta_i+\beta_{jkl}$) and two-way interactions with each other ($\beta_{ij}+\beta_{kl}$)
V	Main effects and two-way interactions are not linearly combined except with higher-order interactions ($\beta_i+\beta_{jklm}$) and ($\beta_{ij}+\beta_{klm}$)

where β_i is the main effect of the factor (i = 1,2, …,p), β_{ij} is the two-way interaction effect between the ith and j^{th} factors, and β_{ijk} is the three-way interaction effect between the ith, j^{th}, and k^{th} factors.

If some main effects are confounded with some 2-level interactions, the resolution is III. Full factorial designs have no confounding and are said to have the resolution "infinity". For most practical purposes, a resolution V design is excellent and a resolution IV design may be adequate. Resolution III designs are useful as economical screening designs.

The fractional factorial design is a type of screening DoE method, which allows the reduction of the test number while keeping the capability of estimating the most important effects. As the most widely and commonly used design method in industry, the construction of the fractional design is critical. To succeed the statistical analysis of DoE, the contribution of all the factors

and their interactions are equal in the design of experiments matrix, that is, orthogonality hypothesis (orthogonal table). In this way, a fractional factorial experiment is extracted from a full factorial experiment, which is naturally orthogonal because it involves all the possible runs to estimate the effects of the factors and their interactions. On the other hand, lower-order effects are more likely to be important than higher-order effects. Thus, interactions introduced by three or more factors could be eliminated and considered as negligible. This assumption provides the possibility of reducing the number of the required tests in the present study.

4.2.2.2 Analysis of Variance (ANOVA)

The design of experiments is realized by getting the independent responses to the factors with several repetitions. But the calculation of an effect isn't enough to determine which are the significant parameters for the process. Therefore, a reliable criterion that manifests the variability of the system regarding to the controlled factors should be used. One of the most used statistical method to deal with the above-mentioned challenge is the analysis of variance (ANOVA). ANOVA is a statistical technique that assesses potential differences in a scale-level dependent variable by a nominal-level variable having 2 or more categories [113].

The hypothesis used in ANOVA is called null hypothesis H_0, as shown below. There is no relevant difference between specified populations (repetition), and any observed difference being due to sampling or experimental error.

$$H_0: \mu_1 = \mu_2 = \mu_3 = \ldots = \mu_k$$

k is the number of independent comparison groups.

To verify this hypothesis, an ANOVA table is used, as shown in

Table 14. If the variability between groups is large relatively to the variability within groups, it suggests that the means of the populations from which the data were drawn are significantly different. That is how the F statistic is calculated: it is a ratio of a measurement of the variability between groups to a measurement of the variability within groups. If F is large, the variability between groups is large relatively to the variation within the group, the null hypothesis of equal means is rejected. If F is small, the variability between groups is small relative to the variation within groups, the null hypothesis of equal means failed to be rejected.

Table 14: ANOVA table.

Source of variations	Sums of Squares (SS)	Degrees of freedom (Dof)	Mean Squares (MS)	F-value	P-Value
Between/Treatments	SSB	k -1	$MSB = \dfrac{SSB}{k-1}$	$\dfrac{MSB}{MSE}$	
Within/Error	SSE	$N - k$	$MSE = \dfrac{SSE}{N-k}$		
Total	SST	N - 1			

To better understand this table, the terms and calculation steps are explained below:

k = the number of groups/levels of treatment

n_i = the sample size taken from group i

x_{ij} = the jth response sampled from the ith group

$\bar{x}_i$ = the sample mean of responses from the ith group $= \dfrac{1}{n_i}\sum_{j=1}^{n_i} x_{ij}$

s_i = the sample standard deviation from the ith group $= \dfrac{1}{n_i-1}\sum_{j=1}^{n_i}\left(x_{ij}-\bar{x}_i\right)^2$

N = the (total) sample, irrespective of groups $= \sum_{i=1}^{k} n_i$

$\bar{x}$ = the mean of all responses, irrespective of groups $= \dfrac{1}{N}\sum_{ij} x_{ij}$

The total amount of variability SST is computed by summing the squares of the differences between each x_{ij} and $\bar{x}$. Relevantly, SSB represents the variability between group means (variation around the overall mean $\bar{x}$), where SSE represents the variability within groups means (variation of observations about their group mean $\bar{x}_i$). All the calculations are given from Eq. 63 to Eq. 65. Evidently, SST is the sum of SSB and SSE, that is SST = SSB+ SSE.

$$SST = \sum_{i=1}^{k}\sum_{j=1}^{n_i}\left(x_{ij}-\bar{x}\right)^2 \qquad\qquad Eq.\ 63$$

$$SSB = \sum_{i=1}^{k} n_i\left(\bar{x}_i-\bar{x}\right)^2 \qquad\qquad Eq.\ 64$$

$$SSE = \sum_{i=1}^{k} \sum_{j=1}^{n_i} \left(x_{ij} - \overline{x}_i \right)^2 = \sum_{i=1}^{k} \left(n_i - 1 \right) s_i^2 \qquad Eq.\ 65$$

The mean squares MSB and MSE are calculated by dividing the corresponding degree of freedom (Dof). Then, the ratio of MSB to MSE is used to get the value of F statistic, which can determine if accept or reject the null hypothesis. Normally, the *p-value* is combined with F statistic to find out which of the individual variables are statistically significant. The *p-value* is the probability of such an 'extreme' value of the test statistic when H_0 is true. When calculated, if *p-value* is smaller than the given alpha level, the null hypothesis is rejected.

4.2.2.3 DoE matrix of the orthogonal cutting tests

The factorial DoEs were applied to the orthogonal cutting tests, which permitted the investigation of the influences of different cutting parameters (factors) on the cutting force F_c, the thrust force F_T and the *CCR*. In this case, the DoE is composed by 4 factors and 2 levels per factor. A full factorial 2-level design is used for the cutting and thrust forces, as shown in Table 15. In total, there are 16 cutting conditions. Three tests have been repeated for each cutting condition before the average values and the standard deviations were calculated.

Table 15: Full factorial design of experiments for cutting and thrust forces (16 cutting conditions).

γ (°)	r_n (μm)	V_c (m/min)	h (mm)
5	16	20	0,15
5	30	20	0,15
5	16	20	0,20
5	30	20	0,20
5	16	60	0,15
5	30	60	0,15
5	16	60	0,20
5	30	60	0,20
-6	16	20	0,15
-6	30	20	0,15
-6	16	20	0,20
-6	30	20	0,20
-6	16	60	0,15
-6	30	60	0,15
-6	16	60	0,20
-6	30	60	0,20

Table 16 represents a reduced table of experiments for the surface integrity analysis. The effect of each cutting parameter on surface integrity will be investigated by comparing different

cutting conditions. For example, the effect of the cutting speed could be analysed by comparing the results between cutting condition 1 and 2.

Table 16: Selected cutting conditions for surface integrity analysis (7 cutting conditions).

Cutting condition	γ (^{o})	r_n (μm)	V_c (m/min)	h (mm)
1	5	16	60	0.2
2	5	16	20	0.2
3	5	16	60	0.15
4	5	16	20	0.15
5	5	30	60	0.15
6	-6	16	60	0.15
7	-6	30	60	0.15

4.2.3 Experimental setup for orthogonal cutting tests

The orthogonal cutting tests in planning configuration were performed in a 3 axis CNC milling machine from DMG model DMC85V. The tool was clamped in a square supporter which is fixed on the machine head. This milling machine has a linear motor to allows the linear speed to reach up to 120 m/min and acceleration can reach 20 m/s². A gradual acceleration has been performed by a speed loop-back command in order to reach the specified cutting speed in some millimetres before interaction between tool and workpiece.

To measure the tool temperature, type K thermocouples were inserted into the holes of the inserts. These holes were drilled by a hole drilling EDM machine Agie Charmilles DRILL 20 (Fig. 69a). The diameter of drilling electrodes used in the process was 0.8 mm, and this machine gives an accuracy of the hole depth between 0.1 and 0.2 mm. The hole end was about 1 mm far from the cutting edge (Fig. 69b), to avoid the device damage while drilling process. Each test was performed using a new cutting edge to eliminate the tool wear effect.

Fig. 70 shows the scheme of acquisition and synchronization devices in the tests. The specimen was observed by a high speed camera Photron Fastcam SA-Z providing a spatial resolution of 1.6 μm/px on the 1024x1024 pixels with 8-bit dynamic range (256 gray levels). A 1.64×1.64 mm^2 observation area was obtained for each image. The frame rate is set as 20 000 fps with the exposure time 1/80 000 s to ensure the acquisition of enough images (0.05 ms per image). When the cutting speed is 60 m/min, the tool stays in this observation area during 1.6 ms, i.e. 32 images are acquired. In this case, it was necessary to build a precise synchronization between the tool position and the high-speed camera. The camera was triggered by a specific system based on signal counting of the linear encoder in the x-axis of the CNC machine [114]. The

position sinusoidal signals and their conjugates produced in the Heidenhain LC181 encoder were duplicated and converted into transistor-transistor logic (TTL) signals with an interpolation (×2) in the Heidenhain IBV606 splitter box. The interpolated signals were transported to a high-speed 32-bit quadrature counter chip used in the ×4 mode. Thus, a 2 µm x-position resolution was achieved.

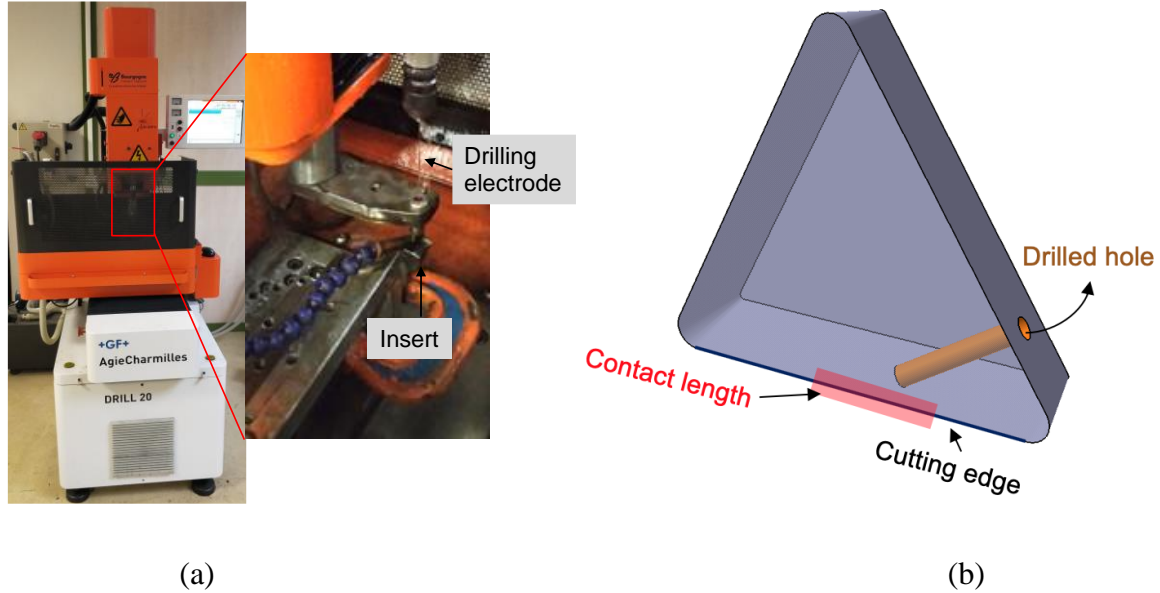(a)   (b)

Fig. 69: (a) Drilling EDM machine; (b) Drilled insert.
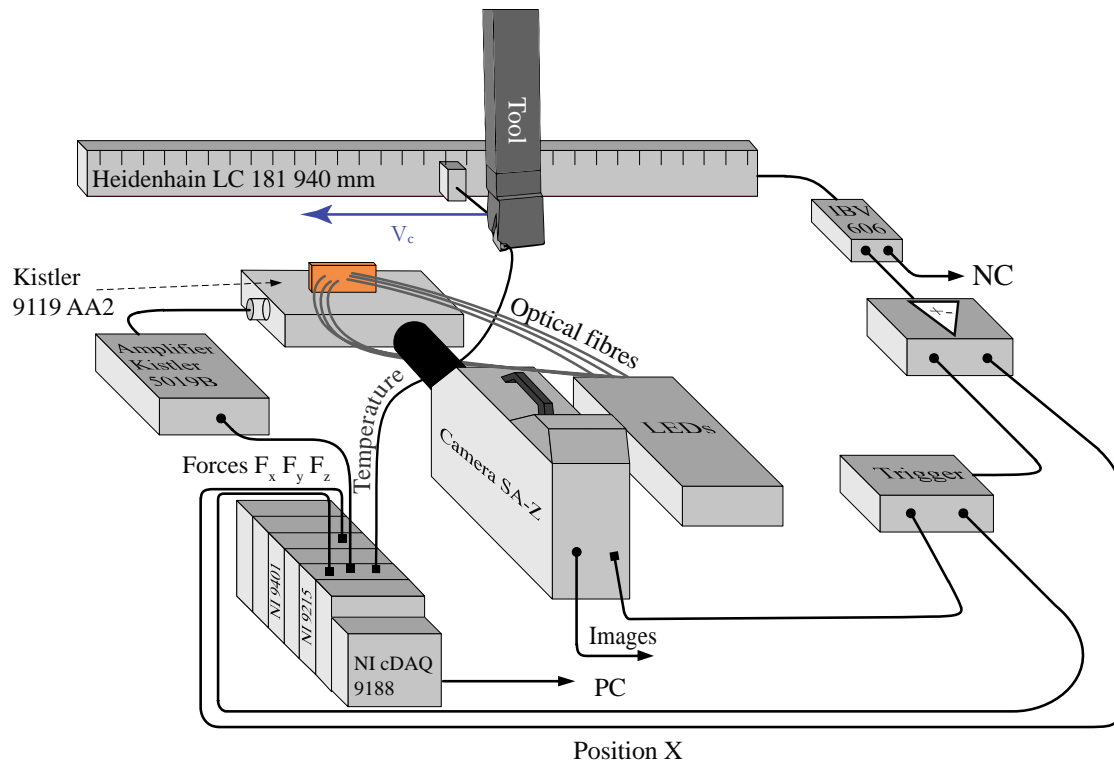

Fig. 70: Scheme of acquisition and synchronization devices in orthogonal cutting test [114].

104

The cutting force F_c and thrust force F_T were measured by a Kistler piezoelectric dynamometer 9119AA2, combined with a charge amplifier Kistler 5019B. The K-type thermocouple was inserted into the hole of the insert to measure the cutting temperature near the cutting edge. All signals were recorded synchronously at 10 kHz sampling rate, using a NI cDAQ9188 rack with the NI 9401, NI 9215 and NI 9205 acquisition cards for x-position, forces/triggering signals and thermocouple temperature, respectively. Additionally, to get a clear detection of the tool in the images taken by the camera, the insert has been grounded by using a grinding machine to obtain a flat surface normal to the camera axis. A DIC software CorreliQ4 was used to analyze the images obtained by the high speed cameras. It uses a finite element type global approach based on Q4P1 shape functions [115].

4.2.4 Specimens

The thickness of the specimens used in orthogonal cutting tests should not be too large due to the capacity of piezoelectric dynamometer which is used to measure the cutting forces. On the other hand, the thickness should be big enough to ensure the plane strain condition in the tests. As a result, the machined specimens used in this set of experiments were a 40(L) × 20(H) × 4(W) mm^3 cuboid samples that were extracted from the same block which had also been used in the mechanical tests. A conventionnel milling machine and a saw abrasive cutting machine were used to manufacture those specimens. After that, the 40 × 20 mm flat surface of the specimens were polished to remove the superficial deformed layer produced by the previous manufacturing processes. A layer of about 0.1 mm thickness was removed from the A side of the specimen by polishing, as shown in Fig. 71. Then, preliminary planning tests were performed with an uncut chip thickness 0.05 mm to remove the deformed layer from the face B.

In the orthogonal cutting tests with DIC system, the surface of specimen was shot-peened to generate a suitable pattern for DIC analysis. The surface quality was determined by two parameters: shot-peening time, T_{sp} and shot-peening pressure P_{sp} (bar). To choose the appropriate parameters, five different shot-peening configurations are evaluated. The specimens were shot-peened with glass micro-spheres with diameters between 50 and 100 μm. Fig. 72 shows the histogram of the specimen surfaces under those different configurations. The abscissa axis means the grey level, while the ordinate axis shows their frequency in the image. The optimum shot-peening parameters is the one that gives the widest grey level on the surface.

As a result, the parameters used in the following surface treatments were $P_{sp} = 4$ bar and $T_{sp} = 9$ s.
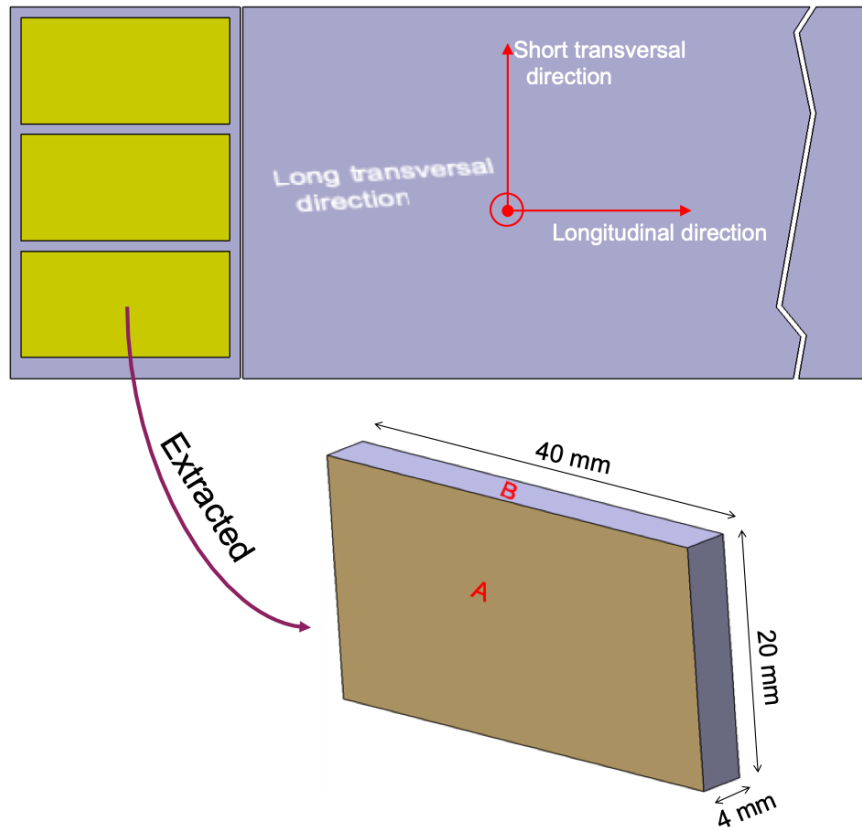

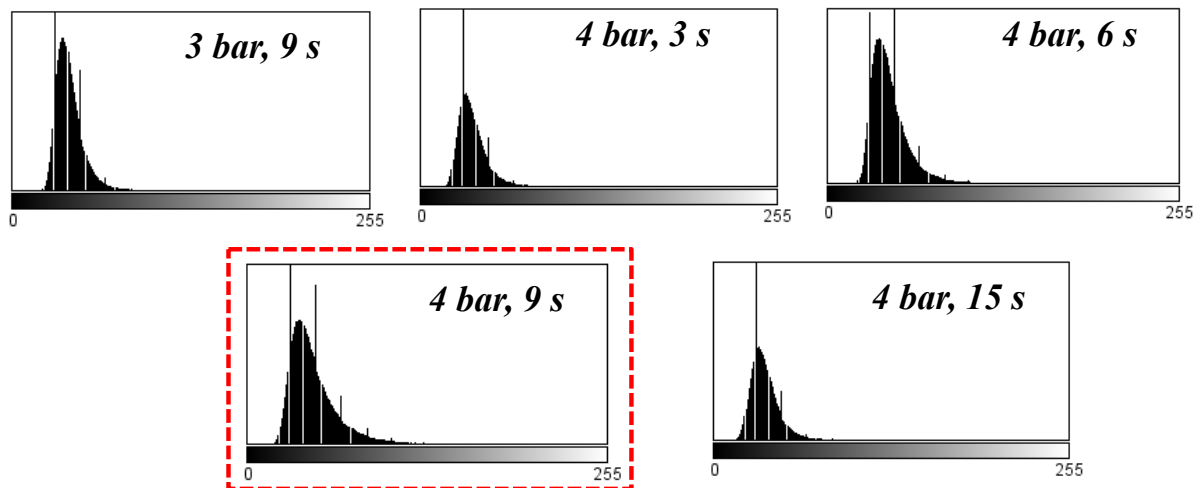Fig. 71: Specimen used in orthogonal cutting tests.

Fig. 72: Histogram of the pattern distribution under different shot-peening conditions.

4.3 Experimental results and analysis

4.3.1 Tool temperature

Fig. 73 shows the curves of temperature in function of the time measured by thermocouples for all cutting conditions. Each curve represents an average of three tests for the same cutting condition. Typically, the temperature increased with the cutting time until reached a peak value, before decreasing to the room temperature. However, the measured temperatures are relatively small, less than 100ºC. One reason is that the cutting length is too short (40 mm), and a stable temperature could not be detected in the limited cutting time. The other reason is that the end of the thermocouple is 1 mm far from the cutting edge, this long distance reduced the accuracy of measurement of the cutting temperature in the interface between the cutting edge and the workpiece. These results can be improved by increasing the cutting length and decreasing the distance between cutting edge and thermocouple.

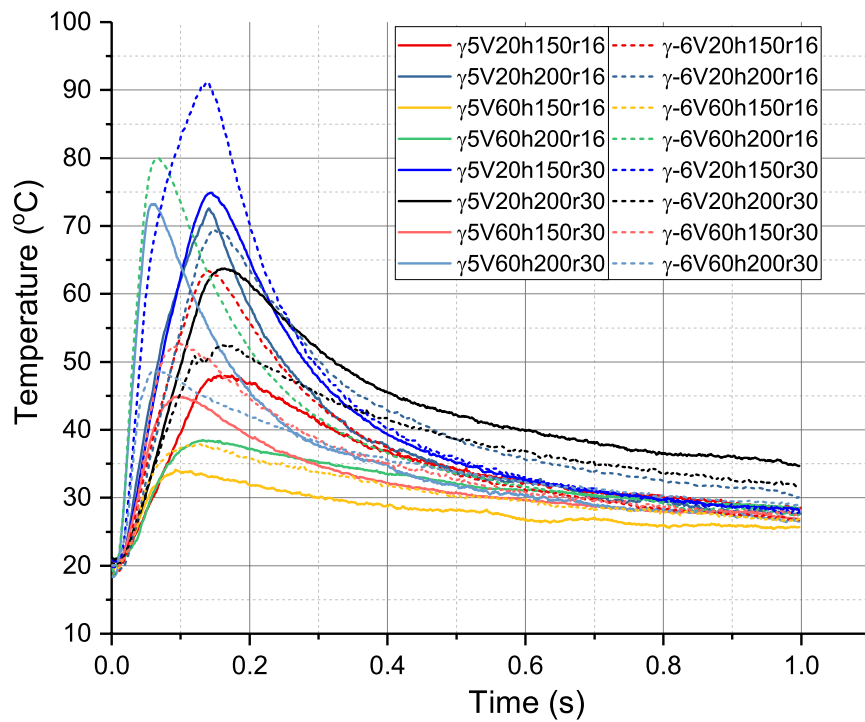Fig. 73: Temperature history in orthogonal cutting tests.

4.3.2 Cutting force and thrust force

Fig. 74 presents a typical history of the cutting force and the thrust force obtained in the experiments. The values of cutting forces and thrust forces were calculated in the zone where the signals were stable. Each cutting condition was performed 3 times to get the average values and the standard deviation.

107
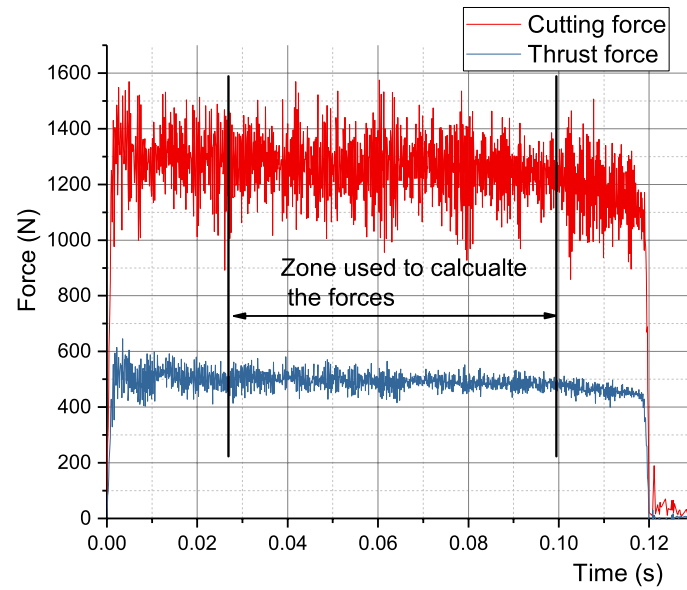
Fig. 74: History of cutting and thrust forces ($\gamma = 5°$, $V_c = 20$ m/min, $h = 0.15$ mm, $r_n = 16$ µm).

Fig. 75 summarizes the values of cutting forces and thrust forces for all the designed cutting conditions. The text below abscissa axis represents the different cutting conditions. For example, $\gamma5V_c20h150r_n16$ corresponds to a tool rake angle of 5°, cutting speed of 20 m/min, uncut chip thickness of 0.15 mm and edge radius of 16 µm. This naming rule is applied to the other cutting conditions. This figure shows that the cutting force is higher than the thrust force, which is often observed in in metal cutting in general.

Fig. 75: Results of the cutting force and thrust force for all designed conditions.

After gathering the necessary data (the cutting and thrust force), an ANOVA was performed to investigate the effect of the cutting conditions (factors) on the forces (responses). Fig. 76 gives the main effects plot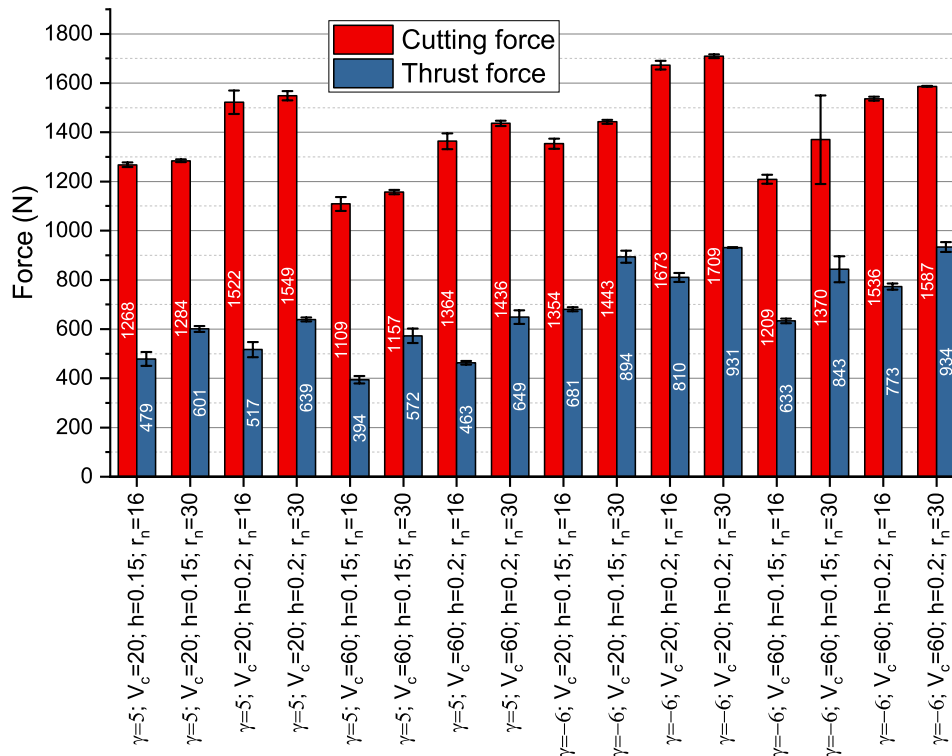 for the cutting force, including the effects of the rake angle, the cutting speed, the uncut chip thickness and the edge radius. The cutting force decreases when the rake angle increases. In the machining process, increasing the rake angle leads to a reduction of the tool-chip contact length, which could induce less deformation, less friction and easy chip disposal in the flow zone. Fig. 76 also reveals that increasing cutting speeds results in lower cutting forces. This reduction can be attributed to the thermal softening induced by the increase of the temperature with the high cutting speed [116]. In contrast, the cutting force increases as the uncut chip thickness and the edge radius increase. It is evident that larger uncut chip thickness has a longer tool-chip contact length, which needs more energy to deform the material in front of the tool. Wyen and Wegener [117] investigated the influence of the cutting edge radius on the cutting forces in machining Ti-6Al-4V alloy and concluded that the friction coefficients on the tool-chip interface are dependent on the cutting edge radius. Specifically, the friction coefficients become bigger as the cutting edge radius increases.
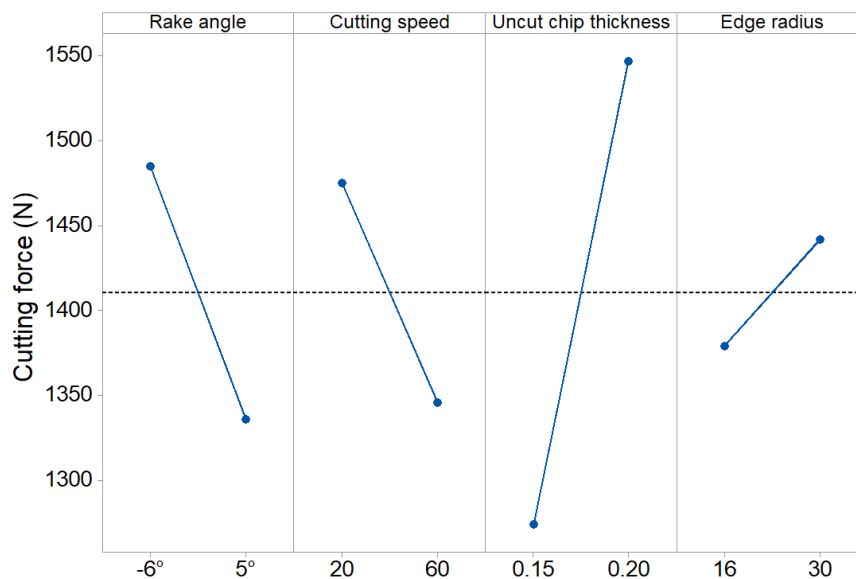
Fig. 76: Effects of the cutting parameters on the cutting force.

Table 17 shows the ANOVA table of the cutting force in orthogonal cutting of Ti-6Al-4V alloy. It indicates that the most significant factors are the tool rake angle (A), the cutting speed (B), the uncut chip thickness (C) and the tool edge radius (D). All the interactions between these effects did not show any influence on the cutting force. Thus, the cutting force could be only tied to these four factors.

Table 17: ANOVA table of the cutting force in orthogonal cutting of Ti-6Al-4V alloy.

Factor / Interactions	Dof	SS	MS	F-value	P-value	Significant (Y/N)
Rake angle (A)	1	266028	266028	110.84	0	Y
Cutting speed (B)	1	200230	200203	83.41	0	Y
Uncut chip thickness (C)	1	893076	893076	372.1	0	Y
Edge radius (D)	1	46908	46908	19.54	0	Y
AB	1	1199	1199	0.5	0.485	N
AC	1	1125	1125	0.47	0.499	N
AD	1	5566	5566	2.32	0.138	N
BC	1	135	135	0.06	0.814	N
BD	1	5139	5139	2.14	0.153	N
DC	1	3141	3141	1.31	0.261	N
ABC	1	606	606	0.25	0.619	N
ABD	1	14	14	0.01	0.939	N
ACD	1	7361	7361	3.07	0.089	N
BCD	1	332	332	0.14	0.713	N
ABCD	1	967	967	0.4	0.530	N
Error	32	76804	2400			
Total	47	1508602				

Similarly, ANOVA was applied to analyze the effects of cutting parameters on the thrust force. Fig. 77 illustrates the results of this analysis. It can be seen that the thrust force is more sensitive to a change in the edge radius than the other cutting parameters.
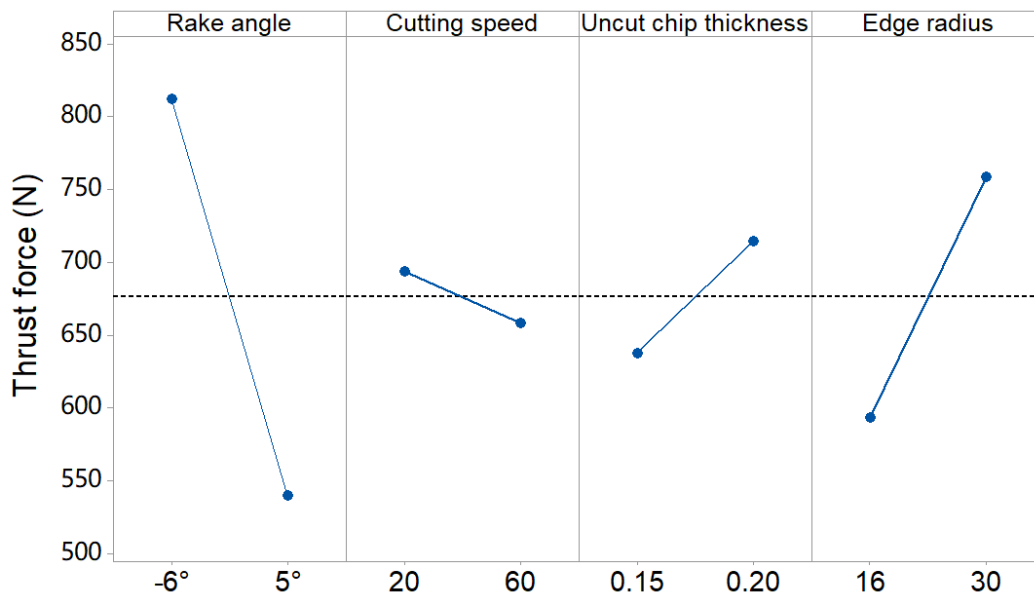

Fig. 77: Effects of the cutting parameters on the thrust force.

The significance of the cutting parameters on the thrust force is presented in Table 18. The whole four cutting parameters influenced significantly the thrust force. Moreover, it shows that

some interactions between factors have also a significant influence on the thrust force, including the two-way interactions: AC, BC, BD and CD, and the three-way interactions: ACD.

Table 18: ANOVA table of the thrust force in orthogonal cutting of Ti-6Al-4V alloy.

Factor / Interactions	Dof	SS	MS	F-value	P-value	Significant (Y/N)
Rake angle (A)	1	890516	890516	1783	0	Y
Cutting speed (B)	1	15000	15000	30.03	0	Y
Uncut chip thickness (C)	1	70336	70336	140.83	0	Y
Edge radius (D)	1	326844	326844	654.44	0	Y
AB	1	62	62	0.12	0.728	N
AC	1	6148	6148	12.31	0.001	Y
AD	1	1489	1489	2.98	0.094	N
BC	1	2960	2960	5.93	0.021	Y
BD	1	5009	5009	10.03	0.003	Y
DC	1	3730	3730	7.47	0.01	Y
ABC	1	1	1	0	0.967	N
ABD	1	1549	1549	3.1	0.088	N
ACD	1	3784	3784	7.58	0.01	Y
BCD	1	358	358	0.72	0.403	N
ABCD	1	362	362	0.72	0.401	N
Error	32	15982	499			
Total	47	1344129				

4.3.3 Chip geometry

During the orthogonal cutting tests, the chips were collected and saved separately after each test. Then, the optical microscope was used to evaluate the chip geometry, as can be seen in Fig. 78. Specimens for metallographic analysis were prepared according to the standard ASTM E3-11 [118]. The chips were fixed into cylindrical resin specimen holders under high temperature and pressure. Meanwhile, the chip was placed perpendicular to the base of the resin specimen, so the cross section of the chip could represent well the chip geometry. Then, this base was mirror polished. At last, the polished surface was placed under the optical microscope to investigate the chip geometry.

Three parameters were used to characterize the chip geometry: peak, pitch and valley (Fig. 79a). The peak represents the thickness of the chip, the pitch means the distance between the segments of the chip, and the valley corresponds to the minimum thickness of chip. In addition, using a mechanical probe is a convenient method to measure the chip thickness, as shown in Fig. 79b. The chip was placed between a horizontal plane and the spindle of the probe. Each cutting condition was measured 5 times to guarantee the repeatability. At last, the *CCR* was

calculated based on the measured chip thickness. Fig. 80 presents the measured *CCR* for the different cutting conditions.
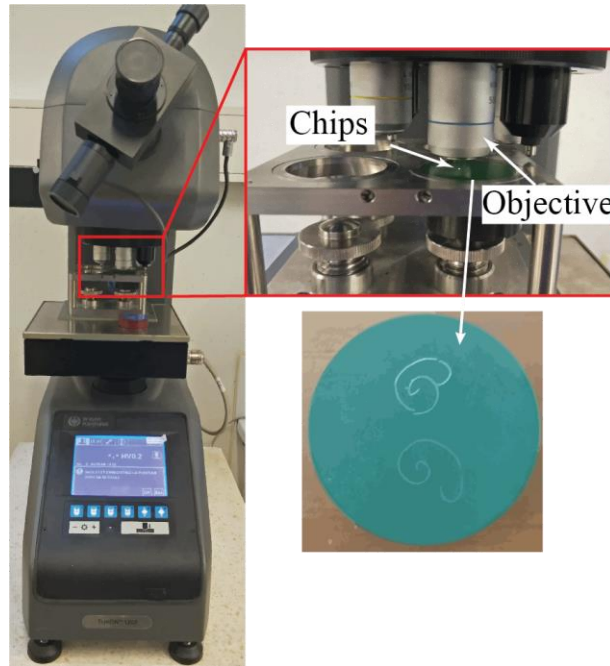

Fig. 78: Optical microscope to observe the chips.

| (a) | (b) |
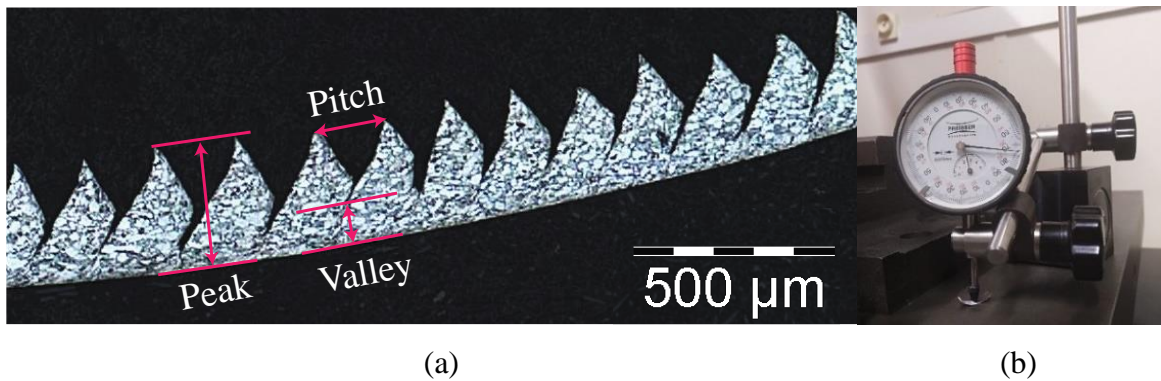
Fig. 79: (a) Chip geometry measured by optical microscope; (b) mechanical probe to measure the chip thickness.

As mentioned by Astakhov and Shvets [11], *CCR* can be used as the prime parameter for the optimization of the metal cutting process because it revealed the energy consumed in cutting with the consideration of plastic deformation of the workpiece. Therefore, the AVONA was also performed for the *CCR*. However, the values of *CCR* for the cutting conditions $\gamma = 5°$, V_c = 20 m/min, $h = 0.15$ mm, $r_n = 30$ µm and $\gamma = -6°$, $V_c = 20$ m/min, $h = 0.15$ mm, $r_n = 30$ µm were not available due to the experimental intricacy, so the effect of edge radius was neglected in ANOVA.
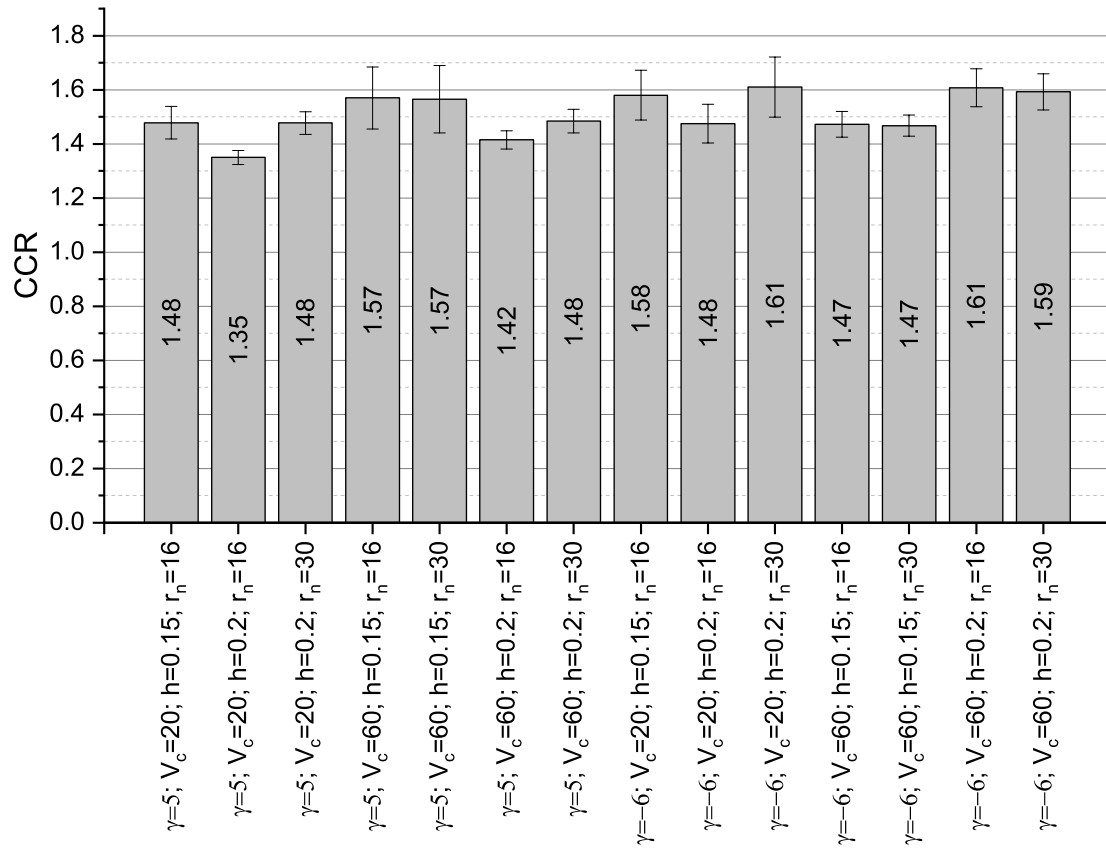
Fig. 80: Measured *CCR*.

Fig. 81 gives the main effects plot for *CCR*. It can be seen that the *CCR* raises as the rake angle increases. This trend was also observed in the machining of AISI 1045 steel and Ti-1023 titanium alloy [119]. The higher cutting speed could also enlarge the value of *CCR*. However, Ren et.al. [120] found that the *CCR* increased only when the cutting speed was between 70 m/min and 120 m/min. To certify the effect of cutting speed on *CCR*, more levels of cutting speed need to be investigated. The variation of the *CCR* with the uncut chip thickness revealed a decreasing trend, which is similar to the literature [120], [121].

Fig. 81: Effects of the cutting parameters on *CCR*.

An ANOVA table for *CCR* is presented in Table 19. It was found that the most significant factors are the rake angle, the interac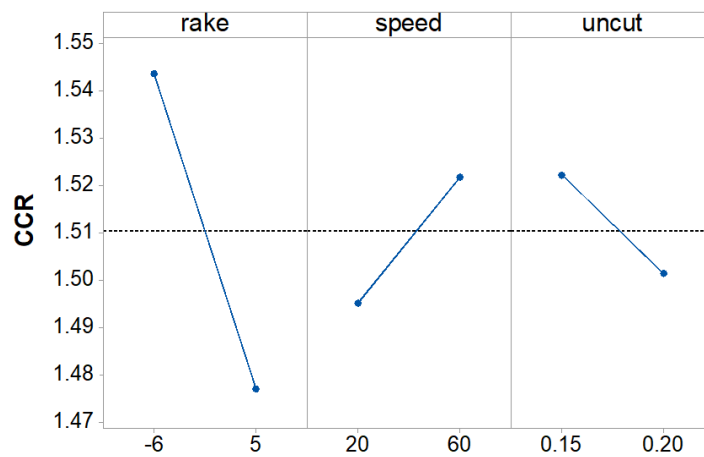tion between rake angle and uncut chip thickness and the interaction among the rake angle, cutting speed and uncut chip thickness.

Table 19: ANOVA table of the *CCR* in orthogonal cutting of Ti-6Al-4V alloy.

Factor / Interactions	Dof	SS	MS	F-value	P-value	Significant (Y/N)
Rake angle (A)	1	0.064	0.064	10.17	0.003	Y
Cutting speed (B)	1	0.004	0.004	0.66	0.42	N
Uncut chip thickness (C)	1	0.006	0.006	1.03	0.316	N
AB	1	0.025	0.025	3.98	0.052	N
AC	1	0.061	0.061	9.57	0.003	Y
BC	1	0.010	0.010	1.64	0.207	N
ABC	1	0.039	0.039	6.18	0.016	Y
Error	48	0.304	0.006			
Total	55	0.543				

4.3.4 Plastic strain distribution

Fig. 82 presents the images taken by the high speed camera in the orthogonal cutting tests. These images were then applied in the DIC analysis. The image taken before the tool-workpiece contact was used as the reference, as no load was applied into the workpiece. When the tool advanced into the workpiece, the segmentation of the chip was formed. The images taken in this stage were compared with the reference one to get the displacement and strain distribution.

Fig. 82b shows the zone of interest (ZOI) of the workpiece which was in the dashed orange frame used to get the strain in the first deformation zone. It should be noted that an undetectable zone in the chip formation root (near the tool cutting edge) could not be analyzed due to the severe material deformation. The path which goes through the middle of the uncut chip layer was chosen to export the strain distribution. Then, the maximum equivalent strain on this curve is used to represent the strain in the deformation zone of this image. As the image related with the cutting time, analyzing the images sequentially could give the history of plastic strain in the first deformation zone.

After the tool passed through the workpiece, the residual strain beneath the surface of the workpiece was also investigated. The ZOI presented in Fig. 82c was used to calculate the residual strain. Due to the highest plastic deformation and the appearance of lateral burrs on the machined workpiece, in particular for the negative rake angle (-6°) and the large cutting edge

radius (30 µm), the DIC could not calculate the strains for a thin layer near the surface. The maximum thickness of this layer is evaluated to be about 1.6 µm.

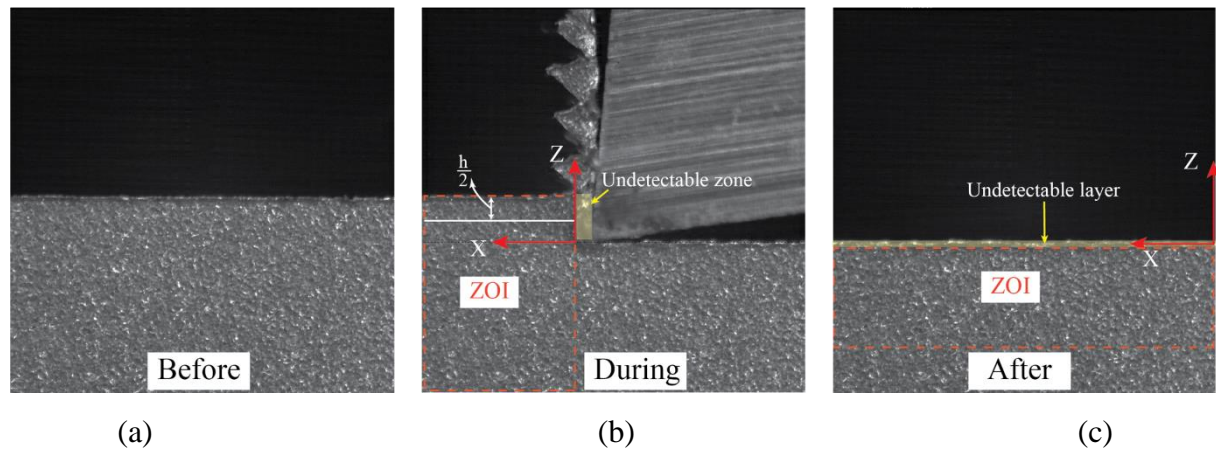(a)   (b)   (c)

Fig. 82: Images taken in the orthogonal cutting tests: (a) before; (b) during; (c) after the contact between the tool and the workpiece.

The history of the equivalent plastic strain in the first deformation zone was presented in Fig. 83. It shows that the strain varies in a cyclic way because of the cyclic nature of the chip formation.
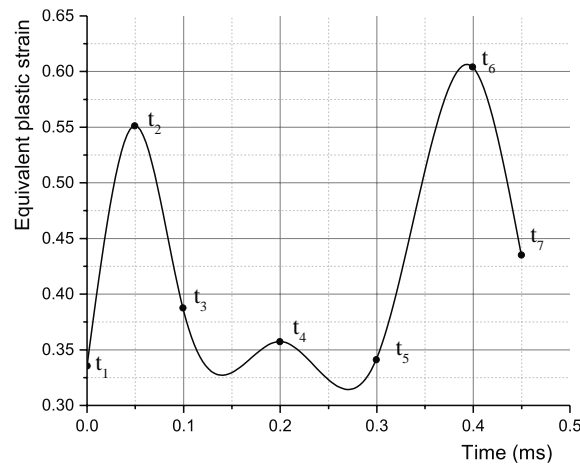
Fig. 83: History of the equivalent plastic strain in the first deformation zone ($\gamma = -6°$, $V_c = 20$ m/min, $h = 0.15$ mm, $r_n = 16$ µm).

Then, the residual equivalent plastic strains were calculated beneath the machined surface for several cutting conditions. Fig. 84a shows an example of the equivalent plastic strain distributions obtained by DIC analysis. The residual equivalent plastic strains in function of the depth from the machined surface (z-direction) for different cutting conditions are presented in Fig. 84b. It is observed that the thickness of the hardened layer after the machining process was about 10 µm.

<div align="center">(a)   (b)</div>

Fig. 84: (a) Distribution of residual equivalent plastic strain (γ = -6°, V_c = 20 m/min, h = 0.2 mm, r_n = 30 µm); (b) Profiles of residual equivalent plastic strain for different conditions.
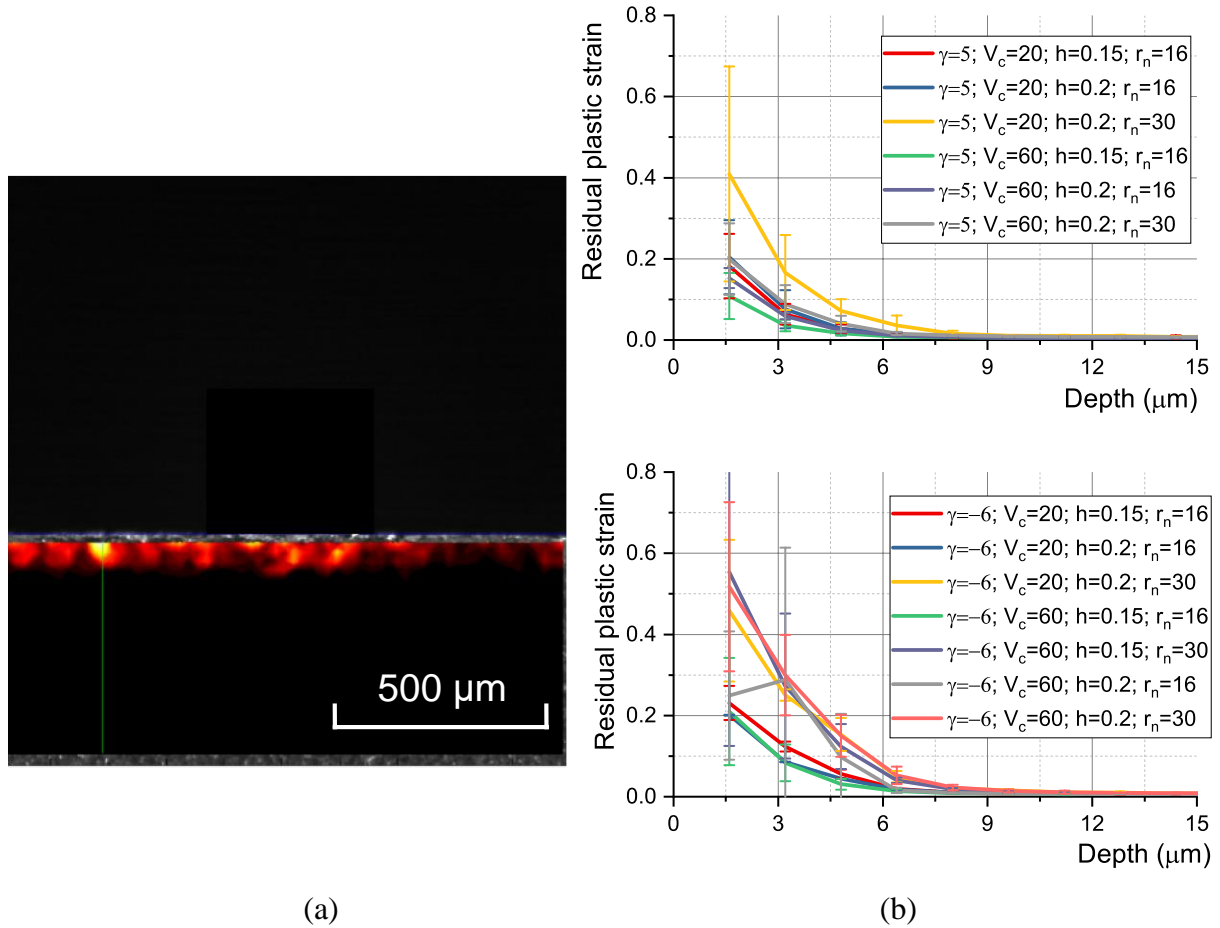
4.3.5 Surface integrity

To study the effects of the cutting conditions on surface integrity, seven cutting conditions were selected, as shown in Table 16. Surface integrity was evaluated based on the microstructure observation (plasticly deformed layer thickness) and X-ray diffraction analysis (residual stresses and peak breadth width).

4.3.5.1 Microstructure

Concerning the microstructure analysis, the central portion of the machined specimens which was close to the machined surface was extracted, and then mounted in the resin and polished. Additionally, a chemical attack with Kroll chemical solution (100 ml water, 1 - 3 ml hydrofluoric and 2 - 6 ml nitric acid) was used to reveal the microstructure. Finally, the specimens were observed under the optical microscope OM-Olympus Vanox-T AH-2. The thin plastic deformed layer was investigated, and the corresponding thickness was measured for the 7 cutting conditions. The microstructures of the machined subsurface for two conditions were

shown in Fig. 85. Table 20 summarizes the thicknesses of the plasticly deformed layers which vary from 3.6 µm to 9.6 µm. Identical results were obtained using the residual equivalent plastic strain curves obtained from DIC.

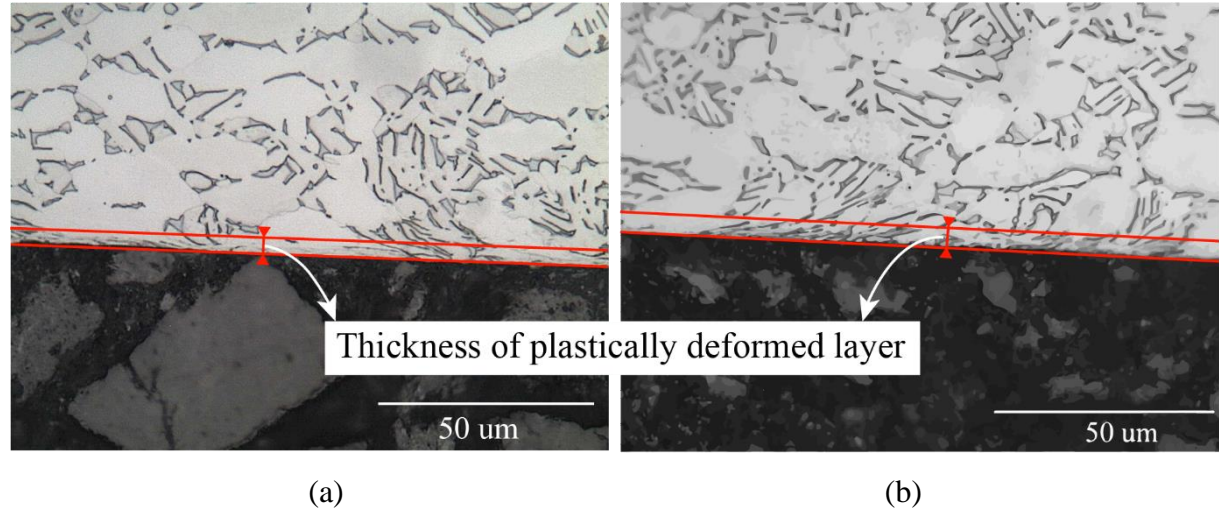(a)   (b)

Fig. 85: Microstructure of the machined subsurface: (a) $\gamma 5V_c 60h150r_n 16$, (b) $\gamma 5V_c 60h150r_n 30$.

Table 20: Deformed layer thickness.

Rake angle, γ (°)	Cutting speed, V_c (m/min)	Uncut chip thickness, h (mm)	Edge radius, r_n (µm)	Thickness of deformed layer (µm)
5	60	0,2	16	9,6
5	20	0,2	16	6,6
5	60	0,15	16	3,6
5	20	0,15	16	3,7
5	60	0,15	30	4,2
-6	60	0,15	16	5,0
-6	60	0,15	30	6,4

4.3.5.2 Residual stress and FWHM peak analysis

The profiles of residual stresses were measured using the X-ray diffraction technique in the longitudinal and transversal directions with a Seifert XRD 3000 PTS equipment. Measurements were made with the diffraction of copper K-α radiation from the {213} cyrstallograhpic plane of the Ti-6Al-4V alloy. Diffractograms were recorded for 29 tilt angles ψ varying between – 45° and +45°. Fig. 86 shows the position of residual stress measurements in the machined specimen. Measurements were performed in the center of the machined surface. The irradiation zone had a length, L = 4-6 mm and width, W = 2 mm. The penetration depth of the X-Ray radiation was about 5 µm. To measure the residual stress beneath the surface, the layers were successively removed by electrolytic polishing method with a Presi Polisec C20 equipment.

To calculate the residual stress, the classical $\sin^2\psi$ method was used [122]. The X-Ray Elasticity Constants (XEC) ½ S_2 and S_1 providing the proportionality between measured strains and calculated stresses have been calculated owing to an elastic self-consistent model: ½ $S_2 = 11.68\times10^{-6}$ MPa^{-1}, $S_1 = -2.83\times10^{-6}$ MPa^{-1}. Meanwhile, the Full Width at Half Maximum (FWHM) [122] of the X-ray diffraction peak is investigated, which is the peak breadth width at 50% of the intensity maximum. This parameter can be used to determine experimentally the thickness of the work hardened or plastically deformed layer induced by machining.
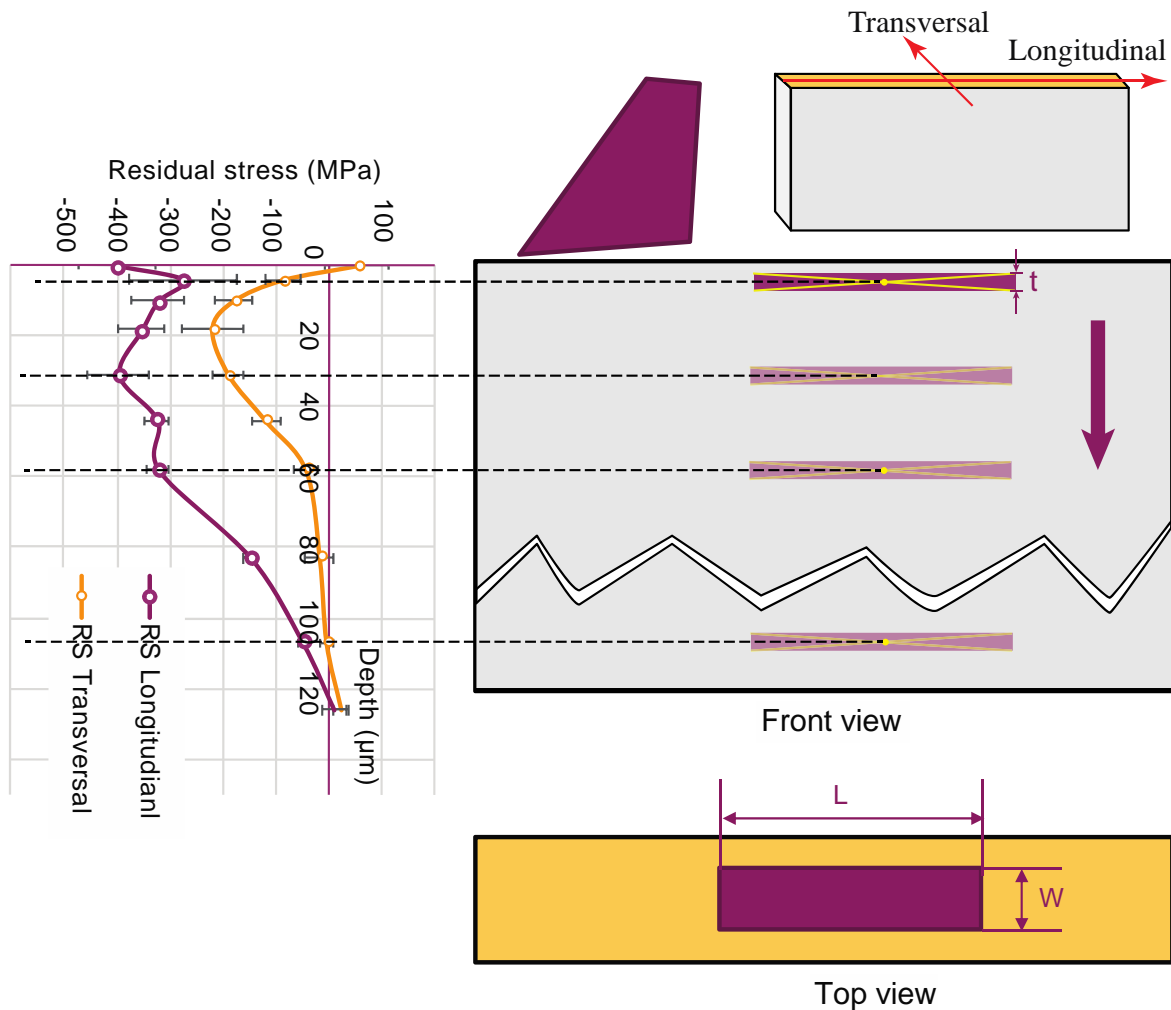
Fig. 86: Position of residual stress analysis in the machined specimen.

Fig. 87 illustrates the typical in-depth residual stress profiles in both longitudinal and transversal directions after machining Ti-6Al-4V alloy. The residual stresses at surface are high compressive in longitudinal direction and low compressive or tensile in the transverse direction. The level of residual stresses in both directions changes continuously with depth down to a certain maximum value below the surface for most of the cutting conditions, and then gradually decreases stabilizing at the level corresponding to that found in the work material before

118

machining. The actual depth at which the circumferential residual stresses reach the zero stress value can be thought of as the thickness of the layer affected by residual stresses due to machining. Several parameters are used to characterize the in-depth residual stress profile (Fig. 87): *SRS* is the residual stress at the machined surface; *MRS* is maximum residual stress in compression beneath the surface and *Depth_MRS* is the corresponding depth where these maximum stresses are located; *Layer_RS* is the thickness of the layer affected by residual stresses due to machining. In the next section, both simulated and experimental in-depth residual stress profiles are compared.
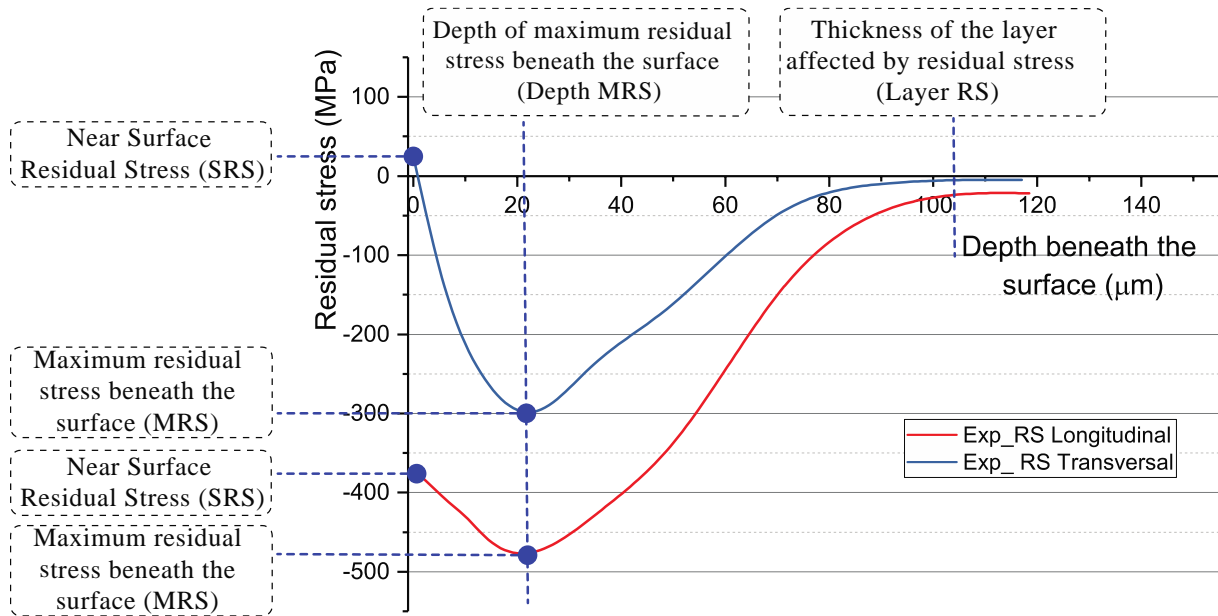
Fig. 87: Typical in-depth residual stresses profile.

4.4 Comparison between measure and predicted results

The same cutting conditions selected for the experimental surface integrity analysis (see Table 16) are used in the orthogonal cutting simulations. Then, the predicted and measured results are compared, as described in the next sections.

4.4.1 Comparison between predicted and measured forces, chip geometry and CCR

Fig. 88 shows an example of the comparison between predicted and measured forces, chip geometry and *CCR* for $\gamma = 5°$, $r_n = 16$ µm, $V_c = 20$ m/min and $h = 0.15$ mm. Fig. 88a presents the von-Mises stress distribution in the workpiece and chip. This figure shows a chip segmentation characteristic of machining Ti-based alloys. The predicted shape of the chip

segments is very close to those observed experimentally (also shown in Fig. 88a). Moreover, Fig. 88a shows a maximum stress value in the FDZ, that can reach about 1700 MPa. This maximum stress and the size of the region of high stresses in the workpiece ahead of the cutting tool vary cyclically during the cutting process. This is due to the cyclic nature of the chip formation process, which is characteristic to machining Ti-based alloys.

The equivalent plastic strain distribution in the workpiece and the chip is given in Fig. 88b. As can be seen in this figure, the plastic strain is localized in narrow bands in the chip (refereed in the literature as shear bands), also characteristic of machining Ti-based alloys. In addition, the comparison between experimental and simulated results concerning to chip geometry and chip compression ratio is also presented. The values of peak, valley and pitch obtained in the experiments are close to the simulated ones, which is also the case for the *CCR* value.

The simulated cutting forces and thrust forces are shown in the Fig. 88c. The cutting force is well predicted compared with the experimental data, while there is a noticeable difference between the experimental and simulated thrust force. There are two main reasons for this difference. One is the position of the tool in the y axis direction in the orthogonal cutting model, which is a bit far away from the top surface of the workpiece. The contact between the tool and the workpiece would be reduced. However, if the tool locates just above the top surface of workpiece, the elements in the top surface would be distorted excessively as the tool advances. A better position of the tool in y axis direction needs to be investigated. The other reason is accounting for the contact conditions over the tribological interfaces that are carried out through the relation between the friction coefficient and the sliding speed, which is obtained by an inverse method. To improve the modelling of the contact stress distributions, a better model should be developed considering the results of tribological experiments to be conducted.

Fig. 88d shows the predicted temperatures during the cutting simulation, including the cutting temperature (maximum integral temperature at the tool-chip interface) and the maximum temperature in the FDZ and TDZ. The cutting temperature increases rapidly to 600°C in less than 1 ms before reaching a stable value, while the temperature in FDZ varies almost cyclically around 220°C, putting in evidence the influence of the cyclic nature of chip formation in this temperature. The temperature in the FDZ is not enough to influence the mechanical behavior of the work material. The temperature in the TDZ stays around 300°C.
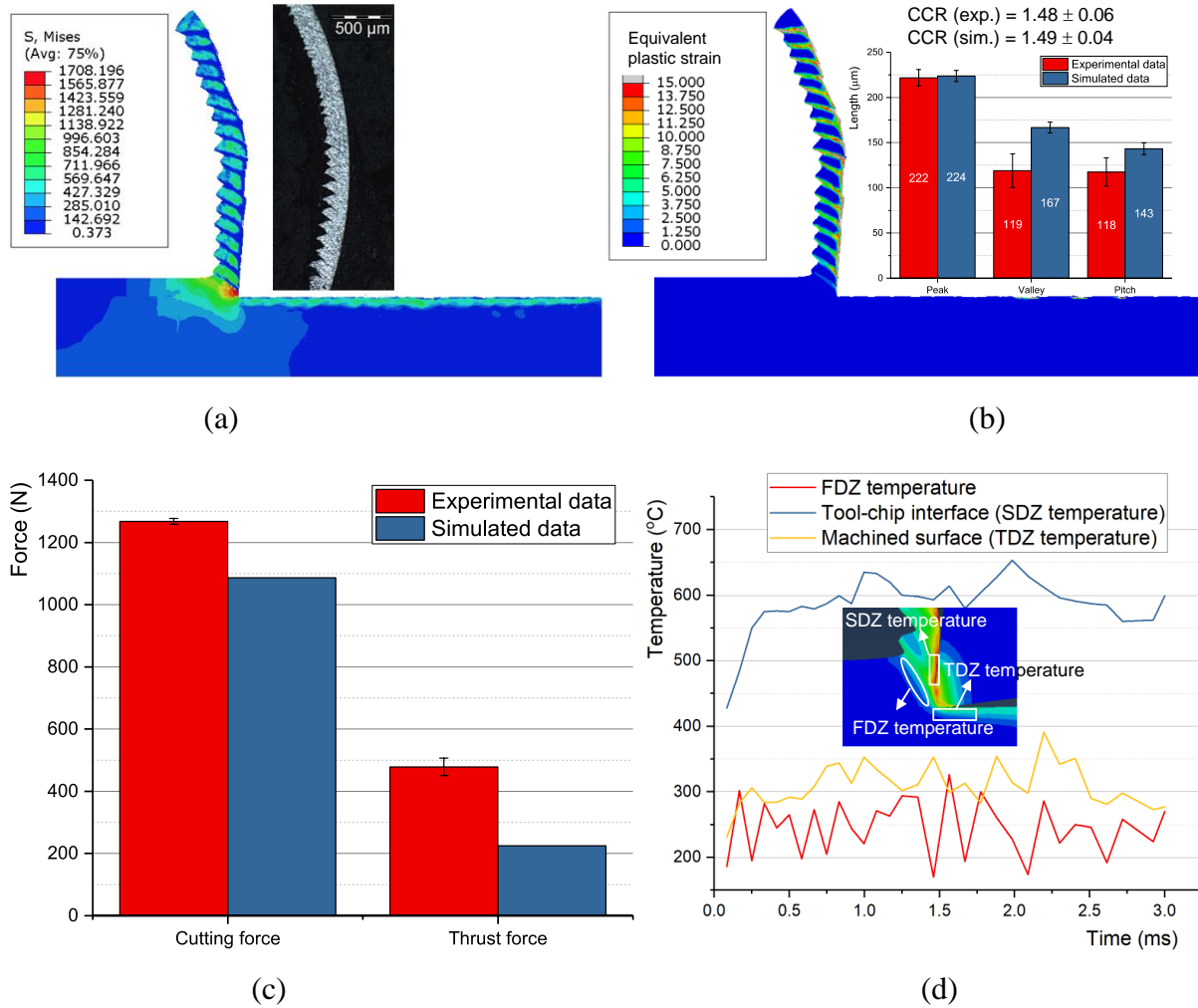
(a)

(b)

(c)

(d)

Fig. 88: Simulated and experimental results of orthogonal cutting ($\gamma = 5°$, $V_c = 20$ m/min, $h = 0.15$ mm, $r_n = 16$ µm): (a) Von-Mises stress distribution, (b) Equivalent plastic strain distribution, (c) experimental and simulated force, (d) History of simulated temperature.

For the other cutting conditions, the simulated results are also compared with the experimental ones, including the chip geometry, cutting and thrust forces. Fig. 89 shows the comparison between experimental and simulated cutting and thrust forces for seven cutting conditions. Like Fig. 88, the cutting force is well predicted where the difference between measured and predicted value is less than 14%, but it isn't the case of the thrust force, where the maximum difference can reach 53%.

As far as the chip geometry is concerned, the peak and pitch parameters are also quite well predicted, but small differences between experimental and simulated values of the chip valley are observed (Fig. 90). Specifically, the average differences for chip peak and pitch are only 7% and 14% respectively, while the average difference for chip valley is 51%. These differences are also found in the other literature for the simulation of the orthogonal cutting of Ti-6Al-4V

alloy [68], [123], [124]. According to Chen et al. [68], it is caused by the micro crack formed between adiabatic shear bands near the chip free surface. On the other hand, Yameogo [123] pointed out that the difference could be explained by the instability of chip segmentation (irregular segmentation) under low cutting speeds and low feeds.
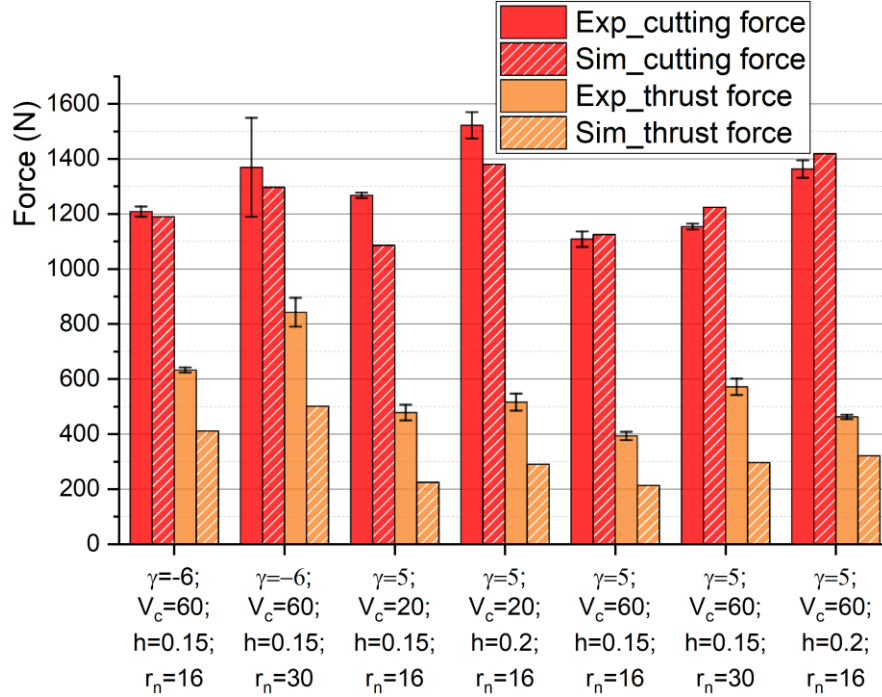

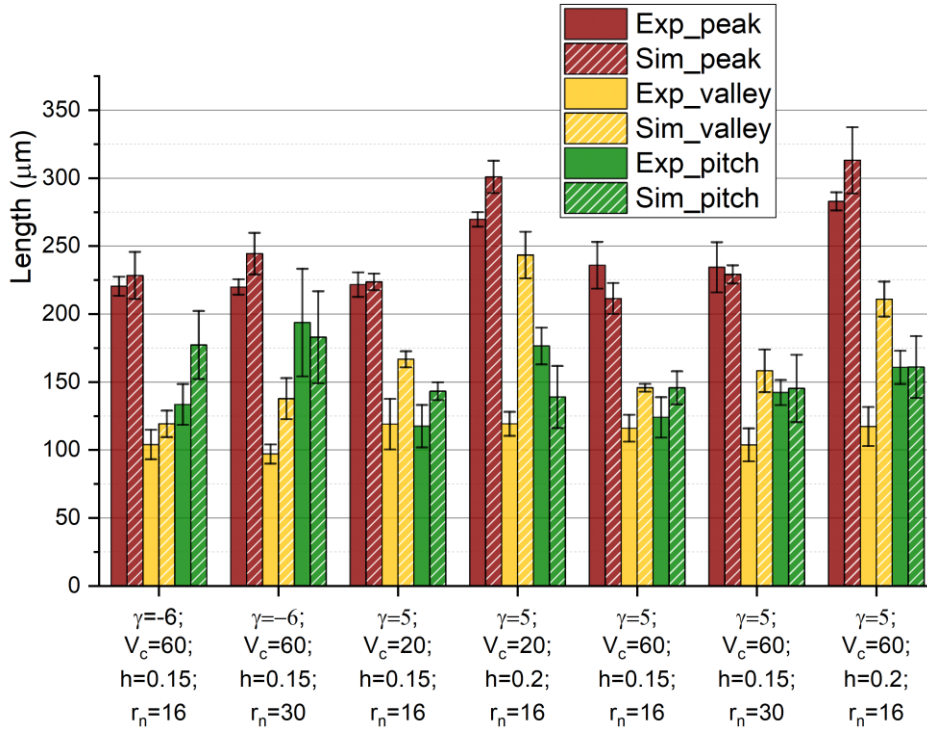Fig. 89: Comparison between the simulated and experimental forces.

Fig. 90: Comparison between simulated and experimental chip geometry.

4.4.2 Comparison between predicted and measured residual stresses and plastically deformed layer

Fig. 91 shows both measured in-depth residual stresses profiles determined experimentally by XRD technique and those stress profiles predicted using the orthogonal cutting model for the seven selected cutting conditions.

Experimentally, for all the cutting conditions the residual stress in the longitudinal direction is more compressive than the stress in the transversal direction. At the machined surface, the residual stress in longitudinal direction is always high compressive for all the cutting conditions, reaching about -600 MPa, whereas in the transversal direction low compressive and low tensile stresses can be found. The level of residual stress in the transversal direction changes continuously with depth down to a certain maximum value below surface, reaching -400 MPa (*MRS*) between 20 and 40 µm below surface (*Depth_MRS*). Then, it gradually decreases stabilizing around zero. This kind of in-depth residual stress profile can also be found in the longitudinal direction, except for the cutting condition indicated Fig. 91a where the MRS is shifted the machined surface. The thickness of the layer affected by residual stresses due to machining (*Layer_RS*) varies from 110 µm to 150 µm depending on the cutting conditions.

Fig. 91 shows some differences between the measured and predicted in-depth residual stresses profiles. The biggest differences are observed for the following two cases:

- Between the measured and predicted longitudinal stresses until about 20 µm below the surface (hereby called near surface residual stresses) for all the seven cutting conditions. In this case, the predicted residual stresses in longitudinal direction are much lower in compression than the measured ones.

- Between the measured and predicted transversal stresses after about 20 µm below the surface for three cutting conditions indicated in Fig. 91a/d/g.
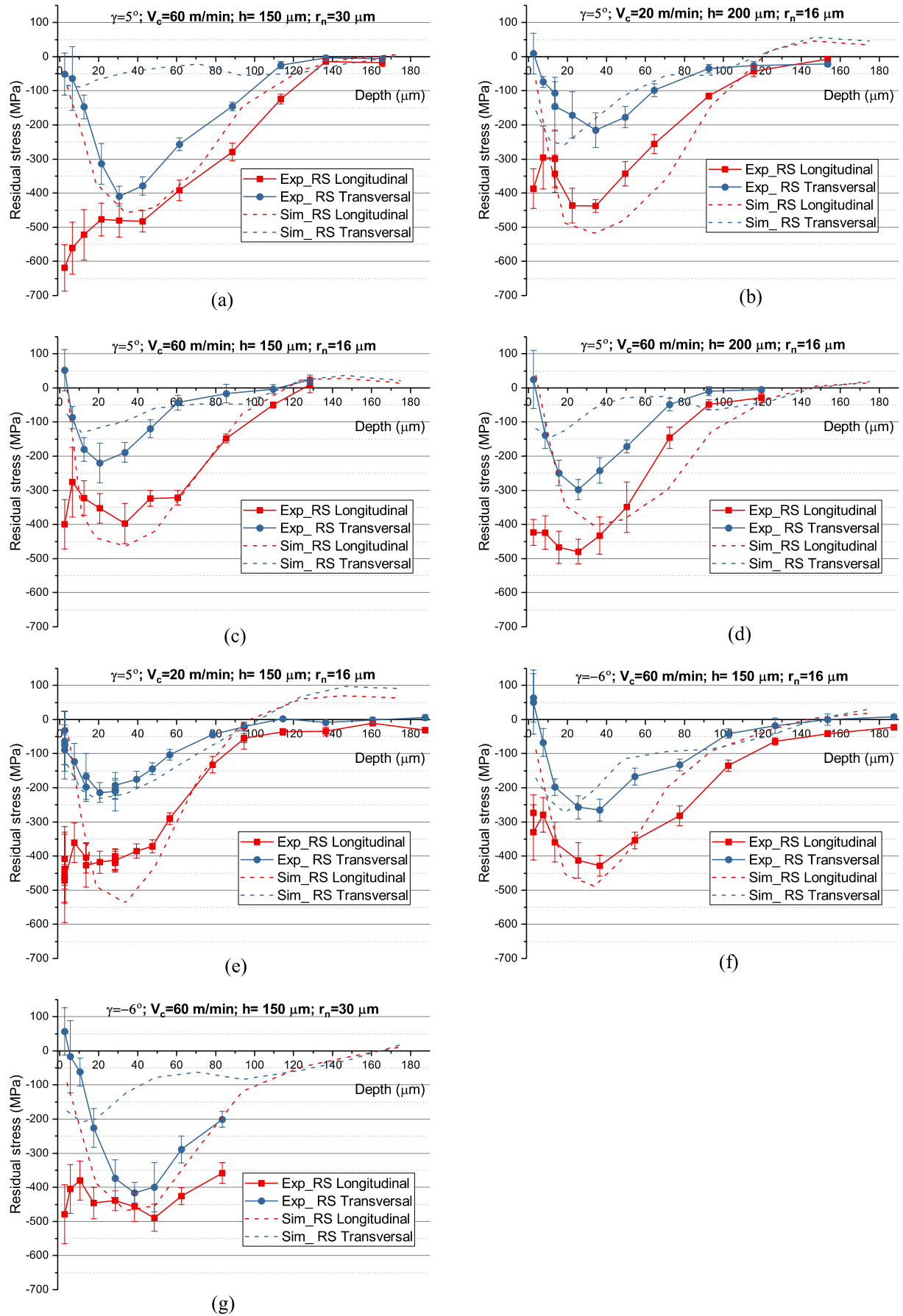
Fig. 91: Comparison between simulated and experimental distribution of residual stress.

Except these two cases, the predicted residual stresses are very close to those measured. In particular:

- The predicted near surface residual stresses in transversal direction are close to the measured ones.

- The predicted longitudinal residual stresses are close to the measured ones for depth higher than about 20 μm below the surface.

- The thickness of the layer affected by residual stresses due to machining (*Layer_RS*) is very well predicted.

- The predicted values of thickness of the plastically deformed layer due to machining are in the same range of the thicknesses determined experimentally.

The simulated and measured residual stresses at machined surface (SRS) for all the conditions are shown in Fig. 92. As mentioned above, the difference between simulated and measured residual stresses in longitudinal direction is very significant. The SRS in transversal direction could not either be predicted correctly, although the difference between simulated and measured residual stresses is inferior when compared to those stresses in the longitudinal direction.

Fig. 93 shows the maximum simulated and measured residual stress in compression beneath the surface (MRS) for all the conditions. The difference between simulated and measured residual stresses in transversal direction can reach about 36% in average, while in the longitudinal direction this difference is only about 17% in average. Therefore, the MRS is reasonable well predicted by the numerical simulation.

Fig. 94 presents the simulated and measured thickness of the layer affected by residual stresses induced by orthogonal cutting (*Layer_RS*). In general, this thickness is quite well predicted by the simulation, where the maximum difference between predicted and measured thicknesses is less than 19%.

Fig. 95 shows the evolution of the *FWHM* of the X-ray diffraction peak in function of the depth beneath the surface. *FWHM* decrease as the depth increases, stabilizing around 1.35°. The depth at which the *FWHM* stabilizes corresponds to the thickness of the plastically deformed layer induced by machining. For these six conditions, the values of thicknesses are ranging from 100 μm to 140 μm, which is highlighted by a grey region in Fig. 95. This thickness is also determined by numerical simulation using the evolution of the equivalent plastic strain in function of the depth beneath the machined surface, as shown in Fig. 96. The depth at which

the equivalent plastic strain reaches zero corresponds to the thickness of the plastically deformed layer induced by machining. As can be seen in Fig. 96, these thicknesses are in the same range of the thicknesses determined experimentally.

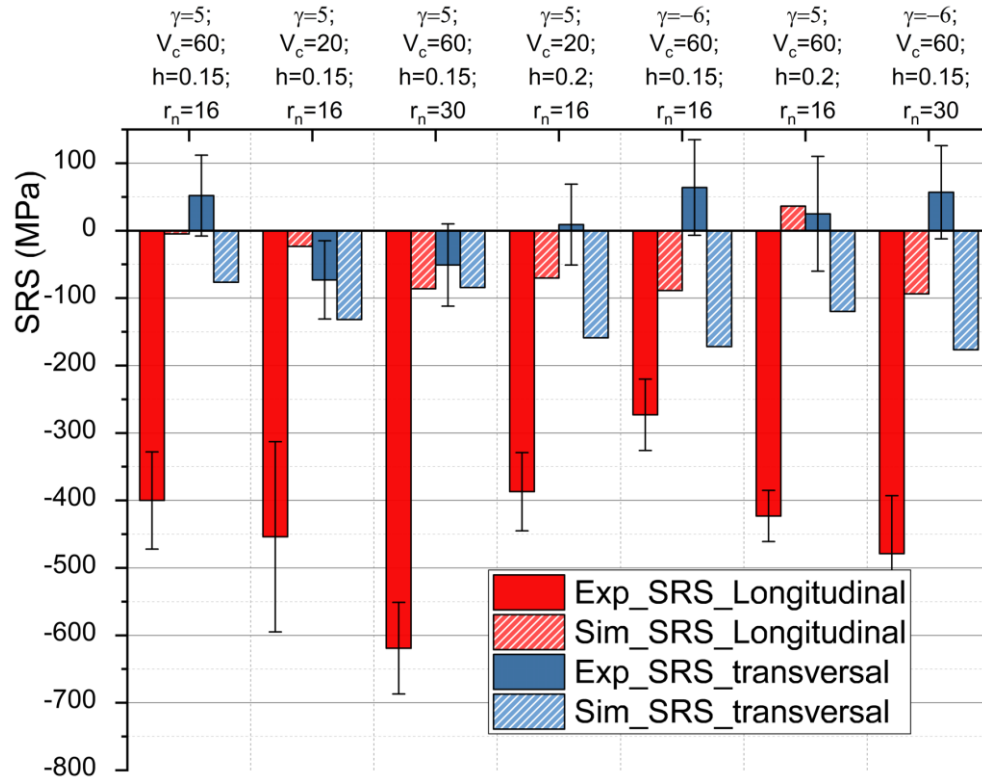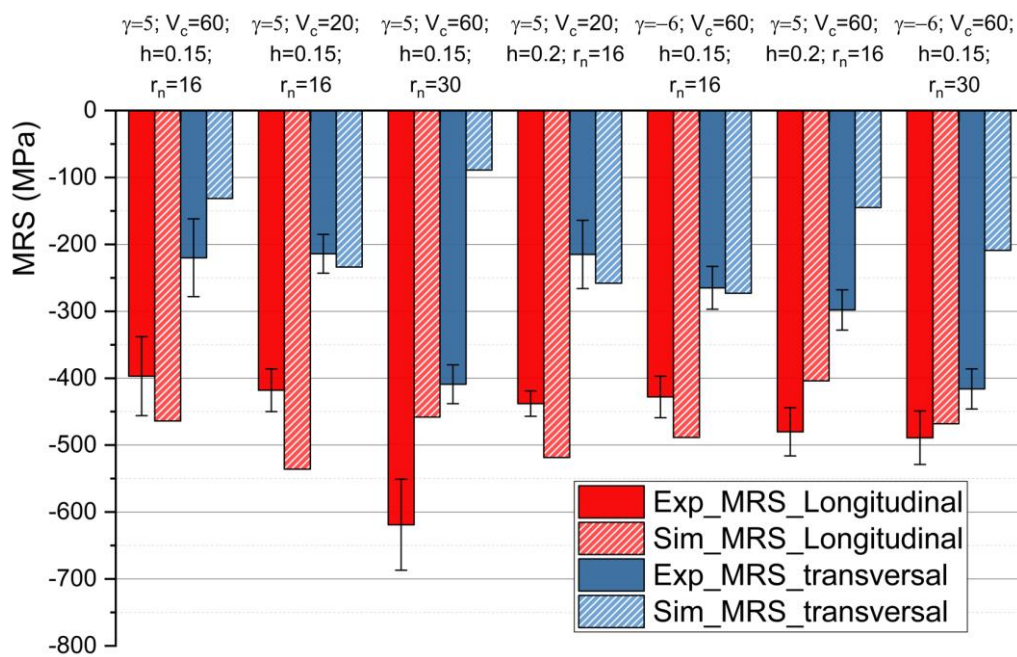Fig. 92: Simulated and measured residual stresses at machined surface (SRS).

Fig. 93: Simulated and measured maximum residual stresses below the machined surface maximum (MRS).
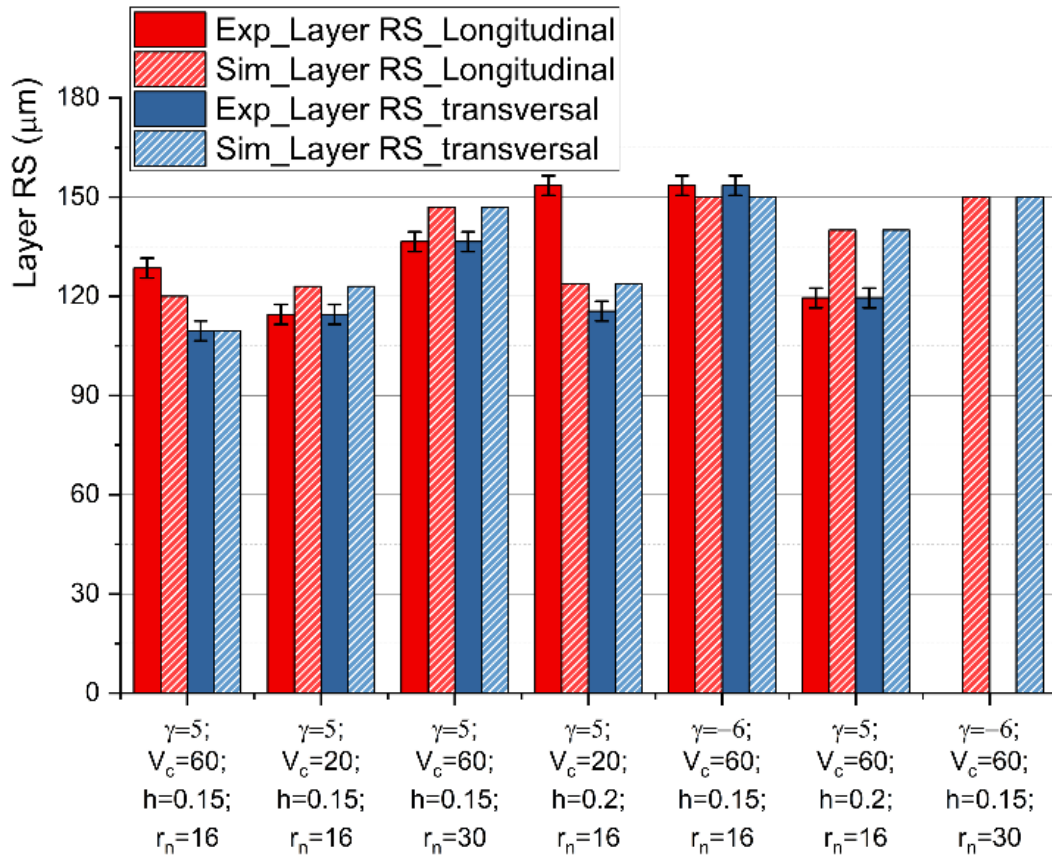
126

Fig. 94: Simulated and measured thickness of the layer affected by residual stresses induced by orthogonal cutting (*Layer_RS*).
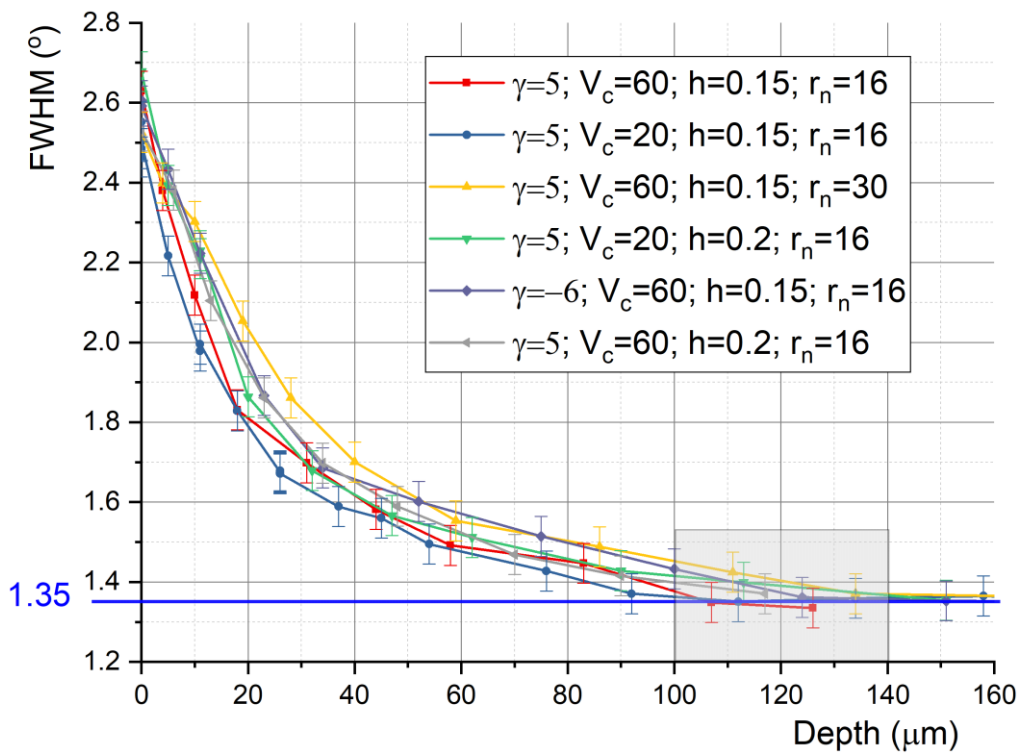

Fig. 95: Evolution of the FWHM of the X-ray diffraction peak in function of the depth beneath the machined surface.
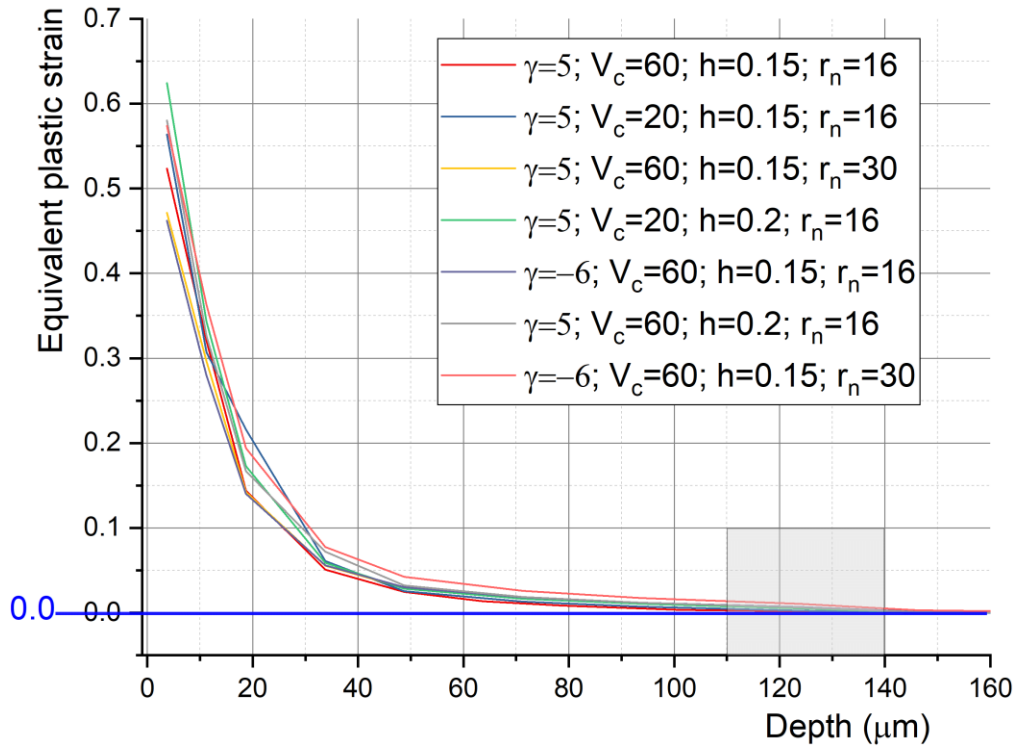
Fig. 96: Evolution of the simulated equivalent plastic strain in function of the depth beneath the machined surface.

The observed differences between the measured and predicted residual stresses profiles can be attributed to the excessive distortion of the elements of the machined surface during the cutting simulation (Model I in Fig. 66). These distorted elements affect the values of the near surface residual stresses in the longitudinal direction during the residual stresses simulation (Model II in Fig. 66). Another reason is the tool-workpiece contact model that may not reproduce the exact contact between the tool and the machined surface. Moreover, the friction coefficients in function of the contact conditions (pressure, sliding speed, temperature, …) need to be determined by tribological tests, for the same tool/workpiece materials pairs used in the machining tests. Finally, although the temperature in the FDZ is around 220°C (see Fig. 88d), thus not affecting the mechanical behavior of the work material in this region, the temperature in the TDZ can reach 300°C according to the simulations. These predicted values of temperature in the TDZ need to be confirmed by accurate temperature measurements, since the excessive distortion of the elements of the machined surface will also affects the temperature prediction in this surface. If these measurements confirm these temperature values, then the temperature effect must also be considered in the constitutive model for the residual stresses simulation.

4.5 Summary of the chapter

In this chapter, a 2D orthogonal cutting model of Ti-6Al-4V alloy including the proposed constitutive model was developed. ABAQUS FEA software was used to perform the numerical simulations using the Lagrangian FEM formulation. The constitutive model was implemented in ABAQUS FEA software through a VUMAT and UMAT subroutines. The orthogonal cutting model is composed by the tool and workpiece, being the former composed by an intermediate layer where the element deletion technique is applied to simulate the physical separation of the layer being removed (in the form of chips) from the rest of workpiece. The contact conditions at the tool-chip and the tool-workpiece interfaces were modelled using the Zorev's model and using the friction coefficient in function of the sliding speed taken from the literature. Coupled thermo-mechanical analyse was performed to predict the most relevant results for this research work, including: cutting and thrust forces, chip geometry, chip compression ratio, temperature distribution in the cutting zone, residual stresses and plastic strain distributions in the machined surface and subsurface.

Orthogonal cutting tests of Ti-6Al-4V alloy were performed and the surface integrity of the machined samples was analysed. A DoE composed by 4 factors (cutting speed, uncut chip thickness, tool rake angle and cutting edge radius) and 2 levels per factor was adopted. ANOVA was performed to determine the most significant factors affecting the results (forces and chip compression ratio), and to investigate the influence of the cutting conditions on these results. Several experimental techniques and equipment were used in these tests, including: i) piezoelectric dynamometer to measure the cutting forces; ii) DIC technique to determine the plastic strain in the FDZ and the residual plastic strain in the machined subsurface; ii) chip geometry and microstructure of the machined surface were investigated by optical microscopy; iv) X-Ray diffraction (XRD) technique to determine the residual stresses.

Finally, experimental results obtained from selected seven cutting conditions were compared with those results obtained from 2D orthogonal cutting simulations. The cutting force is well predicted for all the cutting conditions, while the thrust force is underestimated. The parameters of the chip geometry (peak and pitch) are also well predicted, except the chip valley, where small differences between measured and predicted values are observed. For the residual stress in longitudinal direction, the predicted values are close to the measured ones when the depth is higher than about 20 μm below the surface for all the cutting conditions. In contrast, the measured and predicted transversal stresses after about 20 μm below the surface for three out

of seven cutting conditions (indicated in Fig. 91a/d/g) are not matching, while the SRS in transversal direction is well predicted. Finally, the thicknesses of the layer affected by both residual stresses and plastic deformation due to machining are very well predicted. Orthogonal cutting model must be improved to accurate predict the residual stresses, especially in the near surface.

Chapter 5:

Assessment of machining performance and

surface integrity in turning of Ti-6Al-4V

using the developed constitutive model

5.1 3D model of turning

5.1.1 Model description

A 3D model of turning including the proposed constitutive model was also developed and applied to predict the thermal and mechanical phenomena during cutting (forces and temperatures), and the surface integrity (residual stresses and plastic strain in the machined surface and subsurface). The CAD model of the insert used in the turning model was provided by SECO Tools, and shown in Fig. 97b. Only a small part of the CAD model of the insert was used in the simulations (Fig. 97c), which reduces the computational cost.

(a)   (b)   (c)
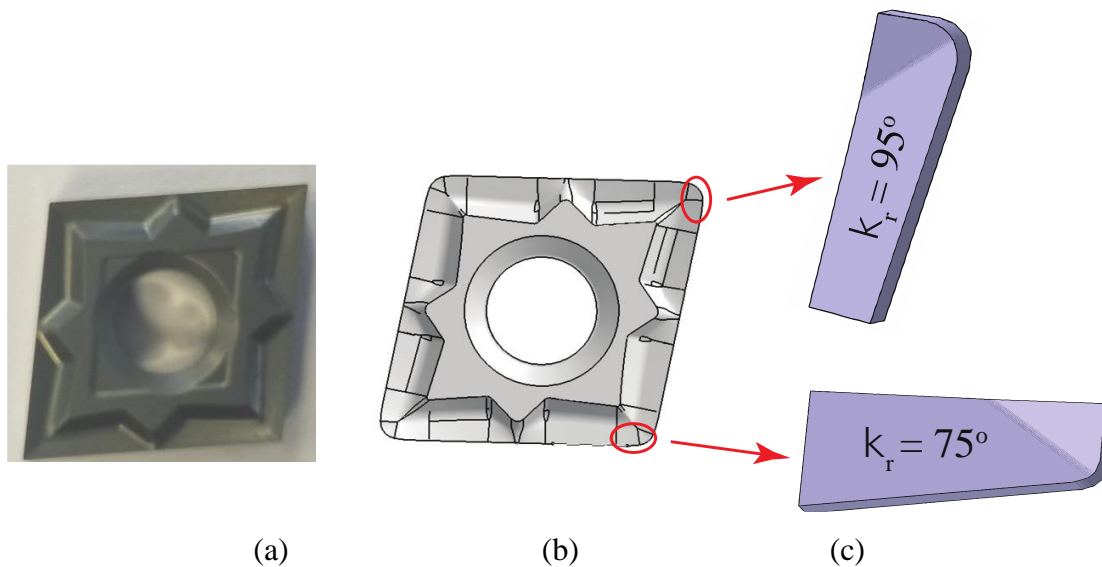
Fig. 97: (a) Insert used in the turning tests; (b) CAD model of insert; (c) CAD model of insert used in the turning model.

In the beginning, a turning model considering an intermediate layer had been used to simulate the chip formation, like the method applied in the 2D orthogonal cutting model. However, using this model the simulation often aborted due to excessive element distortion. The solution found to fix this problem was to remove the intermediate layer from the model, and to apply the element deletion to the uncut chip layer to simulate the chip formation. Therefore, the final turning model is composed by three parts: the uncut chip layer, the workpiece and the tool, as can be seen in Fig. 98a.

(a)

(b)

(c)

(d)
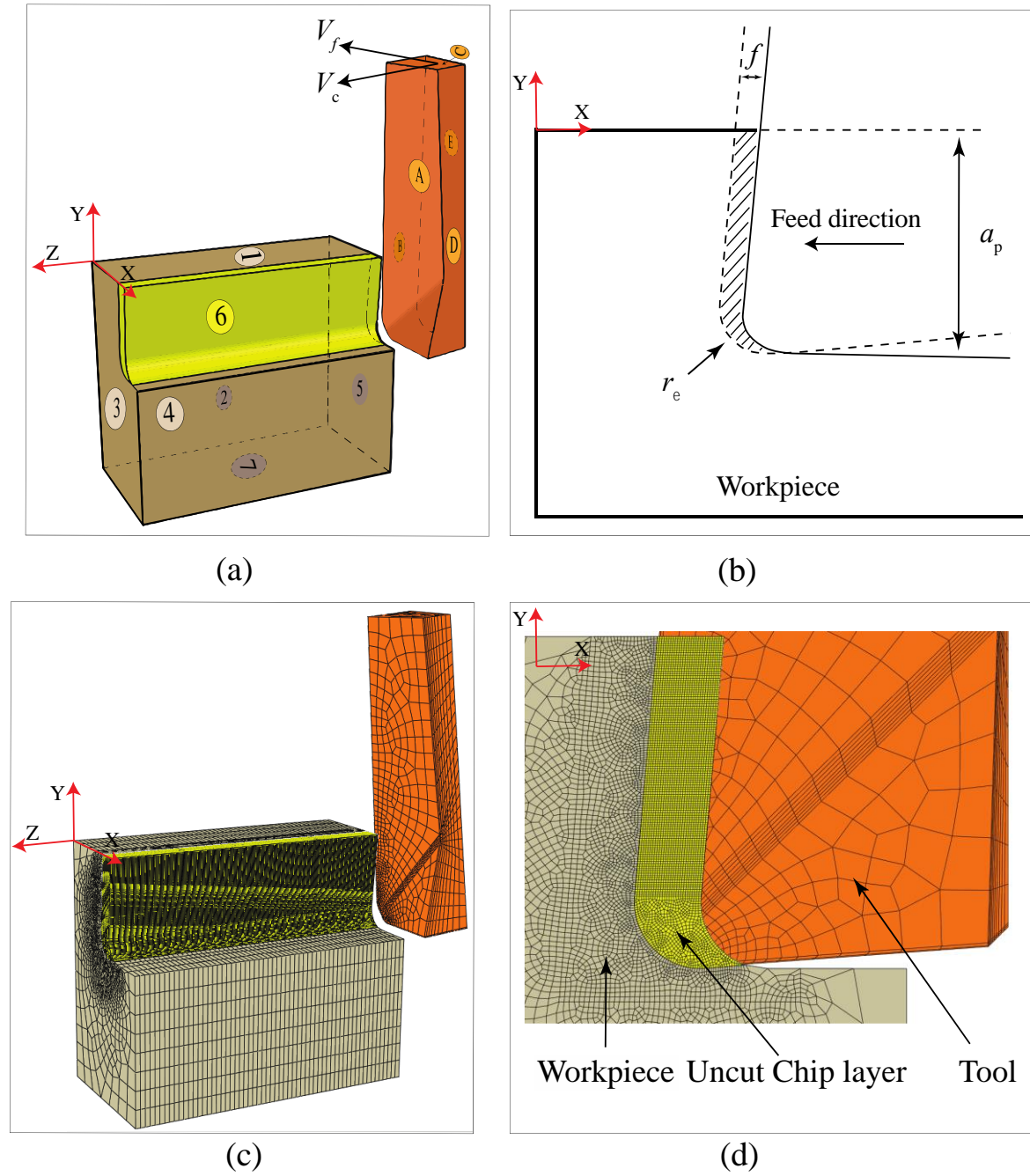
$$\text{Boundary condition}\begin{cases}\text{Displacement}\begin{cases}\text{Constrained X direction: surface 2 \& 4}\\[4pt]\text{Constrained Y direction: surface 7}\\[4pt]\text{Constrained Z direction: surface 3}\end{cases}\\[12pt]\text{Temperature}\quad T_{room}=20\ ^{o}C:\quad\text{surface 2, 7 \& C, D, E}\\[8pt]\text{Heat convection}\quad h_{conv}=23\ W/m^2/^{o}C:\ \text{surface 1, 5, 6 \& A, B}\end{cases}$$

Fig. 98: (a) 3D turning model; (b) cross section of turning model; (c) mesh geometry of the turning model; (d) cross section of mesh geometry.

Fig. 98b illustrates the cross section of the turning model, representing the feed, depth of cut and nose radius (f, a_p and r_ε respectively). Fig. 98c and Fig. 98d show the mesh details of each part of the model. The hexahedral continuum elements C3D8RT with reduced integration are used in the coupled temperature-displacement simulations in ABAQUS/Explicit. The minimum/maximum element size used in each part composing the model is: $7\mu m \times 7\mu m \times 50\mu m$/ $10\mu m \times 10\mu m \times 50\mu m$ for the uncut chip layer, $15\mu m \times 7\mu m \times 50\mu m$/$200\mu m \times 200\mu m \times 50\mu m$ for the workpiece, and $10\mu m \times 10\mu m \times 8\mu m$/$118\mu m \times 145\mu m \times 90\mu m$, for the tool. A mesh refinement in the uncut chip layer and in the workpiece around the machined surface is used in order to accurate calculate the thermomechanical phenomena and the surface integrity generated by turning.

The boundary conditions presented in the bottom of Fig. 98 are applied in the surfaces of the model represented in Fig. 98a. The workpiece is fixed in three directions, X, Y and Z, while the tool is moving at a constant cutting speed, V_c, and cutting feed, V_f. A constant temperature of 20°C was applied to both the tool and the workpiece at the surfaces 2 and 7 for the workpiece, and at surfaces C and D for the tool. Moreover, an initial temperature of 20 °C was also imposed to both the tool and the workpiece. Finally, a heat convection of 23 $W/m^2/°C$ [125] is imposed at surfaces 1, 5 and 6 of the workpiece and A and B of the tool.

The constitutive and contact models used in the orthogonal cutting model were also used in the turning model. The same is valid for the thermal and elastic properties of the Ti-6Al-4V and of the tool.

5.1.2 Residual stress simulation

After the turning process (hereby designed by Model I) is simulated in ABAQUS/Explicit, a model to simulate the residual stress formation (hereby designed by Model II) in the machined surface and subsurface using ABAQUS/Standard (implicit) is developed (Fig. 99). Like the orthogonal cutting model, the initial state of Model II is obtained from the last step of Model I. To reduce the calculation time, only the geometry and material of the workpiece are transferred from Model I to Model II. Therefore, the distributions of temperature, stress and strain in the workpiece are also transferred from Model I to Model II. The constitutive model was implemented in ABAQUS/Standard through a UMAT subroutine. The boundary conditions were similar to the Model I, as shown in Fig. 98b.
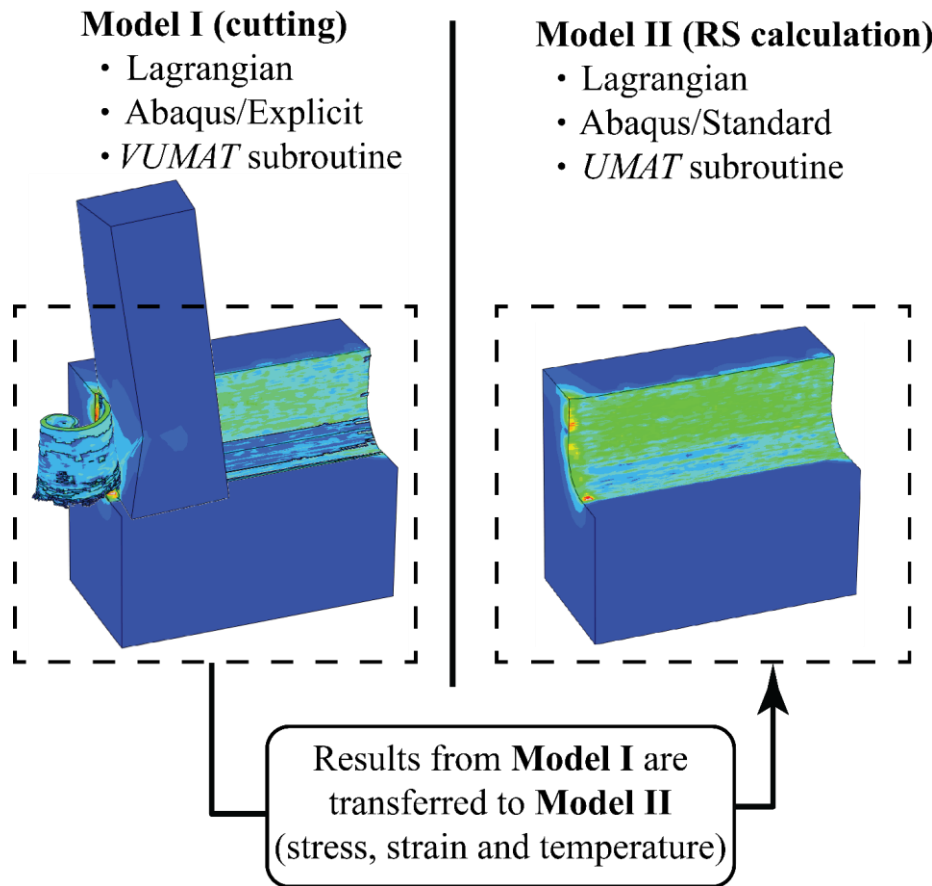
Fig. 99: Procedure of the residual stress analysis.

5.2 Experimental setup and cutting conditions

5.2.1 Tool geometry/material and cutting regime parameters

Uncoated (WC-Co) and coated ((Ti, Al)N+TiN, PVD coating) cemented carbide inserts (references CNGG120402, CNGG120404 and CNGG120408) and tool holders (references DCLNL2525K12 and DCBNL2525M12) used in the turning tests are provided by SECO Tools, as shown in Fig. 100. The tool holders permitted to obtain two cutting edge angles: 75° and 95°. Three different nose radii were used: 2 mm, 4 mm and 8 mm. The edge radii of inserts were measured using Alicona 3D optical microscope machine, and the results are represented in Fig. 101. The variation in the edge radius between the inserts is negligible. Thus, the edge radii for all the uncoated inserts is equal to 6.0 ± 2.0 μm and for all the coated inserts is equal to 9.0 ± 1.2 μm.

Fig. 100: Tool holders and inserts used in turning of Ti-6Al-4V alloy.
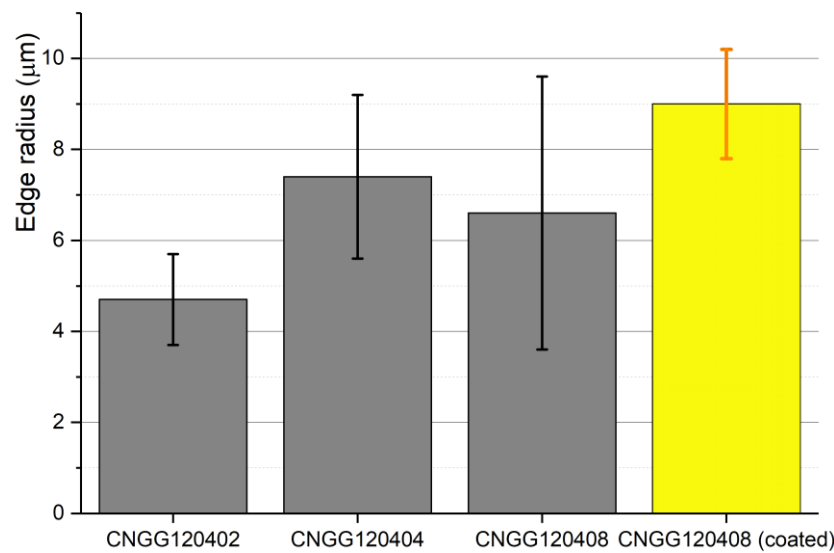
Fig. 101: Measured edge radii of the inserts.

As far as the other parameters of the tool geometry according to the ISO standard 3002-1:1982 [126] is concerned, they were determined based of the information provided by SECO tools. This information includes the CAD model of inserts and tool holders. These CAD models were used to determine the normal rake and clearance angles. A reference plane P_r, a cutting edge plane P_s and a cutting edge normal plane P_n were created according to the standard ISO 3002-1:1982 [126]. Fig. 102 shows an example about how to measure the normal rake and clearance angles in one point of the cutting edge. The normal rake angle γ_n is the angle between the rake face and the reference plane P_r measured in the normal plane P_n, while the normal clearance angle α_n is the angle between the flank face and the cutting edge plane P_s measured in the normal plane P_n. These angles were measured at different positions on the cutting edge. Then, the average and standard deviation were calculated, being equal to $7.3^o \pm 0.5$ and $6.8^o \pm 1.0$ for

the normal rake and normal clearance angles, respectively. Table 12 summed up the whole tool geometry and cutting regime parameters. All the turning tests were performed under dry cutting conditions.
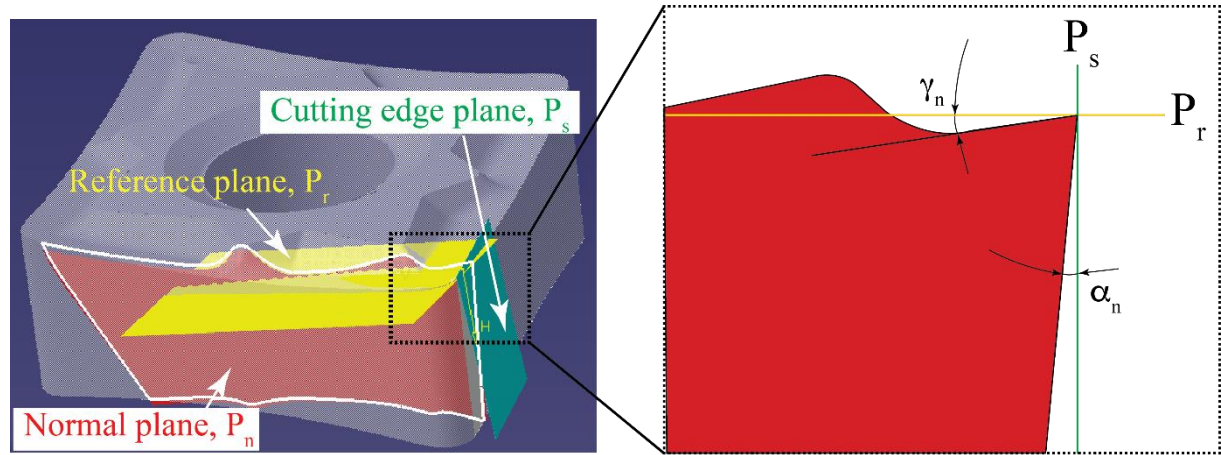
Fig. 102: Determination of the normal rake and clearance angles according to the ISO 3002-1:1982 [126].

Table 21: Cutting regime parameters and tool geometry/material used in turning.

Cutting regime parameters	
Cutting speed, V_c (m/min)	60
Feed, f (mm/rev)	0.1 and 0.2
Depth of cut, a_p (mm)	0.5 and 1
Tool geometry and material	
Tool material	Uncoated: WC-Co Coated: WC-Co/(Ti, Al)N+TiN coating
Cutting edge angle, κ_r (°)	75 and 95
Tool minor cutting edge angle, κ'_r (°)	5°
Inclination angle, λ_s (°)	-6°
Nose radius, r_ε (mm)	0.2, 0.4 and 0.8
Edge radius, r_n (µm)	6.0 ± 2.0 (uncoated) 9.0 ± 1.2 µm (coated)
Normal rake angle, γ_n (°)	7.3 ± 0.5
Normal clearance angle, α_n (°)	6.8 ± 1.0
Cooling conditions	Dry cutting

5.3 Experimental setup

5.3.1 Specimen

Wire EDM is used to obtain four cylindrical specimens on Ti-6Al-4V alloy from the same block used in the mechanical and orthogonal cutting tests. Fig. 103 presents the geometry of the cylindrical specimens used in the turning tests. Except a small workpiece length use for clamping the workpiece in the three-jaw chuck, the remain length of the specimens was divided into 5 tracks of 8 mm length each, referenced from *a* to *e* in Fig. 103. The turning tests were performed from right to left, and each test corresponds to one track. As a result, one cylindrical specimen can include 5 tracks for surface integrity analyse.
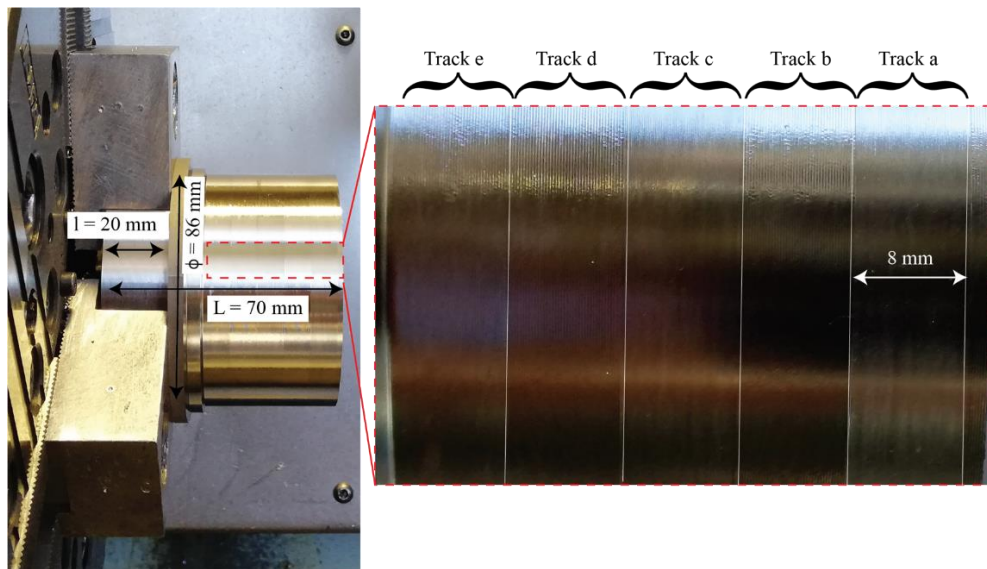
Fig. 103: Geometry of the cylindrical specimens used in the turning tests.

5.3.2 Forces measurement

All the turning tests were conducted using a SOMAB T500 CNC lathe machine (Fig. 104). The cutting force F_c, feed force F_f and penetration force F_p were measured by a piezoelectric dynamometer from Kistler model 9121 combined with a charge amplifier also from Kistler model 5019. The tool holder was mounted on the dynamometer. The electrical signals were transmitted to the multi-channel charge amplifier through the connecting cable, then to a data acquisition card installed in a PC with Dasylab software. The forces gain in the amplifier were set as 100 N/V and the acquisition frequency was equal to 20 KHz. Each test was performed using a new cutting edge to eliminate a possible tool wear effect.

Fig. 105 shows a typical evolution of the cutting force in function of the time obtained during a turning test. Identical evolutions were obtained for the feed and penetration forces. Each cutting condition was performed 3 times to calculate the average and the standard deviation values. They were calculated in the region where the forces signals were stable.

Fig. 104: CNC lathe machine from SOMAB model T500.
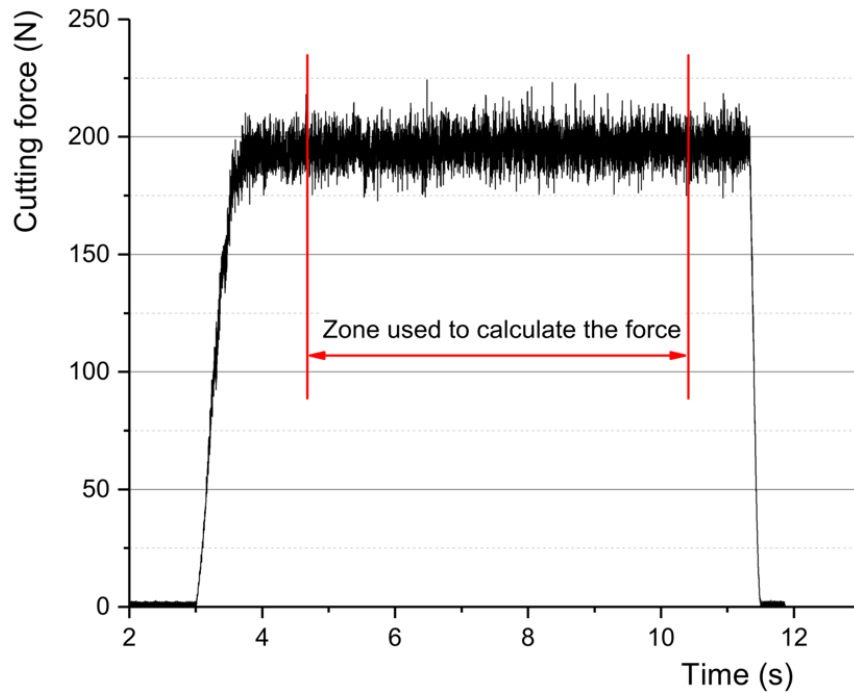
Fig. 105: Typical evolution of the cutting force in function of the time in a turning test. Cutting condition: $\kappa_r = 95^o$, $r_\varepsilon = 0.8$ mm, $V_c = 60$ m/min, $f = 0.2$ mm, $a_p = 0.5$ mm.

5.3.3 Chip geometry measurement

After each turning test, the chip was collected for further metallographic analysis. Fig. 106a shows an example of a portion of a collected chip. Before the chip was inserted into the resin,

a relatively straight part was extracted from the chip and then fixed vertically with a metallic spring (Fig. 106b). After polishing, the chip geometry (peak, valley and pitch) was measured using the optical microscope, as shown Fig. 106c. Five measurements were done for each chip, followed by the calculation of the values of the average and standard deviation.

(a)   (b)

(c)
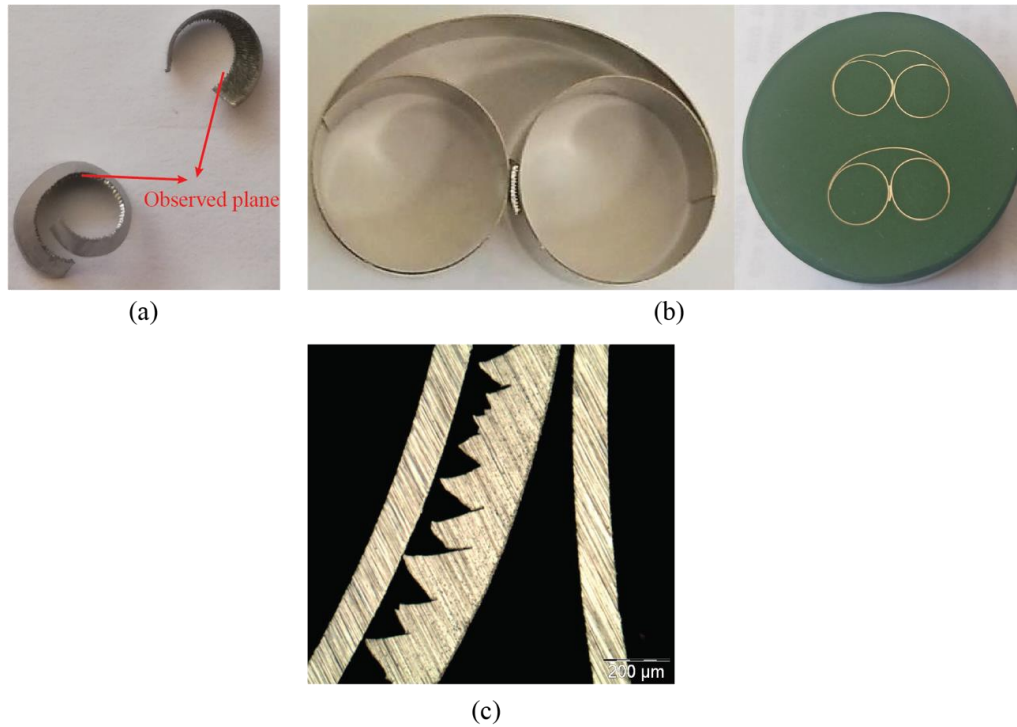
Fig. 106: Chip geometry measurement: a) collected chips after turning tests; b) chips inserted into the resin; c) chip geometry.

5.3.4 Residual stresses and work hardening measurements

The in-depth residual stresses profiles were determined by XRD technique [122] using a SEIFERT XRD 3000 PTS equipment. 17 ψ angles varying between -45° and +45° and for three ϕ angles equal to 0°, 45° and 90° were used during the peak acquisition. The other XRD parameters were the same used in the residual stress analysis of the orthogonal cutting specimens. The sin²ψ method was used to calculate the residual stresses in two directions: X-direction (hereby designed by axial direction, i.e. in the direction of the feed motion) and Y-direction (hereby designed by circumferential direction, i.e. in the direction of the primary motion or cutting speed direction). These directions are represented in Fig. 107. To determine the in-depth residual stress profiles, successive layers of material were removed by electropolishing using a Presi Polisec C20 equipment, thus avoiding the reintroduction of additional residual stresses. Further corrections to the data were made for the volume of the material removed.
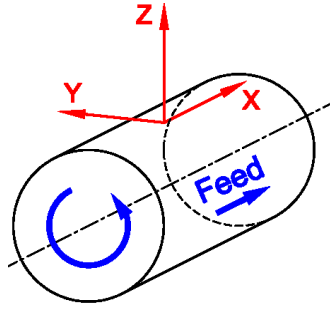
Fig. 107: Direction of the residual stresses measurements in the specimens obtained by turning.

5.4 Comparison between measure and predicted results

5.4.1 Comparison between predicted and measured forces and chip geometry

Table 22 shows eleven cutting conditions used in turning simulations by varying the cutting edge angle, nose radius, feed and depth of cut. One additional cutting condition not presented in this table (coated insert, $\kappa_r = 75°$, $r_\varepsilon = 0.8$ mm, $V_c = 60$ m/min, $f = 0.2$ mm/rev, $a_p = 0.5$ mm) was considered to investigate the mixed influence of the tool coating (TiN coating) and cutting edge radius.

Table 22: Cutting conditions for the turning simulations using uncoated inserts.

Cutting edge angle, κ_r (^{o})	Nose radius, r_ε (mm)	Cutting speed, V_c (m/min)	Feed, f (mm/rev)	Depth of cut, a_p (mm)
95	0.2	60	0.2	1
75	0.2	60	0.1	1
75	0.4	60	0.2	1
95	0.4	60	0.1	1
75	0.2	60	0.2	0.5
75	0.8	60	0.2	0.5
75	0.2	60	0.1	0.5
75	0.8	60	0.1	0.5
95	0.8	60	0.2	0.5
95	0.2	60	0.1	0.5
95	0.2	60	0.2	0.5

Fig. 108 shows an example of the comparison between the measured and predicted results for the cutting condition: uncoated insert, $\kappa_r = 95°$, $r_\varepsilon = 0.4$ mm, $V_c = 60$ m/min, $f = 0.1$ mm/rev and $a_p = 1$ mm. Fig. 108a presents the von-Mises stress distribution in the cutting zone. The largest value of stress locates at the FDZ reaching about 2000 MPa. This figure also shows both measured and predicted chip geometry. Although chip curl is predicted, there are no chip

segmentations in the simulation, and the predicted chip thickness is almost as half as the experimental one. The reason is that the element deletion technique used in the uncut chip layer of the workpiece leads to the reduction of the chip thickness.

Fig. 108b and Fig. 108d show the predicted temperature distribution zones in turning of Ti-6Al-4V alloy and the temperature in function of the time for the three deformation zones, respectively. The cutting temperature (maximum integral temperature at the tool-chip interface) increases rapidly, reaching about 700°C, while the temperature in the FDZ and the TDZ reach about 200°C. The predicted temperatures in the FDZ and TDZ are not high enough to influence the mechanical behavior of the work material.

(a)   (b)

(c)   (d)
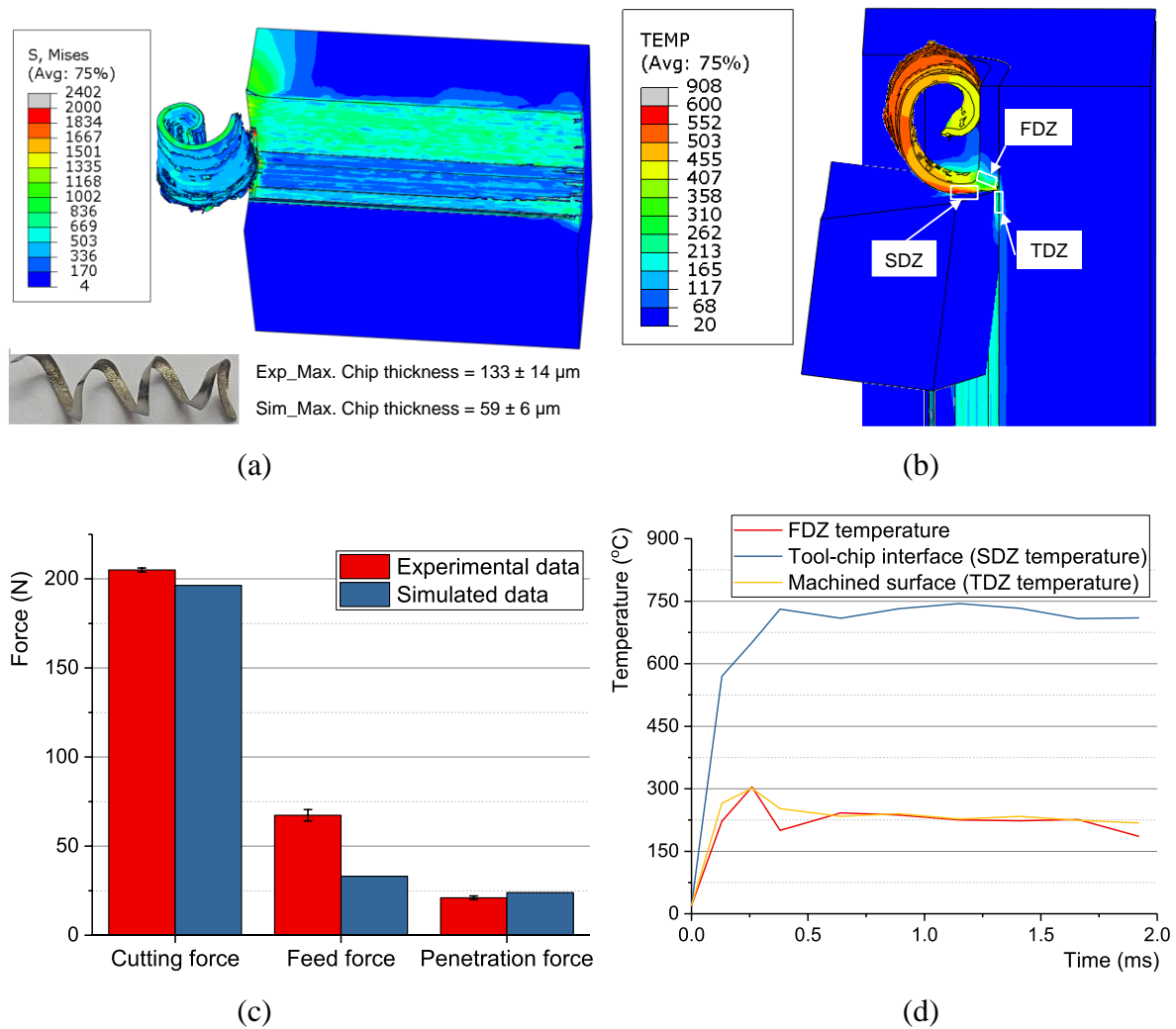
Fig. 108: Predicted and measured results in turning of Ti-6Al-4V (κ_r=95°, r_ε = 0.4 mm, V_c = 60 m/min, f = 0.1 mm/rev and a_p =1 mm): (a) distribution of the Von-Mises stress in the deformation zone and measured chip geometry; (b) temperature distribution in the deformation zone; (c) forces, (d) temperature in the three deformation zones in function of the time.

141

The simulated cutting, feed and penetration forces are presented in Fig. 108c. The cutting and penetration forces are well predicted when compared with the experimental ones, while a non-negligible difference exist between the experimental and simulated feed force. The lower predicted feed force is often observed in the numerical simulation of metal cutting. For example, Imbrogno [127] also found lower predicted feed force when compared to the measured feed force in the simulation of turning of Ti-6Al-4V alloy using the remeshing technique to form the chip. More investigations need to be performed to find an explanation for this difference.

The simulated results are also compared with the experimental ones for the other cutting conditions used in turning. Fig. 109 shows the comparison between experimental and simulated forces for all the cutting conditions. Except for few conditions, the cutting and penetration forces are well predicted for all the cutting conditions. However, this is not the case of the feed force, where the difference can reach 60%. As far as the thickness chip is concerned, the turning model is underestimating it about 50% for all the cutting conditions due to the application of the element deletion to the uncut chip layer.
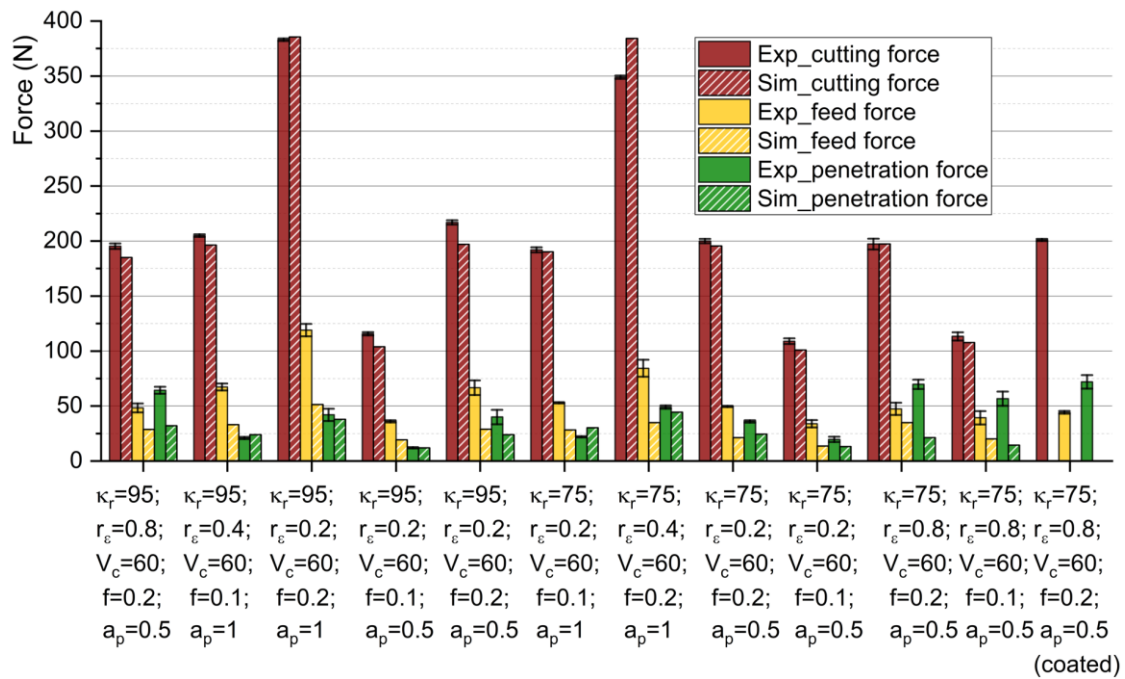

Fig. 109: Comparison between the simulated and experimental forces in turning tests.

5.4.2 Comparison between predicted and measured residual stresses and plastically deformed layer

Fig. 110 shows both simulated and the measured in-depth residual stresses profiles for three cutting conditions.

142

Experimentally, the residual stress at the machined surface in the circumferential direction is higher compressive (reaching about -600 MPa) than the residual stress in axial direction (reaching about -300 MPa). The level of residual stress in the axial direction changes continuously with depth down to a maximum value ranging from 315 to 480 MPa below surface (*MRS*), located between 5 and 10 μm below it (*depth_MRS*). Then, it gradually decreases stabilizing around zero. In contrast, *MRS* in circumferential direction is located at the machined surface, and then the stress decreases continuously with depth down until stabilizes around zero. The thickness of the layer affected by residual stresses due to machining (*Layer_RS*) varies from 50 μm to 100 μm depending on the cutting conditions. As far as the in-depth residual stress profiles are concerned, the predicted residual stresses in both directions are near the same of those measured for the cutting condition shown in Fig. 110a ($\kappa_{r=}75^{o}$, $r_\varepsilon = 0.2$ mm, $V_c = 60$ m/min, $f = 0.1$ mm/rev and $a_p =0.5$ mm). When the nose radius increases, the difference between predicted and measured in-depth residual stresses profiles slightly increases, as shown in Fig. 110d. Whereas, this difference becomes significant when the feed increases, as shown in Fig. 110b. Then, the difference is reduced when both nose radius and feed increase, as shown in in Fig. 110c. That is, the difference can reach about 460 MPa when only the feed increases from 0.1 to 0.2 m/rev (Fig. 110b). and 100 MPa when also the nose radius increases from 0.2 mm to 0.8 mm (Fig. 110c).

The simulated and measured residual stresses at machined surface (SRS) for four conditions are shown in Fig. 111. The difference between simulated and measured residual stresses in axial direction can reach about 38% in average, while in the circumferential direction this difference is only about 10% in average. This figure also shows that the residual stress in the circumferential direction generated by the coated inserts is higher in compression (23% more compressive) than those stress generated by the uncoated insert for the same cutting condition. However, both coated and uncoated inserts generate the same axial residual stress. As stated by Rech and Moisan [128], the use of coated tools (TiN coating) results in less tensile residual stresses in finish hard turning of case-hardened steels due to the better tribological behavior (less friction and therefore less heat generation).

The residual stress induced by turning Ti-6Al-4V alloy were also predicted by other researchers. Özel and Ulutan [129] found a better residual stress prediction in the circumferential direction when compared to the radial direction. In their study, the remesh technique with the modified J-C constitutive model considering thermal softening effects [130] were used in the 3D turning

model. Additionally, Holmberg et al. [131] applied Particle Finite Element (PFEM) technique and *J-C* constitutive model in the turning simulation of Ti-6Al-4V alloy. They found a big difference between the simulated and experimental residual stresses, and they claimed that these differences are due to the constitutive and contact models. Concerning with the observed differences between the measured and predicted residual stresses in axial direction in Fig. 110b, it can also be attributed to the contact and constitutive model as discussed in the 2D orthogonal cutting.
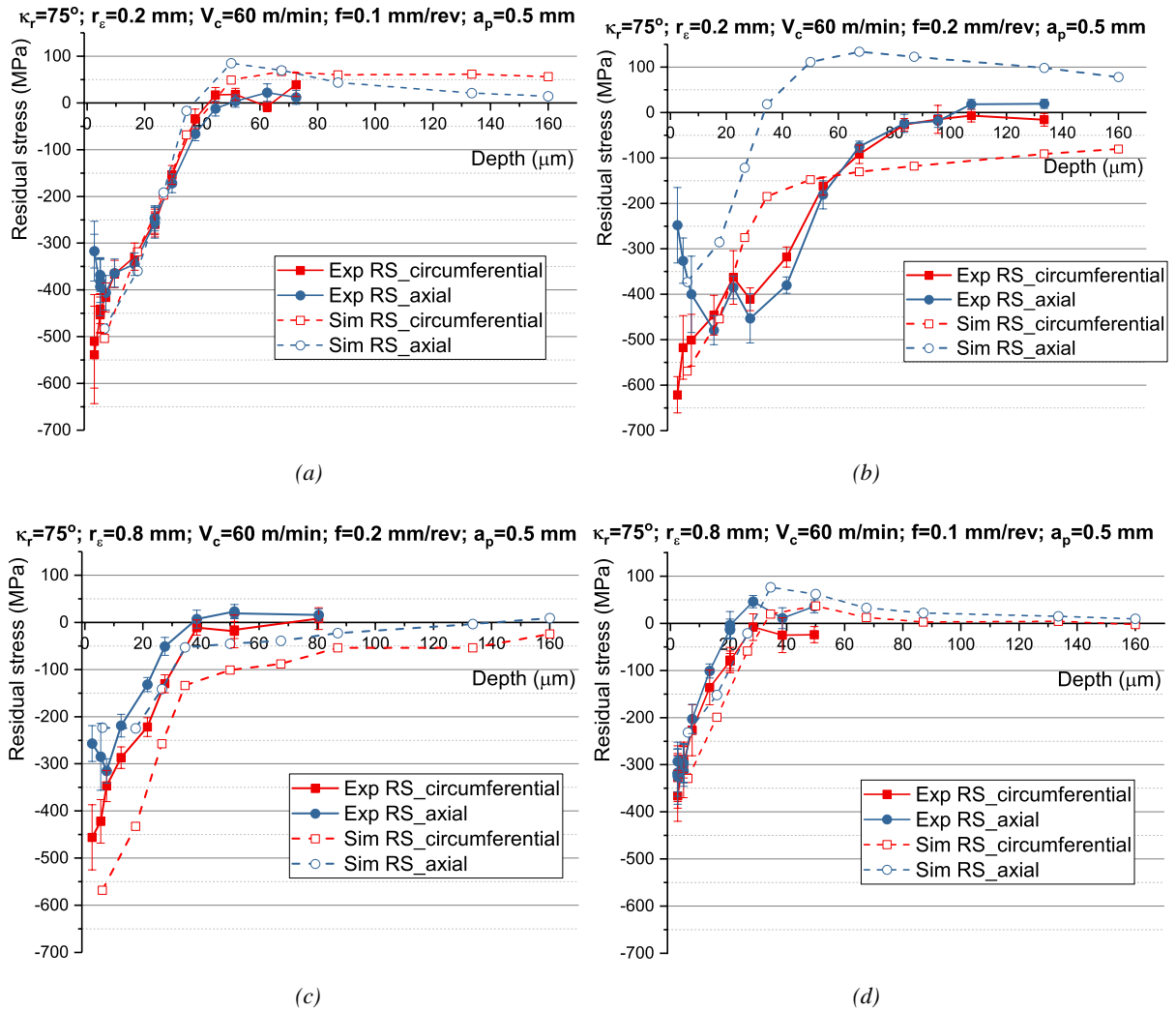
Fig. 110: Simulated and measured in-depth residual stresses profiles.

Fig. 112 presents the simulated and measured thickness of the layer affected by residual stresses induced by turning (*Layer_RS*). In general, this thickness is quite well predicted by the simulation, where the maximum difference between predicted and measured thicknesses do not exceed 29%.
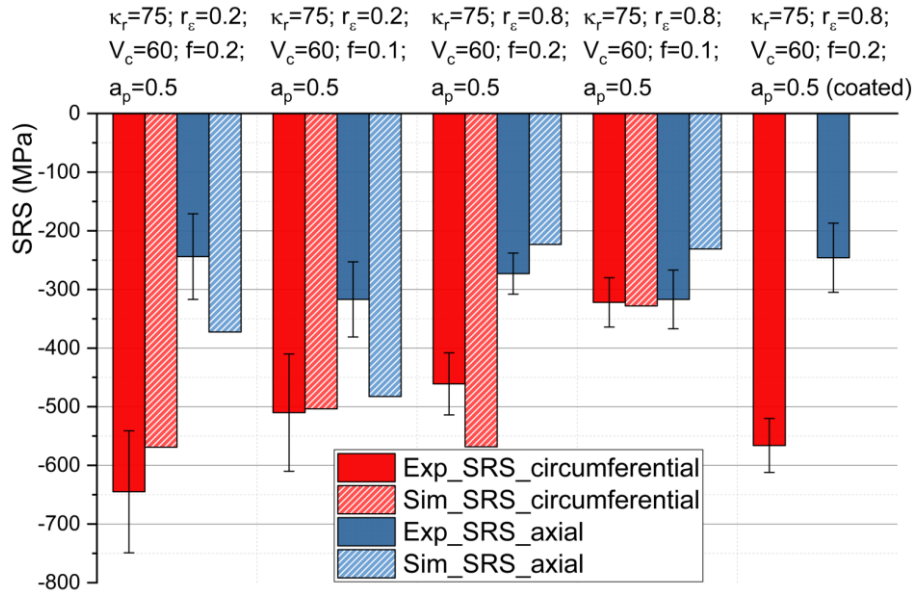
Fig. 111: Simulated and measured residual stresses at machined surface (SRS).
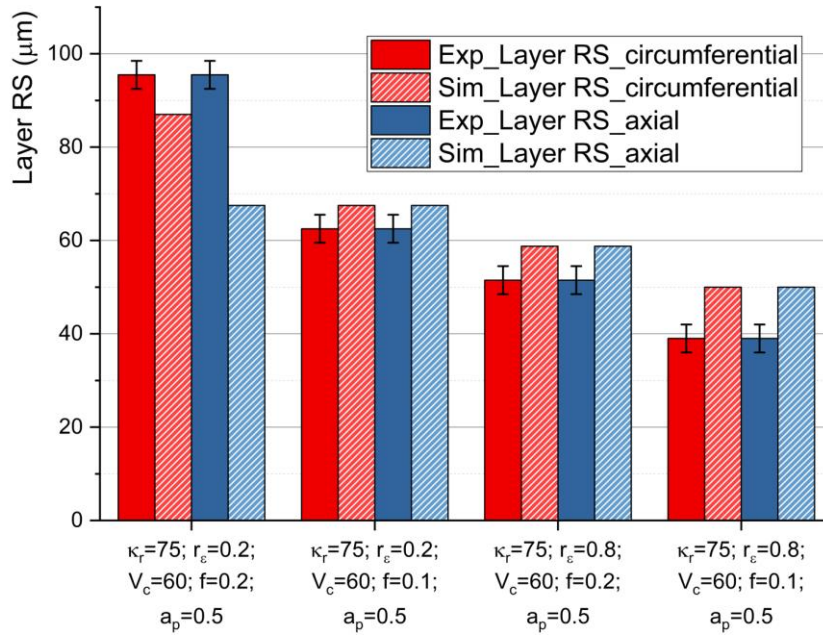
Fig. 112: Simulated and measured thickness of the layer affected by residual stresses induced by turning (*Layer_RS*).

As mentioned in residual stress analysis of orthogonal cutting test, the thickness of the plastically deformed layer induced by machining can be determined experimentally and by simulation using the evolution of the FWHM (Fig. 113) and of the equivalent plastic strain (Fig. 114) in function of the depth beneath the machined surface, respectively. Fig. 113 shows that *FWHM* decrease as the depth increases, stabilizing around 1.5°, which corresponds to the thickness plastically deformed layer. In Fig. 114, this thickness is represented by the depth at which the equivalent plastic strain reaches zero. Fig. 115 compares the measured and predicted

thicknesses of the plastically deformed layer obtained experimentally and by simulation. For the four conditions indicated in this figure, the difference between them is less than 32%.
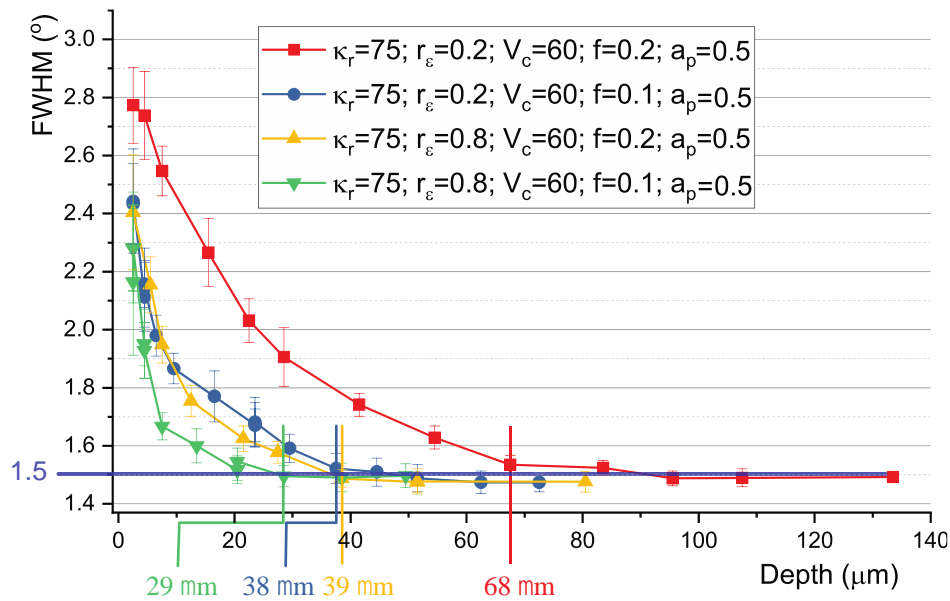
Fig. 113: Evolution of the FWHM of the X-ray diffraction peak in function of the depth beneath the machined surface.
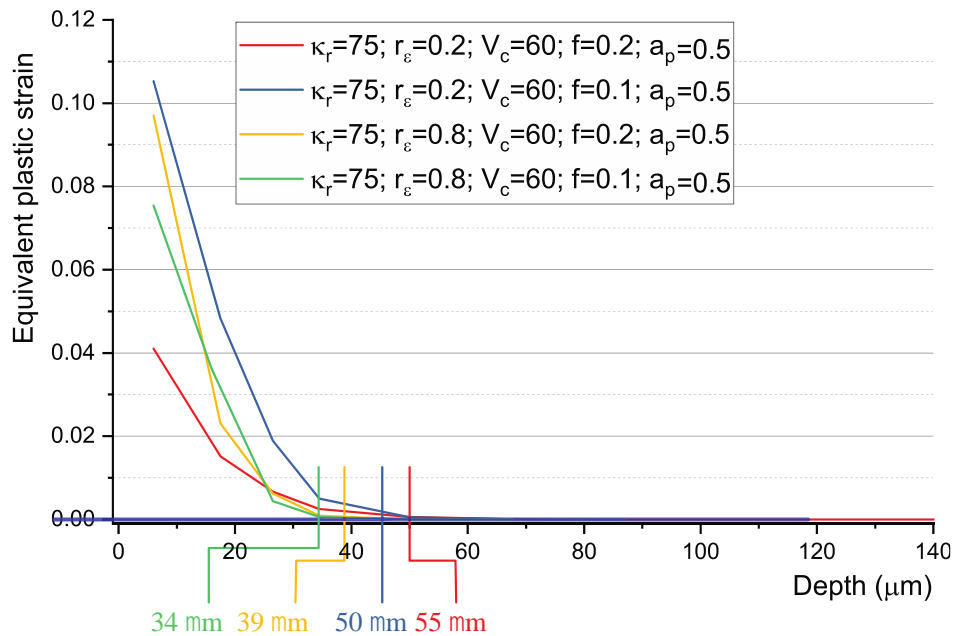
Fig. 114: Evolution of the simulated equivalent plastic deformation in function of the depth beneath the machined surface.
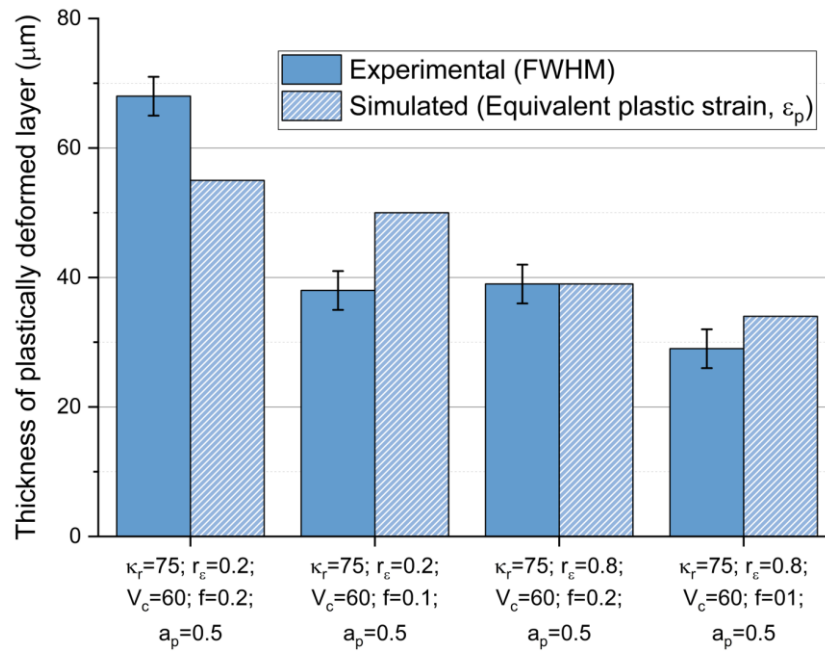
Fig. 115: Comparison between the thickness of the work hardened layer estimated using the FWHM of the X-ray diffraction peak and the simulated thickness of the plastically deformed layer.

5.5 Summary of the chapter

In this chapter, a 3D turning model of Ti-6Al-4V alloy including the proposed constitutive model was developed in ABAQUS FEA software using the Lagrangian FEM formulation. The constitutive model was implemented through a *VUMAT* and *UMAT* subroutines. The element deletion was applied to the uncut chip layer to simulate the chip formation. The tool-chip/workpiece contact model is the same used in the orthogonal cutting model. A coupled thermo-mechanical analyse was performed to predict the most relevant results for this research work, including: forces, chip thickness, temperature distribution in the cutting zone, residual stresses in the machined surface and subsurface, and thickness of the plastic deformed layer.

A comparison between simulated and measured results have shown that the cutting and penetration forces are well predicted. Nevertheless, the simulated feed force is lower than the measured. The simulated chip thickness was largely underestimated due to the deletion of the elements of the chip layer. Besides a significant difference between the measured and predicted axial residual stresses for one cutting condition (shown in Fig. 110b), the in-depth residual stresses profiles are relatively well predicted for the other three conditions. The difference between measured and predicted thickness of the plastically deformed layer induced by machining is small.

General conclusions and recommendations for future work

6.1 General conclusions

The aim of this thesis is to propose a constitutive model of Ti-6Al-4V and apply it to the metal cutting simulation of this alloy. Since metal cutting is the purposeful fracture of the layer being removed to form the chip, occurring due to the continuous change of the state of stress in the first deformation zone (FDZ), this constitutive model should include both material plasticity and damage behaviors. A literature review about constitutive models and deformation mechanisms of Ti-6Al-4V permitted to identify the relevant parameters affecting the mechanical behavior of this alloy in the FDZ: strain hardening, strain-rate and the state of stress. Therefore, a constitutive model including these parameters was formulated, based on existing models available in the literature.

To determine the constitutive model coefficients, mechanical tests are performed using a specially designed experimental setup (including tailored specimen geometries) to generate the wide range of state of stress (i.e. stress triaxiality η and the Lode angle parameter $\bar{\theta}$), found in machining operations. Four types of specimens geometry were used in the mechanical tests: the cylindrical specimens, round bars, double notched specimens and notched flat plates. The state Simulations of the mechanical tests were performed to determine the specific specimens geometry and the corresponding values of the states of stress. Then, the mechanical tests were conducted, and the experimental force-displacements were obtained. During these tests, DIC technique had been successfully applied to obtain the strain distribution on the flat surfaces of double notched specimens and notched flat plates and curved surfaces of round bars.

Based on the data from mechanical tests, an optimization-based procedure was developed to determine the coefficients of the constitutive model. This procedure was implemented in LS-Opt optimization software, connected with ABAQUS/Explicit for the numerical simulations. The comparison between predicted and measured plastic strain distributions in the deformed samples has demonstrated the robustness of the proposed optimization-based procedure to determine the constitutive model coefficients. Furthermore, the simulations of the tensile tests of notched flat plates confirmed that not only the stress triaxiality but also the Lode angle parameter has a significant effect on the plasticity of Ti-6Al-4V titanium alloy.

As far as damage initiation is concerned, the state of stress (η and θ) and the equivalent plastic strain ($\bar{\varepsilon}_i^p$) at damage initiation were determined using both experimental and simulated fracture tests. Then, the asymmetrical fracture surface was obtained by applying a three-dimensional

surface fitting to the obtained points ($\bar{\varepsilon}_i^p$, η, $\bar{\theta}$), using the equivalent plastic strain ($\bar{\varepsilon}_i^p$) function. Concerning the damage evolution, the coefficients were determined by applying the same optimization-based procedure used for determining the coefficients of the plasticity model. To verify the accuracy of the proposed damage model, the experimental (by *DIC*) and simulated plastic strain distributions in the specimens after damage initiation were compared.

The full proposed constitutive model (plasticity and damage) was implemented in ABAQUS FEA software through *VUMAT* and *UMAT* user subroutines. Before performing the machining simulations of Ti-6Al-4V alloy, simulations of mechanical tests considering the proposed constitutive model and the Johnson-Cook model were performed to demonstrate the strong ability of the proposed constitutive model to represent the mechanical behavior of the Ti-6Al-4V alloy under different states of stress. These simulations show the importance of the stress triaxiality and the Lode angle in the improvement of constitutive model accuracy.

An orthogonal cutting (*OC*) model of Ti-6Al-4V including the proposed constitutive model is developed and applied to predict the forces, temperatures, chip geometry, chip compression ratio (*CCR*), and residual stresses distributions in the machined surface and subsurface. Simulation of the cutting process in ABAQUS/Explicit using *VUMAT* subroutine were performed to obtain the forces, temperatures, chip geometry and *CCR*. Then, the temperature, stress and strain distributions in the machined part were transferred to ABAQUS/Standard model using *UMAT* subroutine to simulate the residual stress formation. To determine the accuracy of the *OC* model to predict the above-presented results, orthogonal cutting tests were performed. Different experimental techniques and equipment were used to determine: i) the forces (piezoelectric dynamometer), ii) the plastic strain in *FDZ* and residual plastic strain below the machined surface (*DIC*), iii) the chip geometry, *CCR* and the microstructure of machined surface (optical microscope); and iv) the residual stresses distributions in the machined surface and subsurface and the thicknesses of the affected plastically deformed layer (X-ray diffraction).

A comparison between simulated and experimental results permitted to conclude that: i) cutting force was well predicted while the thrust force was underestimated by the simulation; ii) chip geometry parameters (peak, pitch and valley) were also quite well predicted, except for the chip valley where small differences existed between experimental and simulated values. These results confirm that the constitutive model can successfully predict the mechanical behavior of workpiece in FDZ of orthogonal cutting process. As far as the residual stresses results are

concerned, the thickness of the layer affected by the residual stress and plastic deformation and the location of the maximum residual stress in compression direction beneath the surface were well predicted. However, the difference between measured and predicted in-depth residual stress profiles is noticeable. This difference is may due to the strong element distortion in the top surface of workpiece, material volume loss of the uncut chip thickness due to the element deletion technique, and the incorrect of workpiece-tool flank contact.

Like the orthogonal cutting, turning tests and simulations of Ti-6Al-4V alloy were also conducted to predict/measure the same output parameters. A 3D model of the turning operation including the proposed constitutive model was developed and simulated in ABAQUS/Explicit & ABAQUS/Standard using both *VUMAT* and *UMAT* subroutines. The accuracy of the turning model was evaluated by comparing the simulated and experimental results. Both cutting and penetration forces were well predicted, while the predicted feed force is underestimated when compared to the experimental one. Additionally, the simulated chip thicknesses were much smaller than the measured ones. The main reason for this underestimation of the feed force and chip thickness is the material volume loss of the uncut chip thickness due to the element deletion technique. Finally, besides a significant difference between the measured and predicted axial residual stresses for one cutting condition, the in-depth residual stresses profiles and the thickness of plastically deformed layer are relatively well predicted for the other three conditions. This difference can also be due to the above-mentioned reasons.

6.2 Recommendations for future work

The developed machining models including the proposed constitutive model can provide quite good predictions concerning to the forces and chip geometry. Concerning to the residual stresses, the quality of these predictions changes with the cutting conditions. Therefore, machining models need to be improved for better predicting the residual stresses, and the following recommendations are proposed.

Although the effect of the temperature in the mechanical behavior the work material in the FDZ in metal cutting can be neglected, it may be important for describing correctly the mechanical behavior of the material in the machined surface, where simulated results have shown a maximum temperature around 300°C. Moreover, the accuracy of the residual stresses calculations after machining will be also improved if this effect is included in the constitutive model.

Another important factor influencing the predictability of the machining models is the tool-chip/workpiece contact. Even if the simple Zorev contact model using the friction coefficient in function of the sliding speed (estimated based on tribological tests from literature and machining simulations) was used, a new contact model and tribological tests are required to better represent the contact stresses between the tool and the chip/workpiece in metal cutting.

As far as numerical aspects are concerned, a technique able to represent correctly the physical separation of the material from the workpiece to form the chip needs to be implemented in the metal cutting simulations. The classical element deletion technique cannot represent correctly this separation, compromising the residual stresses predictability in the machined surface and near it (until few microns below this surface). In the beginning of this thesis the XFEM (extended finite element method) technique was considered as a potential candidate to simulate this material separation, as the crack can propagate inside the XFEM elements. In this case, the elements around the crack do not need to be refined and no elements will be deleted. However, a tentative to simulate problems involving large material displacements and contact conditions (including machining simulation) have demonstrated that XFEM technique is not suitable for simulating the material separation in metal cutting. Finally, an alternative method to minimize or even avoid the element distortion associated to the Lagrangian formulation, and simultaneously able to reproduce the physical separation of the material in metal cutting, need to be implemented. Meshless methods can be a good alternative to FEM, although the large computational cost of these methods.

References

[1]   A. Ginting and M. Nouari, "Surface integrity of dry machined titanium alloys," International Journal of Mechanical Sciences, vol. 49, no. 3, pp. 325–332, 2009.

[2]   T. Bell, A. K. Srivastava, and X. Zhang, "Investigations on turning Ti-6Al-4V titanium alloy using super-finished tool edge geometry generated by micro-machining process (MMP)," CIRP Annals Manufacturing Technology, 2011.

[3]   V. P. Astakhov, Metal Cutting Mechanics. CRC Press, 1998.

[4]   Y. M. Abushawashi, "Modeling of metal cutting as purposeful fracture of work material," Thesis, Michigan State University, Michigan, 2013.

[5]   A. G. Atkins, "Modelling metal cutting using modern ductile fracture mechanics: quantitative explanations for some longstanding problems," International Journal of Mechanical Sciences, vol. 45, no. 2, pp. 373–396, Feb. 2003.

[6]   W. CHNEG, J. Outeiro, J.-P. Costes, R. M'Saoubi, F. Auzenat, H. Karaouni, and V. Astakhov, "Machining simulation of titanium alloy Ti6Al4V using a constitutive model considering the state of stress and strain-rate effects," presented at the Proceedings of Machines et Usinage à Grande Vitesse MUGV conference, Bordeaux, 2018, p. 10.

[7]   I. Time, Resistance of metals and wood to cutting. St. Petersbourg, Russia, Dermacow Press House, 1870.

[8]   V. P. Astakhov, Geometry of single-point turning tools and drills: fundamentals and practical applications. Springer Science & Business Media, 2010.

[9]   M. E. Merchant, "Mechanics of the metal cutting process. I. Orthogonal cutting and a type 2 chip," Journal of Applied Physics, vol. 16, no. 5, pp. 267–275, 1945.

[10]   V. Piispanen, "Lastunmuodostumisen Teoriaa (Theory of Chip Formation)," Teknillinen Aikakauslehti, vol. 27, no. 9, pp. 315–322, 1937.

[11]   V. P. Astakhov and S. Shvets, "The assessment of plastic deformation in metal cutting," Journal of Materials Processing Technology, vol. 146, no. 2, pp. 193–202, 2004.

[12]   S. N. Melkote, W. Grzesik, J. Outeiro, J. Rech, V. Schulze, H. Attia, P.-J. Arrazola, R. M'Saoubi, and C. Saldana, "Advances in material and friction data for modelling of metal machining," CIRP Annals - Manufacturing Technology, vol. 66, no. 2, pp. 731–754, 2017.

[13]   A. P. Markopoulos, "Cutting Mechanics and Analytical Modeling," in Finite Element Method in Machining Processes, Springer, 2nd ed., vol. 78, no. 8, pp. 11–27, 2013

[14]   B. Li, X. Wang, Y. Hu, and C. Li, "Analytical prediction of cutting forces in orthogonal cutting using unequal division shear-zone model," Int J Adv Manuf Technol, vol. 54, no. 5, pp. 431–443. 2010.

[15]   V. P. Astakhov, M. O. M. Osman, and M. T. Hayajneh, "Re-evaluation of the basic mechanics of orthogonal metal cutting: velocity diagram, virtual work equation and upper-bound theorem," International Journal of Mechanical Sciences, vol. 41, no. 3, pp. 393–418, 2001.

[16]   M. Peters and C. Leyens, Titanium and titanium alloys: Fundamentals and applications. John Wiley & Sons, 2003.

[17]   P. Heinl, L. Müller, C. Körner, R. F. Singer, and F. A. Müller, "Cellular Ti–6Al–4V structures with interconnected macro porosity for bone implants fabricated by selective electron beam melting," Acta Biomaterialia, vol. 4, no. 5, pp. 1536–1544, Sep. 2008.

[18]   J. Breme, E. Eisenbarth, and V. Biehl, Titanium and its Alloys for Medical Applications. Weinheim, FRG: John Wiley & Sons, Ltd, 2005.

[19]   E. O. Ezugwu, D. A. Fadare, J. Bonney, R. B. Da Silva, and W. F. Sales, "Modelling the correlation between cutting and process parameters in high-speed machining of Inconel 718 alloy using an artificial neural network," International Journal of Mechanical Sciences, vol. 45, no. 12, pp. 1375–1385, 2005.

[20]   M. Peters, J. Kumpfert, C. H. Ward, and C. Leyens, "Titanium Alloys for Aerospace Applications," Advanced Engineering Materials, vol. 5, no. 6, pp. 419–427, 2003.

[21]   E. O. Ezugwu, Z. M. Wang, and A. R. Machado, "The machinability of nickel-based alloys: a review," Journal of Materials Processing Tech., vol. 86, no. 1, pp. 1–16, 1999.

[22]   E. O. Ezugwu, J. Bonney, R. B. Da Silva, and O. Çakir, "Surface integrity of finished turned Ti–6Al–4V alloy with PCD tools using conventional and high pressure coolant supplies," International Journal of Mechanical Sciences, vol. 47, no. 6, pp. 884–891, 2007.

[23]   D. Ulutan and T. Özel, "Machining induced surface integrity in titanium and nickel alloys A review," International Journal of Mechanical Sciences, vol. 51, no. 3, pp. 250–280, 2011.

[24]   A. Shokrani, V. Dhokia, and S. T. Newman, "Investigation of the effects of cryogenic machining on surface integrity in CNC end milling of Ti–6Al–4V titanium alloy," Journal of Manufacturing Processes, vol. 21, pp. 172–179, 2016.

[25]   K. Moussaoui, M. Mousseigne, J. Senatore, R. Chieragatti, and F. Monies, "Influence of milling on surface integrity of Ti6Al4V—study of the metallurgical characteristics: microstructure and microhardness," Int J Adv Manuf Technol, vol. 67, no. 5, pp. 1477–1489, 2012.

[26]   C. H. Che-Haron and A. Jawaid, "The effect of machining on surface integrity of titanium alloy Ti–6% Al–4% V," Journal of Materials Processing Technology, vol. 166, no. 2, pp. 188–192, 2005.

[27]   M. B. Mhamdi, M. Boujelbene, E. Bayraktar, and A. Zghal, "Surface Integrity of Titanium Alloy Ti-6Al-4 V in Ball end Milling," Physics Procedia, vol. 25, pp. 355–362, 2012.

[28]   E. A. Rahim and H. Sasahara, "Investigation of tool wear and surface integrity on MQL machining of Ti-6AL-4V using biodegradable oil," Proceedings of the Institution of Mechanical Engineers, Part B: Journal of Engineering Manufacture, vol. 225, no. 9, pp. 1505–1511, 2011.

[29]   J. I. Hughes, A. R. C. Sharman, and K. Ridgway, "The effect of tool edge preparation on tool life and workpiece surface integrity," Proceedings of the Institution of Mechanical Engineers, Part B: Journal of Engineering Manufacture, vol. 218, no. 9, pp. 1113–1123, 2005.

[30]   F. Wang, J. Zhao, A. Li, and J. Zhao, "Experimental Study on Cutting Forces and Surface Integrity in High-Speed Side Milling of Ti-6Al-4V Titanium Alloy," Machining Science and Technology, vol. 18, no. 3, pp. 448–463, 2014.

[31] J. L. Cantero, M. M. Tardio, J. A. Canteli, M. Marcos, and M. H. Miguélez, "Dry drilling of alloy Ti–6Al–4V," International Journal of Mechanical Sciences, vol. 45, no. 11, pp. 1246–1255, 2005.

[32] R. Li, L. Riester, T. R. Watkins, P. J. Blau, and A. J. Shih, "Metallurgical analysis and nanoindentation characterization of Ti–6Al–4V workpiece and chips in high-throughput drilling," Materials Science & Engineering A, vol. 472, no. 1, pp. 115–124, 2008.

[33] G. Rotella, O. W. Dillon, D. Umbrello, L. Settineri, and I. S. Jawahir, "The effects of cooling conditions on surface integrity in machining of Ti6Al4V alloy," Int J Adv Manuf Technol, vol. 71, no. 1, pp. 47–55, 2013.

[34] J. Sun and Y. B. Guo, "A comprehensive experimental study on surface integrity by end milling Ti–6Al–4V," Journal of Materials Processing Technology, vol. 209, no. 8, pp. 4036–4042, 2009.

[35] J. C. Outeiro, D. Umbrello, R. M'Saoubi, and I. S. Jawahir, "Evaluation of present numerical models for predicting metal cutting performance and residual stresses," Machining Science and Technology, vol. 19, no. 2, pp. 183–216, 2015.

[36] A. W. Warren and Y. B. Guo, "Machined surface properties determined by nanoindentation: Experimental and FEA studies on the effects of surface integrity and tip geometry," Surface and Coatings Technology, vol. 201, no. 1, pp. 423–433, 2006.

[37] K. J. TRIGGER, "An Analytical Evaluation of Metal-Cutting Temperatures," Trans. ASME, vol. 73, p. 57, 1951.

[38] H. BLOK, "Theoretical Study of Temperature Rise at Surfaces of Actual Contact under Oiliness Lubricating Conditions," Proc. Instn. Mech. Engrs. (General discussion on lubrication and lubricants), vol. 2, p. 222, 1937.

[39] H. T. Young and T. L. Chou, "Modelling of tool/chip interface temperature distribution in metal cutting," International Journal of Mechanical Sciences, vol. 36, no. 10, pp. 931–943, 1994.

[40] R. Radulescu and S. G. Kapoor, "An Analytical Model for Prediction of Tool Temperature Fields during Continuous and Interrupted Cutting," J. Eng. Ind, vol. 116, no. 2, pp. 135–143, 1994.

[41] K. W. Kim and H.-C. Sins, "Development of a thermo-viscoplastic cutting model using finite element method," International Journal of Mechanical Sciences, vol. 36, no. 3, pp. 379–397, 1996.

[42] T. Moriwaki, N. Sugimura, and S. Luan, "Combined Stress, Material Flow and Heat Analysis of Orthogonal Micromachining of Copper," CIRP Annals - Manufacturing Technology, vol. 42, no. 1, pp. 75–78, 1993.

[43] S. Lei, Y. C. Shin, and F. P. Incropera, "Thermo-mechanical modeling of orthogonal machining process by finite element analysis," International Journal of Mechanical Sciences, vol. 39, no. 5, pp. 731–750, 1999.

[44] T. Özel, "The influence of friction models on finite element simulations of machining," International Journal of Mechanical Sciences, vol. 46, no. 5, pp. 518–530, 2006.

[45] N. N. Zorev, "Inter-relationship between shear processes occurring along tool face and shear plane in metal cutting," International research in production engineering, vol. 49, pp. 143–152, 1963.

[46]   E. Usui and T. Shirakashi, "Mechanics of machining—from descriptive to predictive theory," On the Art of Cutting Metals—75 Years Later, vol. 7, pp. 13–35, 1982.

[47]   M. H. Dirikolu, T. H. C. Childs, and K. Maekawa, "Finite element simulation of chip flow in metal machining," International Journal of Mechanical Sciences, vol. 43, no. 11, pp. 2699–2713, 2001.

[48]   T. Childs, K. Maekawa, T. Obikawa, and Y. Yamane, "Metal machining: theory and applications," 2000.

[49]   E. M. Trent and P. K. Wright, Metal cutting. Butterworth-Heinemann, 2000.

[50]   E. Ceretti, M. Lucchi, and T. Altan, "FEM simulation of orthogonal cutting: serrated chip formation," Journal of Materials Processing Tech., vol. 95, no. 1, pp. 17–26, 1999.

[51]   H. Bil, S. E. Kılıç, and A. E. Tekkaya, "A comparison of orthogonal cutting data from experiments with three different finite element models," International Journal of Mechanical Sciences, vol. 44, no. 9, pp. 933–944, 2004.

[52]   J. Limido, C. Espinosa, M. Salaün, and J. L. Lacome, "SPH method applied to high speed cutting modelling," International Journal of Mechanical Sciences, vol. 49, no. 7, pp. 898–908, 2007.

[53]   Y. Xi, M. Bermingham, G. Wang, and M. Dargusch, "SPH/FE modeling of cutting force and chip formation during thermally assisted machining of Ti6Al4V alloy," Computational Materials Science, vol. 84, pp. 188–197, 2014.

[54]   I. S. Jawahir, E. Brinksmeier, R. M'Saoubi, D. K. Aspinwall, J. C. Outeiro, D. Meyer, D. Umbrello, and A. D. Jayal, "Surface integrity in material removal processes: Recent advances," CIRP Annals - Manufacturing Technology, vol. 60, no. 2, pp. 603–626, 2011.

[55]   G. R. Johnson and W. H. Cook, "Fracture characteristics of three metals subjected to various strains, strain rates, temperatures and pressures," Engineering Fracture Mechanics, vol. 21, no. 1, pp. 31–48, 1985.

[56]   H. Pan, J. Liu, Y. Choi, C. Xu, Y. Bai, and T. Atkins, "Zones of material separation in simulations of cutting," International Journal of Mechanical Sciences, vol. 115, no. C, pp. 262–279, 2016.

[57]   Y. Zhang, J. C. Outeiro, and T. Mabrouki, "On the Selection of Johnson-cook Constitutive Model Parameters for Ti-6Al-4V Using Three Types of Numerical Models of Orthogonal Cutting," Procedia CIRP, vol. 31, pp. 112–117, 2015.

[58]   S. B. Yang, J. Xu, Y. Fu, and W. Wei, "Finite element modeling of machining of hydrogenated Ti-6Al-4V alloy," Int J Adv Manuf Technol, vol. 59, no. 1, pp. 253–261, 2012.

[59]   M. G. Cockcroft and D. J. Latham, "Ductility and the workability of metals," J Inst Metals, vol. 96, no. 1, pp. 33–39, 1968.

[60]   D. Umbrello, R. M'Saoubi, and J. C. Outeiro, "The influence of Johnson–Cook material constants on finite element simulation of machining of AISI 316L steel," International Journal of Mechanical Sciences, vol. 47, no. 3, pp. 462–470, 2007.

[61]   K. S. V. Sekar and M. P. Kumar, "Finite element simulations of Ti6Al4V titanium alloy machining to assess material model parameters of the Johnson-Cook constitutive equation," Journal of the Brazilian Society of Mechanical Sciences and Engineering, vol. 33, no. 2, pp. 203–211, 2011.

[62]   Y. Bao and T. Wierzbicki, "On fracture locus in the equivalent strain and stress triaxiality space," International Journal of Mechanical Sciences, vol. 46, no. 1, pp. 81–98, 2004.

[63]   B. Wang and Z. Liu, "Evaluation on fracture locus of serrated chip generation with stress triaxiality in high speed machining of Ti6Al4V," Materials and Design, vol. 98, no. C, pp. 68–78, 2016.

[64]   M. L. Wilkins, R. D. Streit, and J. E. Reaugh, "Cumulative-strain-damage model of ductile fracture: simulation and prediction of engineering fracture tests," 1980.

[65]   J. Liu, Y. Bai, and C. Xu, "Evaluation of Ductile Fracture Models in Finite Element Simulation of Metal Cutting Processes," J. Manuf. Sci. Eng., vol. 136, no. 1, pp. 011010–14, 2014.

[66]   A. Hillerborg, M. Modéer, and P. E. Petersson, "Analysis of crack formation and crack growth in concrete by means of fracture mechanics and finite elements," Cement and Concrete Research, vol. 6, no. 6, pp. 773–781, 1976.

[67]   T. Mabrouki, F. Girardin, M. Asad, and J.-F. Rigal, "Numerical and experimental study of dry cutting for an aeronautic aluminium alloy (A2024-T351)," International Journal of Mechanical Sciences, vol. 48, no. 11, pp. 1187–1197, 2008.

[68]   G. Chen, C. Ren, X. Yang, X. Jin, and T. Guo, "Finite element simulation of high-speed machining of titanium alloy (Ti–6Al–4V) based on ductile failure model," Int J Adv Manuf Technol, vol. 56, no. 9, pp. 1027–1038, 2011.

[69]   M. Calamaz, D. Coupard, and F. Girot, "A new material model for 2D numerical simulation of serrated chip formation when machining titanium alloy Ti–6Al–4V," International Journal of Mechanical Sciences, vol. 48, no. 3, pp. 275–288, 2008.

[70]   G. Rotella and D. Umbrello, "Finite element modeling of microstructural changes in dry and cryogenic cutting of Ti6Al4V alloy," CIRP Annals - Manufacturing Technology, vol. 63, no. 1, pp. 69–72, 2014.

[71]   Q. Wang, Z. Liu, B. Wang, Q. Song, and Y. Wan, "Evolutions of grain size and micro-hardness during chip formation and machined surface generation for Ti-6Al-4V in high-speed machining," Int J Adv Manuf Technol, vol. 82, no. 9, pp. 1725–1736, 2015.

[72]   D. Umbrello, S. Rizzuti, J. C. Outeiro, R. Shivpuri, and R. M'Saoubi, "Hardness-based flow stress for numerical simulation of hard machining AISI H13 tool steel," Journal of Materials Processing Technology, vol. 199, no. 1, pp. 64–73, 2008.

[73]   S. Buchkremer, B. Wu, D. Lung, S. Münstermann, F. Klocke, and W. Bleck, "FE-simulation of machining processes with a new material model," Journal of Materials Processing Tech., vol. 214, no. 3, pp. 599–611, 2014.

[74]   Y. Bai and T. Wierzbicki, "A new model of metal plasticity and fracture with pressure and Lode dependence," International Journal of Plasticity, vol. 24, no. 6, pp. 1071–1096, 2008.

[75]   F. J. Zerilli and R. W. Armstrong, "Dislocation-mechanics-based constitutive relations for material dynamics calculations," Journal of Applied Physics, vol. 61, no. 5, pp. 1816–1825, 1987.

[76]   R. Liu, S. Melkote, R. Pucha, J. Morehouse, X. Man, and T. Marusich, "An enhanced constitutive material model for machining of Ti–6Al–4V alloy," Journal of Materials Processing Tech., vol. 213, no. 12, pp. 2238–2246, 2013.

[77] P. S. Follansbee and U. F. Kocks, "A constitutive description of the deformation of copper based on the use of the mechanical threshold stress as an internal state variable," Acta Metallurgica, vol. 36, no. 1, pp. 81–93, 1988.

[78] S. N. Melkote, R. Liu, P. Fernandez-Zelaia, and T. Marusich, "A physically based constitutive model for simulation of segmented chip formation in orthogonal cutting of commercially pure titanium," CIRP Annals - Manufacturing Technology, vol. 64, no. 1, pp. 65–68, 2015.

[79] N. Allahverdizadeh, A. Gilioli, A. Manes, and M. Giglio, "An experimental and numerical study for the damage characterization of a Ti–6AL–4V titanium alloy," International Journal of Mechanical Sciences, vol. 93, no. C, pp. 32–47, 2015.

[80] N. Kotkunde, H. N. Krishnamurthy, P. Puranik, A. K. Gupta, and S. K. Singh, "Microstructure study and constitutive modeling of Ti6Al4V alloy at elevated temperatures," Materials and Design, vol. 54, no. C, pp. 96–103, 2014.

[81] J. M. Huang and J. T. Black, "An Evaluation of Chip Separation Criteria for the FEM Simulation of Machining," American Society of Mechanical Engineers, 1996.

[82] M. Sima and T. Özel, "Modified material constitutive models for serrated chip formation simulations and experimental validation in machining of titanium alloy Ti–6Al–4V," International Journal of Mechanical Sciences, vol. 50, no. 11, pp. 943–960, 2010.

[83] T. dos Santos, J. C. Outeiro, R. Rossi, and P. Rosa, "A New Methodology for Evaluation of Mechanical Properties of Materials at Very High Rates of Loading," Procedia CIRP, vol. 58, pp. 481–486, 2017.

[84] B. Xu and X. Liu, Applied mechanics: elasticity and plasticity. Beijing: Tsinghua university press, 1995.

[85] M. Algarni, Y. Choi, and Y. Bai, "A unified material model for multiaxial ductile fracture and extremely low cycle fatigue of Inconel 718," International Journal of Fatigue, vol. 96, pp. 162–177, 2017.

[86] S. P. F. C. Jaspers and J. H. Dautzenberg, "Material behavior in conditions similar to metal cutting: flow stress in the primary shear zone," Journal of Materials Processing Tech., vol. 122, no. 2, pp. 322–330, 2002.

[87] R. Liang and A. S. Khan, "A critical review of experimental results and constitutive models for BCC and FCC metals over a wide range of strain rates and temperatures," International Journal of Plasticity, vol. 15, no. 9, pp. 963–980, 1999.

[88] L. Denguir, J. C. Outeiro, G. Fromentin, V. Vignal, and R. Besnard, "A physical-based constitutive model for surface integrity prediction in machining of OFHC copper," Journal of Materials Processing Tech., vol. 248, pp. 143–160, 2017.

[89] A. Bejan, Heat transfer. NewYork: John Wiley & Sons, 1993.

[90] J. R. Rice and D. M. Tracey, "On the ductile enlargement of voids in triaxial stress fields," Journal of the Mechanics and Physics of Solids, vol. 17, no. 3, pp. 201–217, 1969.

[91] Y. M. Abushawashi, X. Xiao, and V. Astakhov, "A novel approach for determining material constitutive parameters for a wide range of triaxiality under plane strain loading conditions," International Journal of Mechanical Sciences, vol. 74, no. C, pp. 133–142, 2013.

[92] M. Giglio, A. Manes, and F. Viganò, "Ductile fracture locus of Ti–6Al–4V titanium alloy," International Journal of Mechanical Sciences, vol. 54, no. 1, pp. 121–135, 2012.

[93] Y. Bai and T. Wierzbicki, "A comparative study of three groups of ductile fracture loci in the 3D space," Engineering Fracture Mechanics, vol. 135, pp. 1–21, 2015.

[94] B. Erice and F. Gálvez, "A coupled elastoplastic-damage constitutive model with Lode angle dependent failure criterion," International Journal of Solids and Structures, vol. 51, no. 1, pp. 93–110, 2014.

[95] L. Xue and T. Wierzbicki, "Numerical simulation of fracture mode transition in ductile plates," International Journal of Solids and Structures, vol. 46, no. 6, pp. 1423–1435, 2009.

[96] Y. Bai, X. Teng, and T. Wierzbicki, "Study on the effect of the third stress invariant on ductile fracture," Report,Cambridge, 2006.

[97] Y. Bai and T. Wierzbicki, "Application of extended Mohr–Coulomb criterion to ductile fracture," Int J Fract, vol. 161, no. 1, pp. 1–20, 2009.

[98] M. Algarni, Y. Bai, and Y. Choi, "A study of Inconel 718 dependency on stress triaxiality and Lode angle in plastic deformation and ductile fracture," Engineering Fracture Mechanics, vol. 147, no. C, pp. 140–157, 2015.

[99] Y. M. Abushawashi, "Modeling of metal cutting as purposeful fracture of work material," Thesis, Michigan State University, Michigan, 2013.

[100] ASTM E112-12, "Standard Test Methods for Determining Average Grain Size," 2012.

[101] M. Dunand and D. Mohr, "Optimized butterfly specimen for the fracture testing of sheet materials under combined normal and shear loading," Engineering Fracture Mechanics, vol. 78, no. 17, pp. 2919–2934, 2011.

[102] ASTM E209, "Standard practice for compression tests of metallic materials at elevated temperatures with conventional or rapid heating rates and strain rates," ASTM, 2010.

[103] ISO 3002-1: 1982, "Tensile Testing: Initial Experience from the Practical Implementation of the New Standard," 2009.

[104] C. Su and L. Anand, "A new digital image correlation algorithm for whole-field displacement measurement," 2003.

[105] H. W. Meyer Jr and D. S. Kleponis, "Modeling the high strain rate behavior of titanium undergoing ballistic impact and penetration," International Journal of Impact Engineering, vol. 26, no. 1, pp. 509–521, 2001.

[106] W.-S. Lee and C.-F. Lin, "High-temperature deformation behavior of Ti6Al4V alloy evaluated by high strain-rate compression tests," Journal of Materials Processing Tech., vol. 75, no. 1, pp. 127–136, 1998.

[107] D. Leseur, "Experimental investigations of material models for Ti-6A1-4V and 2024-T3," May 1999.

[108] N. Stander, W. ROUX, T. Eggleston, and K. Craig, "LS-OPT user's manual–a design optimization and probabilistic analysis tool for the engineering analyst," Livermore Software Technology Corporation, Livermore, 2007.

[109] K. Witowski, M. Feucht, and N. Stander, "An effective curve matching metric for parameter identification using partial mapping," th European LS-DYNA Users Conference, pp. 1–12, 2011.

[110] C. Courbon, F. Pusavec, F. Dumont, J. Rech, and J. Kopac, "Influence of cryogenic lubrication on the tribological properties of Ti6Al4V and Inconel 718 alloys under extreme contact conditions," Lubr. Sci., vol. 26, no. 5, pp. 315–326, 2014.

[111] B. Bettonvil and J. P. Kleijnen, "Searching for important factors in simulation models with many factors: Sequential bifurcation," European Journal of Operational Research, vol. 96, no. 1, pp. 180–194, 1997.

[112] J. P. Davim, Design of experiments in production engineering. Springer, 2016.

[113] M. R. Dahman, "AMSM-Multivariate Inferential Statistics-Chapter Eight," 2018.

[114] T. Baizeau, "Développements expérimentaux et numériques pour la caractérisation des champs cinématiques de la coupe de l'acier 100 CrMo 7 durci pour la prédiction de l'intégrité de surface," Thesis, Arts et Métiers ParisTech, 2016.

[115] G. Besnard, F. Hild, and S. Roux, "'Finite-element' displacement fields analysis from digital images: application to Portevin–Le Châtelier bands," Exp Mech, vol. 46, no. 6, pp. 789–803, 2006.

[116] J. Hou, W. Zhou, H. Duan, G. Yang, H. Xu, and N. Zhao, "Influence of cutting speed on cutting force, flank temperature, and tool wear in end milling of Ti-6Al-4V alloy," Int J Adv Manuf Technol, vol. 70, no. 9, pp. 1835–1845, 2014.

[117] C. F. Wyen and K. Wegener, "Influence of cutting edge radius on cutting forces in machining titanium," CIRP Annals - Manufacturing Technology, vol. 59, no. 1, pp. 93–96, 2010.

[118] ASTM E3-11, "Standard Guide for Preparation of Metallographic Specimens," 2011.

[119] M. Storchak, P. Rupp, H.-C. Möhring, and T. Stehle, "Determination of Johnson–Cook Constitutive Parameters for Cutting Simulations," Metals, vol. 9, no. 4, p. 473, 2019.

[120] C. Ren, Z. Ke, G. Chen, and J. Wu, "Modeling of tool-chip contact length for orthogonal cutting of Ti-6Al-4V alloy considering segmented chip formation," Transactions of Tianjin University, vol. 22, no. 6, pp. 525–535, 2016.

[121] S. A. Iqbal, P. T. Mativenga, and M. A. Sheikh, "A comparative study of the tool–chip contact length in turning of two engineering alloys for a wide range of cutting speeds," Int J Adv Manuf Technol, vol. 42, no. 1, p. 30, 2008.

[122] I. C. Noyan and J. B. Cohen, Residual stress: measurement by diffraction and interpretation. New York: Springer, 2013.

[123] D. I. Yameogo, "Étude expérimentale et modélisation multi-physique de l'évolution de la microstructure dans les procédés d'usinage de l'alliage de titane Ti-6Al-4V," Thesis, Université de Lorraine, 2019.

[124] Y. C. Zhang, T. Mabrouki, D. Nelias, and Y. D. Gong, "Chip formation in orthogonal cutting considering interface limiting shear stress and damage evolution based on fracture energy approach," Finite Elements in Analysis and Design, vol. 47, no. 7, pp. 850–863, Jul. 2011.

[125] L. Kops and M. Arenson, "Determination of Convective Cooling Conditions in Turning," CIRP Annals - Manufacturing Technology, vol. 48, no. 1, pp. 47–52, 1999.

[126] ISO 3002-1: 1982, "Basic quantities in cutting and grinding," 1982.

[127] S. Imbrogno, S. Sartori, A. Bordin, S. Bruschi, and D. Umbrello, "Machining simulation of Ti6Al4V under dry and cryogenic conditions," Procedia CIRP, vol. 58, pp. 475–480, 2017.

[128] J. Rech and A. Moisan, "Surface integrity in finish hard turning of case-hardened steels," International Journal of Mechanical Sciences, vol. 43, no. 5, pp. 543–550, 2003.

[129] T. Özel and D. Ulutan, "Prediction of machining induced residual stresses in turning of titanium and nickel based alloys with experiments and finite element simulations," CIRP Annals - Manufacturing Technology, vol. 61, no. 1, pp. 547–550, 2012.

[130] D. Ulutan, M. Sima, and T. Özel, "Prediction of Machining Induced Surface Integrity Using Elastic-Viscoplastic Simulations and Temperature-Dependent Flow Softening Material Models in Titanium and Nickel-Based Alloys," AMR, vol. 223, pp. 401–410, 2011.

[131] J. Holmberg, J. M. R. Prieto, J. Berglund, A. Sveboda, and P. Jonsén, "Experimental and PFEM-simulations of residual stresses from turning tests of a cylindrical Ti-6Al-4V shaft," Procedia CIRP, vol. 71, pp. 144–149, 2018.

[132] V. P. Astakhov, "On the inadequacy of the single-shear plane model of chip formation," International Journal of Mechanical Sciences, vol. 47, no. 11, pp. 1649–1672, Nov. 2005.

[133] M. A. Davies, Q. Cao, A. L. Cooks, and R. Ivester, "On the measurement and prediction of temperature fields In machining AISI 1045 steel," CIRP Annals - Manufacturing Technology, vol. 52, no. 1, pp. 77–80, 2003.

[134] V. P. Astakhov, "Tribology of metal cutting," vol. 52, 2006.

[135] M. C. Shaw and J. O. Cookson, "Metal cutting principles," vol. 2, 2005.

[136] E. P. Whitenton and E. P. Whitenton, "High-speed dual-spectrum imaging for the measurement of metal cutting temperatures," National Institute of Standards and Technology, NISTIR No. 7650, 2010.

.

Appendix

Appendix A – Specimen drawings and geometry inspection

Different specimens are designed to cover a wide range of state of stress, including the cylindrical specimens, double notched specimens, round bars and notched flat plates. Firstly, the technical drawing s and geometry inspection are performed for the double notched specimens. There are 5 different dimensions, and each dimension has one replica. Fig. 116 - Fig. 120 show the comparison between measured results and tolerances of drawing for double notched specimens. Fig. 121 - Fig. 123 and Fig. 124 - Fig. 125 present the geometry inspections for the round bars and notched flat plates, respectively.
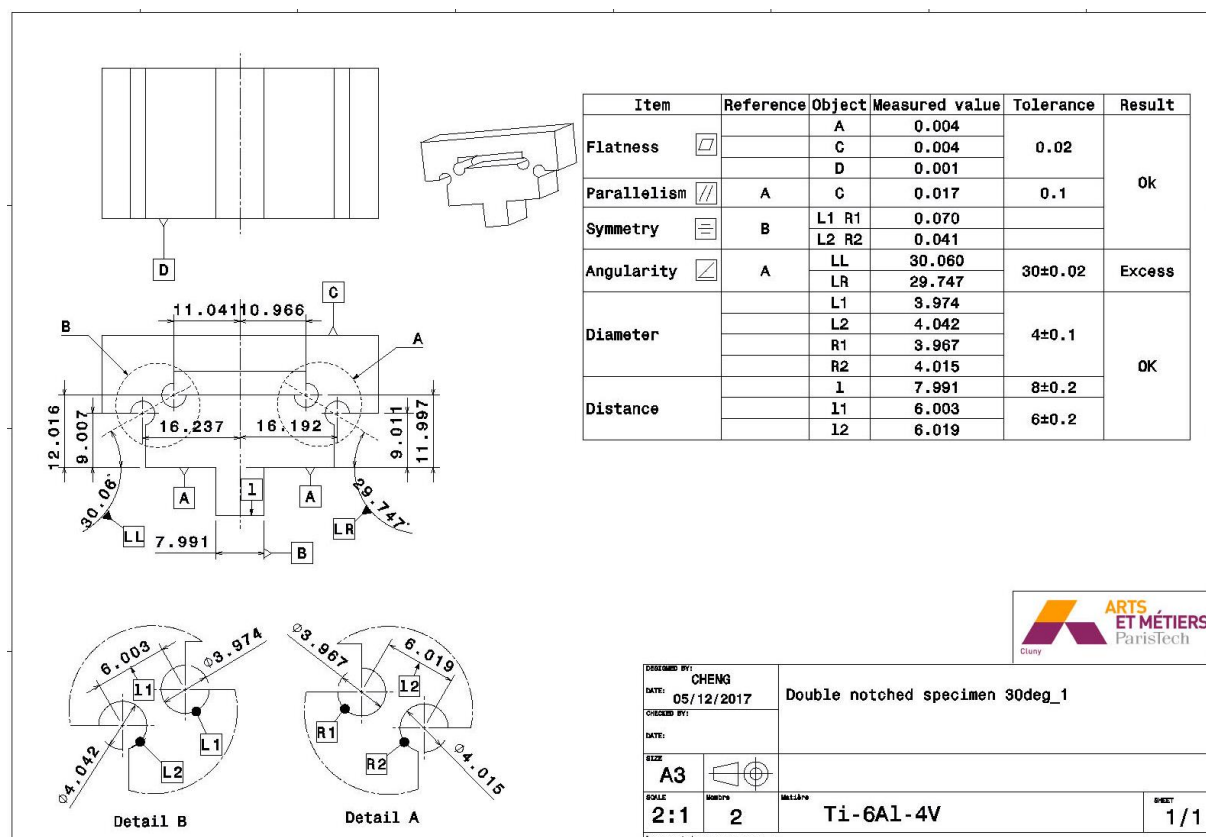

Fig. 116: Geometry inspections for double notched specimens with pressure angle 30º.
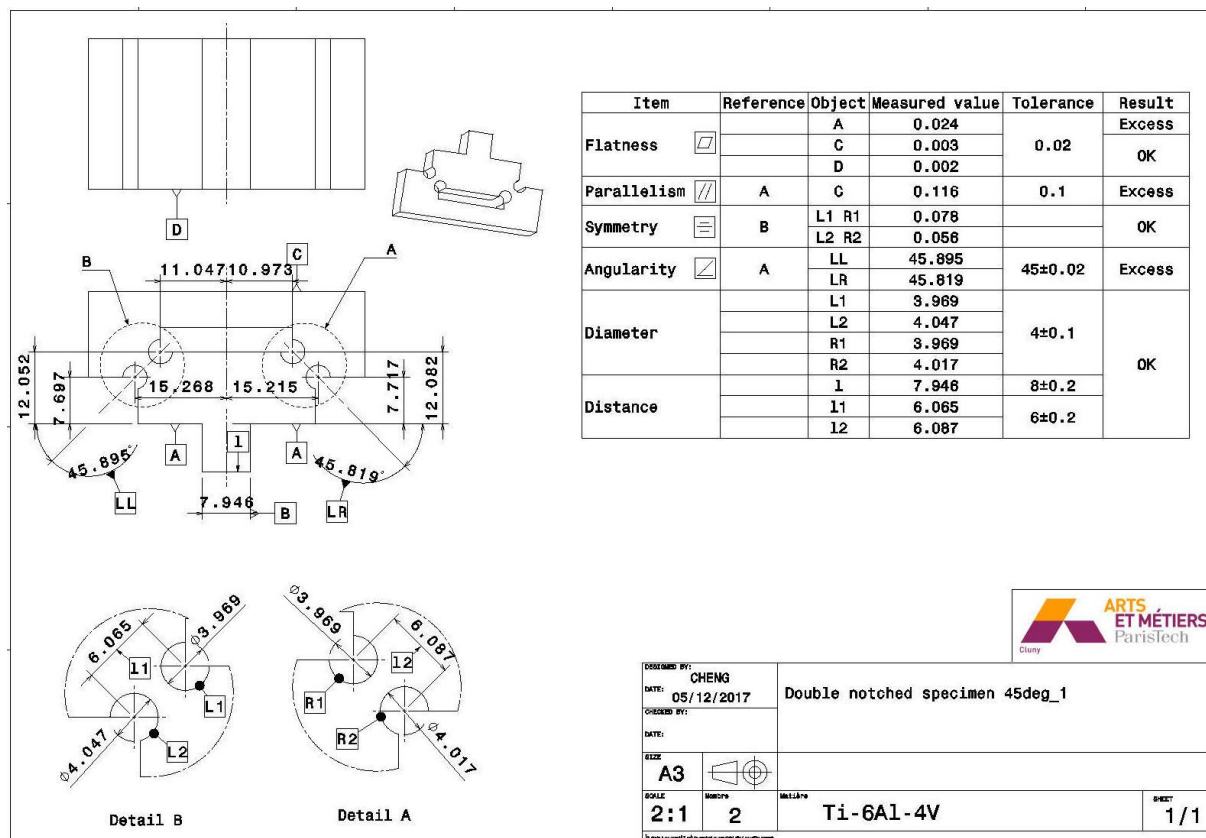
Item	Reference	Object	Measured value	Tolerance	Result
Flatness		A	0.024		Excess
		C	0.003	0.02	OK
		D	0.002		
Parallelism	A	C	0.116	0.1	Excess
Symmetry	B	L1 R1	0.078		OK
		L2 R2	0.056		
Angularity	A	LL	45.895	45±0.02	Excess
		LR	45.819		
Diameter		L1	3.969		
		L2	4.047	4±0.1	
		R1	3.969		
		R2	4.017		OK
Distance		l	7.946	8±0.2	
		l1	6.065	6±0.2	
		l2	6.087		

Fig. 117: Geometry inspections for double notched specimens with pressure angle 45º.

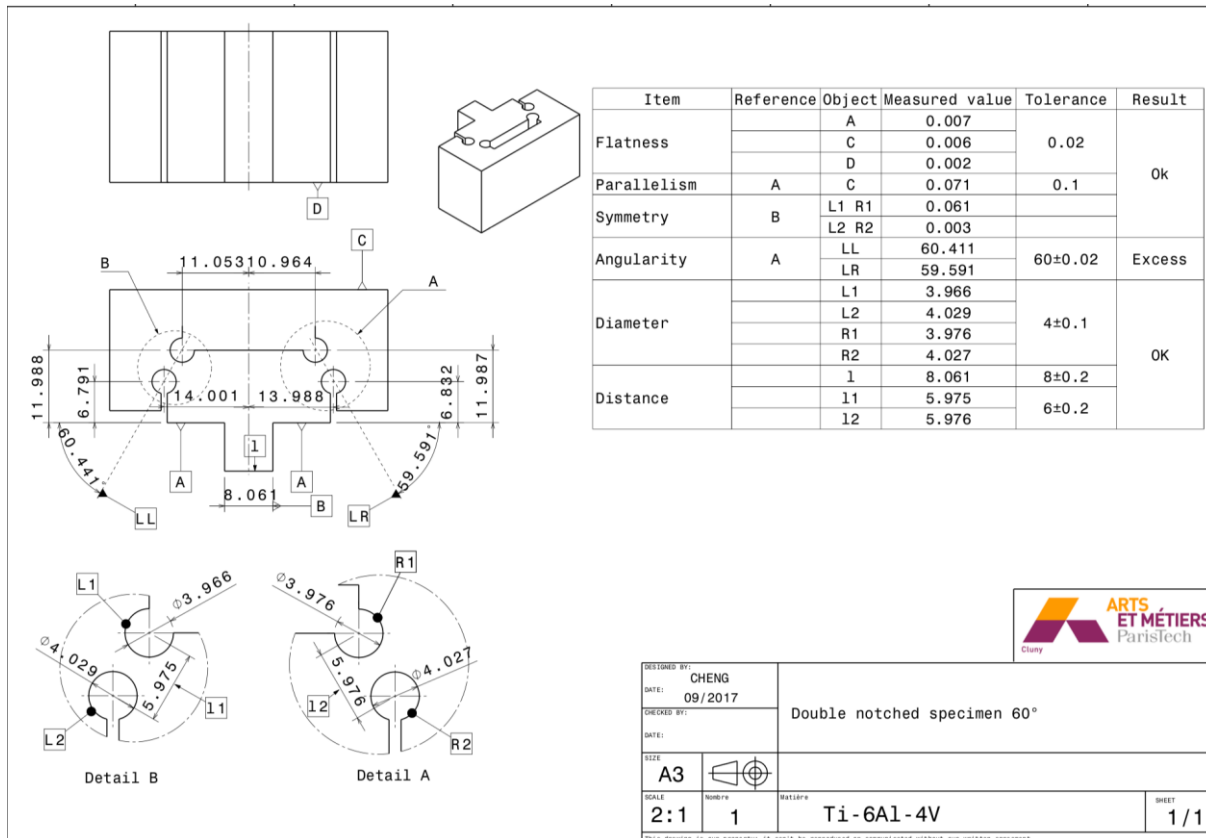| Item	Reference	Object	Measured value	Tolerance	Result
Flatness		A	0.007		
		C	0.006	0.02	
		D	0.002		Ok
Parallelism	A	C	0.071	0.1	
Symmetry	B	L1 R1	0.061		
		L2 R2	0.003		
Angularity	A	LL	60.411	60±0.02	Excess
		LR	59.591		
Diameter		L1	3.966		
		L2	4.029	4±0.1	
		R1	3.976		
		R2	4.027		OK
Distance		l	8.061	8±0.2	
		l1	5.975	6±0.2	
		l2	5.976		

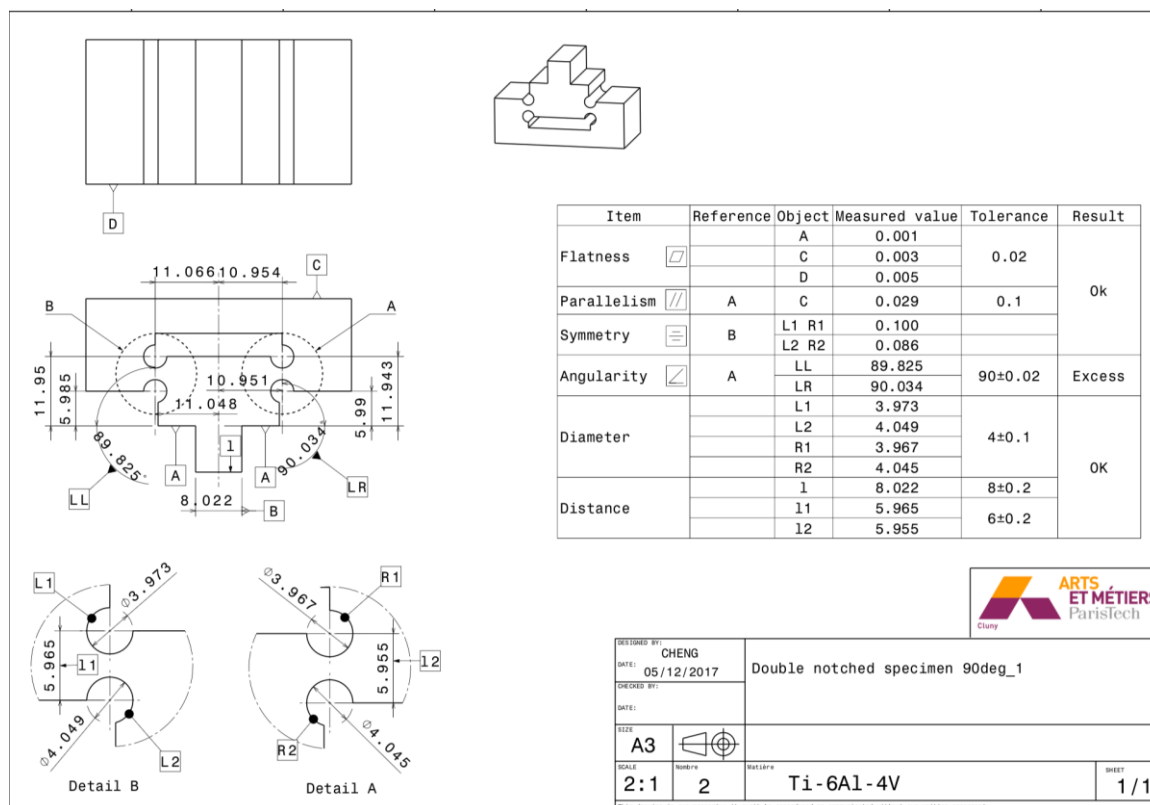Fig. 118: Geometry inspections for double notched specimens with pressure angle 60º.

Fig. 119: Geometry inspections for double notched specimens with pressure angle 90º.
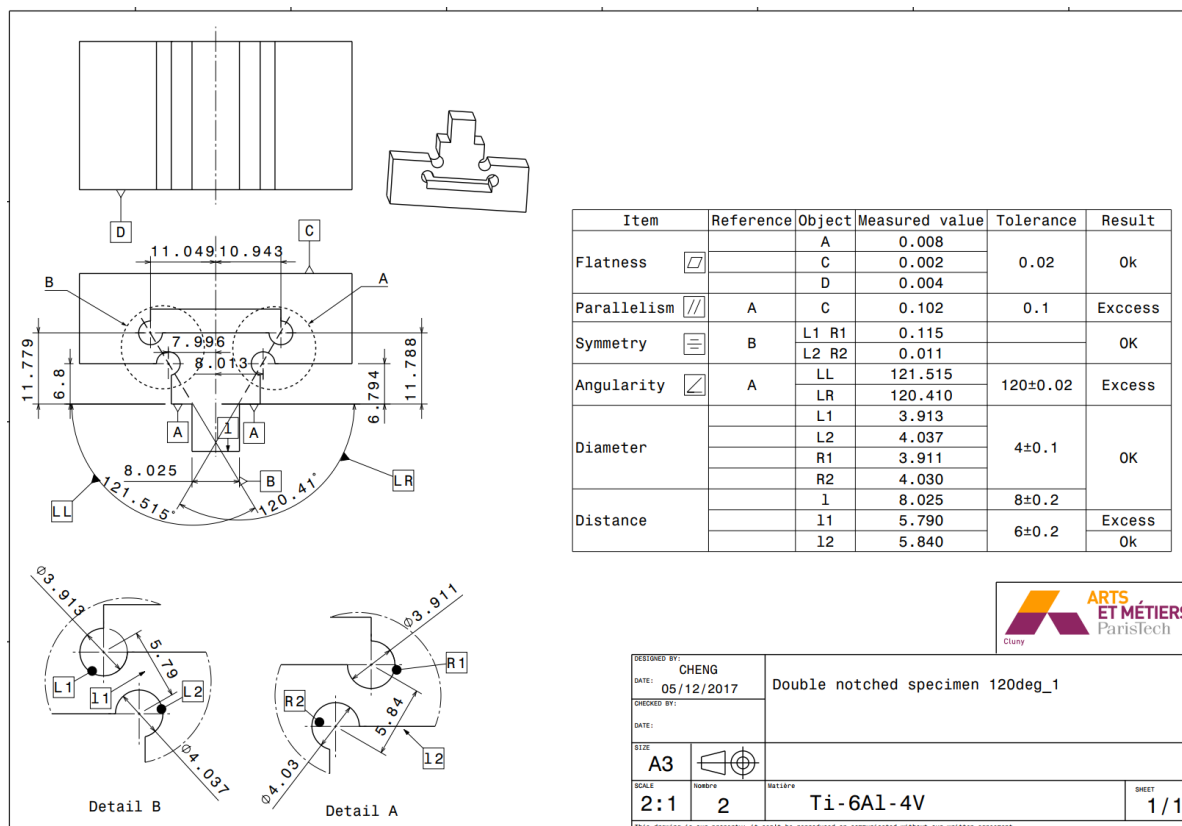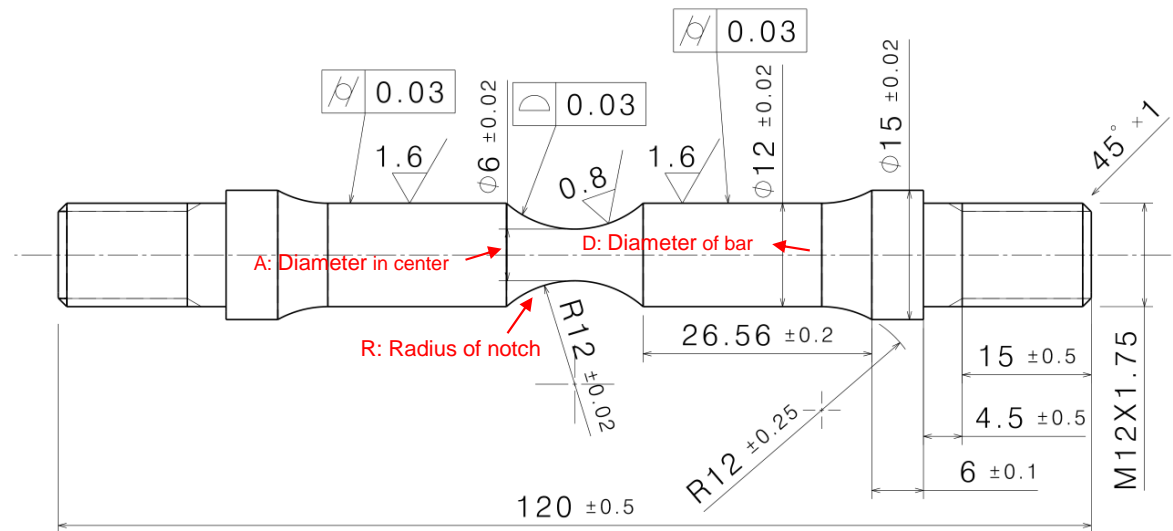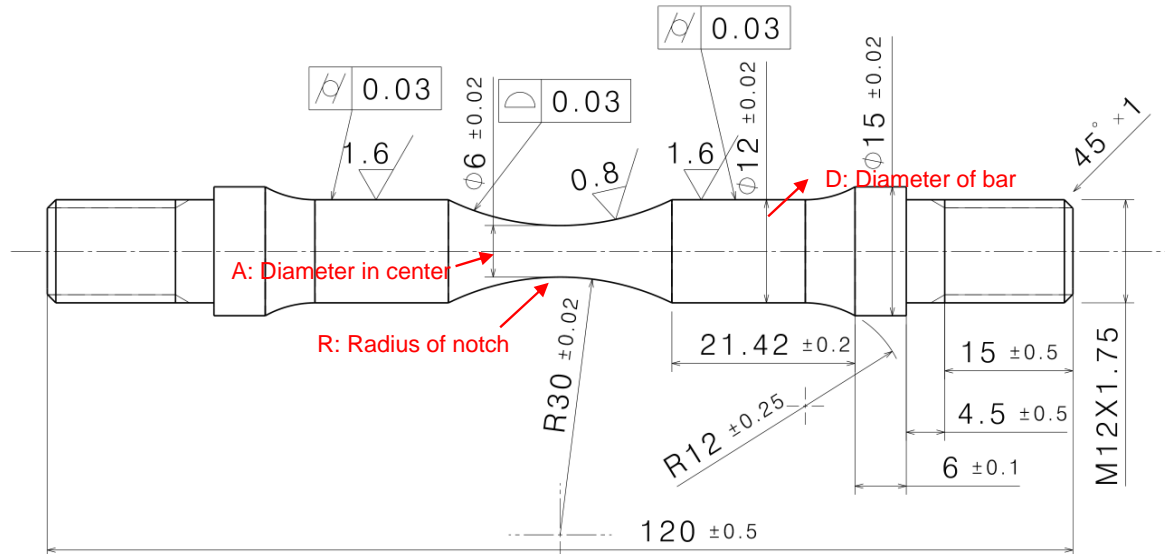

Fig. 120: Geometry inspections for double notched specimens with pressure angle 120º.
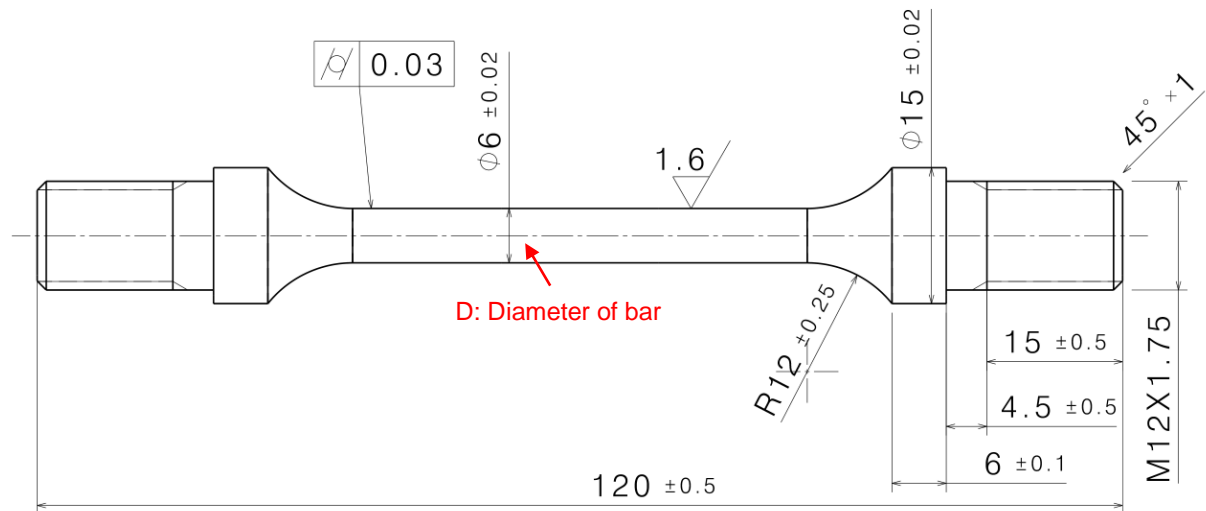
No.	A (mm)	R (mm)	D (mm)
#1	6,059 ± 0.007	12,044 ± 0.032	11,992 ± 0.006
#2	6,115 ± 0.005	12,042 ± 0.045	11,988 ± 0.002
#3	6,149 ± 0.001	12,049 ± 0.008	11,934 ± 0.018
#4	6,07 ± 0.000	12,044 ± 0.021	11,989 ± 0.007

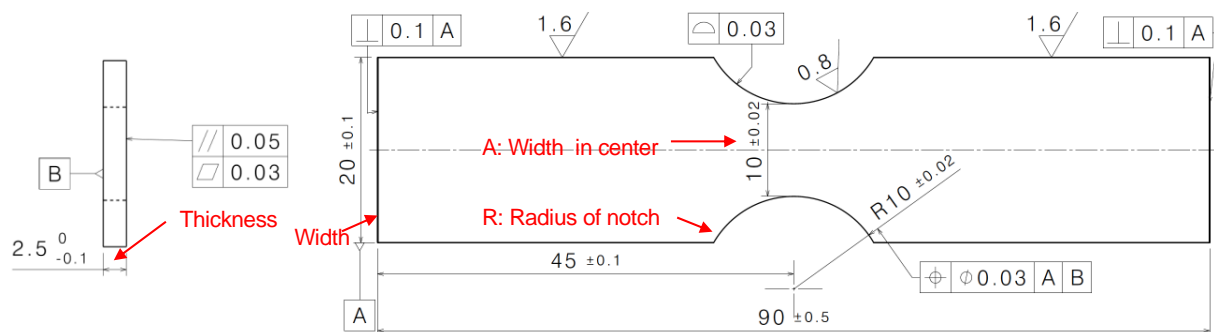Fig. 121: Results of the geometry inspection of round bars: NRB_R12.

No.	A (mm)	R (mm)	D (mm)
#1	6,145 ± 0.003	30,052 ± 0.061	11,982 ± 0.004
#2	6,108 ± 0.006	30,092 ± 0.030	11,984 ± 0.005
#3	6,111 ± 0.002	30,006 ± 0.048	11,976 ± 0.007
#4	6,080 ± 0.006	30,048 ± 0.057	11,985 ± 0.008

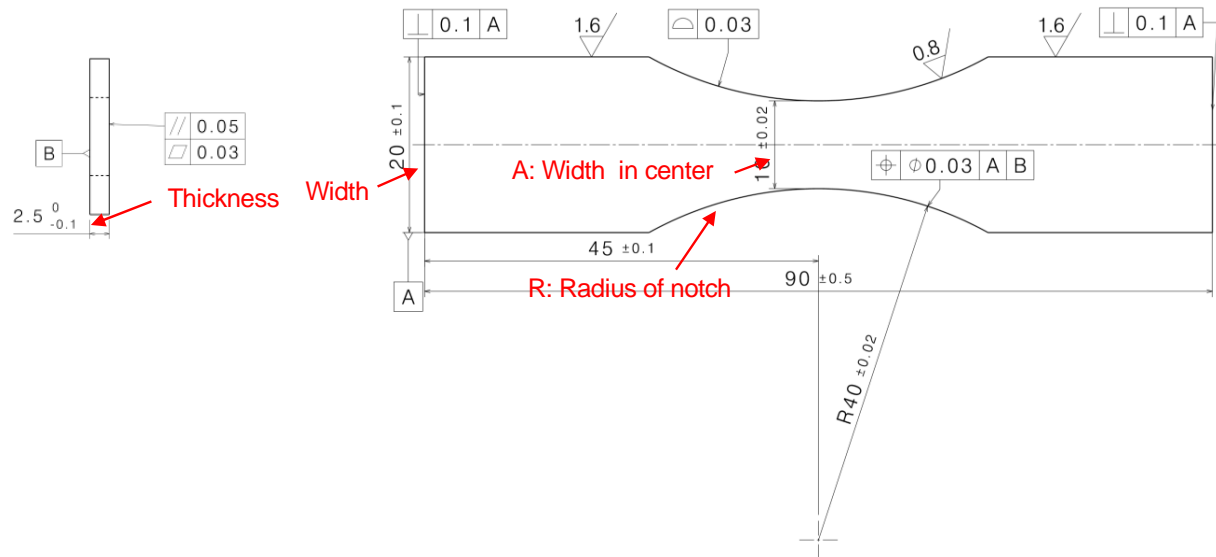Fig. 122: Results of the geometry inspection of round bars: NRB_R30.

No.	D (mm)
#1	5,986 ± 0.008
#2	5,99 ± 0.005
#3	5,998 ± 0.010
#4	5,984 ± 0.006

Fig. 123: Results of the geometry inspection of round bars: SMR.

No.	A (mm)	R (mm)	Thickness (mm)	Width (mm)
#1	9,774	10.036 ± 0.002	2,351 ± 0.011	19,700 ± 0.023
#2	9,732	10.014 ± 0.002	2,356 ± 0.013	19,627 ± 0.019
#3	9,866	9.999 ± 0.028	2,232 ± 0.008	19,735 ± 0.011
#4	9,910	10.010 ± 0.033	2,387 ± 0.003	19,729 ± 0.016

Fig. 124: Results of the geometry inspection of notched flat plates: NFP_10.

No.	A (mm)	R (mm)	Thickness (mm)	Width (mm)
#1	9,681	39.742 ± 0.021	2,351 ± 0.009	19,754 ± 0.007
#2	9,385	39.849 ± 0.042	2,351 ± 0.004	19,731 ± 0.023
#3	9,297	39.783 ± 0.051	2,368 ± 0.004	19,783 ± 0.009
#4	9,888	39.868 ± 0.123	2,270 ± 0.011	19,775 ± 0.003

Fig. 125: Results of the geometry inspection of notched flat plates: NFP_30.

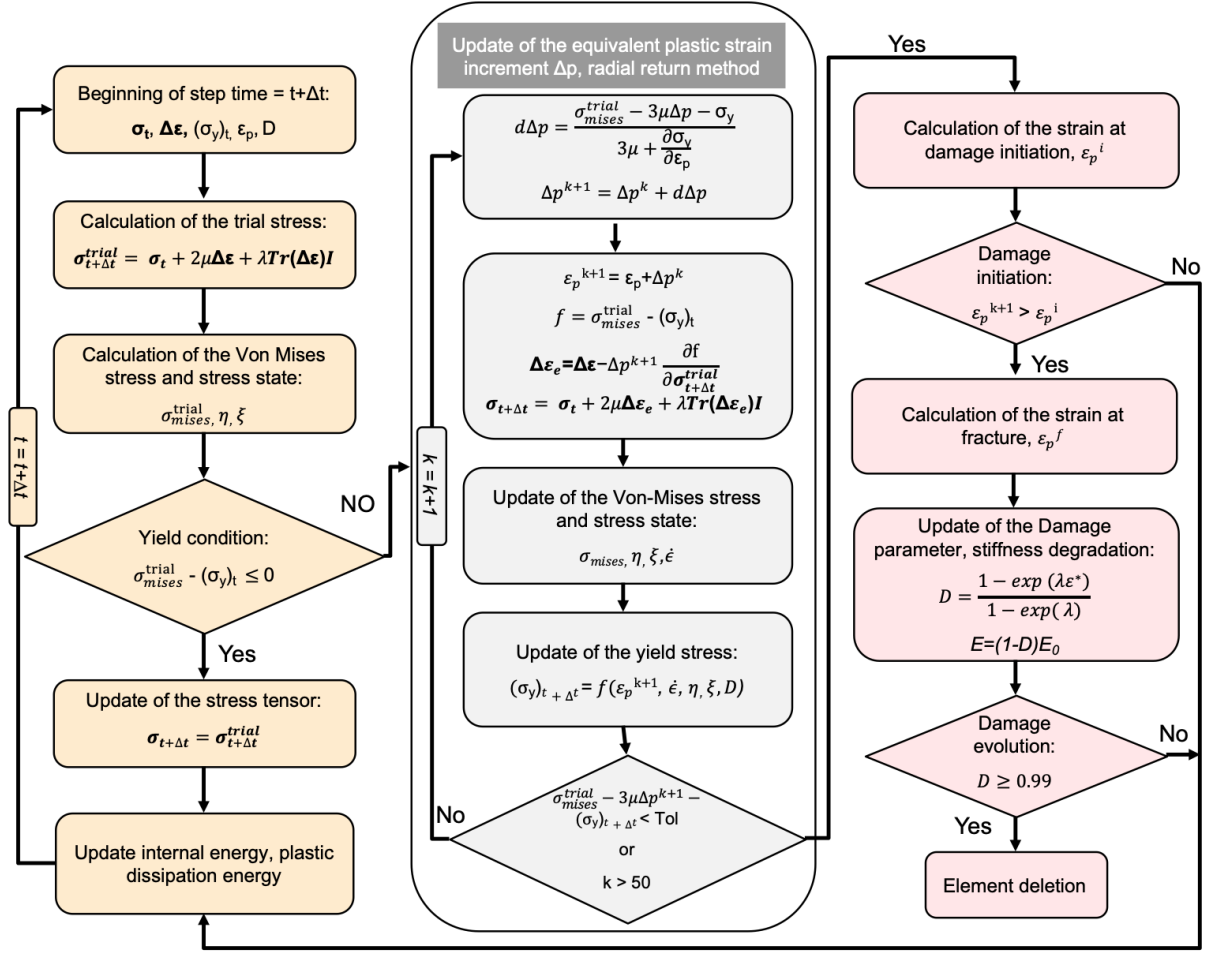# Appendix B – Structure of the subroutine

Fig. 126: Structure of subroutine used in the ABAQUS.

List of the publications related to the thesis

Journal paper:

- W. Cheng, J.C. Outeiro, J.-P. Costes, R. M'Saoubi, H. Karaouni, and V. Astakhov, "A constitutive model for Ti6Al4V considering the state of stress and strain rate effects", Mechanics of Materials, vol. 137, pp. 103103, Oct. 2019.

Conference proceedings:

- W. Cheng, J.C. Outeiro, J.-P. Costes, R. M'Saoubi, H. Karaouni, S. Dietrich, B. Marcon, and P. Rosa, "Optimization-based procedure for the determination of the constitutive model coefficients used in machining simulations", Procedia CIRP, vol. 82, pp. 374–378, 2019.

- W. Cheng, J.C. Outeiro, J.-P. Costes, R. M'Saoubi, H. Karaouni, L. Denguir, V. Astakhov, and F. Auzenat, "Constitutive model incorporating the strain-rate and state of stress effects for machining simulation of titanium alloy Ti6Al4V", Procedia CIRP, vol. 77, pp. 344–347, 2018.

- W. Cheng, J.C. Outeiro, J.-P. Costes, R. M'Saoubi, F. Auzenat, H. Karaouni, and V. Astakhov, "Machining simulation of titanium alloy Ti6Al4V using a constitutive model considering the state of stress and strain-rate effects", Proceedings of "Machines et Usinage à Grande Vitesse MUGV" conference, Bordeaux, pp.10, 2018.

Modélisation de l'usinage de l'alliage de titane Ti-6Al-4V utilisant un modèle constitutif prenant en compte l'état de contrainte dans la zone de déformation

RESUME

L'objectif de cette thèse est de proposer un modèle constitutif du comportement mécanique de l'alliage de titane Ti-6Al-4V et de l'appliquer à la simulation du procédé d'usinage. Ce modèle prend en compte les paramètres les plus influents sur le comportement mécanique (plasticité et endommagement) de l'alliage de titane Ti-6Al-4V lors de la coupe (l'état de contrainte et la vitesse de déformation). Des échantillons spéciaux ont été conçus pour générer une large gamme d'états de contrainte (triaxialité et angle de Lode) lors d'essais mécaniques, qui sont représentatifs du procédé de coupe. Une procédure d'optimisation a été développée pour déterminer avec précision les coefficients du modèle constitutif. La précision de ce modèle pour représenter le comportement mécanique de l'alliage Ti-6Al-4V sous différents états de contrainte a été confirmée en comparant les résultats expérimentaux aux simulés des essais mécaniques. Enfin, des modèles de la coupe orthogonale et du tournage de l'alliage Ti-6Al-4V, intégrant le modèle constitutif proposé, ont été développés et appliqués pour prévoir les forces, les températures, la géométrie des copeaux et l'intégrité de la surface usinée. La précision de ces modèles d'usinage a été évaluée en comparant les résultats simulés et expérimentaux.

Mots clés : Ti-6Al-4V ; modèle constitutif ; état de contrainte ; simulation de l'usinage ; intégrité de surface.

Modelling of machining of Ti-6Al-4V titanium alloy using a constitutive model accounting for the state of stress in the deformation zone

ABSTRACT

The aim of this thesis is to propose a constitutive model of Ti-6Al-4V titanium alloy and apply it to the metal cutting simulation. This constitutive model includes the most relevant parameters affecting the mechanical behavior (plasticity and damage) of Ti-6Al-4V titanium alloy in metal cutting (i.e. the state of stress and the strain-rate). Special specimens were designed to generate a wide range of states of stress (i.e. triaxiality and Lode angle) in mechanical testing, which are representative of the metal cutting process. An optimization-based procedure was developed to determine the coefficients of the constitutive model with high accuracy. The accuracy of the proposed constitutive model to describe the mechanical behavior of Ti-6Al-4V alloy under different states of stress was confirmed by comparing the experimental and simulated results of the mechanical tests. Finally, orthogonal cutting and turning models of Ti-6Al-4V including the proposed constitutive model were developed and applied to predict the forces, temperatures, chip geometry and the surface integrity in the machined surface and subsurface. The accuracy of these machining models was evaluated by comparing the simulated and experimental results.

Keywords: Ti-6Al-4V alloy; constitutive model; state of stress; machining simulation; surface integrity.

Arts et Métiers · Sciences et Technologies

HESAM UNIVERSITÉ